ZANCO Journal of Pure and Applied Sciences
The official scientific journal of Salahaddin University-Erbil
https://zancojournals.su.edu.krd/index.php/JPAS

ISSN (print):2218-0230, **ISSN (online):** 2412-3986, **DOI:** **http://dx.doi.org/10.21271/zjpas**

RESEARCH PAPER

Comparison of the water movement by Richard and Darcy

[1]Dana Khider Mawlood ,[2]Kurdistan Neyaz Adnan

1.Department of Civil, College of Engineering, Salahaddin University-Erbil, Kurdistan Region, Iraq.
2.Department of dams and water resources engineering, Salahaddin University-Erbil, Kurdistan Region, Iraq

ABSTRACT:

Simulations of water movement in the soil are pervasive, Darcy's law, Darcy- Buckingham's law and Richard's equation are all approved equations for this purpose. The Richard's equation is the most reliable model which is introduced by Lewis Richardson who was the first one to propose that Darcy's law was originally fabricated for flow in the saturated zone while for flow in vadose zone Darcy-Buckingham's law can be used in case of steady state condition. Since it is impossible in nature for flow to be steady, Richard proposed a highly nonlinear partial differential equation (PDE) equation which a combination of Darcy's law and continuity equation. Hydraulic conductivity $K(LT^{-1})$ and moisture content θ $(L^{3}L^{3})$ are two important variables of Richard's equation. Considering the nonlinearity of its variables Richard's equation lacks a general closed form solution. For this purpose, many researchers derived numerical and analytical models to solve Richard's equation. In this paper, Green Ampt Infiltration Equation is presented to solve Richard's equation which is one of the most widely used analytical methods.

KEY WORDS: Darcy law; Darcy- Buckingham law; Richard equation; Vadose zone; Green Ampt method.
DOI: http://dx.doi.org/10.21271/ZJPAS.32.1.1
ZJPAS (2020) , 32(1);1-6 .

1.INTRODUCTION :

The vadose zone is commonly called the unsaturated zone, the word vadose is derived from a Latin word vadosus, meaning shallow. Which is located between the land surface and the groundwater table. The Vadose zone is a three-phase system contains soil, air, and water (Ballestero et al., 2005).

Vadose zone is of great importance in understanding the groundwater condition, contamination transport, biological degradation. As it acts as a buffer zone between the land surface and aquifers by removing undesirable materials before reaching to aquifers (Selker et al., 1999).

Henry Darcy (1803-1858) a French scientist who was impressed by flow through a porous medium (Brown, 2002). Darcy designed a special experiment to quantum the flow rate comparing to other physical parameters. His finding the linear relation between pressure differences and the flow rate is of great importance for different scientific disciplines related to porous media. Darcy's law is recognized as the basic law for describing fluid flow in the saturated zone (Kovalchuk and Hadjistassou, 2019).

Edgar Buckingham [1907] was able to make Darcy's law applicable for the vadose zone by making some modifications on the law, where the maximum value at saturation θs is higher than actual water content in the medium θ. The fundamental hypothesis is that the saturated hydraulic conductivity Ks, can be replaced by a function of capillary pressure Ψor water content θ

---

* **Corresponding Author:**
Dana Khider Mawlood E-mail:
Article History: **dana.mawlood@su.edu.krd**
Received: 28/03/2019
Accepted: 15/09/2019
Published: 25/02 /2020

as the characteristic of the unsaturated porous medium. Buckingham's work comprises an achievement in the historical background of soil science and the movement of fluid in porous media ((Liu), (Narasimhan, 2007)).

There are two types of flow in nature steady state condition and transient state condition. In the steady state condition, Buckingham law is used where, the influx and outflux rate are equal while for transient state the influx and outflux are not equal in case of heavy rainfall large amount of water enters the soil, some of the water starts to evaporate lessening the amount of the original water by this the influx and outflux rates are different (Hou et al., 2019). Addressing the water in the column and also addressing the precipitation and the evaporation. To describe this, The term of Continuity equation is used that is the derivative of the volumetric water content in respect to time equals the derivative of the flow with respect to space $\frac{\partial \theta}{\partial t} = -\frac{\partial q}{\partial z}$ meaning that whatever changes in time need to be changed in space (Kuntz and Grathwohl, 2009). To describe flow in transient state condition under the action of capillary and gravity Richard combined aspects of Darcy's law and mass continuity law (Pinder and Celia, 2006), Richard obtained a nonlinear partial differential equation (PDE), defining the water flow both in the saturated and unsaturated porous media (Navon, 2009).

Due to the complicated relationship between hydraulic conductivity and infiltration parameters Richard's equation becomes nonlinear and difficult to be solved. Many researchers have developed numerical models ((Pour et al., 2011), (Farthing and Ogden, 2017), (Chávez-Negrete et al., 2018), (Oulhaj et al., 2018)) and analytical models ((Yuan and Lu, 2005), (Tracy, 2006), (Menziani et al., 2007), (Tracy, 2007) (Zhang et al., 2016)) to solve Richard's equation. One of the analytical methods that is used in this paper is Green Ampt Infiltration Equation. This equation is widely used in hydrologic models for *it is acceptable physical basis and it is accurate results.*

Energy state (matric potential and gravitational potential) has a basic role in the distribution of water with depth at a given time. If there is no flow, it is obvious that the gradient of total potential is zero. Figure 1 (a) shows the hydrostatic profile for the case where the water table is present. If water flows vertically downward at a steady rate in a homogeneous medium, the total gradient must be constant, but the matric pressure does not cancel out the gravitational potential, as illustrated in Figure 1 (b). While if water flows vertically upward such as evaporation the condition becomes drier and the hydraulic potential becomes negative like the example in Figure 1 (c) (Hillel, 2012).

STUDY AREA:

The study was carried out on a yard at College of Engineering, Salahaddin University as shown in figure (2). The geographical coordinates of the research site are 36.1632°N and 44.0162°E. The laboratory tests were carried out in the soil laboratory of the civil engineering department at the College of Engineering Salahaddin University-Erbil. The soil samples were analyzed for particle size distribution by the hydrometer method. Soil samples were collected by excavating to a depth of 1.10 m. pickaxe was utilized in the digging process. Samples were collected at three depths 50, 80 and 110 cm. samples were carried in Ziploc bags and labeled. Soil texture classes are shown in table 2.

The soil texture at the 50 cm depth is classified as silty clay according to USDA (United States Department of Agriculture) soil texture identification triangle, the soil in the second layer at 80 cm depth is classified as clay while the soil at the third layer at 110 cm is classified as silty clay loam.

2. MATERIALS AND METHODS

Three equations have been discussed here Darcy law, Darcy- Buckingham law and Richard's equation.

2.1 Darcy's law

Darcy's law is applicable to the saturated zone where there are only two phases water and soil (Simmons, 2008). Darcy interpreted his experimental data from a vertical column of sand with an equation of the form:

$$q = -k\frac{\Delta h}{L} \qquad \dots\dots\dots \qquad (1)$$

Where, q is the flux (discharge per unit area, with units of length per time [LT^{-1}]), K is hydraulic conductivity at saturation [LT^{-1}] and $\frac{\Delta h}{L}$ is hydraulic gradient. The negative sign in Darcy's law is due to the flow of fluid from high pressure to low pressure.

2.2. Darcy- Buckingham extension law

The Darcy-Buckingham equation is adequate for describing unsaturated flow only if the soil water content is not changing in time ($\frac{\partial \theta}{\partial t} = 0$). In nature, this is difficult. When θ and q alter in time, must combine Eq. (1) with the equation of continuity. The equation of continuity relates the time rate of change of θ to the spatial rate of change of q, $\frac{\partial \theta}{\partial t} = -\frac{\partial q}{\partial z}$. The resulting differential equation is strongly non-linear and its solution even for simple conditions is most difficult. Generally, equation (1) itself is not satisfactory for the solution of such hydrologically important processes as evaporation, infiltration, drainage, subsurface flow (Kutilek et al., 2007). Darcy-Buckingham is only valid for steady-state condition as shown in equation (2):

$$q = -k(\Psi m)\left[\frac{\partial \Psi m}{\partial z} + \frac{\partial \Psi z}{\partial z}\right] \quad \text{........} \qquad (2)$$

Since $\frac{\partial \Psi z}{\partial z} = 1$, so Eq. (2) becomes:

$$q = -k(\Psi m)\left[\frac{\partial \Psi m}{\partial z} + 1\right] \quad \ldots\ldots\ldots \qquad (3)$$

Where, z is vertical axis (L) and Ψm is matric potential function (L).

Matric pressure and water content in the vadose zone have an impact on the porous media and in turn, are affected by the conditions in the saturated zone and land surface. (Nimmo et al., 2005)

2.3Richard's equation

Richard's equation, the partial differential equation (PDE) that describes the fluid flow in the variably saturated porous media is accomplished by merging Darcy's law with continuity equation (Nimmo, 2006). Richard's equation is written as:

$$\frac{\partial \theta}{\partial t} = \frac{\partial}{\partial z}\left(K(\Psi)\left(\frac{\partial \Psi}{\partial z} + 1\right)\right) \ldots\ldots\ldots\ldots \qquad (4)$$

Where θ is volumetric water content [L^3/L^3], t is time (T), z is the elevation (L), Ψ is pressure head (L) and K is hydraulic conductivity (LT^{-1}).

Green Ampt Infiltration Equation simulates infiltration rate by the following equation (Rawls et al., 1983):

$$f = k\left[\frac{|\Psi|\Delta\theta + F}{F}\right] \quad \ldots\ldots\ldots\ldots \qquad (5)$$

where k is hydraulic conductivity (cm h^{-1}*), f is infiltration rate (cm* h^{-1}*), F is cumulative infiltration (cm),* Ψ *is suction head (cm) and* Δθ is the difference between initial water content and saturated water content ($cm^3\ cm^{-3}$).

Darcy's law simulates water flows into the soil by equation (1). The q in equation (1) is similar to the infiltration rate (f) of Green Ampt method with opposite sign.

$$f = K(h)\frac{\partial H}{\partial z} \quad \ldots\ldots\ldots.. \qquad (6)$$

$$F(t) - |\Psi|\Delta\theta \ln\left(\left|1 + \frac{F(t)}{|\Psi|\Delta\theta}\right|\right) = K(t) \quad \ldots(7)$$

$$\Delta\theta = \theta_e(1 - \sigma_e) \quad \ldots\ldots\ldots.. \qquad (8)$$

Where θ_e is Porosity and σ_e is Effective saturation.

3. RESULTS:

The value of parameters of Green Ampt Equation are obtained from the table of (Green and Ampt Parameters According to Soil Texture Classes (Rawls et al., 1983)), shown in table 1.

The soil at 0-50 cm is silty clay the parameters are obtained from table 1. Infiltration rate is computed as follows:

Assume $\sigma_e = 0.30$

therefore,

Δθ = 0.424 (1- 0.30) = 0.297

$$F(t) - |30.66| * \Delta\theta * \ln\left(\left|1 + \frac{F(t)}{|30.66| * \Delta\theta}\right|\right) = 0.04$$
(t)

At time = 0.2 hour

F= -1.88

$$f = k\left[\frac{|\Psi|\Delta\theta + F}{F}\right]$$

f = *-0.153 cm/hr, q= 0.153cm/hr.*

The soil at 50-80 cm is clay, the parameters are obtained from table1. Infiltration rate is computed as follows:

Assume $\sigma_e = 0.30$
therefore,
$\Delta\theta = 0.412\ (1- 0.30) = 0.288$
$$F(t) - |27.72| * \Delta\theta * \ln\left(\left|1 + \frac{F(t)}{|27.72|*\Delta\theta}\right|\right) = 0.03\ (t)$$
At time = 0.2 hour
F= 1.56

$$f = k\left[\frac{|\Psi|\Delta\theta + F}{F}\right]$$

f = *0.18 cm/hr, q= 0.18 cm/hr.*

The soil at 80-110 cm is silty clay loam, the parameters are obtained from table 1. Infiltration rate is computed as follows:
Assume $\sigma_e = 0.30$
therefore,
$\Delta\theta = 0.451\ (1- 0.30) = 0.316$
$$F(t) - |21.54| * \Delta\theta * \ln\left(\left|1 + \frac{F(t)}{|21.54|*\Delta\theta}\right|\right) = 0.06\ (t)$$
At time = 0.2 hour
F= 1.99
$$f = k\left[\frac{|\Psi|\Delta\theta + F}{F}\right]$$
f = *0.26 cm/hr, q= 0.26 cm/hr.*

4. DISCUSSION:

This paper is intended to show the difference between Darcy law and Richard's equation on the state of the science for calculating the flow of water in the unsaturated zone. The focus is mostly on the vadose since it's a critical zone and it is considered as a controlling agent for most of the groundwater cases.

Darcy's law is an empirical equation that has been developed for the saturated zone. Where all the pores are filled with water. While it is not applicable for the unsaturated zone, where the pore spaces are not fully saturated with water so the remaining portions are filled with air. Physical properties of saturated and unsaturated zone play a great role in the applicability of the equations. In unsaturated zone, two factors actuate water flux, pressure head (Ψ) and properties of the medium (hydraulic conductivity (K)). Because of high the dependency of K on Ψ it is not possible to directly solve Richard's equation.

5. CONCLUSION:

The governing equation for flow in saturated media is Darcy's law. While for unsaturated media Richard's equation is considered as the governing equation. The interaction of multiple phases of vadose zone complicates the dynamics of vadose zone water. Vadose zone phenomena are tremendously reactive to the proportions of the phases. Richard's equation is a complicated nonlinear (PDE). In order to solve Richard's equation, there are several methods for simplifying Richard's equation, Analytical solutions as Green Ampt Infiltration Equation, numerical solutions by using the finite difference or finite element methods. Because of this nonlinearity and complications in the unsaturated zone, it is exposed to a greater degree of inaccuracy than most disciplines of physical science There are also software that numerically calculates the water movement such as HYDRUS program.

Conflicts of interest:
We have no conflicts of interest to disclose.

Table 1 (Green and Ampt Parameters According to Soil Texture Classes.)

Soil texture class	Effective porosity ($cm^{-3}\ cm^{-3}$)	Wetted capillary pressure, **Ψ** (cm)	Hydraulic conductivity, K($cm\ h^{-1}$).
Silty clay	0.424	30.66	0.04
Clay	0.412	27.72	0.03
Silty clay loam	0.451	21.54	0.06

Table 2(Physical properties of the soil at the three layers.)

Depth (cm)	Sand (%)	Silt(%)	Clay (%)	Texture class
0-50	8.63	46.27	44.73	Silty clay
50-80	6.14	28.88	64.44	Clay
80-110	4.36	63.40	32.07	Silty clay loam

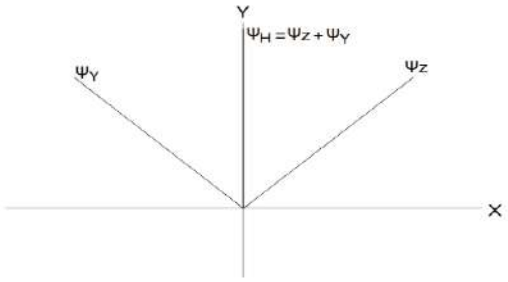

Figure 1(a) Profile of gravitational, matric potential and total potential at static water.

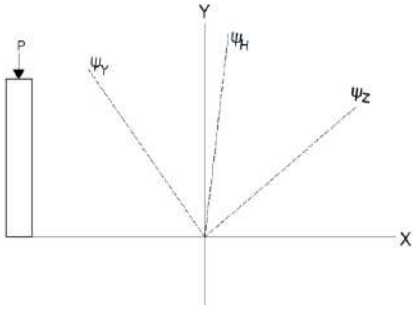

Figure 1 (b) Profile of gravitational, matric potential and total potential at steady downward (precipitation)

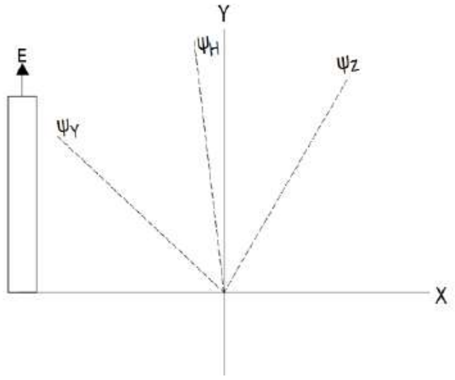

Figure 1 (c) Profile of gravitational, matric potential and total potential at unsteady flow.

Ψ_Y = Matric potential

Ψ_z = *Gravitational potential*

Ψ_H = Total potential

P= precipitation

E= Evaporation

Figure 2 The location of the study area.

REFERENCES:

BALLESTERO, T., HERZOG, B. & THOMPSON, G. 2005. Monitoring and sampling the vadose zone. *Practical Handbook of Environmental Site Characterization and Ground-Water Monitoring.* CRC Press.

BROWN, G. J. W. R. R. 2002. Henry Darcy and the making of a law. 38**,** 11-1-11-12.

CHÁVEZ-NEGRETE, C., DOMÍNGUEZ-MOTA, F., SANTANA-QUINTEROS, D. J. C. & GEOTECHNICS 2018. Numerical solution of Richards’ equation of water flow by generalized finite differences. 101**,** 168-175.

FARTHING, M. W. & OGDEN, F. L. J. S. S. S. O. A. J. 2017. Numerical solution of Richards’ Equation: a review of advances and challenges. 81**,** 1257-1269.

HILLEL, D. 2012. *Soil and water: physical principles and processes*, Elsevier.

HOU, X., VANAPALLI, S. & LI, T. J. C. G. J. 2019. Water flow in unsaturated soils subjected to multiple infiltration events.

KOVALCHUK, N. & HADJISTASSOU, C. J. T. E. P. J. E. 2019. Laws and principles governing fluid flow in porous media. 42**,** 56.

KUNTZ, D. & GRATHWOHL, P. J. J. O. H. 2009. Comparison of steady-state and transient flow conditions on reactive transport of contaminants in the vadose soil zone. 369**,** 225-233.

KUTILEK, M., NIELSEN, D. & REICHARDT, K. J. T. L. N. C. O. S. P., INTERNATIONAL CENTRE FOR THEORETICAL PHYSICS 2007. Soil water retention curve, interpretation.

LIU, H.-H. Fluid Flow in the Subsurface.

MENZIANI, M., PUGNAGHI, S. & VINCENZI, S. J. J. O. H. 2007. Analytical solutions of the linearized Richards equation for discrete arbitrary initial and boundary conditions. 332**,** 214-225.

NARASIMHAN, T. J. V. Z. J. 2007. Central ideas of Buckingham (1907): A century later. 6**,** 687-693.

NAVON, I. M. 2009. Data assimilation for numerical weather prediction: a review. *Data assimilation for atmospheric, oceanic and hydrologic applications.* Springer.

NIMMO, J. R., HEALY, R. W. & STONESTROM, D. A. J. E. O. H. S. 2005. Aquifer recharge. 4**,** 2229-2246.

NIMMO, J. R. J. E. O. H. S. 2006. Unsaturated zone flow processes.

OULHAJ, A. A. H., CANCÈS, C. & CHAINAIS-HILLAIRET, C. 2018. Numerical analysis of a nonlinearly stable and positive Control Volume Finite Element scheme for Richards equation with anisotropy.

PINDER, G. F. & CELIA, M. A. 2006. *Subsurface hydrology*, John Wiley & Sons.

POUR, M. A., SHOSHTARI, M. M. & ADIB, A. J. W. A. S. J. 2011. Numerical solution of Richards equation by using of finite volume method. 14**,** 1838-1842.

RAWLS, W. J., BRAKENSIEK, D. L. & MILLER, N. J. J. O. H. E. 1983. Green-Ampt infiltration parameters from soils data. 109**,** 62-70.

SELKER, J. S., MCCORD, J. T. & KELLER, C. K. 1999. *Vadose zone processes*, CRC Press.

SIMMONS, C. T. J. H. J. 2008. Henry Darcy (1803–1858): Immortalised by his scientific legacy. 16**,** 1023.

TRACY, F. J. J. O. H. 2007. Three-dimensional analytical solutions of Richards’ equation for a box-shaped soil sample with piecewise-constant head boundary conditions on the top. 336**,** 391-400.

TRACY, F. J. W. R. R. 2006. Clean two- and three-dimensional analytical solutions of Richards' equation for testing numerical solvers. 42.

YUAN, F. & LU, Z. J. V. Z. J. 2005. Analytical solutions for vertical flow in unsaturated, rooted soils with variable surface fluxes. 4**,** 1210-1218.

ZHANG, Z., WANG, W., YEH, T.-C. J., CHEN, L., WANG, Z., DUAN, L., AN, K. & GONG, C. J. J. O. H. 2016. Finite analytic method based on mixed-form Richards’ equation for simulating water flow in vadose zone. 537**,** 146-156.

ZANCO Journal of Pure and Applied Sciences
The official scientific journal of Salahaddin University-Erbil
https://zancojournals.su.edu.krd/index.php/JPAS

ISSN (print):2218-0230, **ISSN (online):** 2412-3986, **DOI: http://dx.doi.org/10.21271/zjpas**

RESEARCH PAPER

Estimating Seepage Quantity through Homogenous Earth-Fill Dam with Horizontal Drainage Using Different Methods

Jehan M. Sheikh Suleimany[1], Bruska S. Mamand[2]

[1,2]Department of Dams & Water Resources Engineering, college of Engineering, Salahaddin University- Erbil ,Kurdistan Region, Iraq

ABSTRACT

Seepage is the main cause of failure of earthen dams; to prevent this failure, excessive seepage problems should be controlled. In this study, lowest seepage quantity through homogenous earth dam with horizontal filter by different methods was estimated. SEEP/W code in (GeoStudio software 2012) and (Slide software 6.025) was used to investigate 972 models with various upstream and downstream face slopes, horizontal filter lengths, free boards, top widths, dam heights and permeability coefficients.

Results showed that, comparing the seepage rates obtained from Slide and GeoStudio softwares has average differences of ratio of seepage discharge to permeability coefficient and filter length (q/kL) was less than 2%. Furthermore, nonlinear empirical equation was developed using (SPSS 22) program. The comparison of seepage quantity measured by SEEP/W and Slide versus its quantity calculated from empirical equations gave a coefficient of determination ($R^2 = 0.815, 0.788$) respectively.

Multilinear perceptron (MLP) was used as suitable type of artificial neural network (ANN) with a base structure (5-4-1) in which 75% of data sets were for training and 17.2% were for testing. The quantity of seepage predicted by ANN compared with obtained seepage rates from SEEP/W and Slide has ($R^2=0.923, 0.942$) respectively.

Finally, the average percent of errors of empirical equation, Slide Program and ANN was 15.814%, 8.519% and 1.060% respectively. This means that, seepage quantities obtained from ANN was more accurate than other methods may be due to different ways of analysis.

KEY WORDS: Homogenous dam; Seepage quantity; Horizontal filter; SEEP/W; Slide software.
DOI: http://dx.doi.org/10.21271/ZJPAS.32.1.2
ZJPAS (2020) , 32 (1);7-18 .

1. INTRODUCTION

Earth dams are important structures used as artificial reservoirs consists from impervious compacted layers of soils for its core and permeable materials on their upstream and downstream faces to be safe against sliding and overturning forces. Seepage is the quantity of water through an earth dam starts from upstream of the reservoir level to the downstream toe of the dam. The upper surface of this stream of percolating water is known as the phreatic surface.

For the purpose of controlling this phenomenon in the dam, different types of filters should be designed. The Laplace equation which governs water seepage cannot be solved analytically, except for cases with very simple and special boundary conditions. In the literature reviews, the numerical example that proposed equations is simple to use; hence the designers may find these equations as an additional check to their design by the conventional flow net method (Chahar, 2004). While, a series of tests and different drain sizes including different filter thicknesses and lengths were applied to a physical model of an embankment dam to check the stability in steady and transient seepage conditions using a number of piezometers and pressure sensors (Malekpour *et*

---

* **Corresponding Author:**
Jehan M. Sheikh Suleimany
E-mail: jehanmohammed.sheikhsuleimany@su.edu.krd

Article History:
Received: 07/04/2019
Accepted: 18/09/2019
Published: 25/02 /2020

al., 2012). Seepage and Stability of earth dam were analyzed Using Ansys and GeoStudio Softwares, the significant difference of two programs is related to safety factor deducted that Ansys answer is more acceptable (Kamanbedast and Delvari, 2012).

The other investigation performed the numerical simulation to find the effect of horizontal drain length and cutoff wall on seepage and uplift pressure in heterogeneous earth dam (Mansuri and Salmasi, 2013). The case study on "Hub" earthen dam located on (Karachi city-Pakistan) also investigated. SEEP/W simulation compared with field observations for seepage analysis. Calibration of the material properties is made on the basis of minimization of error while comparing observed hydraulic heads with the simulated ones (Arshad and Babar, 2014). Alnealy and Alghazali (2015) analyzed of seepage under hydraulic structures using Slide program. Single and multi- layers soils and its effect on structures with inclined cut-off were studied.

Casagrandi and Dupuits assumptions were analyzed to estimate seepage through homogeneous earth dam without filter (Jamel, 2016). Çalamak *et al.* (2016) investigated the suitability and the effectiveness of blanket and chimney drains in earth fill dams for various properties of the drainage system. (Irzooki, 2016) was used SEEP/W code to run on homogenous earth dam models with horizontal toe drain, a new equation was found for computing the quantity of seepage. (Omofunmi *et al.*, 2017) reviewed on effects and control of seepage through earth-fill dams. San Luis dam used to evaluate the unsaturated and transient seepage analysis in which pore-water pressures at failure and progression of the phreatic surface through the fine-grained core for drawdown stability analyses (Stark *et al.*, 2017).

The goal of this research is to examine the capabilities of different software's that estimate the lowest quantities of seepage to verify the accurate and optimum one.

2. THORETICAL CONSIDERATION

As clearly explained by Harr (1962), there were many different assumptions for determining the seepage quantity as explained below:

- **Dupuit's Assumptions**: Both discharge quantity and free surface are independent of the slopes of the dam. The discharge (per unit width) through any vertical section of the dam for the condition of tail water at potential seepage face are shown in Figure (1-a).
- **Schaffernak & Van Iterson**: The first approximate method that accounts for the development of the surface of seepage considering an earth dam on an impervious base shown in Figure (1-b) with no tail water.
- **L. Casagrande's**: Recommended that point D_o shown in Figure (1-c) instead of point D be taken as the starting point of the line of seepage (D_o is 0.3Δ from point D at the upstream reservoir surface). The actual entrance condition is then obtained by sketching in the arc DF normal to the upstream slope and tangent to the parabolic free surface.
- **Pavlovsky's Solution:** Considered the dam divided into three zones as shown in figure (1-d). The upper section (I) bounded by the upstream slope and y-axis, the central section (II) by the y-axis and a vertical line through the discharge point of the free surface and the lower section (III) by the latter vertical line and the downstream slope. The streamline in zone (I) are known to be curvilinear (dotted curves *cd*); however, Pavlovsky assumed that they may be replaced by horizontal streamline of almost equivalent length (*ed)* then assuming purely horizontal flow in zone (I).

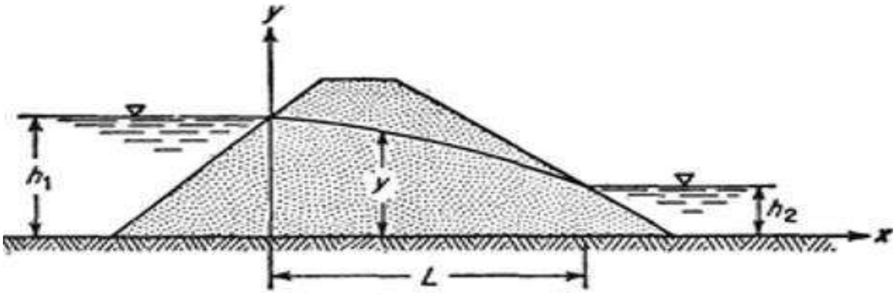

a. Dupuit's assumptions: $q = \frac{k(h_1^2 - h_2^2)}{2L}$

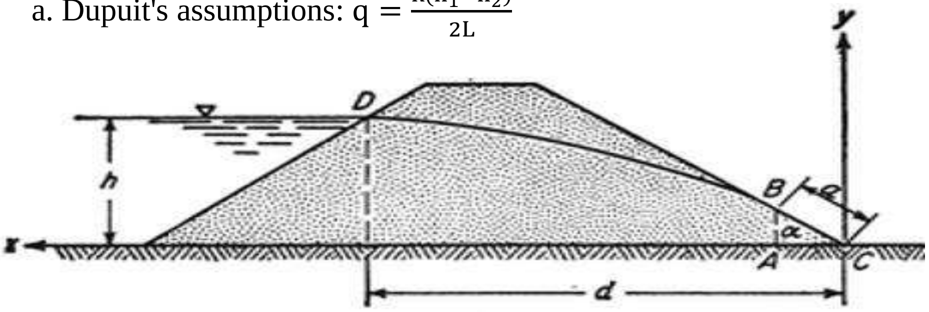

b. Schaffernak & Van Iterson: $q = k\ a\ \sin(\alpha)\ \tan(\alpha)$

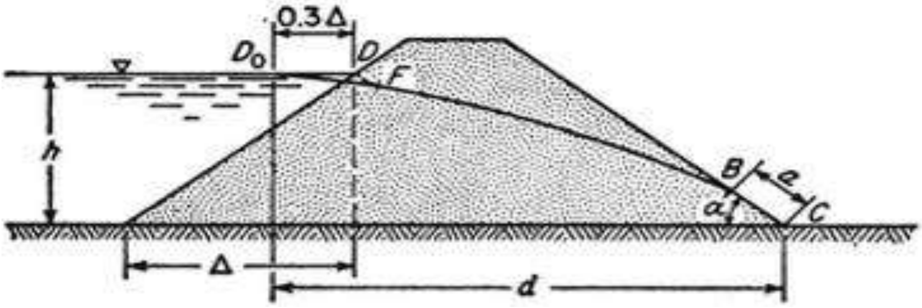

c. L. Casagrande: $q = k\ a\ sin^2\ \alpha$

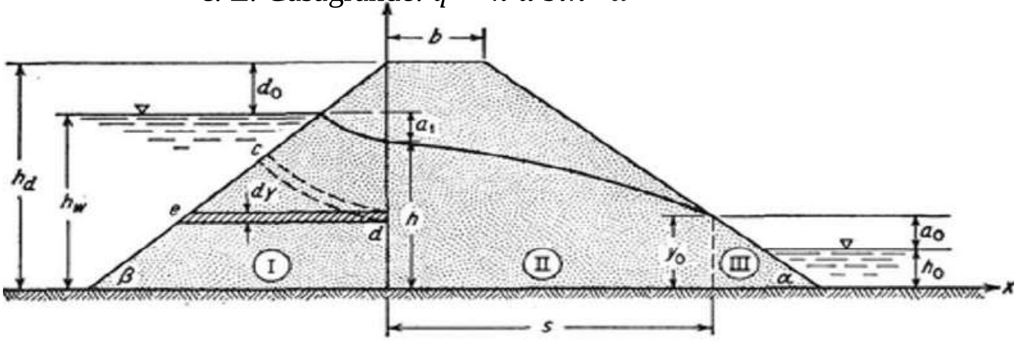

d. Pavlovsky's Solution: $dq = k\frac{a_1}{\cot \beta\ (h_d - y)}dy$

Figure 1. Assumptions of seepage quantity through earth dam (Harr, 1962).

2.1 Dimensional Analysis

Dimensional analysis is an important tool to investigate the relationship between different variable’s and categorize to convert them into a smaller number of dimensionless parameters to identify any phenomenon. In the present study, the Buckingham's π- theorem was used for evaluation of the manner in which the variables controlled the seepage quantity through a homogenous earth dam. The expected factors that affecting on the seepage quantity for a general section of homogenous earth dam with horizontal drainage blanket as sketched in Figure (2), was defined in Equation (1):

$$q = f\,(H, k, L\,, b, F_B, \rho, \tan\theta\,, \tan\alpha,)\; .\,.\,.\,.\,.\,.\,.\,.\; (1)$$

The basic variables are (L, q and ρ) taken as repeated variables in all π-terms, and each of other variables are presented in each π-terms. After performing the dimensional analysis, new expression was found as shown in Equation (2):

$$q = kL\;\; f\left(\tan\theta\,, \tan\alpha\,, \frac{F_B}{H}\,, \frac{b}{L}\right)\; .\,.\,.\,.\,.\,.\,.\,.\,.\,.\,.\,.\,.\; (2)$$

In which the obtained dimensionless parameters from the above equation can be defined as: (θ) is the slope of the upsteam face of the dam, (α) is the slope of the downsteam face of the dam, (F_B/H) is the dimensionless ratio of the dam freeboard to its height, (b/L) is the proportion of top width of the dam to the span of the horizontal blanket filter and (q/kL) ratio related to the permeability coeffeicient of the soil with seepage quantity and the length of horizontal blanket filter.

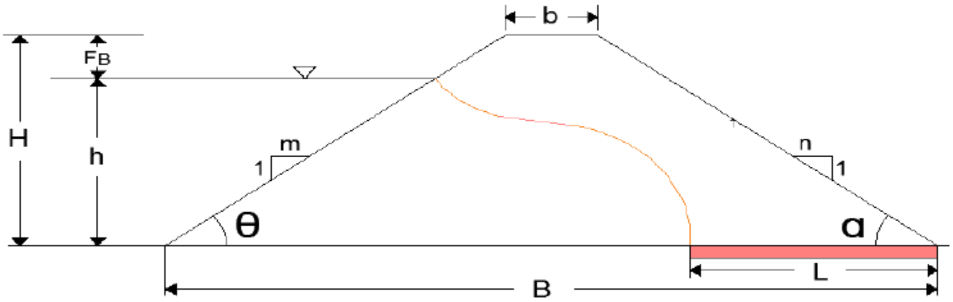

Figure 2. Overall sector of homogenous earth dam.

3. METHODOLOGY OF THE STUDY

Methodology of this study was conducted on the total of 972 homogenous earth dam models. These models includes the summation of 486 runs that done by GeoStudio (SEEP/W code) and also 486 runs done by (Slide) software taking into consideration the same models for each test in both software. Different geometries of homogenous dam were created and the material for dam body and filter modeled with hydraulic conductivity data point function. The details of selected variables are shown in Table (1), in which it consists of two different upstream and downstream slopes of the dam and three different values for each: dam height, filter length, permeability coefficient, free board and top width.

As explained in Figure (3), the upstream boundary blue nodes are designated as head boundaries with total head equal to the water level in the reservoir. The downstream toe is assigned a total head of 0.0 m (H = elevation). The downstream slope is assigned a potential seepage face type of boundary condition. Also the Slide software can be automatically utilized by the seepage analysis engine because it has the capability to carry out a finite element groundwater seepage analysis for steady state or transient conditions.

Table (1). Conducted dam section variables for both GeoStudio & Slide programs.

D/S & U/S slope (α, θ)	Variables	1	2	3
α_1= 2:1 θ_1=2.5:1	H: Dam Height (m)	14	16	18
	b: Top Width (m)	4	6	7
	L: Filter Length (m)	10	20	25
α_2= 2.5:1 θ_2=3:1	F_B: Free Board (m)	1	1.5	2
	k: Permeability Coefficient (m/s)	$1*10^{-4}$	$1*10^{-5}$	$1*10^{-6}$

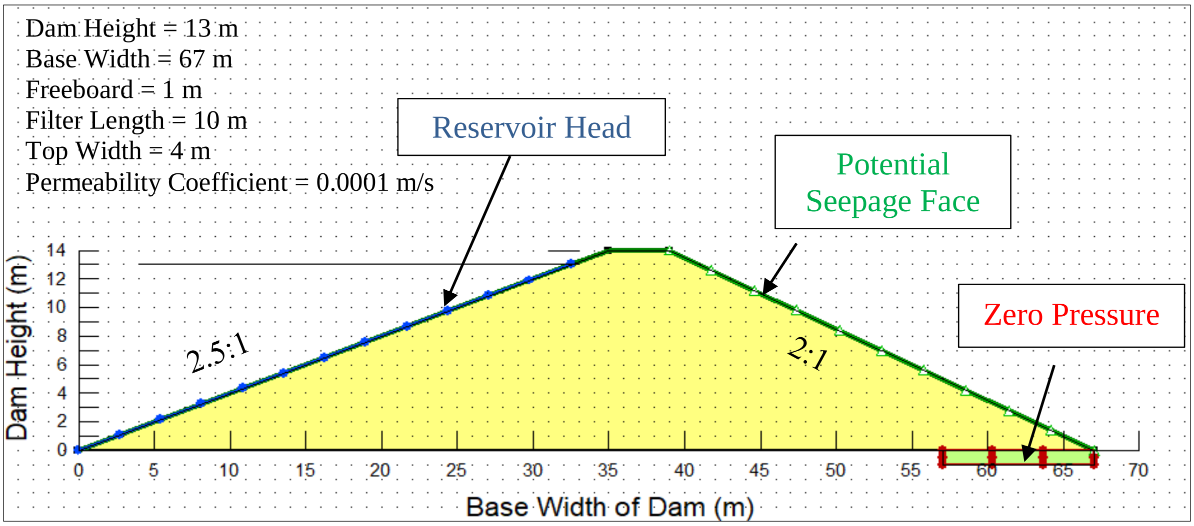

Figure 3. Location of the boundary conditions of homogenous earth dam.

4. RESULTS AND DISCUSSION

The main sections of this study deal with the effect of dimensionless parameters in regards of homogenous dam on the seepage quantity of the dam itself. Results of each part were concluded separately in the following configurations:

4.1 Mesh Size Dependence

In order to test mesh dependence on the amount of seepage discharge, four types of meshes as quads and triangles, triangles only, rectangular grid of quads and triangular grid of quads was investigated. The result of each method on the first run is shown in Table (2). The differences in seepage quantities was a small fractions but quads and triangles grid type was selected in all runs because of the lowest seepage quantity.

Table (2). Seepage quantification using different grid types.

Grid Type	No. of Elements	No. of Nodes	Seepage discharge (m^3/s)
Quads and triangles	500	559	$3.726*10^{-6}$
Triangles only	495	299	$3.782*10^{-6}$
Rectangular grid of quads	497	545	$3.844*10^{-6}$
Triangular grid of quads / triangles	468	512	$3.799*10^{-6}$

4.2 Effect of the Thickness of Filter

In this study the thickness of filter was investigated and compared with the dam section assuming filter thickness as zero. For this purpose two tests were done, first test was on the dam section having one grid thickness of the horizontal filter. The results of seepage quantity for 13m reservoir head was ($3.7243*10^{-4}$ m^3/s) as shown in Figure (4-a); whereas the second test of dam section with no filter thickness gave as ($3.7375*10^{-4}$ m^3/s) as a seepage quantity inside the dam body as shown in Figure (4-b).The difference between seepage quantities of both runs was ($1.32*10^{-6}$ m^3/s) which can be ignored.

4.3 Effect of the Dimensionless Parameters on Seepage Quantity

In this section, the effect of dimensionless parameters that computed from SPSS was clearly investigated. Figure (5) and Figure (6) demonstrate the relationship between the dimensionless parameter (q/kL) versus upstream and downstream slopes respectively. Results showed that the quantity of seepage obtained from Slide software was smaller than that of SEEP/W for the same effecting variables on the dam. In which the average difference of (q/kL) between both software was 1.696%. Also, both figures explained that seepage quantity increases as the upstream and downstream face slopes were increased.

Figure (7) shows the relationship between (q/kL) and (F_B/H) for Slide and SEEP/W software's. The effect of the freeboard on the seepage quantity was investigated in which seepage quantity decrease with increasing the height of freeboard when a height of dam not more than 18m.

Figure (8) demonstrates the relation between (q/kL) and (b/L). For the range of (b/L = 0.2 to 0.6) the seepage quantity decreases with increasing the top width of the dam. While, it increased with increasing length of horizontal toe drain.

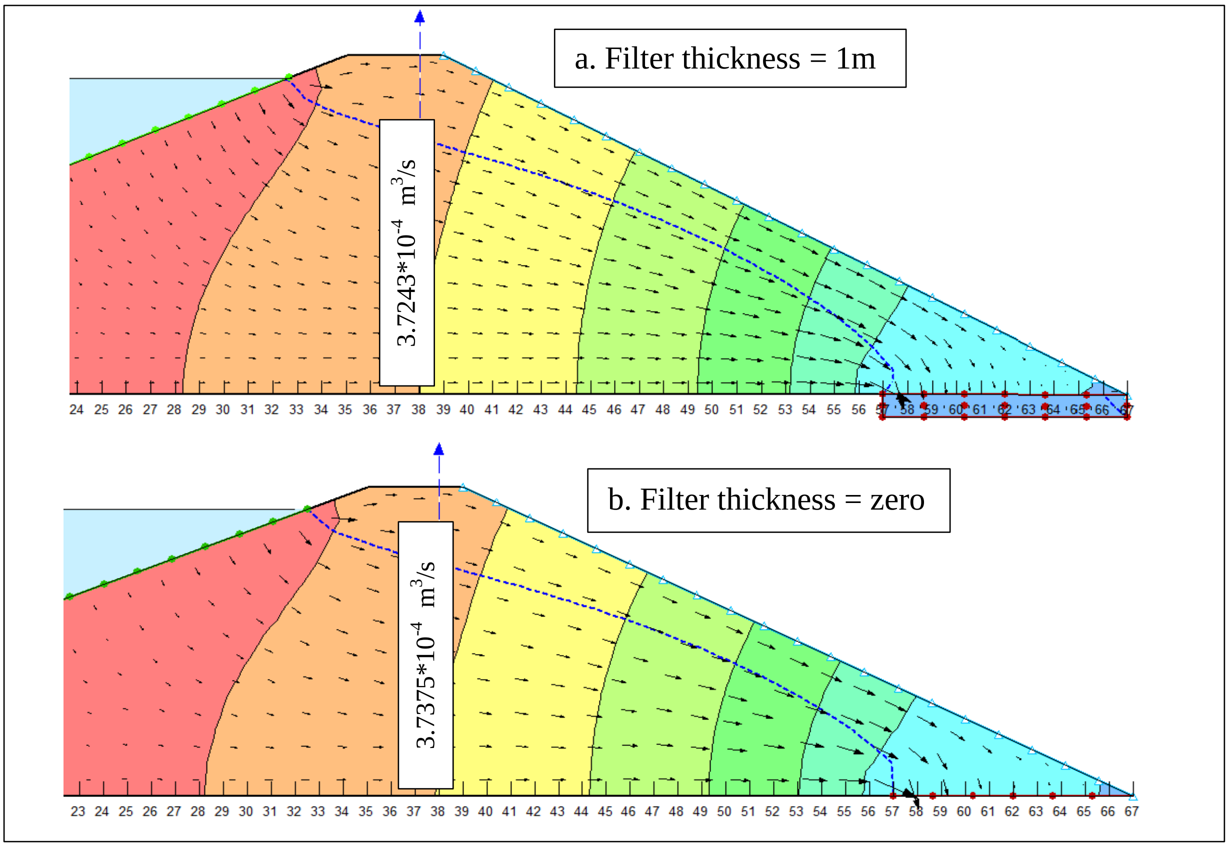

Figure 4. SEEP/W runs to explain the effect of filter thickness.

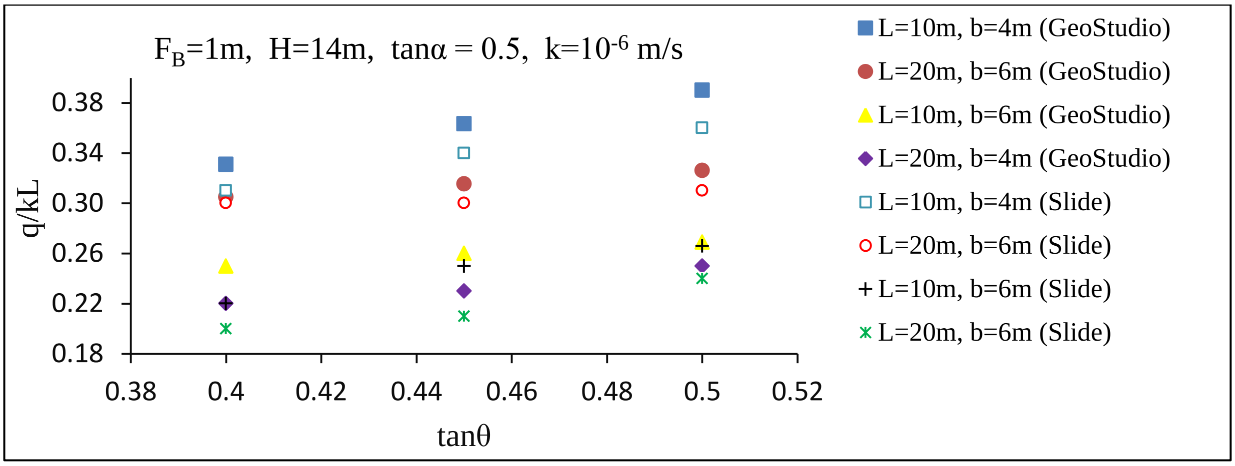

Figure 5. Relationship between (q/kL) and (tanθ).

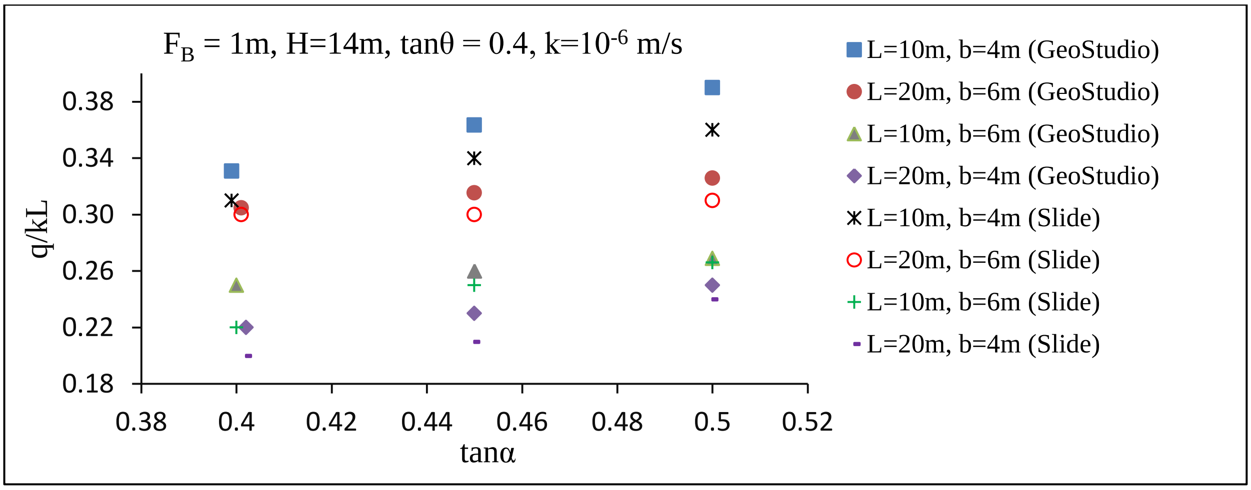

Figure 6. Relationship between (q/kL) and (tanα).

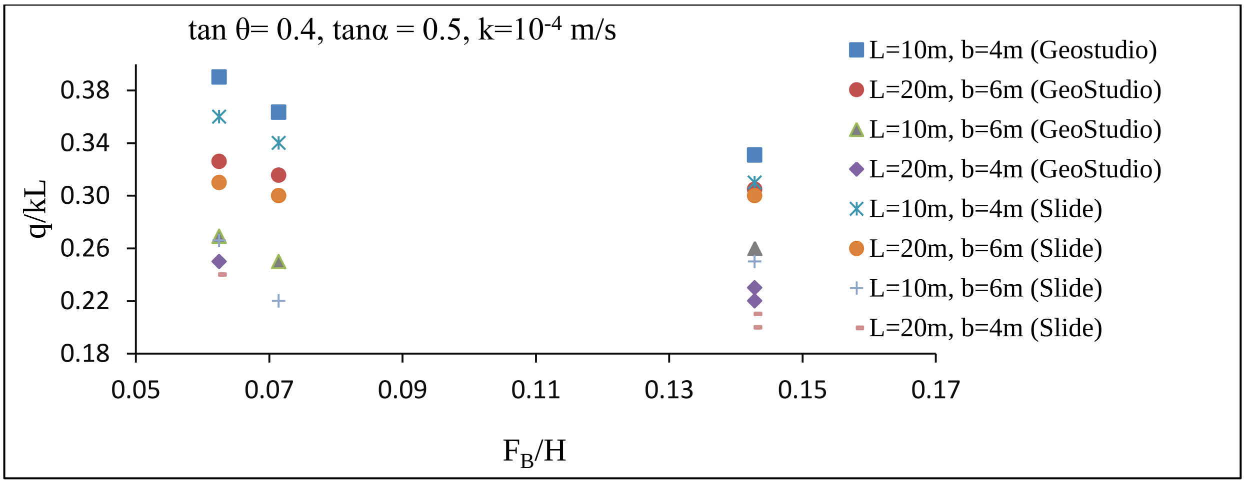

Figure 7. Relationship between (q/kL) and (F_B/H).

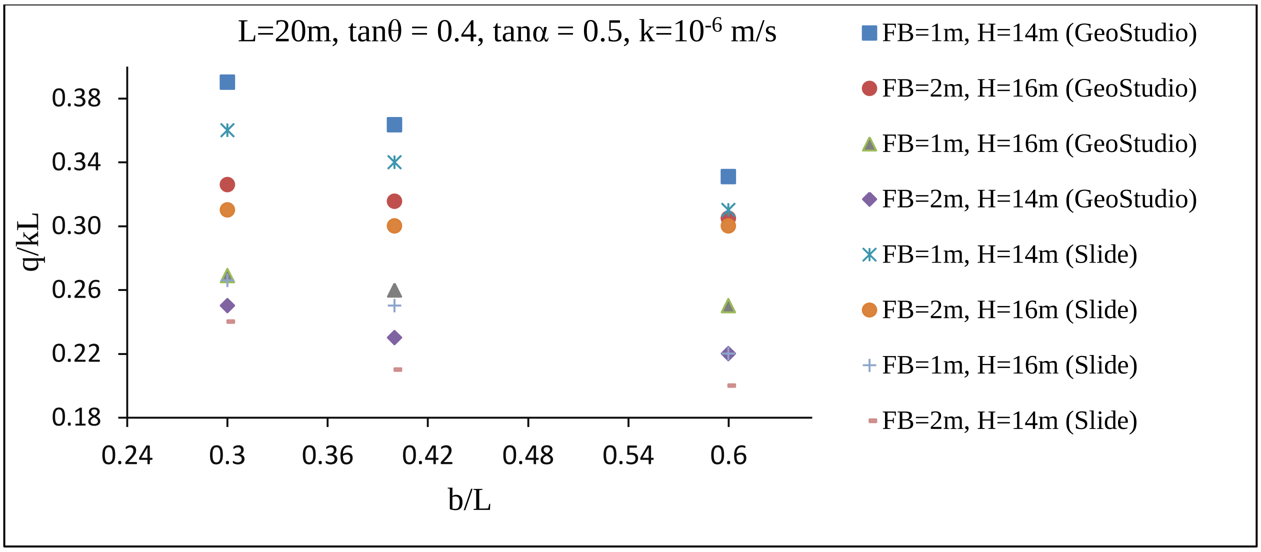

Figure 8. Relationship between (q/kL) and (b/L).

4.4 Empirical Equation for Determining the Seepage Quantity

In this section, the SPSS statistical software was used for predicting empirical general relationships. This relations was represented the relating independent pi-terms which significantly affect the seepage quantity per unit width. For this purpose the seepage quantities that obtained from SEEP/W and Slide software were examined in SPSS based on the dimensional analysis pi-terms. Two new expressions were obtained as Equation (3) based on GeoStudio results and equation (4) based on seepage quantities obtained from Slide software.

$$q = \frac{(\tan\theta)^{3.652}\ \ (\tan\alpha)^{3.573}\ \ (kL)^{0.4}}{(\frac{F_B}{H})^{0.231}\ \ (\frac{b}{L})^{0.226}} \ldots\ldots\ldots\ldots\ (3)$$

$$q = \frac{(\tan\theta)^{3.804}\ \ (\tan\alpha)^{3.734}\ \ (kL)^{0.381}}{(\frac{F_B}{H})^{0.272}\ \ (\frac{b}{L})^{0.218}} \ldots\ldots\ldots\ldots (4)$$

The empirical equation in regards of calculated values of seepage discharge should be compared with the measured seepage discharges. For the purpose of predict a best relation, non-linear regression equations were founded. Figure (9) shows the seepage quantities obtained from GeoStudio and Slide program was compared with its quantities calculated from Equations (3 and 4) respectively. Best fitting intercept line was selected to show a better regression depends on high determination coefficient (R^2). Eventually, results explained that the seepage rates from SEEP/W code versus Equation (3) gave higher determination coefficient (R^2=0.815), whereas it was (R^2=0.788) in comparison between seepage rates from Slide software versus Equation (4).

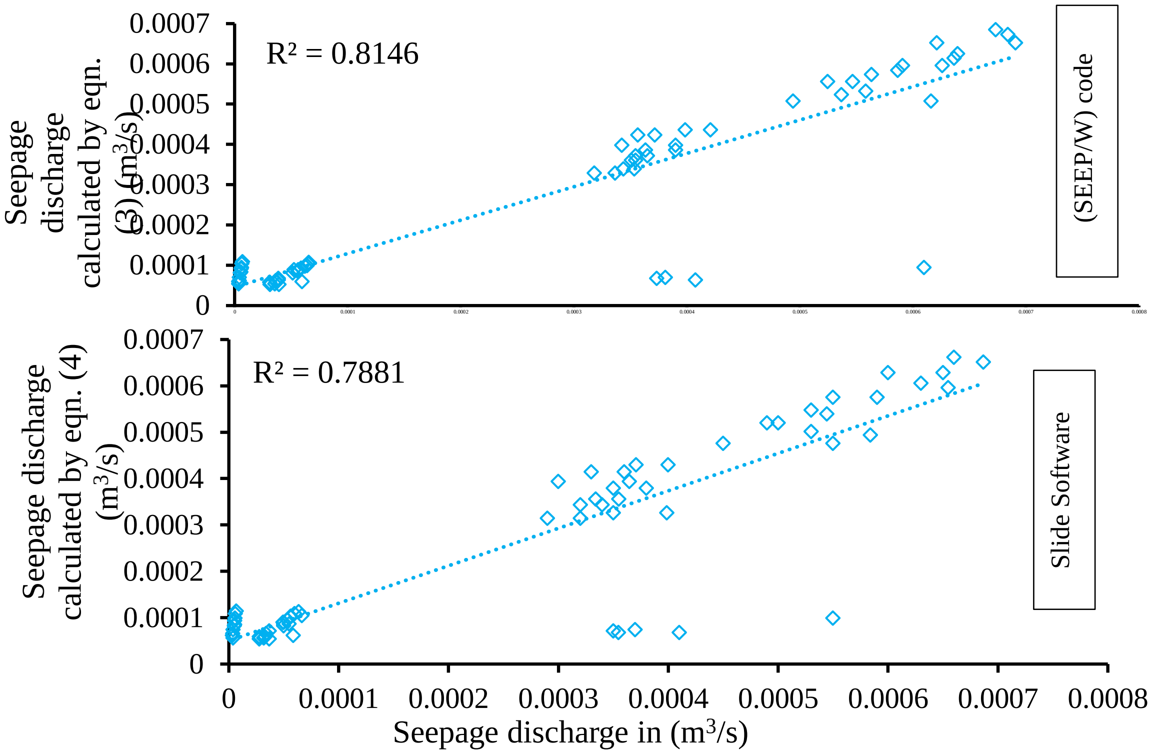

Figure 9. Comparisons of seepage rates found from GeoStudio and Slide with calculated seepage rates from empirical equations.

4.5 Artificial Neural Network (ANN)

ANN is a nonlinear mathematical model that can simulate arbitrarily complex nonlinear processes that relate the inputs and outputs of any system. In many complex mathematical problems that lead to solving complex nonlinear equations, Multilayer Perceptron (MLP) and radial basis function (RBF) networks are common types of ANN that are widely used in water resources engineering (Parsaie and Haghiabi, 2018). In this investigation, the MLP model was used to define of appropriate functions, weights and bias that should be considered. For this purpose the seepage quantity through homogenous earthen dam sections were collected. The datasets were divided in to two groups as training and testing, 75% was for training and 17.2% was for testing with 7.8% for validation (holdout). An ANN may have different values of input, hidden and output layers. Therefore the base structure of this investigation was (5-4-1) this means that: five inputs, four hidden layers and one output. Figure (10) shows that the accuracy of the ANN models for calculating the seepage discharge through homogenous earth dam. The quantity of seepage predicted by ANN was compared with the seepage quantity from SEEP/W and Slide software, the determination coefficients for these relations was R^2= 0.923 and R^2= 0.942 respectively. This means that slide software gave accurate results than that of SEEP/W code.

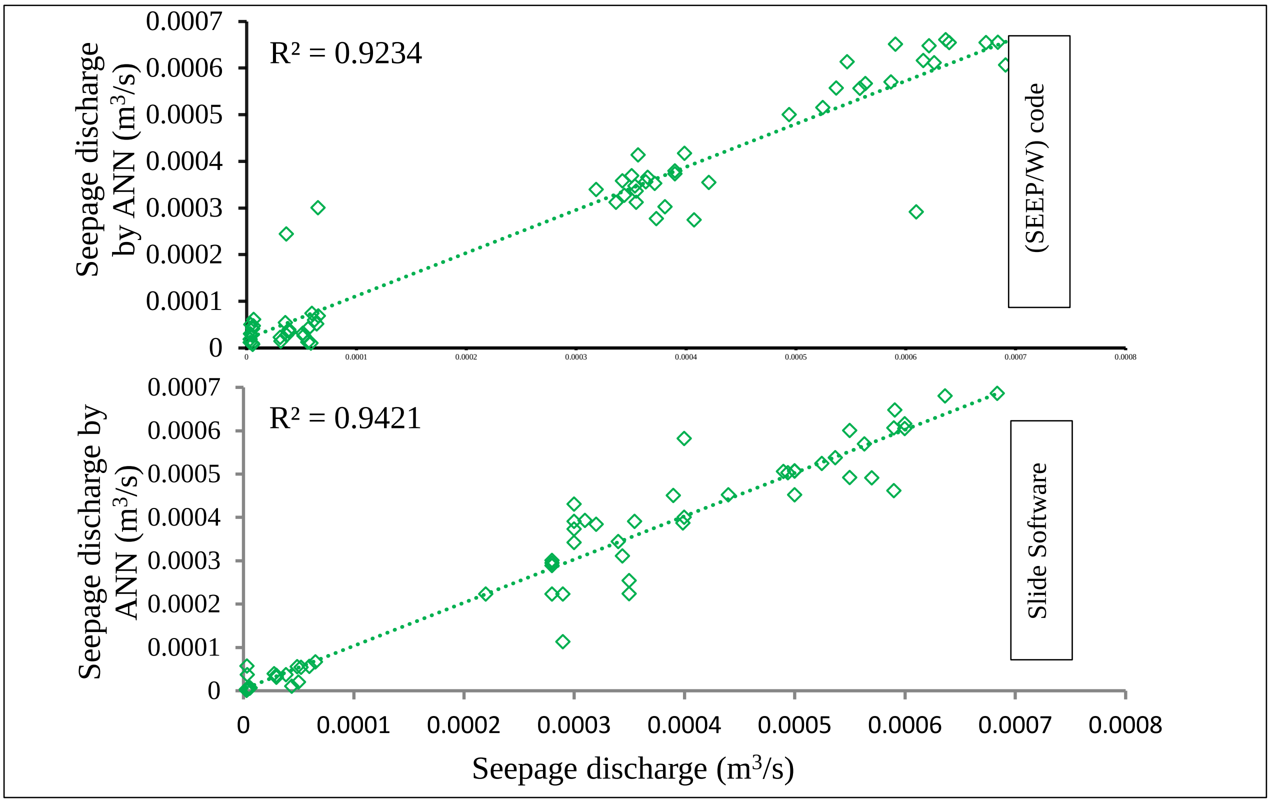

Figure 10. Comparisons of seepage rates found from GeoStudio and Slide with calculated seepage rates from ANN.

4.6 Comparison of Seepage Quantity by Different Methods

Figure (11) shows the comparison between seepage discharges obtained from different methods. It seems that among 64 runs of each method, the seepage quantities were divided as group points based on the same dimensions of the dam, reservoir level and permeability coefficient. There are small fractions in differences between them. In which; seepage quantities that obtained from SEEP/W code was much greater than the amount that obtained from slide software for the condition of ignoring tail water at the potential seepage face and approximated phreatic line of the homogenous dam.

For more details on the differences in seepage rates, the average percent of errors in each method based on the seepage quantities obtained from SEEP/W code was shown in Table (3). This table demonstrates that SEEP/W seepage quantities compared with its quantity obtained from ANN and Slide software has the average percent errors about 1.060% and 8.519% respectively. On the other hand, SEEP/W quantities compared with its quantity obtained from Equation (3) of this investigation, it has 15.814% average errors in seepage rates.

Eventually, the maximum seepage quantity obtained from ANN was ($6.856*10^{-4}$ m^3/s) which is less seepage rates than the quantities measured by other methods taking into consideration of the same affecting dimensionless parameters.

Table (3). Different % errors of seepage quantity with comparing to SEEP/W.

Seepage quantities obtained from:	Empirical Equation (eqn. 3)	Slide Program	Artificial Neural Network
Average Errors:	15.814 %	8.519 %	1.060 %

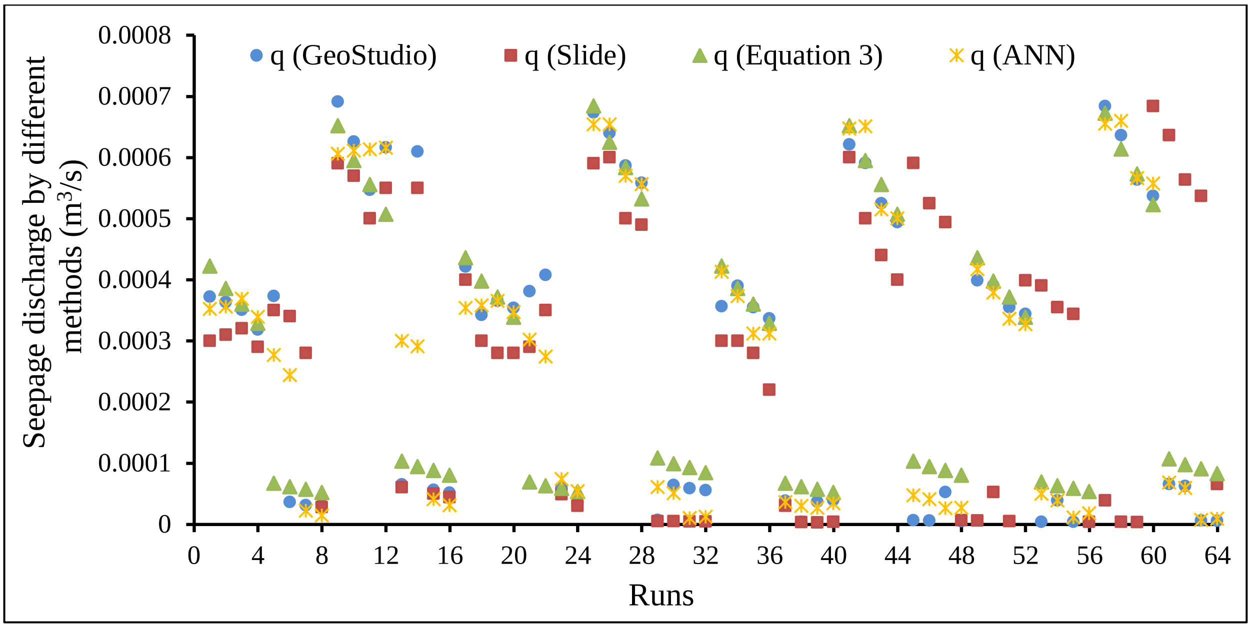

Figure 11. Comparison of seepage quantities by different methods.

5. CONCLUSIONS

The key messages of this study are the following:

1. The slight increasing in quantity of seepage was observed with increasing the upstream and downstream slopes of the earth dam.
2. The quantities of seepage increases with increasing horizontal toe drain and decreasing top width of the earth dam.
3. The seepage quantity obtained from GeoStudio software was greater than its quantity attained from Slide software. In which, the average difference of dimensionless parameter (q/kL) between Slide software and SEEP/W code was 1.696 %.
4. The seepage rates measured by Slide software was compared with its quantity achieved by ANN. This relation gave a higher determination coefficient ($R^2 = 0.942$) than nonlinear empirical equations found from SPSS.
5. SEEP/W seepages compared with its quantity obtained from ANN and Slide software has the average percent of errors less than 1.5 % and 9 % respectively.

6. REFERENCES

Arshad E.I. and Babar M.M. (2014), 'Comparison of SEEP/W Simulations with Field Observations for Seepage Analysis through an Earthen Dam (Case Study: Hub Dam- Pakistan)', International Journal of Research, Vol. 1, Issue 7, pp. 57-70.

An example: 'Seepage through a Dam Embankment', GEO-SLOPE International Ltd, Calgary, Alberta, Canada.

Alnealy H.K.T. and Alghazali N.O.S. (2015), 'Analysis of Seepage Under Hydraulic Structures Using Slide Program', American Journal of Civil Engineering. Vol. 3, Issue 4, pp. 116-124.

Chahar B.R. (2004), 'Determination of Length of a Horizontal Drain in Homogeneous Earth Dams', Journal of Irrigation and Drainage Engineering, Vol. 130, Issue 6, pp. 530-536.

Çalamak M., Bingöl A. N. and Yanmaz A. M. (2016), 'Effect of Drainage Properties on Seepage Behavior of Earth-Fill Dams', Conference: 12th International Congress on Advances in Civil Engineering, Istanbul, Turkey.

Harr M.E. (1962), 'Ground water and seepage-book', school of civil engineering, purdue university, McGraw Hill, New York 91-37779.

Irzooki R.H.(2016), 'Computation of Seepage through Homogenous Earth Dams with Horizontal Toe Drain', Engineering and Technology Journal, Vol. 34, Issue 3 part (A), pp. 430-440.

Jamel A.A. (2016), 'Analysis and Estimation of Seepage through Homogeneous Earth Dam without Filter', Diyala Journal of Engineering Sciences, Vol. 9, No. 2, pp. 38-49.

Kamanbedast A. and Delvari A. (2012), 'Analysis of Earth Dam: Seepage and Stability Using Ansys and

GeoStudio Software', World Applied Sciences Journal, Vol. 17, No. 9, pp.1087-1094.

Malekpour A., Farsadizadeh D., Dalir A. H. and Sadrekarimi J. (2012), 'Effect of horizontal drain size on the stability of an embankment dam in steady and transient seepage conditions', Turkish Journal of Engineering and Environmental Sciences, Vol. 36, No. 2, pp.139-152.

Mansuri B., Salmasi F. (2013), 'Effect of Horizontal Drain Length and Cutoff Wall on Seepage and Uplift Pressure in Heterogeneous Earth Dam with Numerical Simulation', Journal of Civil Engineering and Urbanism, Vol. 3, No. 3, pp.114-121.

Omofunmi O. E., Kolo J. G., Oladipo A. S., Diabana P. D., and Ojo A. S. (2017), 'A Review on Effects and Control of Seepage through Earth-fill Dam' Journal of Applied Science and Technology, Vol. 22, No. 5, pp.1-11.

Parsaie A. and Haghiabi A.H. (2018), 'Prediction of side weir discharge coefficient by radial basis function neural network', MedCrave Online Journal of *Civil Engineering*, Vol. 4, issue 2.

Stark T.D., Jafari N.H., Zhindon J.S.L. and Baghdady A. (2017), 'Unsaturated and Transient Seepage Analysis of San Luis Dam', Journal of Geotechnical and Geoenvironmental Engineering, Vo.143, Issue. 2.

ZANCO Journal of Pure and Applied Sciences
The official scientific journal of Salahaddin University-Erbil
https://zancojournals.su.edu.krd/index.php/JPAS

ISSN (print):2218-0230, **ISSN (online):** 2412-3986, **DOI:** **http://dx.doi.org/10.21271/zjpas**

RESEARCH PAPER

Indoor Place Recognition and Localization Using Histogram of Oriented Gradient with Deep Learning

Zina Khaleel Jalal [1],Moayad Y. Potrus[2], Abbas M. Ali[3]

Department of Software and Informatics Engineering,College of Engineering, Salahaddin University-Erbil,Kurdistan Region, Iraq

ABSTRACT:

Indoor place recognition is a crucial and challenging field of computer science. It is widely used in robotics and computer vision for various applications. The challenges in indoor place recognition comes from the fact that recognizing localized places like office, corridor, and others may fall under various environmental effects of weather, illumination and others. In this paper, an indoor place recognition and localization system is proposed. The system utilizes the great recognition capabilities of Convolutional Neural Network (CNN) and AlexNet with the use of feature image for training. The feature images are constructed using Histogram of Gradient (HOG). The main contribution of this work is the use of 2D feature constructed image from HOG instead of the scene image used with CNN. The proposed system was compared to other previous systems, in which, it achieved better recognition accuracy when tested on COLD and IDOL standard indoor image datasets.

KEY WORDS: Place recognition, Localization, CNN, AlexNet, SIFT, HOG
DOI: http://dx.doi.org/10.21271/ZJPAS.32.1.3
ZJPAS (2020) , 32(1);19-30 .

1.INTRODUCTION :

Place recognition can be described as a technique that allows robots to determine if a captured image of a place has been visited before or not (Bai et al., 2018). Actually, robots must be capable of working in entirely various places, under many different environmental conditions (Mancini et al., 2018).

To realize long term autonomy and localization, specific problems in the area of changing environments must be treated. These environmental changes may include illumination changes, weather and point of view, which impact the accuracy of place recognition(Kumar et al., 2017).

Despite of many researches proposed for the reinforcement of place recognition, enhancing reliability and accuracy of place recognition, but still it's a challenging issue that needs an optimum solution (Kumar et al., 2017). Place recognition techniques traditionally depend on representing images visual content by utilizing local features, like SURF (Bay et al., 2006), SIFT (Lowe, 2004) or by means of "Bag of visual Words (Bovw)" model(Kenshimov et al., 2017). In computer vision, after the remarkable successfulness of deep learning, the focus of place recognition studies has lately changed from using conventional handcrafted features like SURF or SIFT to more generic features based on deep learning (Chen et al., 2017b).

Deep learning can be described as a particular branch of machine learning that utilizes multiple layers that consist of nonlinear transformation units (Chollet, 2018) one of the networks used for

---

* **Corresponding Author:**
Zina Khaleel Jalal
E-mail: zenaalassaff@gmail.com
Article History:
Received: 27/07/2019
Accepted: 29/09/2019
Published: 25/02 /2020

deep learning is Convolutional Neural Network. CNN is categorized as a deep learning model (Li et al., 2011). CNNs involve a large number of layers as Compared to original neural networks (Tobías et al., 2016). Convolutional neural networks are attaining significance in various tasks (Lopez-Antequera et al., 2017) like affordance prediction (Porzi et al., 2016), object classification (He et al., 2016) and depth estimation (Xu et al., 2017).

A basic convolutional neural network and AlexNet are presented in this work to perform place recognition under several illumination conditions such (cloudy, sunny and night) for training and testing both models. Two commonly available datasets, COLD and IDOL, are utilized for this purpose. HOG and SIFT were utilized with both networks for calculating the accuracy of recognition. The proposed modification and contribution of the work is achieved by transforming the Hog and Sift feature vector into 2D vector for CNN training. The organization of the research paper is in this order: Section 2 represents the related works. Section 3 introduces work steps, feature extractors and the networks that have been utilized. Section 4 introduces the results and comparison results that have been achieved in this research work. Finally, Section 5 illustrates our conclusion.

2. Related works

Place recognition has been focused on by many researchers and a huge number of works have done in this field. FAB-MAP by (Cummins and Newman, 2008) was one of the earliest works which proposed the utilization of Bag of words in place recognition. In their work, depending on the appearance of every position, suggested the probabilistic way of place recognition.

(Park et al., 2018) Presented a light-weight visual place recognition which is depending on CNN. The presented architecture is particularly designed for mobile robots which supplied with embedded systems. The architecture has a fewer filter and five convolutional layers. According to the computational time and accuracy in custom and KTHIDOL2 datasets, the results outperformed the traditional algorithms based on CNN approaches.

Researchers in (Lopez-Antequera et al., 2017) proved that the task of place recognition can be solved better by training a network discriminatively. They trained CNN under appearance changes like seasons, weather, point of view and time of day. For training CNN, they utilized triplet-based learning schema to place images in a low dimensional space. Such that, where small Euclidean distances are delegating of place sameness and conditions are demanding. They claimed that their presented network outperformed all general methods.

A new approach was suggested by (Kenshimov et al., 2017) which addresses the issue of the cross-season place recognition. It has the ability to raise the robustness of cross-season place recognition. It creates an image descriptor of lower dimensionality through deleting the activation of filters which correlates to environmental variations. Then, to extract the entire output of an intermediate layer of CNN.

For treating domain generalization in the state of semantic place classification, a new version of a deep learning model introduced by researchers in (Mancini et al., 2018). They built CNN architecture with added layers of weighted form of batch normalization. The architectures were AlexNet and ResNet. They tested the architecture on COLD dataset with various illumination conditions like sunny, night and cloudy. Their experimentations proved that using the new WBN layers on visual place recognition benchmark, achieved a better accuracy of place categorization.

3. Materials and methods:

Indoor Place recognition using extracting features then analyzing and recognizing them is a common method in the field. The proposed system uses CNN and AlexNet with Hog features. The whole process has been illustrated in Figure 1. The following subsection detail each of the proposed framework steps.

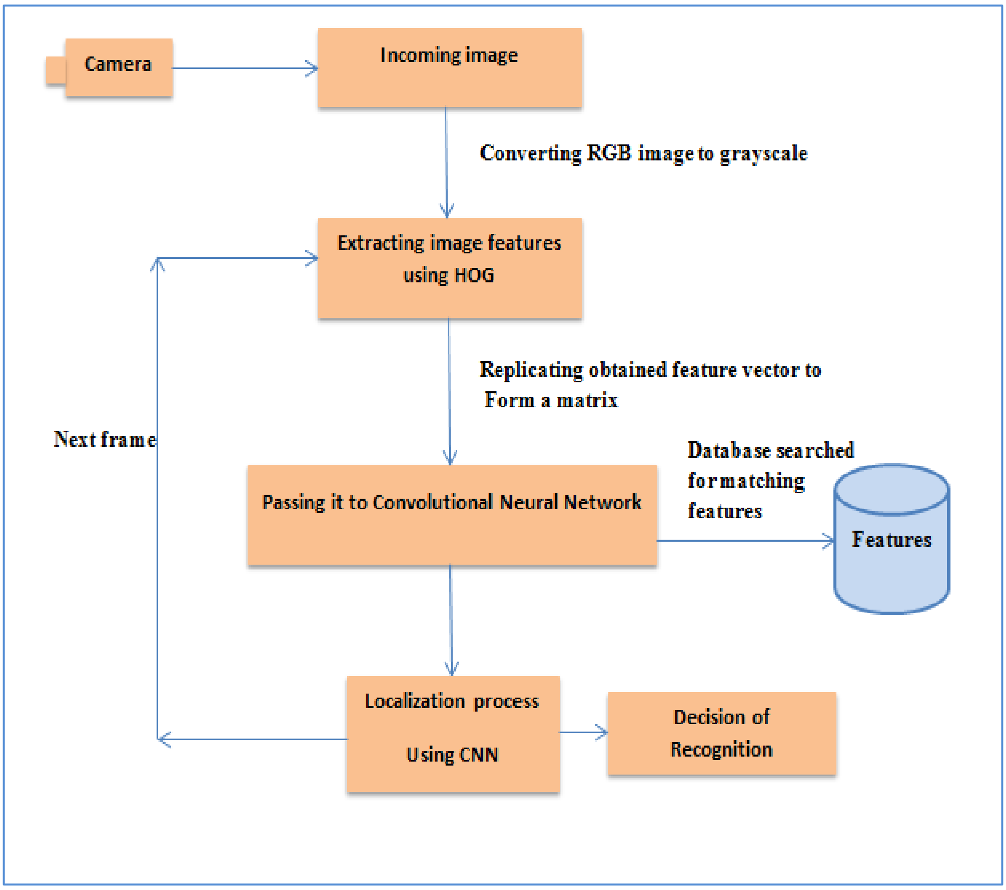

Figure 1: The whole process of proposed work

3.1.Pre-processing:

Images were imported from the COLD and IDOL datasets which are RGB images of size 640x480 pixels and 309x240 pixels respectively. Then these images were converted to grayscale images for next step of feature extraction.

3.2. Feature extraction:

In this section, feature extraction methods which have been utilized in this work such as HOG (Dalal and Triggs, 2005) and SIFT (Ledwich and Williams, 2004) with soft assignment of BOW, are discussed.

The following sections explain these methods.

3.2.1. Histogram of Oriented Gradient (HOG):

HOG is among the widespread features suggested by (Dalal and Triggs, 2005). The fundamental concept beyond HOG features is that appearance and local object shape inside an image can be described by the distribution of edge trends or intensity gradients. HOG partitions the image into small joint regions, named cells, and for every cell, it combines a histogram of gradient trends for the pixels inside the cell. Every pixel within the cell throws a weighted vote for an orientation-based histogram channel based on the values found in the gradient computation. The histogram channels are equally publishing over 0 to 180 degrees. The feature vector was represented by the integration of these cell histograms (Ren and Li, 2014). After generating feature vectors from HOG which has been produced nx1 feature vector, then the feature vector is horizontally stacked a column vector n times to generate a square matrix to be ready for input to both models. Figure 2 illustrates our contribution to HOG.

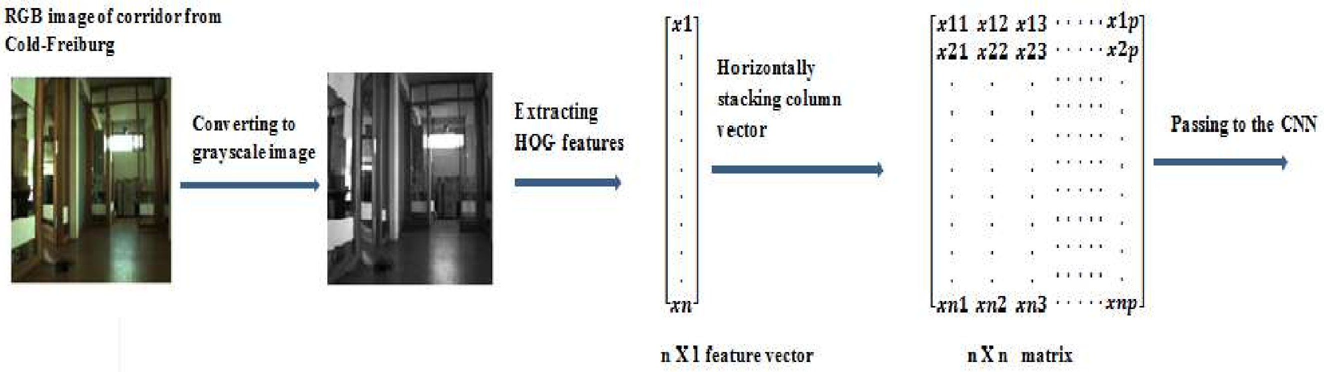

Figure 2: Process of converting HOG feature vector to a square matrix

3.2.2. Scale invariant feature transform (SIFT):

SIFT can be defined as one of the widely utilized local visual descriptors. It includes two steps in which, the first step, is about feature detection of images, the second step describes the extracted features (Sykora et al., 2014). SIFT detector is strong and stable to rotations, scaling, translation and partly stable to illumination variations and viewpoint of the camera (Mansourian et al., 2015). There are four stages in the algorithm. First, the images are checked under different octaves and scales for insulating image points that are different from their environments these points are defined as extreme points. Thereafter, points badly placed on an edge plus points which have low contrast have been removed (Mansourian et al., 2015). After this depending on local image properties a stable orientation is appointed to the key points. The keypoint descriptor usually utilizes a set of 16 histograms. This is placed in a 4x4 grid and each grid has 8 orientation bins. There is one for every of the major compass trends and for every central-points of these trends. This generates a feature vector which includes 128 items. Figure 3 shows generating keypoint descriptor (Lowe, 2004).

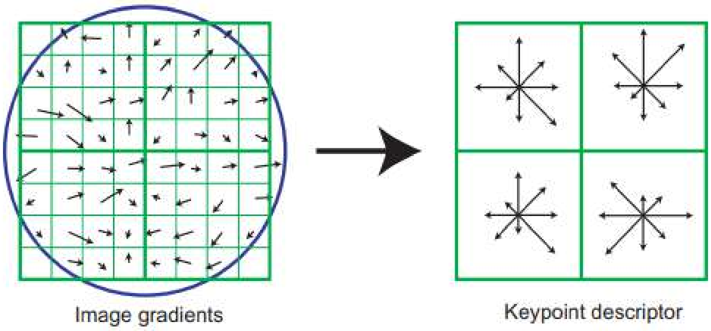

Figure 3: Generation of keypoint descriptor (Lowe, 2004)

3.2.3. Bag of Words (BOW):

BOW is defined as one of the most common representation ways for object classification. The basic concept behind it is to quantize every extracted key point into one of the visual words, and after that, every image will be represented by a histogram of visual words. For creating visual words, the mostly utilized clustering algorithm is (K-means) as shown in Figure 4 (Zhang et al., 2010).

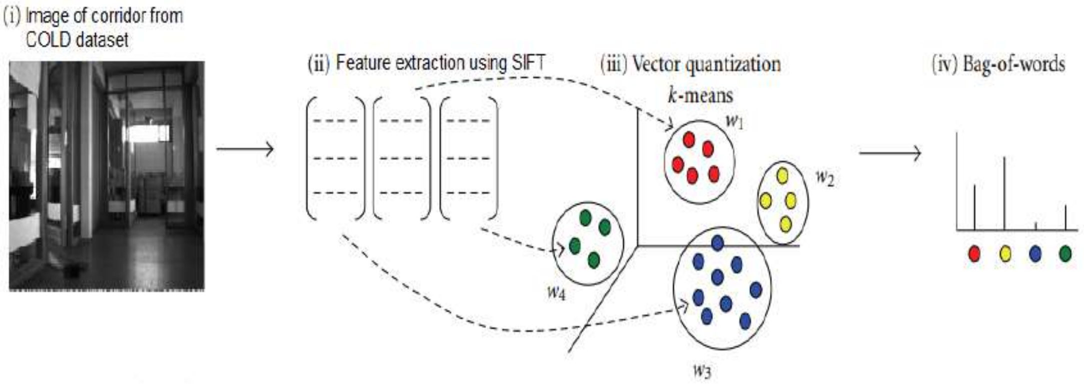

Figure 4: Steps for constructing bag of word

3.3. Convolutional Neural Network (CNN):

Feature vectors which are obtained from feature extractors are converted to a square matrix then passed as input to the CNN. After the localization process by CNN, the next frames will be read from the live images thereafter returning back to the feature extraction step to compute features for new frames. In this work, for training a CNN from scratch, 15 layers are used. These layers are 1 input layer, 3 convolutional layers with the filter size of 3x3, 2 max pooling layers, 3 batch normalization layers, 3 rectified liner unit layers, 1 fully connected layer, 1 softmax layer and 1 classification layer.

The following are the description of the layers:

3.3.1. Input layer:

It is the first layer which takes images and resizes them for passing it into the next layers (Sharma et al., 2018).

3.3.2. Convolution layers:

Convolution layers are distinguished through filter values. For each layer, there are multiple convolutions with a stable size also every kernel with a stable stride applied over the complete image (Tobías et al., 2016). Here the features of images will be found and then passed into the pooling layer (Sharma et al., 2018) Equation(1) represents the convolution operation (Chen et al., 2017a):

$$y^j = \max\left(0, b^j + \sum_i k^{ij} * x^i\right) \qquad (1)$$

y^j is the j-th output map and x^i is the i-th input map, k^{ij} represents the convolution kernel between j-th output map and the i-th input map also * represents the convolution operation.

3.3.3. Max Pooling Layer:

This layer takes the big sized images and shrinks them down while keeping the most significant information in them. From every window, it retains the maximum value; it keeps the finest fits of every feature in the window (Sharma et al., 2018). The operation of max pooling is illustrated in Equation (2) (Chen et al., 2017a).

$$y^{i}_{j,k} = \max_{0\le m,n\le r}\left(x^{i}_{jxr+m,kxr+n}\right) \qquad (2)$$

Every activation $y_{j,k}^{i}$ in the i-th pooling map y^{i} pools above $r\ by\ r$ non overlapping region in the i-th input map x^{i} .

3.3.4. Rectified Linear Units Layers (ReLU):

Each negative number of the pooling layer will be changed with zero. This layer is utilized after the convolution layer, which aids the CNN to remain mathematically steady (Sharma et al., 2018). It is represented by Equation (3) below (Tobías et al., 2016):

$$F(x) = max\,(0, x) \qquad (3)$$

3.3.5. Batch normalization layer:

It is another layer that can be placed in the architecture of the model, such as a convolutional or fully connected layer. It supplies an introduction for input feed-forwarding and calculating gradients with regard to the parameters (Schilling, 2016).

3.3.6. Softmax layer:

Generally, deep learning provides a solution for classification problem, by utilizing a function of softmax as their classification function (final layer). The function of softmax identifies the discrete probability P allocation for K classes. This can be indicated by $\sum_{k=1}^{k} pk$ (Yosinski et al., 2014).

If x be as the activation, and θ be as its weight parameters at the softmax layer, then o can be represented as input to the softmax layer,

$$. \quad o = \sum_{i}^{n-1} \theta ixi \qquad (4)$$

Consequently

$$pk = \frac{\exp(o_k)}{\sum_{k=0}^{n=1} \exp(o_k)} \qquad (5)$$

Hence, the predicted class would be $\hat{y}$

$$\hat{y} = \underset{i \in 1 \ldots N}{\arg\max}\ pi \qquad (6)$$

3.4. AlexNet:

AlexNet is a vastly utilized CNN architecture (Tobías et al., 2016). For this work, basic AlexNet architecture is used which is pre-trained on ImageNet (Deng et al., 2009). The network includes 3 fully-connected and the collection of 5 convolutional layers. The latest FC layer is linked to the softmax layer resulting in 1000 class. For complete experiments on AlexNet in this work, the inputs which are obtained from replicating feature vectors are rescaled to 227x227x3.This will fit the feature vector into the network. In addition, the latest fully connected layer are fine-tuned to output 5 classes instead of 1000 as this paper has five classes used from each of COLD and IDOL datasets. Fine-tuning (Yosinski et al., 2014) means utilizing a formerly trained network as the starting of the training step, for a given task and training datasets (Tobías et al., 2016). Figure 5 presents the architecture of pre-trained AlexNet.

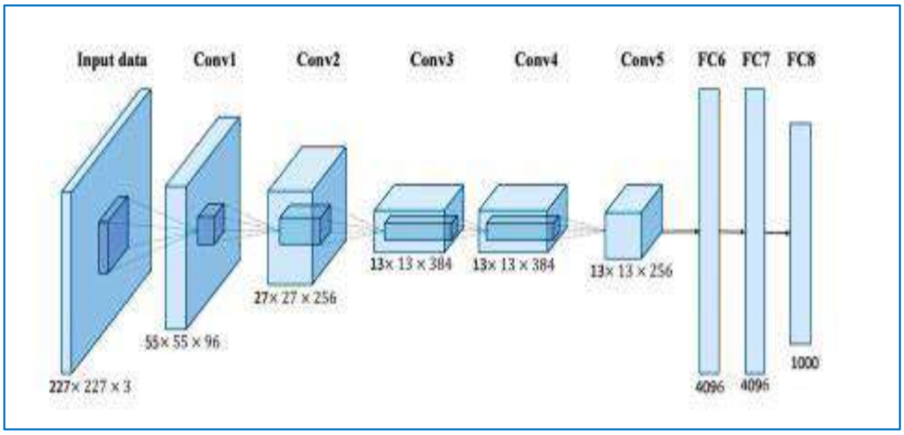

Figure 5: AlexNet architecture (Han et al., 2017)

4. Results and Discussion

In the proposed work, for calculating recognition accuracy, CNN and AlexNet have been used with two feature extractor methods HOG and SIFT. They both were applied to two common datasets COLD and IDOL.

COLD stands for Cosy Localization Database which includes three autonomously gathered sub-datasets (COLD-Freiburg, COLD-Ljubljana and COLD Saarbrucken) collected from three distinct interior laboratory environments using different robots. The COLD database is a typical testbed for evaluating the robustness of place recognition algorithms and localization. It is captured according to the dynamic and categorical changes established by human activity and illumination changes (Pronobis and Caputo, 2009). Figure 6 presents some images from the COLD database.

IDOL is an abbreviation which points to an Image Database for Robot Localization. The database includes 24 image series obtained by utilizing two moving robot platforms. The acquisition was carried out inside an interior laboratory environment which contains five rooms of various employments (corridor, two-person office, one-person office, printer area, and kitchen). Moreover, it was acquired under different illumination changes such as night, sunny and cloudy (Luo et al., 2006). Figure 7 presents some images from IDOL database.

For the COLD dataset when CNN utilized with SIFT gets higher recognition accuracy in the COLD night images which is 94.77%. Also, AlexNet with SIFT achieves higher accuracy in the COLD night images with accuracy of 92.47%. The results show that CNN has better accuracy than AlexNet as shown in Table 1.

For improving the accuracy of recognition, HOG has been used with both CNN and AlexNet. In the COLD dataset, CNN with HOG achieved higher accuracy in COLD cloudy images of about 98.36%, and for AlexNet by using HOG features achieves more accurate results in COLD night images which are 97.07%. These results are shown in Table 2. The results show a noticeable improvement in the recognition accuracy by using HOG rather than SIFT. Furthermore, for the IDOL dataset, CNN with HOG achieves higher accuracy for Idol night images of 97.31%. Also, for AlexNet with HOG in the same dataset gets higher accuracy for Idol night images of 95.03%. The results are presented in Table 3.

The achieved results of AlexNet by using HOG for the COLD dataset is compared with the work of (Mancini et al., 2018) for place recognition. In the work of Mancini et al. a batch normalization (BN) layer was added after each fully connected layer of Alex Net, but in the proposed work base AlexNet has been used and achieves higher accuracy for COLD night images it achieved better results as average of accuracy which is 96.13% compared to Mancini et al average accuracy of 94.6%. These are for the COLD-Freiburg group as shown in Figure 8.

Moreover, the proposed work added BN layer after each convolutional layer of base AlexNet with HOG features. The proposed setup was compared with the work of Mancini et al, which added the BN layer after each fully connected layer. The proposed AlexNet using BN layer gave a better accuracy for both COLD sunny and COLD night images and obtained better results with average of accuracy of 97.38% compared to Mancini work of 94.6% average of accuracy. As shown in Figure 9. These implementations are only for the COLD Freiburg group. The proposed CNN+HOG was compared with the work of (Mancini et al., 2017) which integrates CNN with Naive Bayes Nearest Neighbor (NBNN) model in the COLD-Freiburg dataset. The results showed that the proposed CNN achieves higher average accuracy than the work of Mancini et al., 2017. This is illustrated in Table 4.Finally, the proposed Alexnet+HOG and CNN+HOG were compared with the (ResNet + BN) and (ResNet+ Weighted BN (WBN)) by Mancini et al., 2018 applied to COLD-Freiburg dataset. The proposed work outperforms ResNet network which presented in Table 5.

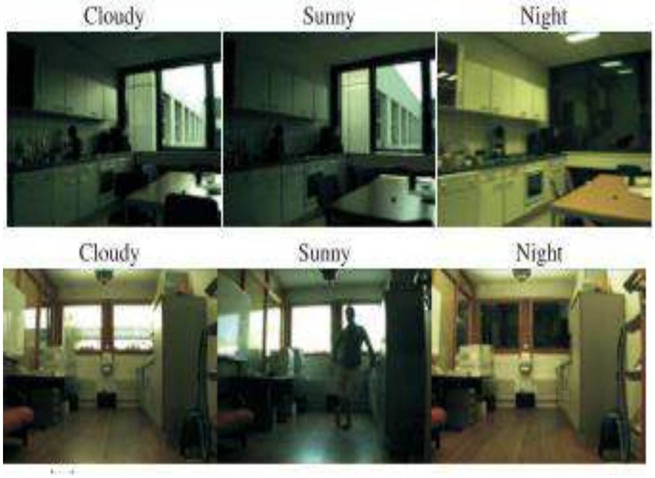

Figure 6: Images under different illumination from Cold dataset (Pronobis and Caputo, 2009)

Figure 7: Sample images from Idol dataset with various Illuminations (Luo et al., 2006)

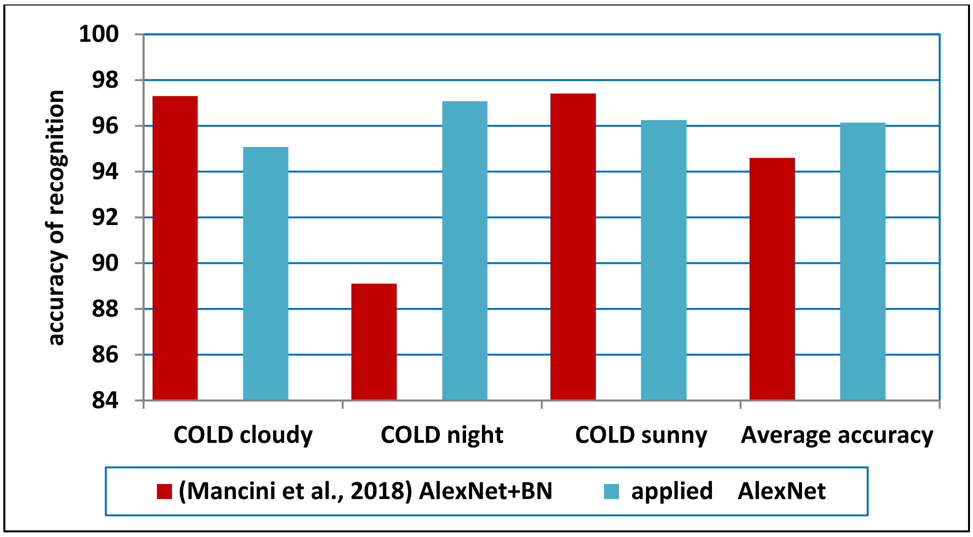

Figure 8: Comparing results for applied (AlexNet by utilizing HOG) and (AlexNet with BN layer) in (Mancini et al., 2018) for Cold-Freiburg.

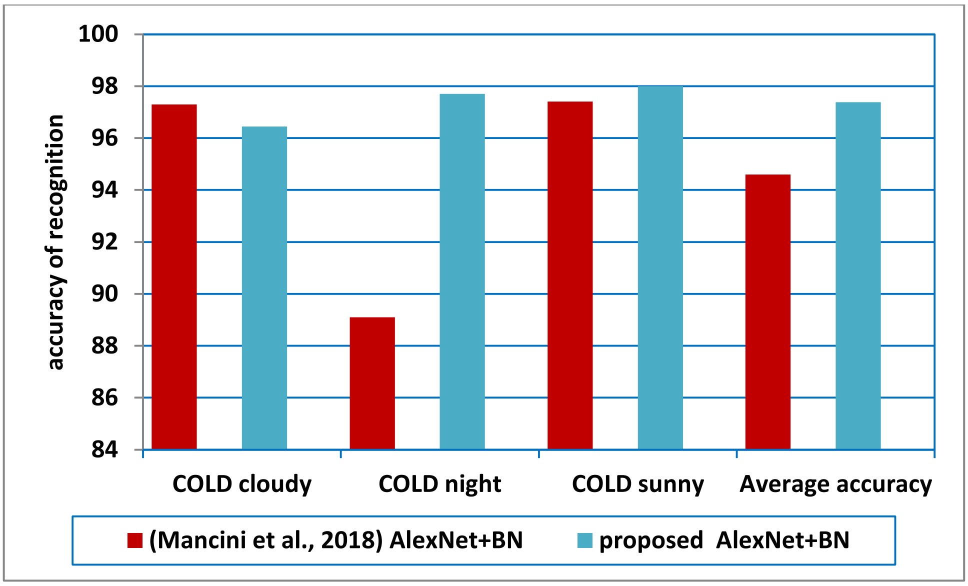

Figure 9: Comparing results of proposed (AlexNet with BN layer) and (AlexNet with BN layer) in (Mancini et al., 2018) for Cold-Freiburg.

Table 1: Recognition accuracy of CNN and AlexNet by utilizing SIFT in COLD dataset

SIFT with model	**COLD cloudy**	**COLD sunny**	**COLD night**
SIFT + CNN	88.49%	92.25%	94.77%
SIFT + AlexNet	86.58%	86.75%	92.47%

Table 2: Recognition accuracy of CNN and AlexNet by utilizing HOG in COLD dataset

HOG with model	**COLD cloudy**	**COLD sunny**	**COLD night**
HOG + CNN	98.36%	98.25%	97.49%
HOG + AlexNet	95.07%	96.25%	97.07%

Table 3: Recognition accuracy of CNN and AlexNet by utilizing HOG in IDOL dataset

HOG with model	**IDOL cloudy**	**IDOL sunny**	**IDOL night**
HOG + CNN	96.51%	97.09%	97.31%
HOG + AlexNet	93.68%	92.84%	95.03%

Table 4: Results of comparison of proposed (CNN + HOG) with (CNN + NBNN)

Method	**Average accuracy on COLD-Freiburg**
CNN with NBNN(Mancini et al., 2017)	95.2
Proposed CNN with HOG	**98.03**

Table 5: Results of comparison of proposed CNN, AlexNet with ResNet (Mancini et al., 2018)

Method	**Average accuracy on COLD-Freiburg**
ResNet + BN (Mancini et al., 2018)	90.2
ResNet + WBN(Mancini et al., 2018)	91.33
Proposed (AlexNet + BN) with HOG	**97.38**
Proposed CNN with HOG	**98.03**

5. Conclusion

In this research paper, CNN and AlexNet have been used for indoor place recognition and localization. This work attempted to find out the accuracy of recognition of two models applied to Further, when comparing AlexNet result with the work of Mancini et al., 2018 it demonstrated its superior performance in getting better results in terms of accuracy average. Moreover, the proposed CNN+HOG is compared with CNN+NBNN Mancini et al.,2017 in COLD-Freiburg dataset that shows proposed CNN two common datasets (COLD and IDOL) under different illumination conditions such as cloudy, night and sunny. The results on these two datasets demonstrated that the proposed CNN with HOG features significantly outperforms the AlexNet. outperforms CNN+NBNN. Finally, CNN+HOG and proposed (AlexNet+BN with HOG) are compared with the CNN architecture (ResNet with (BN and WBN)) in Mancini et al., 2018 which showed the proposed networks achieve higher accuracy average for recognition than of ResNet.

References

BAI, D., WANG, C., ZHANG, B., YI, X. & YANG, X. 2018. Sequence searching with CNN features for robust and fast visual place recognition. Computers & Graphics, 70, 270-280.

BAY, H., TUYTELAARS, T. & VAN GOOL, L.2006. Surf: Speeded up robust features. European conference on computer vision.Springer, 404-417.

CHEN, Z., JACOBSON, A., SÜNDERHAUF, N., UPCROFT, B., LIU, L., SHEN, C., REID, I. & MILFORD, M.2017. Deep learning features at scale for visual place recognition.IEEE International Conference on Robotics and Automation (ICRA). IEEE, 3223-3230.

CHEN, Z., MAFFRA, F., SA, I. & CHLI, M.2017. Only look once, mining distinctive landmarks from convnet for visual place recognition.IEEE/RSJ International Conference on Intelligent Robots and Systems (IROS). IEEE, 9-16.

CHOLLET, F. 2018. Deep Learning mit Python und Keras: Das Praxis-Handbuch vom Entwickler der Keras-Bibliothek, MITP-Verlags GmbH & Co. KG.

CUMMINS, M. & NEWMAN, P. 2008. FAB-MAP: Probabilistic localization and mapping in the space of appearance. The International Journal of Robotics Research, 27, 647-665.

DALAL, N. & TRIGGS, B.2005. Histograms of oriented gradients for human detection.

DENG, J., DONG, W., SOCHER, R., LI, L.-J., LI, K. & FEI-FEI, L.2009. Imagenet: A large-scale hierarchical image database. IEEE conference on computer vision and pattern recognition. Ieee, 248-255.

HAN, X., ZHONG, Y., CAO, L. & ZHANG, L. 2017. Pre-trained alexnet architecture with pyramid pooling and supervision for high spatial resolution remote sensing image scene classification. Remote Sensing, 9, 848.

HE, K., ZHANG, X., REN, S. & SUN, J.2016. Deep residual learning for image recognition. Proceedings of the IEEE conference on computer vision and pattern recognition.770-778.

KENSHIMOV, C., BAMPIS, L., AMIRGALIYEV, B., ARSLANOV, M. & GASTERATOS, A. 2017. Deep learning features exception for cross-season visual place recognition. Pattern Recognition Letters, 100, 124-130.

KUMAR, D., NEHER, H., DAS, A., CLAUSI, D. A. & WASLANDER, S. L.2017. Condition and viewpoint invariant omni-directional place recognition using cnn. 14th Conference on Computer and Robot Vision (CRV). IEEE, 32-39.

LEDWICH, L. & WILLIAMS, S. 2004. Reduced SIFT features for image retrieval and indoor localisation. Australian conference on robotics and automation. Citeseer, 3.

LI, P., LEE, S.-H. & HSU, H.-Y. 2011. Review on fruit harvesting method for potential use of automatic fruit harvesting systems. Procedia Engineering, 23, 351-366.

LOPEZ-ANTEQUERA, M., GOMEZ-OJEDA, R., PETKOV, N. & GONZALEZ-JIMENEZ, J. 2017. Appearance-invariant place recognition by discriminatively training a convolutional neural network. Pattern Recognition Letters, 92, 89-95.

LOWE, D. G. 2004. Distinctive image features from scale-invariant keypoints. International journal of computer vision, 60, 91-110.

LUO, J., PRONOBIS, A., CAPUTO, B. & JENSFELT, P. 2006. The kth-idol2 database. KTH, CAS/CVAP, Tech. Rep, 304.

MANCINI, M., BULÒ, S. R., CAPUTO, B. & RICCI, E. 2018. Robust place categorization with deep domain generalization. IEEE Robotics and Automation Letters, 3, 2093-2100.

MANCINI, M., BULÒ, S. R., RICCI, E. & CAPUTO, B. 2017. Learning deep NBNN representations for robust place categorization. IEEE Robotics and Automation Letters, 2, 1794-1801.

MANSOURIAN, L., ABDULLAH, M. T., ABDULLAH, L. N. & AZMAN, A. 2015. Evaluating classification strategies in bag of sift feature method for animal recognition. Research Journal of Applied Sciences, Engineering and Technology, 10, 1266-1272.

PARK, C., JANG, J., ZHANG, L. & JUNG, J.-I. 2018. Light-weight visual place recognition using convolutional neural network for mobile robots. IEEE International Conference on Consumer Electronics (ICCE). IEEE, 1-4.

PORZI, L., BULO, S. R., PENATE-SANCHEZ, A., RICCI, E. & MORENO-NOGUER, F. 2016. Learning depth-aware deep representations for robotic perception. IEEE Robotics and Automation Letters, 2, 468-475.

PRONOBIS, A. & CAPUTO, B. 2009. COLD: The CoSy localization database. The International Journal of Robotics Research, 28, 588-594.

REN, H. & LI, Z.-N.2014.Object detection using edge histogram of oriented gradient. IEEE International Conference on Image Processing (ICIP). IEEE, 4057-4061.

SCHILLING, F. 2016. The effect of batch normalization on deep convolutional neural networks.

SHARMA, N., JAIN, V. & MISHRA, A. 2018. An analysis of convolutional neural networks for image classification. Procedia computer science, 132, 377-384.

SYKORA, P., KAMENCAY, P. & HUDEC, R. 2014. Comparison of SIFT and SURF methods for use on hand gesture recognition based on depth map. AASRI Procedia, 9, 19-24.

TOBÍAS, L., DUCOURNAU, A., ROUSSEAU, F., MERCIER, G. & FABLET, R. 2016 Convolutional Neural Networks for object recognition on mobile devices: A case study. 23rd International Conference on Pattern Recognition (ICPR). IEEE, 3530-3535.

XU, D., RICCI, E., OUYANG, W., WANG, X. & SEBE, N. 2017. Multi-scale continuous crfs as sequential deep networks for monocular depth estimation. Proceedings of the IEEE Conference on Computer Vision and Pattern Recognition. 5354-5362.

YOSINSKI, J., CLUNE, J., BENGIO, Y. & LIPSON, H. 2014. How transferable are features in deep neural networks? Advances in neural information processing systems. 3320-3328.

ZHANG, Y., JIN, R. & ZHOU, Z.-H. 2010. Understanding bag-of-words model: a statistical framework. International Journal of Machine Learning and Cybernetics, 1, 43-52.

ZANCO Journal of Pure and Applied Sciences
The official scientific journal of Salahaddin University-Erbil
https://zancojournals.su.edu.krd/index.php/JPAS

ISSN (print):2218-0230**, ISSN (online):** 2412-3986**, DOI: http://dx.doi.org/10.21271/zjpas**

RESEARCH PAPER

The Influence of Cutting Edge Angles Included Angle and Nose Radius on Surface Finish of Aluminum Alloy 1050 in Turning.

Rzgar M. Abdalrahman*[1], Shawbo A. Hama Sure[1]

[1]Department of Mechanical Eng./ Production Engineering, Sulaimani Polytechnic University, Sulaimani, Kurdistan Region, Iraq

ABSTRACT:

The tool geometry is one of the most effective factors on the surface quality of turned products. This study aims to investigate the influence of different tool geometries on surface roughness of turned aluminum alloy 1050 that has not been documented well in literature. Various levels of simultaneous cutting edge angles, included angle and tool nose radius were selected. Different single point tools of HSS (5% cobalt) were prepared. Four categories of experiments were performed according to the levels of the included angle. Each category consisted of five sets of tests based on the proposed levels of tool nose radius. The tests within each set were arranged according to the selected levels of end cutting edge angle with constant or simultaneous cutting edge angle. All tests were conducted on a heavy duty lathe machine, while the produced surface qualities were measured by a stylus type roughness tester. Experimental results deduced a proportional relationship between surface roughness and end cutting edge angle with constant cutting edge angle. Also, the results showed that the surface roughness increases with the increase of simultaneous end cutting edge angle up to a certain point called focus point angle after which decreases. Furthermore, the tool nose radius has an inverse effect on roughness, but the included angle affects positively. Finally, the maximum values of simultaneous end cutting edge angle that can produce acceptable surface finish were defined in accordance with the tool nose radii and included angles.

KEY WORDS: Surface roughness, Side cutting edge angle, Simultaneous cutting edge angles, Included angle, Nose radius, Turning process..
DOI: http://dx.doi.org/10.21271/ZJPAS.32.1.4
ZJPAS (2020) , 32(1);31-38 .

ABBREVIATIONS

The tool angles, Figure 1, are specified according to ISO 3002 (1977):

CEA: Cutting edge angle [it is supplementary of (ECEA + IA)]
ECEA: End cutting edge angle
SCEA: Side cutting edge angle [complementary of CEA]
IA : Included angle (or tool nose angle)
r : Tool nose radius (or corner radius)
Ra: Arithmetic average of roughness.
L : Evaluation Length taking on x-axis parallel to the mean line direction.

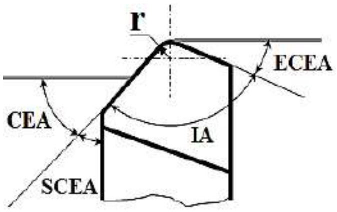

Figure 1: Tool angles in the tool in hand system (ISO 3002, 1977)

* **Corresponding Author:**
Rzgar Mhammed Abdalrahman
E-mail: rzgar.abdalrahman@spu.edu.iq

Article History:
Received: 06/03/2019
Accepted: 30/09/2019
Published: 25/02 /2020

INTRODUCTION

Aluminum alloy 1050 is the common type of aluminum that is utilized in the food, electrical and chemical industries because of its high electrical conductivity, corrosion resistance, and workability. The structural parts of aluminum alloy 1050 suffer from wear during service operations due to roughness and friction. Surface finish is the cheaper and easier factor for improving the wear resistance, frictional resistance, heat transmission ability and fatigue strength or creep life of the machined parts as reported by Mital and Mehta (1988), Rzgar M. A. (2010) and Rao et al. (2013). Ideal roughness in machining processes, among which turning process, is a function of cutting parameters and tool geometry, therefore, the proper setting of tool geometry guarantees high surface finish (Ahmed S. A.; Ramadan H. G., 2017).

Tool shape includes different kinds of angles and geometries, e.g., cutting edge angles, included angle, nose radius etc. The long history of turning process and its importance in machining resulted in a very rich literature in optimizing and selecting the proper geometries of single point tool and hence improving the turning performances of high surface finish and precise dimension. Groover (2007) reported that lower ECEA significantly produces better surface quality. Sung et al. (2014) performed an analytical and experimental investigation about the effect of ECEA on surface roughness of AISI 304 alloy steel rod in finish turning. They deduced that decreasing ECEA considerably improves the surface quality and they found good agreement between the experimental and analytical results.

Also Rico et al. (2010) studied the effect of SCEA on surface roughness of aluminum 1350 in turning operation. Their results show that the SCEA has a significant effect on surface roughness. Moreover, Kolahan et al. (2011) considered both the side and end cutting edge angles during an experimental study to optimize different machining and tool geometry parameters in turning AISI1045 steel. After analyzing the results, they deduced that the optimal surface quality is function of the lowest value of the ECEA and inversely the highest value of SCEA. Surya and Atla (2015) experimented with the influence of CEA of face milling cutter on surface finish of En31 steel material and pointed out linear proportion between them. They explicated the reason due to the increase in the thickness of uncut ridges. Bougharriou et al. (2014) revealed that highly cold worked ridges, corresponding to the tool nose geometry, are left behind on the turned surface with a pitch equals the axial feed.

Regarding the effect of tool IA on surface roughness, Taha et al. (2010) utilized rhombus and triangle inserts of 80° and 60° included angle, respectively, for turning AISI D2 steel at different feed rates. They found that the rhombus type, compared to the triangle, produces 40% higher roughness because its ECEA is larger and causes shallower feed marks. Also, Vasista et al. (2016) used different carbide tip brazed cutting tools of 90^0 , 60^0 , 30^0 nose angles to investigate experimentally their effect on surface roughness of 58CrV4 steel at varied feed rates under dry conditions. They deduced the insignificance of included angle to surface roughness at low feed rates and also the importance of the 60° nose angle tools for profile turning applications.

The importance of the tool nose radius, as the tool geometry factor, in producing acceptable surface finish had also been investigated by many researchers. In a review paper Chaijareenont and Tangjitsitcharoen (2018) concluded that large nose radius produces smoother surface at low feed rates and a high cutting speeds, however it increases the ploughing effect in the cutting zone and the tool flank wear. Singh et al. (2016) studied and analyzed effect of different nose radius (0.4 mm, 0.8 mm, 1.2 mm) of the CNMG cutting tool on surface roughness of aluminum (6061), in CNC turning and dry condition. They deduced that nose radius is the most significant parameter to surface roughness; it decreases with the increase in nose radius.

Lubis et al. (2015) studied the influence of different nose radius of 0.4 mm; 0.8 mm and 1.2 mm of three carbide cutting tools on the surface roughness of steel ST60, using spindle CNC machine and coolant cutting APX. They deduced that the tool nose radius of 1.2 mm performs the lowest roughness of 1.67μm. During an experimental investigation on the dry facing operation of an Al-Cu alloy, Torres et al. (2015) considered different tool nose radius values of up to 1.2 mm to analyze its impact on surface roughness. They found that the larger tool nose radius causes a smoother feed marks and improves surface finish. In contrast Chaijareenont and Tangjitsitcharoen (2018) focused on effect of tool nose radius on surface roughness during turning aluminum alloy (Al 6063). They concluded that surface roughness improves with increasing nose radii to only 0.4 mm and lower, but not more. Therefore, the nose radius is considered as a variable in the current study to determine its effect on surface roughness.

Aforementioned review shows that only the individual impact of the tool geometries, especially the ECEA and CEA, on surface quality have been studied without considering their concurrent change. There is still a lack of information about the effect of nose radius, included angle together with simultaneous cutting edge angles on surface finish of aluminum alloy 1030. Simultaneous means that the tool ECEA and CEA values are changed equally and contrary.

Therefore different levels of simultaneous cutting edge angles, nose radius and included angles are considered and examined in this study to find their effects on the surface quality of aluminum alloy 1050 when turning. The desired values of the simultaneous cutting edge angles are obtained virtually by rotating the lathe machine tool post.

1 EXPERIMENTAL PROCEDURE

1.1 Materials, Machines and Instruments:

The test samples are prepared from a 25 mm diameter shaft of aluminum alloy type 1050 that has shear strength of 60 GPa and its chemical composition illustrated in Table 1.

Table 1: Chemical composition of the sample material

Si	Fe	Cu	Mn	Mg	Zn	Ti	V	Al
0.25	0.4	0.05	0.05	0.05	0.05	0.03	0.05	99.07

This material was chosen due to its ductility. The HSS tools of 5% cobalt, Figure 2, are utilized in order to facilitate implementation the required tool geometry. The inclination, rake and relief angles of the used tools are kept at 3°, 4° and 3°, respectively. All experiments are performed on a heavy duty precision conventional lathe machine, type Excel; model TH8020D of 11kW main spindle motor power.

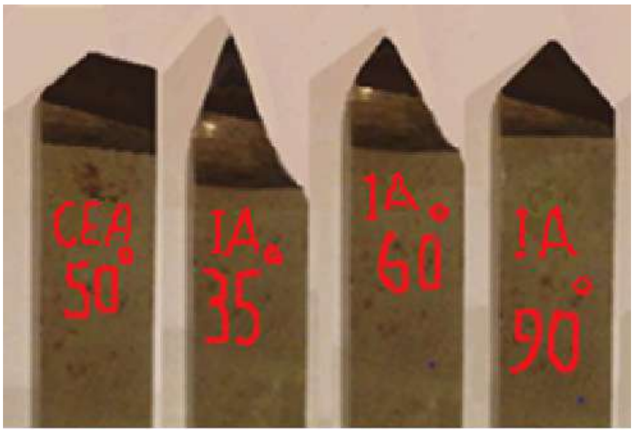

Figure 2: Applied HSS tools.

Surface quality of the test specimens are measured by a stylus type roughness tester, Figure 3, model ISR-C100 and measuring range of 160 µm. A traversing length of 0.8 mm was applied for measuring roughness according to BS1134:2010 (2010). Surface roughness was characterized by the most commonly specified parameter of arithmetic mean surface roughness (Ra), which is obtained from the following relation in micron meter according to UNE-EN-ISO4287:1999 (2010).

$$\mathrm{Ra} = \frac{1}{L}\int_0^L \{f(x)\}dx \qquad (1)$$

The measuring devices of optical profile projector, optical protractor, angle gauge and radius gauge, are utilized to check and ensure the prepared tool geometries of tool angles and nose radius before using.

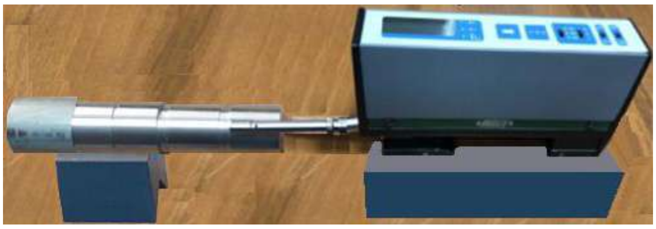

Figure 3: The styles type roughness tester during application

1.2 Experimental set-up

The experimental planning of this study involves a series of tests (200 tests), which are divided into four categories according to the IA values of the utilized cutting tools (Varied, 35°, 60°, 90°). Each experiment category contains five sets of tests according to the selected levels of tool nose radius (0.1mm, 0.2mm, 0.3mm, 0.4mm and 0.5mm). Each individual test set consists of ten tests according to the proposed levels of ECEA, as illustrated in Table 2.

Table 2: The study plan (the proposed variables and their levels).

Test categories					
Test category No		1	2	3	4
IA [°]		Variable	90	60	35
Test sets					
Test set No.	1	2	3	4	5
r [mm]	0.1	0.2	0.3	0.4	0.5
Tests					
Test No	ECEA [°]	CEA[°]			
1	2	50	88	118	143
2	6		84	114	139
3	10		80	110	135
4	20		70	100	125
5	30		60	90	115
6	40		50	80	105
7	45		45	75	100
8	60		30	60	85
9	72.5		17.5	47.5	72.5
10	80		10	40	65

The IA value is varied in the tests of the first test category because the tool CEA is kept constant at 50° and the tool ECEA is variable. Also the tool CEA has different values in the tests of the last three test categories (second, third and fourth) due to its simultaneous change with the ECEA and IA values. The simultaneous values of IA in the first test category and CEA in the last three test categories are determined according to the following relation (Sung et al., 2014):

$$\text{ECEA} + \text{CEA} + \text{IA} = 180° \qquad (2)$$

Prior to each test the HSS tool, as shown in Figure 2, is grinded to its required geometry except the desired simultaneous ECEA and CEA values, in the last three test categories, are obtained practically by rotating the lathe tool post. Then the tool geometry is checked precisely. Constant feed rate of 0.4 mm/rev and cutting depth of 0.12 mm are proposed in order to ensure involvement of the straight main and minor cutting edges during cutting. Also a fixed cutting speed of 20 m/min that ensures good surface finish is applied during the tests. All levels of the proposed test variables (ECEA, IA and tool nose radii) as well as the fixed cutting conditions are selected based on previous experience, characteristics of the cutting tool and the mechanical properties of the test material.

Surface roughness of the samples are measured at three places along the feed direction by rotating the sample about its axis through 90°, then their average are obtained as response variable. A limit of 100 µm is considered for the accepted roughness to allow obtaining clearer data about the effectiveness of the proposed variables on surface roughness. Furthermore, each test is repeated at least three times to obtain more realistic value of the desired response variable of surface roughness.

2 RESULTS AND DISCUSSION

2.1 Effect of ECEA with constant CEA on surface roughness:

Figure 4 exhibits the surface roughness variation by a specified tool of 90° included angle and 50° CEA for different ECEA at different tool nose radius. It shows that the surface roughness of turned aluminum alloy 1050 increases with the increase of ECEA. The increasing rate depends on the tool nose curvature value, which decreases with the increase of its radius. In other words a tool with a specified ECEA and CEA can produce smoother surface, when its nose radius is larger.

Figure 4: Effect of ECEA on surface roughness. CEA = 50°

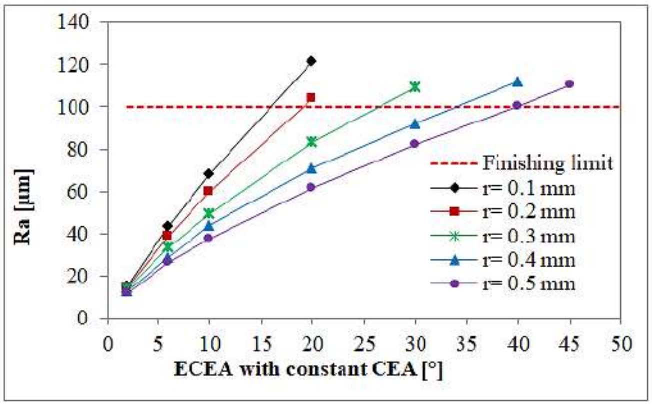

Accordingly, the maximum ECEA that gives acceptable surface roughness by a tool of 0.5mm nose radius is 40° and reduces to 16° when the nose radius is 0.1mm. This is because the increase of ECEA with fixed CEA increases persistently the height of the produced surface ridges, while increment of the tool nose radius escalates the engaged circular cutting edge that provides smoother finish. Figure 5 shows the produced surfaces of some test samples that are accepted or not according to the proposed finishing limit of this study.

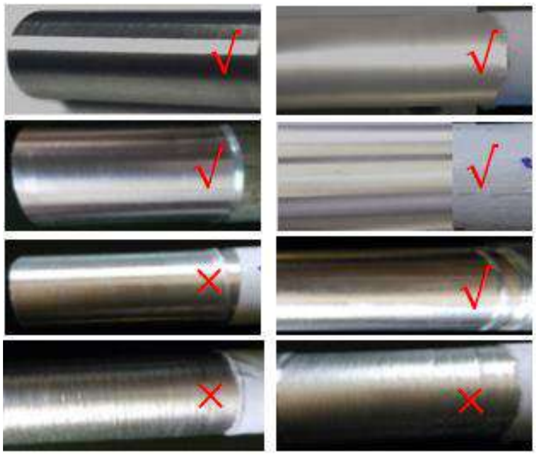

Figure 5: The surface quality of some accepted (√) and unaccepted (×) test samples

2.2 Effect of simultaneous ECEA and CEA on surface roughness:

The relationship between surface roughness of turned aluminum alloy 1050 by three specified tools of 90°, 60° and 35° included angles, for different simultaneous cutting edge angles at different tool nose radii, are illustrated in Figures

6, 7 and 9, respectively. The simultaneous ECEA values are similar in all the three tool types, but the CEA values are differ because they change equally and contrary to the tool ECEA and IA values. All figures, more obvious Figure 6, show that the surface roughness increases with the increase of simultaneous ECEA (or inversely the decrease of CEA) up to a certain point called ‘focus point’ after which reduces. Focus point is the point of equality between ECEA and CEA that can be determined as follows:

$$\text{Focus point angle} = (\text{ECEA} + \text{CEA})/2 = (180° - \text{IA})/2 \qquad (3)$$

Accordingly, the focus point angle for the three tool types of 90°, 60° and 35° included angles are 45°, 60° and 72.5°, respectively. Figure 6 also shows that the tool of 90° nose angle produces acceptable surface roughness (within the suggested limit of this study) at all levels of simultaneous ECEA when the nose radius is 0.4 mm or larger. In contrast when the nose radius is smaller than o.4 mm the surface roughness deteriorates for the tools of 0.3mm, 0.2mm and 0.1mm nose radii at the limited levels of simultaneous ECEA ranging between 25°- 62°, 18°- 66° and 16°- 76°, respectively. This means that the surface roughness improves again at the high levels of simultaneous ECEA and CEA for the 90° included angle tool.

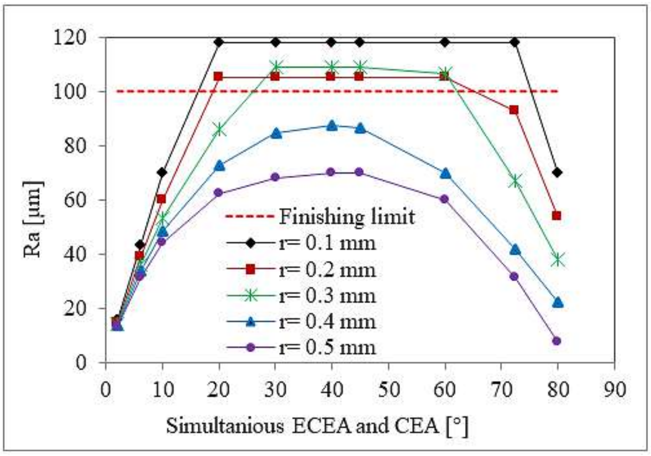

Figure 6: Effect of ECEA with simultaneous CEA on surface roughness, IA = 90°.

Figure 7 exhibits that the tool of 60° included angle produces deteriorated surface, as shown in Figure 8, beyond the simultaneous ECEA values of 30° and 40° at the nose radii of 0.5 mm 0.4 mm, respectively. Moreover, the surface roughness by the tool of 0.4 mm nose radius tends to improve beyond the simultaneous ECEA of 78°. Finally, the maximum active simultaneous ECEA that gives acceptable surface roughness is 42° for the tool of 0.4 mm nose radius, but reduces to 14° when the tool nose radius is 0.1 mm.

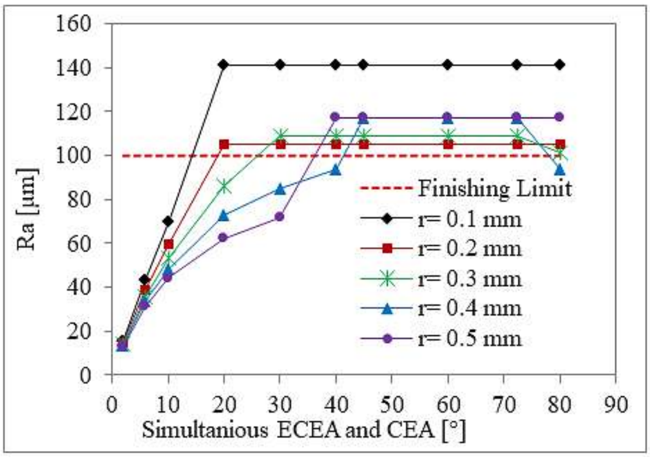

Figure 7: Effect of ECEA with simultaneous CEA on surface roughness, IA= 60°.

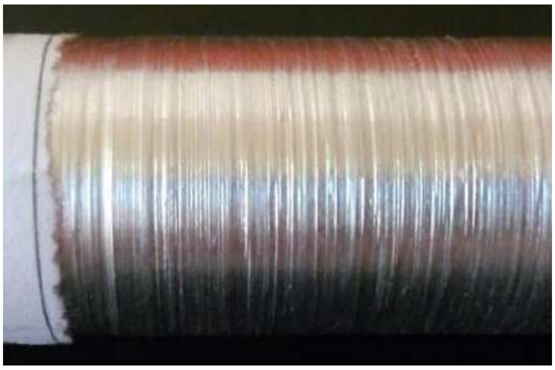

Figure 8: Deteriorated surface (higher than 100 µm) produced by a tool of IA= 60°, ECEA = 50° and r = 0.5 mm.

Figure 9 presents the relationship between the surface roughness, produced by the tool of 35° included angle, and different simultaneous values of ECEA at different nose radii. Although the resulted relationships should be curvilinear, they appear linear as those in Figure 3 because the tool type of 35° included angle has a large focus angle of 72.5°. Additionally, the maximum active simultaneous ECEA that gives satisfied roughness is 42° at the 0.5 mm nose radius tool, but reduces to about 18° for that of 0.1mm. It can be deduced from Figures 6 and 8 that the large focus angle (60° or higher) impedes the improvement of surface roughness at the simultaneous ECEA larger (or the simultaneous CEA lower) than the focus angle.

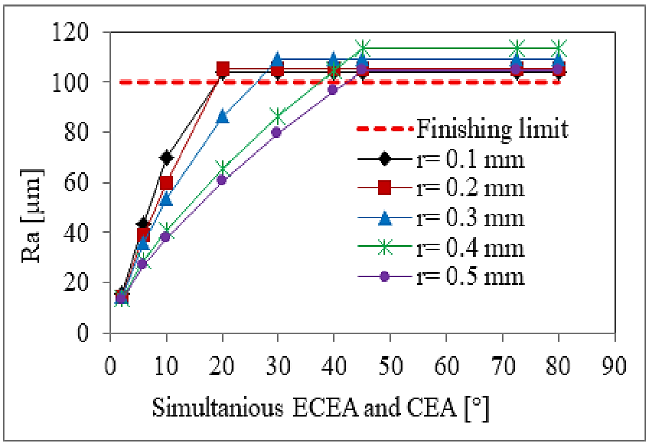

Figure 9: Effect of ECEA with simultaneous CEA on surface roughness. IA = 35°.

Figure 10 shows the effect of different concurrent ECEA on the surface quality of aluminum alloy 1050 by three specified tools of 90°, 60° and 35° included angles and a constant nose radius of 0.3 mm. It presents that despite the difference of IA and CEA in the tools, the simultaneous ECEA has a similar effect on surface roughness up to 30° then differ. This is because the ECEA value approaches the focus angle values that cause different complex engagement of the straight and circular cutting edges. Finally, the proper limits of maximum active simultaneous SCEA that can offer acceptable surface roughness for aluminum alloy 1050 are summarized in Table 3 according to the proposed values of IA tool nose radius.

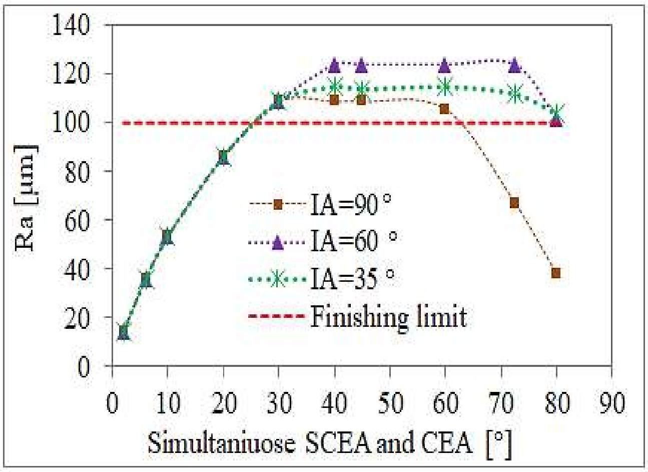

Figure 10: Effect of ECEA with simultaneous CEA on surface roughness by tools of different IA. r = 0.3 mm.

Table 1: The maximum active simultaneous ECEA and CEA that can give acceptable surface roughness

r [mm]	**IA** [°]		
	90°	60°	35°
	simultaneous **ECEA** and **CEA** [°]		
0.1	Up to 16°, then from 76°	Up to 14°	Up to 18°
0.2	Up to 18°, then from 66°	Up to 18°	Up to 18°
0.3	Up to 25°, then from 62°	Up to 25°	Up to 25°
0.4	All angles	Up to 42°, then from 78°	Up to 38°
0.5	All angles	Up to 35°	Up to 42°

2.3 Effect of r and IA on surface roughness:

The effect of tool nose radius on the surface finish of turned aluminum alloy 1050 is illustrated in Figure 11 for the three proposed tool types with constant ECEA of 30°. It shows that the nose radius is the most effective factor and has an inverse effect on surface roughness and the decreasing rates of roughness by the tools are different at the nose radii less than 0.4 mm, but they are similar for those of 0.4 and higher.

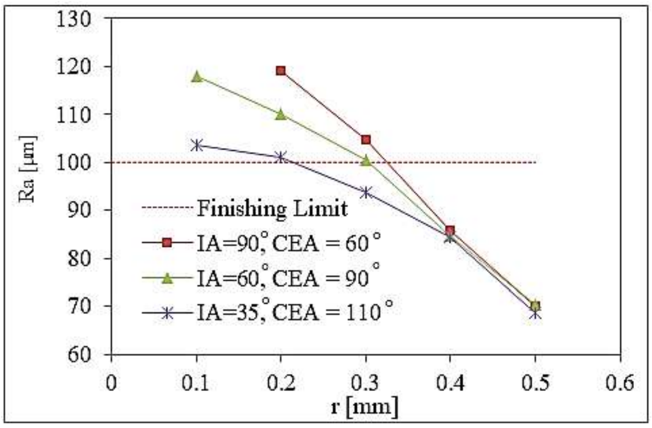

Figure 11: Effect of **r** on surface roughness at different IA. ECEA= 30°

Figure12 exhibits effect of the included angles of 90°, 60° and 35° on the surface roughness at different nose radii. It illustrates that IA has a positive effect on surface roughness for the nose radius smaller than 0.4mm, but it is insignificant for the nose radii of 0.4 mm and larger. This means that the tool with smaller IA produces smoother surface due to the increment of the engaged curved cutting edge that reduces the height of the ridges at the machined surface of the aluminum alloy1050.

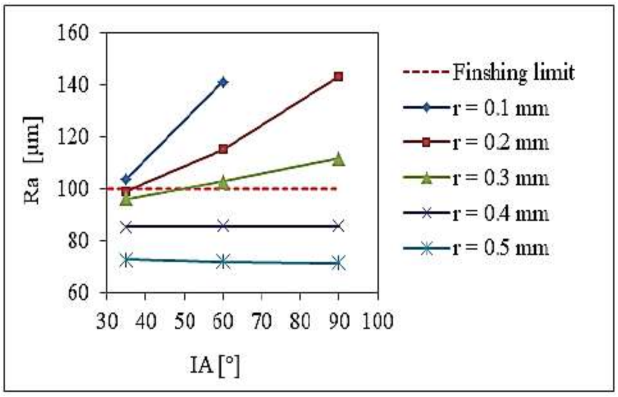

Figure 12: Effect of IA on surface roughness at different **r**. ECEA=30°

3 CONCLUSION

High surface quality, in the turning process, can be achieved by setting the proper levels of the tool geometry. This study investigates the effect of ECEA, with constant and simultaneous CEA, on the surface roughness of aluminum alloy 1050 for different single point tools with various levels of tool nose radius and included angles. The results presented that:

1. Surface roughness increases proportionally with the increase of ECEA, when CEA is constant.
2. When the simultaneous ECEA increases (or the simultaneous CEA decreases), the surface roughness increases up to a certain point called focus angle, then reduces and improves depending on the values of focus angle and tool nose radius.
3. The tools of 90° included angle provides acceptable surface roughness at all levels of simultaneous ECEA, when the nose radius is 0.4 mm or larger.
4. Surface roughness decreases with the increase of tool nose radius and it is the most important and effective tool geometry factor.
5. Included angle has a positive effect on surface roughness at the tool nose radii of 0.3 mm or smaller, but it is insignificant at those higher than o.3 mm.

Finally, further research is recommended about the influence of ECEA with simultaneous CEA on the produced cutting force and tool life, in addition to optimizing the cutting parameters that provides better cutting performances in turning aluminum alloy 1050.

Acknowledgements

The authors would like to acknowledge the support that Polytechnic University of Sulaimani has given to complete this work. Furthermore, the authors would like to thank the staff of the metal cutting lab and workshops of the Department of Mechanical Engineering/ Production Engineering at Sulaimani Polytechnic University, who assisted in all aspects of the experimental work.

References

AHMED S. A.; RAMADAN H. G. 2017. Effect of roller burnishing tool pass on surface roughness of austenitic stainless steel AISI 316L. *ZANCO Journal of Pure and Applied Sciences,* 29**,** 75-81.

BOUGHARRIOU, A., BOUZID, W. & SAI, K. 2014. Analytical modeling of surface profile in turning and burnishing. *The International Journal of Advanced Manufacturing Technology,* 75**,** 547-558.

BS1134:2010 2010. Assessment of surface texture. Guidance and general information. BSI Corporate

CHAIJAREENONT, A. & TANGJITSITCHAROEN, S. Monitoring of Surface Roughness in Aluminium Turning Process. IOP Conference Series: Materials Science and Engineering, ICFMM 2018- International Conference on Functional Materials and Metallurgy 28-30 Nov, 2018 Kuala Lumpur, Malaysia. IOP Publishing:, 012013.

GROOVER, M. P. 2007. *Fundamentals of modern manufacturing: materials processes, and systems*, 3rd Edition, John Wiley & Sons.

ISO 3002 1977. Geometry of the Active Part of Cutting Tools - General Terms, Reference Systems, Tool and Working Angles.

KOLAHAN, F., MANOOCHEHRI, M. & HOSSEINI, A. 2011. Simultaneous optimization of machining parameters and tool geometry specifications in turning operation of AISI1045 steel. *World academy of science, Engineering and Technology,* 74**,** 786-789.

LUBIS, S., SIAHAAN, E. & SUYATNO, T. I. 2015. Effect of Tool Nose Radius on Surface Roughness for Machining St 60 Steel Using Carbide Inserts.

MITAL, A. & MEHTA, M. 1988. Surface finish prediction models for fine turning. *The International Journal of Production Research,* 26**,** 1861-1876.

RAO, C., RAO, D. N. & SRIHARI, P. 2013. Influence of cutting parameters on cutting force and surface finish in turning operation. *Procedia Engineering,* 64**,** 1405-1415.

RICO, L., NORIEGA, S., GARCÍA, J., MARTÍNEZ, E., ÑECO, R. & ESTRADA, F. 2010. Effect of the side cutting-edge angle on the surface roughness for aluminum 1350 in the turning operation by taguchi method. *Journal of Applied Research and Technology,* 8**,** 395-403.

RZGAR M. A., Z. N. H., OMER S.M. 2010. Effect of Surface Roughness on Adhesive Bonding of Aluminum AA-150.1 with Gray Cast Iron ASTM Class 30 Type A. *Zanko, Journal of Pure and Applied Sciences,* 22.

SINGH, D., CHADHA, V. & SINGARI, R. M. 2016. Effect of nose radius on surface roughness during CNC turning using response surface methodology. *International Journal of Recent Advances in Mechanical Engineering,* 5**,** 31-45.

SUNG, A., RATNAM, M. & LOH, W. 2014. Effect of wedge angle on surface roughness in finish turning: analytical and experimental study. *The International Journal of Advanced Manufacturing Technology,* 74**,** 139-150.

SURYA, M. S. & ATLA, S. 2015. Effect of approach angle in face milling using tungsten carbide tool. *International Journal of Recent Advances in Mechanical Engineering,* 4**,** 15-27.

TAHA, Z., LELANA, H. K., AOYAMA, H., ARIFFIN, R., GONZALES, J., SAKUNDANI, N. & BHAKTI, S. Effect of insert geometry on surface roughness in the turning process of AISI D2. Proceedings of the 11th Asia Pacific industrial Engineering and Management Systems Conference, Melaka, Malaysia, 2010.

TORRES, A., PUERTAS, I. & LUIS, C. 2015. Surface roughness analysis on the dry turning of an Al-Cu alloy. *Procedia engineering,* 132**,** 537-544.

UNE-EN-ISO4287:1999 2010. *UNE-EN ISO 4287:1999/A1:2010* Aluminum Association.

VASISTA, S. S., KULKARNI, R. R., RAO, C. R. P., VEDAVYASA & RAJAGOPAL, M. S. 2016. Effect of Nose angle on surface texture while profile turning – An Experimental approach. *International Journal of Engineering Research And Advanced Technology,* 2 (Special Volume)

ZANCO Journal of Pure and Applied Sciences
The official scientific journal of Salahaddin University-Erbil
https://zancojournals.su.edu.krd/index.php/JPAS

ISSN (print):2218-0230**, ISSN (online):** 2412-3986**, DOI: http://dx.doi.org/10.21271/zjpas**

RESEARCH PAPER

Biodiversity of Fishes in Sulaimani Province in Kurdistan Region, Iraq

Younis S. Abdullah[1], Shamall M. A. Abdullah[2], Ridha H. Hussein[3]

[1]Medical Laboratory Dept., Technical College of Health, Sulaimani Polytechnic University, Iraq.
[2] Department of Fish Recourses and Aquatic Animals, College of Agriculture Salahaddin University-Erbil, Kurdistan Region, Iraq
[3]Biology Dept., College of Science, University of Sulaimani, Iraq.

ABSTRACT:

During the current study, random samples of fishes were taken from 26 localities mostly in the Lesser Zab and Sirwan tributaries within Sulaimani Province, Kurdistan Region, Iraq to survey the biodiversity of fish that are naturally found in water bodies of this province. The study was carried out during the period from January to the end of December 2018. A total of 2100 freshwater fishes, belonging to 35 species and eight families were collected. Among these fish species four native species are globally vulnerable. The study also demonstrated that *Cyprinion macrostomum* was the most abundant and wide spread species in this province, while *Leuciscus vorax* was scarce.

KEY WORDS: Freshwater fish, Biodiversity, Native species, Exotic species, Sulaimani province.
DOI: http://dx.doi.org/10.21271/ZJPAS.32.1.5
ZJPAS (2020) , 32(1);39-44 .

1. INTRODUCTION

The first taxonomic studies of ichthyofauna in Iraq started with Heckel 1843 in 19th century. He described 17 species from Tigris River at Mosul City in northern Iraq (Jawad, 2012; Kaya *et al.* 2016). There are a few works on ichthyofauna in Kurdistan Region of Iraq including the study of ichthyofauna in Dokan and Derbandikhan Lakes by Ciepielewski *et al.* (2001), Abdullah (2006), Abdullah *et al.* (2007), Abdullah and Abdullah (2018). The knowledge concerning the fish fauna of Kurdistan Region of Iraq is limited to fish parasitic studies carried out by Abdullah and Rasheed (2004a; 2004b), Abdullah (2005), Abdullah and Abdullah (2013a; 2013b; 2015a; 2015b; 2016; Bilal *et al.*, 2017).

Recently new fish species are being described from this Region. For instance, Freyhof *et al.* (2014) described two new species *Paracobitis molavii* in Zalm stream in Sulaimani province and *Paracobitis zabgawraensis* in Rean stream near Ziraran in Erbil province. Freyhof *et al.* (2016) recorded *Eidinemacheilus proudlovei* a subterranean loach from an aquifer into an ephemeral spring flowed into a small stream, which belongs to the Tabeen drainage in Sulamani province. Freyhof and Abdullah (2017) recorded two new loaches *Oxynoemacheilus gyndes* and *O.*

*** Corresponding Author:**
Younis Sabir Abdullah
E-mail: younis.abdullah@spu.edu.iq
Article History:
Received: 29/06/2019
Accepted: 17/09/2019
Published: 25/02 /2020

hanae in headwater streams of the upper Sirwan in Sulamani province. Also, Freyhof and Geiger (2017) recorded *Oxynoemacheilus zarzianus* in a spring fed stream in the Qalachulan River drainage in Sulamani province. In this investigation, we have summarized the available information on the biodiversity of fishes in Sulaimany Province that were collected in one year alone and ranging from smallest to largest fish size. Apparently, the existing information is incomplete and future studies are required in detail for a complete inventory and assessment of the biodiversity of fishes in this rich watery Province.

The aim of the present study is to currently identify the diversity of fish fauna within water bodies in Sulaimani Province, there is no scientific survey on fish fauna of these water bodies in this area.

2. MATERIALS AND METHODS

2.1. Description of Study Area:

Sulaimani province (Fig. 1) is located in the northeast of Iraq. It is situated between the latitudes of 35^{0} 05' and 36^{0} 30' and between longitudes of '44^{0} 25' and 46^{0} 20'**.** It is located close to the Iraqi-Iranian border. There are many water bodies in this province in addition to the two large rivers, namely, the Lesser Zab and Sirwan Rivers which they pass through this Province. The sampling area divided into eight area and 26 localities (Table 1).

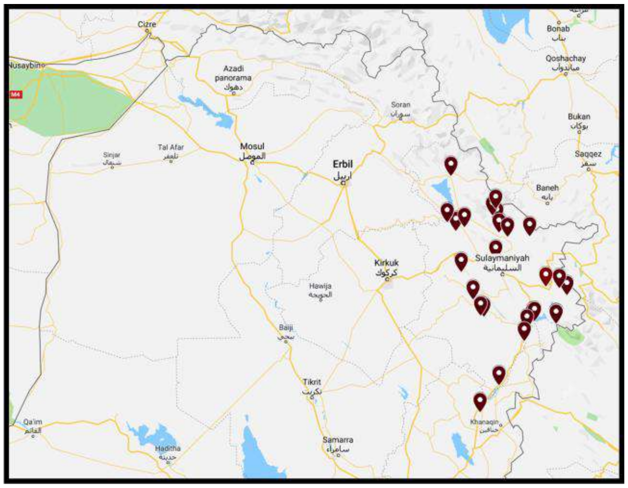

Figure 1: Map of north Iraq showing the study area (Google map 2019).

Table (1) List of sampling locations and their geographical specification.

Area	Localities	Coordinates
Sulaimani city	Sarchnar	N 35.586029^{0} E 45.381129^{0}
Sharbazher	Awkurte	N 35.964140^{0} E 45.396998^{0}
	Bardbard	N 35.915020^{0} E 45.367732^{0}
	Kareza	N 35.78366^{0} E 45.418174^{0}
	Khewata	N 35.75105^{0} E 45.7062^{0}
	Kunamasi	N 35.79695^{0} E 45.41370^{0}
	Qashan	N 35.867406^{0} E 45.403254^{0}
	Wazha	N 35.750105^{0} E 45.496155^{0}
Sharazwr	Darbandikhan lake	N 35.11315^{0} E 45.70650^{0}
	Kawta	N 35.095823^{0} E 45.92079^{0}
	Reeshen	N 35.354654^{0} E 45.961988^{0}
	Saraw	N 35.3722^{0} E 45.8351^{0}
	Shameran	N 35.117285^{0} E 45.719307^{0}
	Taparezina	N 35.30135^{0} E 46.0284^{0}
	Zmkan	N 35.089628^{0} E 45.918118^{0}
Qaradagh	Astely Ashty	N 35.1634^{0} E 45.2600^{0}
	Hazar Kani	N 35.1713^{0} E 45.2252^{0}
Garmyan	Banikhelan	N 35.063475^{0} E 45.648604^{0}
	Kalar	N 34.649567^{0} E 45.379714^{0}
	Kulajo	N 34.452221^{0} E 45.197145^{0}
	Sangaw	N 35.292413^{0} E 45.160485^{0}
Bazyan	Basara	N 35.5001^{0} E 45.0621^{0}
Dukan	Chami Rezan	N 35.8084^{0} E 45.021689^{0}
	Swrqawshan	N 35.872773^{0} E 44.944338^{0}
	Tabin	N 35.8336^{0} E 45.104544^{0}
Ranya	Darbany Ranya	N 36.216218^{0} E 44.99143^{0}

2.2. Collection and Preservation of Fishes

Fishes were mostly caught by pulsed DC electro-shock device (SAMUS 1000). The device was set up as follow: frequency of output pulses 50 Hz, duration of output pulses 5 milliseconds, amplitude of the output pulses 320V, output power 220W . This device just anesthetizes the fishes for a few seconds without harming the fishes or other water creatures. Also, gill netting, and hook were used. After anesthesia, fishes were fixed in 5% formaldehyde and stored in 70% ethanol. The fishes were identified based on their morphometric and meristic characters, so the measurements made point to point never by projections according to Beckman (1962), Kottelat and Freyhof (2007), and Coad (2010) and the scientific names for fishes were identified according to Froese and Pauly (2019).

3. Results and Discussion

A total of 2100 freshwater fish were collected from different water bodies in Sulaimani Province during the period from January to the end of December 2018. Table (2) shows number of fish species in different families, their abundance in this area and status. The fish fauna of this area comprise 35 species in 25 genera and eight families. The most diverse family is Cyprinidae with 23 species (65.7%) followed by Nemacheilidae with 6 species (17.1%), Bagridae, Heteropneustidae, Mastacembelidae, Mugilidae, Siluridae and Sisoridae each with only one species (2.8%).

The native species comprised 30 species (85.7%) in 7 families namely *Alburnus caeruleus, Acanthobrama marmid, Alburnus mossulensis, Arabibarbus grypus, Barbus lacerta, Capoeta trutta, C. umbla, Carasobarbus kosswigi, C. luteus, Chondrostoma regium, Cyprinion kais, C. macrostomum, Garra rufa, Leuciscus vorax, Luciobarbus barbulus, L. esocinus, L. xanthopterus, Squalius cephalus* and *S. lepidus* (Family Cyprinidae), *Mystus pelusius* (Bagridae), *Mastacembelus mastacembelus* (Mastacembelidae), *Planiliza abu* (Mugilidae), *Eidinemacheilus proudlovei, Oxynoemacheilus gyndes, O. hanae, O. kurdistanicus, O. zarzianus* and *Turcinoemacheilus kosswigi* (Nemacheilidae), *Silurus triostegus* (Siluridae), and *Glyptothorax kurdistanicus* (Sisoridae). While, five exotic species (14.2%) were listed in two families including: *Carassius auratus, Cyprinus carpio, Hemiculter leucisculus* and *Hypophthalmichthys molitrix* (Family Cyprinidae), and *Heteropneustes fossilis* (Heteropneustidae). The native distribution of *Carassius auratus* is in northern Asia and China. *Cyprinus carpio* naturally found in Europe and Asia, In Iraq they were first introduced from Holland and Indonesia. *Hemiculter leucisculus* was originally described from Peking, China. The native range of this species is from Maritime Russia south through China to Korea and Viet Nam. *Hypophthalmichthys molitrix* was originally described from China and the natural distribution is from the Amur River in the former U.S.S.R. southward to southern China. Also, *Heteropneustes fossilis* was described from Tranquebar, Tamil Nadu, India. These fishes were introduced into Iraqi water bodies for different purposes such as food fish, phytoplankton control, and as a biological control of mosquito and snail in order to control the parasitic diseases especially malaria and bilharzia (Coad, 2010).

Table (2): Scientific names of fishes collected from different water bodies in Sulaimani province with their numbers and status.

Family and Scientific Names	Number	Status
Family: Cyprinidae Rafinesque, 1815 *Acanthobrama marmid* **Heckel, 1843**	20	LC
Alburnus caeruleus **Heckel, 1843**	7	LC
Alburnus mossulensis **Heckel, 1843**	62	NE
Arabibarbus grypus **(Heckel, 1843)**	123	VU
Barbus lacerta **Heckel, 1843**	7	LC
Capoeta trutta **(Heckel, 1843)**	222	LC
Capoeta umbla **(Heckel, 1843)**	161	LC
Carasobarbus kosswigi **(Ladiges, 1960)**	5	VU
Carasobarbus luteus **(Heckel, 1843)**	89	LC
Carassius auratus **(Linnaeus, 1758)***	54	LC
Chondrostoma regium **(Heckel, 1843)**	52	LC
Cyprinion kais **Heckel, 1843**	10	LC
Cyprinion macrostomum **Heckel, 1843**	322	LC

Cyprinus carpio **Linnaeus, 1758***	195	VU
Garra rufa **(Heckel, 1843)**	57	LC
Hemiculter leucisculus **(Basilewsky, 1855)***	121	LC
Hypophthalmichthys molitrix **(Valenciennes, 1844)***	2	NT
Leuciscus vorax **(Heckel, 1843)**	1	LC
Luciobarbus barbulus **(Heckel, 1849)**	108	NE
Luciobarbus esocinus **Heckel, 1843**	52	VU
Luciobarbus xanthopterus **Heckel, 1843**	31	VU
Squalius cephalus **(Linnaeus, 1758)**	37	LC
Squalius Lepidus **Heckel, 1843**	62	LC
Family: Bagridae Bleeker, 1858		
Mystus pelusius **(Solander, 1794)**	8	LC
Family: Heteropneustidae Hora, 1936a		
Heteropneustes fossilis **(Bloch, 1794)***	8	LC
Family: Mastacembelidae Swainson, 1839		
Mastacembelus mastacembelus **(Banks & Solander, 1794)**	94	LC
Family: Mugilidae Cuvier, 1829		
Planiliza abu **(Heckel, 1843)**	76	LC
Family: Nemacheilidae Regan, 1911		
Eidinemacheilus proudlovei **Freyhof, Abdullah, Ararat, Hamad & Geiger, 2016**	40	NE
Oxynoemacheilus gyndes **Freyhof & Abdullah, 2017**	14	NE
Oxynoemacheilus hanae **Freyhof & Abdullah, 2017**	5	NE
Oxynoemacheilus kurdistanicus **Kamangar, Prokofiev, Ghaderi & Nalbant, 2014**	12	NE
Oxynoemacheilus zarzianus **Freyhof & Geiger, 2017**	2	NE
Turcinoemacheilus kosswigi **Bănărescu & Nalbant, 1964**	2	LC
Family: Siluridae Cuvier, 1816		
Silurus triostegus **Heckel, 1843**	20	LC
Family: Sisoridae Bleeker, 1858		
Glyptothorax kurdistanicus **(Berg, 1931)**	19	DD
Total	**2100**	**-**

***=** Exotic fish, **DD=** Data Deficient, **LC**= Least Concern, **NE=** Not Evaluated, **NT=**Near Threatened, **VU= Vulnerable**

The most abundant and wide spread species recorded in this investigation were *known C. macrostomum* with ratio 15.3%, followed by *Capoeta trutta* with the ratio of 10.5%, then *Cyprinus carpio* as a third rank with the ration 9.2%. It was clarified that *Leuciscus vorax* was scarce with the ratio 0.04%. According to International Union for Conservation of Nature (IUCN) red list of threatened species, four of the native species are vulnerable including *Arabibarbus grypus*, *Carasobarbus kosswigi*, *Luciobarbus esocinus* and *Luciobarbus xanthopterus* (Table 2). Apparently, many factors may affect decreasing these fish species in Sulaimani Providence water bodies such as illegal way of fishing, overfishing, fishing in a spawning season, climate change, flood, water pollutions, instruction of gravel mining on streams and rivers, and introducing the exotic species annually especially common carp which they compete the native species for the place and food. Moreover, demanding of local people on these types of fishes is another reason for more fishing by fisherman. The authors expect that the ichthyofauna of Sulaimani Province could be more than this investigation and need more ichthyologists to find them.

In the past years there were a few works on ichthyofauna in Sulaimani Province; Ciepielewski *et al*. (2001) mentioned the name of 20 species (*Barbus grypus*, *B. barbulus*,, *B. esocinus*, *B. kersin*, *B. longiceps*, *B. luteus*, *B. pectoralis*, *B. rajanonim*, *B. xanthopterus*, *Chondrostoma nasus*, *C. regium*, *Cyprinus carpio*, *Leuciscus cephalus*, *Mastacembelus mastacembelus*, *Silurus glanis*, *S. triostegus*, *Varicorhinus barroisi*, *V. damascinus*, *V. trutta*, *V. umbla*) during their investigation in both Dokan and Derbandikhan Lakes. Abdullah (2006) recorded 23 species (*Acanthobrama marmid*, *Alburmus mossulensis*, *A. sellal*, *Barbus barbulus*, *B. belayewi*, *B. esocinus*, *B. grypus*, *B. kersin*, *B. luteus*, *B. subquincunciatus*, *B. xanthopterus*, *Capoeta trutta*, *Chondrostoma regium*, *Cyprinion macrostomum*, *Cyprinus carpio*, *Garra rufa*, *Leuciscus cephalus*, *L. lepidus*, *Varicorhinus trutta*, *Glyptothorax kurdistanicus*, *Heteropneustes fossilis*, *Liza abu*, *Mastacembelus mastacembelus.*) from Dokan Lake. Abdullah *et al*. (2007) recorded 26 species (*Acanthobrama marmid, Aspius vorax, Barbus barbulus*, *B. esocinus*, *B. grypus*, *B. kersin*, *B. lacerta*, *B. luteus, B. xanthopterus, Capoeta damascinus, C. trutta*, *Chondrostoma regium, Cyprinion macrostomum, Cyprinus carpio, Garra rufa, Hypophthalmicthyes molitrix, Leuciscus cephalus, L. lepidus, L. spurious, Varicorhinus barroisi, V. umbla, Silurus glanis, Glyptothorax kurdistanicus*, *Heteropneustes fossilis*, *Liza abu*, *Mastacembelus mastacembelus*) in Derbandikhan Lake. Rasheed (2011) recorded five species (*Barbus grypus*, *B. esocinus, Capoeta damascinus*, *Carassius auratus*, *Cyprinus carpio*), Abdullah and Abdullah (2018) recorded 17 species (*Arabibarbus grypus, Barbus barbulus, Capoeta trutta, C. umbla*, *Carasobarbus luteus*, *Carassius auratus*, *Chondrostoma regium*, *Cyprinion macrostomum*, *Cyprinus carpio*, *Garra rufa*, *Hemiculter leucisculus*, *Hypophthalmichthys molitrix*, *Luciobarbus esocinus*, *Squalius lepidus*, *Mystus pelusius*, *Silurus triostegus*, and *Mastacembelus mastacembelus*) in the same Lake.

It seems from the previous study that mentioned above the biodiversity of fish species in Sulaimani Province which recorded by researchers was very limited and nearly all of them were recorded the same species and they were not recording a new species, this is due to the way of specimen collection, nearly all researchers depended on the fisherman whom they use gillnetting or hock for fishing, and they couldn’t collect and record those fishes which they never reach to enough size in order to capture by gillnet. Moreover the place of fishing is another reason, most of researcher only collected the fish from the lakes and the large rivers, but they didn’t collect fishes from small streams and springs. The evidence supporting this idea is the size of those fishes which they recorded by the researchers, most of them were fishes which they use as a food by local people and they present in the local markets.

Recommendations

Gravel mining, garbage dumping, oil dumping, wastewater pipeline to river, sewage pollution, introduction of exotic aquatic species, illegal and over fishing are the main threats to fish diversity in Kurdistan Region of Iraq. So, it is suggested avoiding gravel mining on the rivers, treat all waste before discarding, and prevent over and illegal fishing. Also, Identify and manage a geographical area, recognized and managed, through legal or other effective means, as a protected area to achieve long-term conservation of all fish species, particularly threatened species. Moreover, Confirmative diagnosis (molecular study) is necessary for some fish species which closely similar to each other.

Acknowledgments

We are pleased to thank Dr. Jörg Freyhof from Leibniz-Institute of Freshwater Ecology and Inland Fisheries (IGB), Berlin, Germany for his recommendations. Also we thank Mr. Mariwan H. Aziz for his help in providing electro shocker device.

REFERENCES

ABDULLAH, S. M. A. 2005. Parasitic fauna of some freshwater fishes from Darbandikhan lake, north of Iraq. J. Dohuk Univ. 8(1). p. 29-35.

ABDULLAH, S. M. A. 2006. The inhabitant fished in Dokan lake in north of Iraq and methods for developing their culturing. 2nd International Conference of Ecology, South Valley University, 28-30 March 2006. p. 68-78.

ABDULLAH, Y. S. and ABDULLAH S. M. A. 2013a. Protozoans Infections of some Fish Species from Darbandikhan Lake in Kurdistan Region, Iraq. Kurd. Acad. J., -A-, Special Issue: 1st International Conference of Agricultural Sciences, 20-21 Nov. 2013. p. 85-91.

ABDULLAH, Y. S. and ABDULLAH S. M. A. 2013b. Monogenean Infections on Fishes from Darbandikhan Lake in Kurdistan Region, Iraq. Basrah J. Agric. Sci., Vol. 26 (Special Issue 1). p. 117-131.

ABDULLAH, Y. S. and ABDULLAH S. M. A. 2015a. The parasitic infections of some freshwater fishes from Darbandikhan lake, Kurdistan region, Iraq. Journal of Garmyan University, 2nd Scientific Conference, May 6th and 7th, 2015. Vol. 2 (Special issue). p. 874-884.

ABDULLAH, Y. S. and ABDULLAH S. M. A. 2015b. Observasions on fishes and their parasites of Darbandikhan lake, Kurdistan region in north Iraq. American Journal of Biology and Life Sciences, Vol. 3(5). p. 176-180.

ABDULLAH, Y. S. and ABDULLAH S. M. A. 2016. Recording three species of *Paradiplozoon* (Monogenea) from cyprinid fishes in some watersheds in Sharbazher area, Sulaimani city, north of Iraq. Journal of University of Duhok (JUD), Vol. 19(1). (Agric. And Vet. Science). p. 19-25. (special Issue) The 2nd Scientific Agricultural Conference. (April 26 and 27th 2016).

ABDULLAH, Y. S. and ABDULLAH S. M. A. 2018. Ichthyofauna of Darbandikhan lake in Kurdistan Region, Iraq. ZJPAS., 30(6). p. 130-134.

ABDULLAH, S. M. A. and RASHEED A.-R. A.-M. 2004a. Parasitic fauna of some freshwater fishes from Dokan lake, north of Iraq. I: Ectoparasites. Ibn Al-Haitham J. Pure Appl. Sci. 17(1). p. 34-36.

ABDULLAH, S. M. A., and RASHEED A.-R. A.-M. 2004b. Parasitic fauna of some freshwater fishes from Dokan lake, north of Iraq. II: Endoparasites. Ibn Al-Haitham J. Pure Appl. Sci. 17(5). p. 1-12.

ABDULLAH, S. M. A.; RAHEMO Z. I. F., and SHWANI A. A. 2007. The inhabitant fishes in Darbandikhan lake in north of Iraq and methods for developing their culture. Egypt. J. Aquat. Biol. and Fish. 11(3). p. 1-7.

BILAL, S. J.; RAHMAN S. K., ABDULLAH Y. S. and ABDULLAHA S. M.A. 2017. First record of *Rhabdochona* (*Rhabdochona*) *longispicula* (Nematoda) in *Glyptothorax kurdistanicus* from Greater Zab River, Kurdistan Region/ Iraq. ZJPAS., 29 (1). P. 48-53.

BECKMAN, W.C. 1962. The freshwater fishes of Syria and their general biology and management. FAO Fish. Biol. Branch Tech. Pap. No.8: 179pp.

CIEPIELEWSKI, W.; MARTYNIAK A. and SZCZERBOWSKI J. A. 2001. Ichthyofauna in the Dokan and Derbendikhan reservoirs. Arch. Pol. Fish. 9 (1). p. 157-170.

COAD, B. W. 2010. Freshwater fishes of Iraq, Pensoft Publisher, Sofia-Moscow.

CÜNEYT, K.; DAVUT T. and ERHAN Ü. 2016. The Latest status and distribution of fishes in upper Tigris River and two new records for Turkish freshwaters. Turk. J. Fish. Aquat. Sci. 16. p. 545-562.

FROESE, R., and PAULY D. 2019. FishBase. World web electronic publication. www.fishbase.org,version (3/6/2019).

FREYHOF, J.; ABDULLAH Y. S.; ARARAT K.; HAMAD I. and GEIGER M. F. 2016. *Eidinemacheilus proudlovei*, a new subterranean loach from Iraqi Kurdistan (Teleostei; Nemacheilidae). Zootaxa 4173 (3). p. 225–236.

FREYHOF, J., and ABDULLAH Y. S. 2017. Two new species of *Oxynoemacheilus* from the Tigris drainage in Iraqi Kurdistan (Teleostei: Nemacheilidae). Zootaxa, 4238 (1). p. 073-087.

FREYHOF, J. and GEIGER M. 2017. *Oxynoemacheilus zarzianus*, a new loach from the Lesser Zab River drainage in Iraqi Kurdistan (Teleostei: Nemacheilidae). Zootaxa 4273 (2). p. 258–270.

FREYHOF, J.; ESMAEILI, H. R.; SAYYADZADEH, G. and GEIGER, M. 2014. Review of the crested loaches of the genus *Paracobitis* from Iran and Iraq with the description of four new species (Teleostei: Nemacheilidae). Ichthyol. Explor. Freshwaters. 25 (1). p. 11-38.

JAWAD, L. A. 2012. History of the study of the fish fauna of Iraq. Water Research and Management, 2 (3). p. 11-20.

KOTTELAT, M. and FREYHOF J. 2007. Handbook of European freshwater fishes. Kottelat, Cornol and Freyhof, Berlin, xiv + 646 pp.

RASHEED, R. O. 2011. Seasonal variation in fat percentage and water content of muscle tissue of some fishes endemic to Derbendikhan reservoir. J. Babylon Univ. for Pure and Appl. Sci. 19(2). p. 435-443.

ZANCO Journal of Pure and Applied Sciences
The official scientific journal of Salahaddin University-Erbil
https://zancojournals.su.edu.krd/index.php/JPAS

ISSN (print):2218-0230, **ISSN (online):** 2412-3986, **DOI: http://dx.doi.org/10.21271/zjpas**

RESEARCH PAPER

Synthesis and Antibacterial Studies of new mixed ligand transition metal complexes of thioester (1, 3, 4-Oxadiazole) derivative (phozbt) and dppe Ligands.

Rezan A. Saleh[1*], Hikmat. A. Mohammad[2]
[1,2] Department of Chemistry, College of Education, Salahaddin University-Erbil, Kurdistan Region, Iraq

ABSTRACT:

Complexes of transition palladium(II) and platinum(II) metals that possessing two kinds of ligands: S-5-phenyl -1, 3, 4-oxadiazole-2-yl benzothioate (phozbt) and tertiary diphosphine (dppe), were synthesized. The thioester (phozbt) ligand was synthesized by reaction between 2-mercapto-5-phenyl-1,3,4-oxadiazole (PhozSH) with benzoyl chloride and using sodium hydroxide. The synthesized ligand and complexes were described by C, H, N, S analysis, infrared spectra, molar conductivity, UV-visible and magnetic susceptibility measurements. The (dppe) act as bidentate chelate that linked to the metals on both P-donor atoms. According to the spectral analysis of the complexes, a square planer structure were suggested for both metal complexes. The ligand and complexes were studied for antibacterial activity by using agar diffusion method. This study showed positive inhibition zone results, for both ligand and complexes with *S*. aureus and *P*. aeruginosa bacteria.

KEY WORDS: Pd(II), Pt(II), Oxadiazole derivatives, Dppe, Antibacterial activity
DOI: http://dx.doi.org/10.21271/ZJPAS.32.1.6
ZJPAS (2020) , 32(1);45-51 .

INTRODUCTION :

The chemistry of heterocyclic substance is a fascinating field of study since a long time (Pangal and Shaikh, 2013).

Compounds containing the (C-S-CO-C) functionality are identified as thioesters**.** A thioester is an ester with S atom instead of the O atom between the acyl and alkyl groups. Thioesters are a significant section of organosulfur compounds that have an essential role in the manufacture of pharmaceutical, biological, industrial and natural products.

In this consideration, preparation of thioesters is one of the most imperative assignments in organosulfur chemistry. The esterification of thiol groups is the main and most frequent strategy for the synthesis of thioesters (Scheme 1) (Kazemi and Shiri). Thioesters are the most usual type of activated carboxylic acids in a cell (Bruice, 2006).

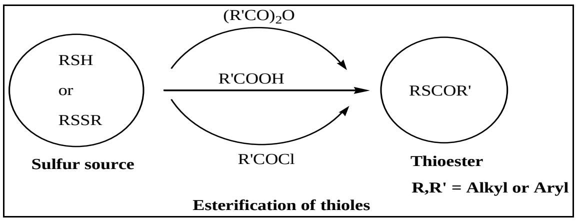

Scheme 1: Preparation of thioester compounds

Oxadiazole is a five member heterocyclic compound containing one O and two N atoms, in

---

*** Corresponding Author:**
Rezan Ali Saleh
E-mail: rezan.saleh@su.edu.krd or rezanali2@gmail.com
Article History:
Received: 22/04/2019
Accepted: 30/09/2019
Published: 25/02 /2020

older literature it was referred as furadiazoles which attracted wide attention of chemist for preparation of different biological active drugs. The biological behavior of oxadiazole are attributable to the presence of -N=C – O linkage (Shubhangi and Pravina, 2013).

This work, reports, the synthesis and Identification of new transition metal Pd(II) and Pt(II) complexes containing both (dppe) and (phozbt) ligands.

1. MATERIALS AND METHODS

2.1. MATERIALS

The (Platinum (II) chloride, Paladium(II) chloride, PhozSH and dppe) (commercial products) were used as supplied. Melting points and decomposed degrees were determined on an electrothermal MPD-100. Infrared spectra were taken on Brooker-ALPHA infrared appliance using potassium bromide disc. Proton and carbon thirty- NMR were recorded in chloroform solution on a Bruker Ac 400 MHz spectrometer using d^6-DMSO as solvent. Uv.-Vis. spectra were acquired using a Perkin-Elmer Lamda 9 spectrophotometer. Conductivity measurements were executed on 10^{-3}M solutions using a conductivity meter type CDM 83 70. Elemental analyses were taken on Carlo-Erba elemental analyzer, type 1106. Magnetic measurements were measured on a Bruker BM6 appliance at room temperature following the Faraday method.

2.2. Synthesis of thioester (phozbt)

Sodium hydroxide (0.003mol, 0.132g) was dissolved in water (15 ml) and (PhoztH) (0.0033mol, 0.587g) was inserted. After stirring for (15 minutes), a solution of appropriate benzoyl chlorides (0.0033mol, 0.463g) in ethanol (5 ml) was inserted drop-wise. The resultant mixture was stirred at room temperature for 3 hours; the observed precipitate was filtered, then recrystallized in methanol to obtain pure target compounds (Scheme 2) (Gurrala *et al.*, 2010). (Formula: $C_{15}H_{10}N_2O_2S$; Yield: 0.7 g, 75.2%; melting point: 138-139 °C; Colour: Off-white).

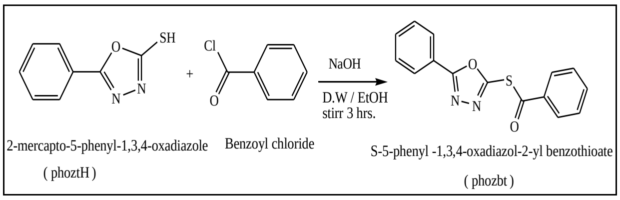

Scheme 2: Preparation of (phozbt) ligand

2.3. Synthesis of [Pd(κ^1-phozbt)Cl(κ^2-dppe)]Cl (1)

This compound can be synthesized by the following steps:

First step: Preparation of [PdCl$_2$(κ^2-dppe)]

Solution of dppe (0.25 mmol, 0.0994 g) in dichloromethane (13 ml) was inserted to a solution of palladium chloride (0.25 mmol, 0.0443 g) that dissolved in a mixture of warm concentrated hydrochloric acid (3 ml) and ethanol (10 ml). The final solution was stirred under reflux about 3hrs. The hot yellow solution was filtered. The resulting yellow colour precipitate was collected when the solvent evaporated (Lassahn *et al.*, 2003). (Formula: $C_{26}H_{24}Cl_2PdP_2$; Yield: 0.137g, 95.3%; decomposition point: 294°C; Colour: Yellow).

Second step: Addition of (phozbt) ligand to the prepared [PdCl$_2$(κ^2-dppe)]

A warm ethanolic solution (10 ml) of (phozbt) (0.13 mmol, 0.0367 g) was inserted to a solution of [PdCl$_2$(κ^2-dppe)] (0.13 mmol,0.0747 g) in dichloromethane (10 ml). The resultant mixture was heated to a reflux for 4 hours. After a few days, when the solvent was evaporated a yellow-brown precipitate was obtained (Formula: $C_{41}H_{34}Cl_2N_2PdO_2P_2S$; Yield: 0.096 g, 86.2%; melting point: 236-239 °C; Colour: Yellow-brown).

2.4. Synthesis of [Pt(κ^1-phozbt)Cl(κ^2-dppe)]Cl (2)

This compound was synthesized by the following steps

First step one: Synthesis of [PtCl$_2$(κ^2-dppe)]

The complex was synthesized as a Light-brown precipitate, by similar mode that applied for preparation of [PdCl$_2$(κ^2-dppe)] complex. (Formula: $C_{26}H_{24}Cl_2PtP_2$; Yield: 0.120 g, 90.5%;

decomposition point: 255 °C; Colour: Light-brown).

Second step: Addition of (phozbt) ligand to [$PtCl_2$(κ^2-dppe)] complex

(0.12 mmol, 0.0796 g) of [$PtCl_2$(κ^2-dppe)] dissolved in (10 ml) of CH_2Cl_2 solvent, then a hot ethanolic (10 ml) solution of (phozbt) ligand (0.12 mmol, 0.0338 g) was inserted and refluxed for 4 hours and filtered. After a few days when the solvent evaporated at room temperature, the light brown solid was observed (Formula: $C_{41}H_{34}Cl_2N_2PtO_2P_2S$; Yield: 0.085 g, 74.9%; melting point: 232-235 °C; Colour: Light-brown).

3. Results and Discussion

3.1. Proton-NMR spectrum of (phozbt)

The ^{1}H-NMR spectral band of the thioester (phozbt) ligand in d_6-dimethyl sulfoxide solvent displayed two doublets at δ (7.99 and 7.65) ppm which referred to (H9 and H3) protons correspondingly. The two triplets appearing at (7.71, 7.62, 7.54 and 7.28) ppm corresponding to the proton of (H11, H10 , H2 and H1) respectively (Dalia and Faiq, 2018).

The dissaperance of the SH band at (2.5) ppm that remarked in (phoztH) ligand indicates the formation of the thioester (phobt) ligand (figure 1) (Husain and Ajmal, 2009)(Kumar *et al.*, 2014).

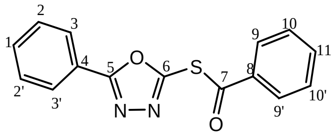

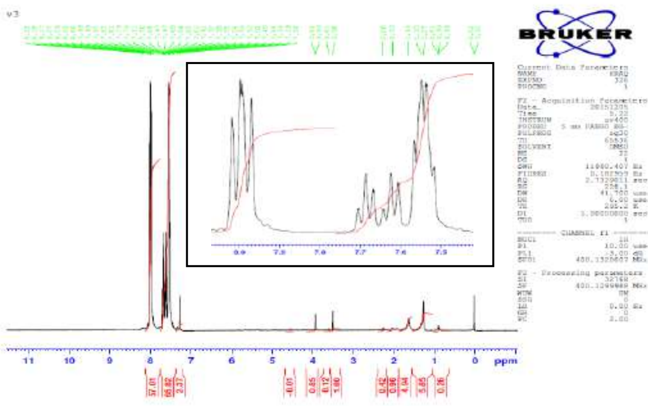

Figure 1: ^{1}H-NMR spectrum of (phozbt) ligand

3.2 ^{13}C-NMR spectrum of (phozbt)

The carbon-NMR spectrum of (phozbt) was recorded in dimethyl sulfoxide solvent. The carbonyl carbon band displayed at (174.43) ppm; C_7 (Joshi *et al.*, 2015).The two carbon atom (C_6 and C_5) of oxadiazole ring occurred at (164.55 and 157.64) ppm respectively (Kumar *et al.*, 2014). The peaks observed at (133.62, 132.81, 130.53 and 128.09) ppm were correspondingly ascribed to aromatic benzo carbon of (C_8, C_{11}, C_{10} and C_9) (Almajan *et al.*, 2008). The aromatic phenyl carbons of (C_2, C_1, C_3 and C_4) were correspondingly observed at signals (130.61, 128.94, 126.74 and 121.31) ppm (figure 2) (Aydoġan *et al.*, 2002)(Aras and Hassan, 2018).

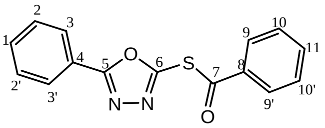

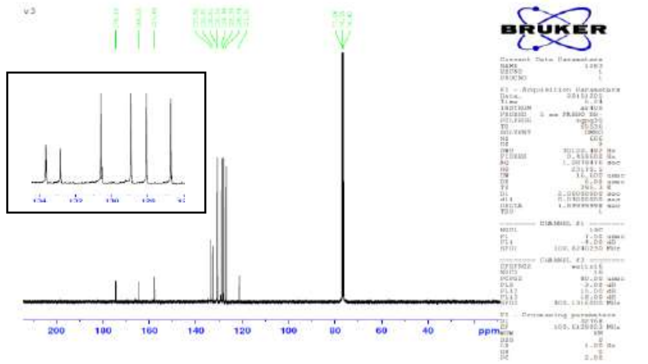

Figure 2: ^{13}C-NMR spectrum of (phozbt) ligand

3.3. CHNS analysis for the synthesized complexes

The elemental analysis of all the complexes are coherent with the proposed stoicheometries (Table 1). Some physical data for the synthesized complexes are also recorded.

Table 1: Molecular weight, melting points and C,H,N,S analysis for the synthesized complexes

No.	Complexes	M.Wt g/mol	M.P. (°C)	(Calculated) Found %			
				C	H	N	S
1	[Pd(κ^1-phozbt)Cl(κ^2-dppe)]Cl	857.33	236-239	(57.38) 56.88	(3.96) 4.07	(3.26) 2.65	(3.74) 2.88
2	[Pt(κ^1-phozbt)Cl(κ^2-dppe)]Cl	946.00	232-235	(52.01) 52.68	(3.59) 4.10	(2.96) 3.22	(3.39) 3.39

3.3 FT-IR spectra for the synthesized complexes

The ν(C-S) stretching vibration of complex (1 and 2) occurred at (704 and 707) cm^{-1} and a new peak was detected at (430 and 437) cm^{-1} were attributed to ν(M-S) stretching vibration correspondingly, which signify of the linkage of S-atom of oxadiazole to the metal center (Al-Jibori *et al.*, 2002). In addition, the ν(P-Ph) vibration in (1 and 2) complexes were occurred at (1435) cm^{-1}, on the other hand, the ν(P-C) vibration displayed at (530 and 511) cm^{-1} correspondingly (Jensen and Nielsen, 1963)(Al-Jibori *et al.,* 2015). These data suggest participation of sulfur atom of (phozbt) and phosphorous of (phosphines) ligands in bonding.

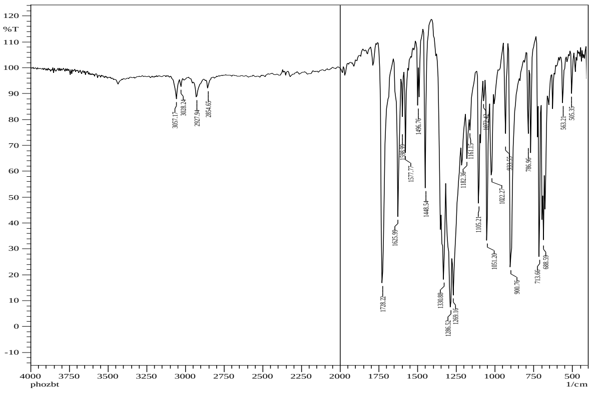

Figure 3: Infrared spectrum of (phozbt) ligand

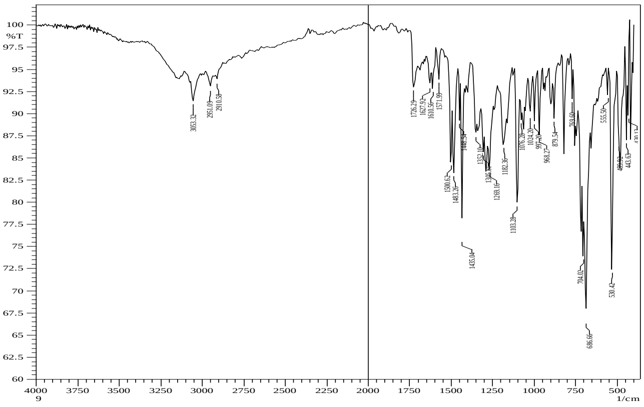

Figure 4: IR spectrum of [Pd(κ^1-phozbt)Cl(κ^2-dppe)]Cl complex (1)

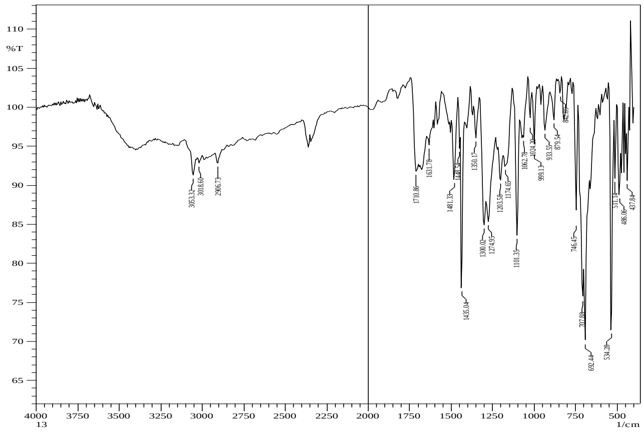

Figure 5: IR spectrum of [Pt(κ^1-phozbt)Cl(κ^2-dppe)]Cl complex (2)

3.4. ^{31}P-{^{1}H}-NMR Spectrum of Complex (2)

The spectrum of [Pt(κ^1-phozbt)Cl(κ^2-dppe)]Cl displayed an AX splitting system comprising of two singlet at δPA(48.69) and δPX(42.50) ppm, each associated with platinum satellites, J(Pt-PA)=2355 Hz and , J(Pt-PX)=3563 Hz, correspondingly attributed to the coordination of S and Cl-coordinated to the platinum metal (figure 6)(Al-Jibori *et al.*, 2013).

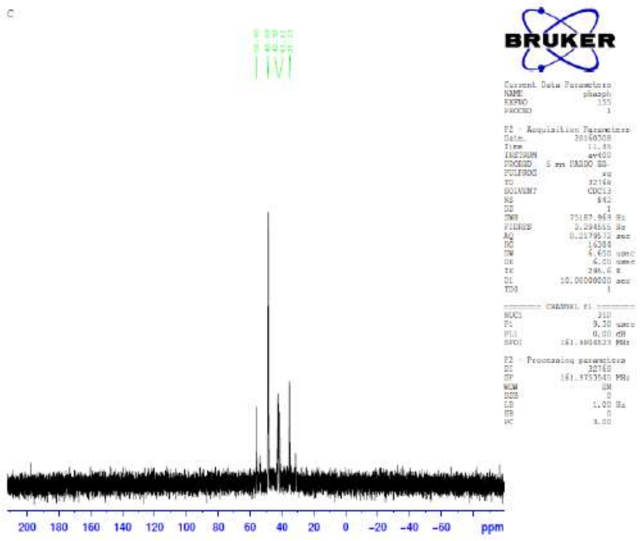

Figure 6: ^{31}P-{^{1}H}-NMR spectrum of [[Pt(κ^{1}-phozbt)Cl(κ^{2}-dppe)]Cl] complex

3.5. UV-Visible Spectra and Magnetic Susceptibility of the Synthesized Complexes

The UV-Vis. spectra of both the synthesized compounds were measured at room temperature in chloroform (10^{-3} M) solution in UV. and Vis. regions. The (phozbt) exhibited two transitions at (41666 and 34482) cm^{-1}, that correpondongly ascribed to the transitions; π- π* and n- π*.

The Pd(II) complex, demonstrated four absorption bands at (23809, 33333, 38461 and 45454) cm^{-1}, the former two transitions attributed to $^{1}A_{1}g\rightarrow{}^{1}B_{1}g$ and $^{1}A_{1}g\rightarrow{}^{1}Eg$ and the next two bands were attributed to C.T transitions. On the other hands, the Platinum (II) complex display three d-d with two C.T transitions. The d-d bands observed at (18181, 19607 and 32258) cm^{-1} that respectively assigned to $^{1}A_{1}g\rightarrow{}^{3}B_{1}g$, $^{1}A_{1}g\rightarrow{}^{1}A_{2}g$ and $^{1}A_{1}g\rightarrow{}^{1}Eg$ and the C. T. transitions appeared at (40000 and 43478) cm^{-1}.

The magnetic susceptibility for the prepared complexes were carried out at 25 °C and the effective magnetic moments data for the synthesized complexes are listed in Table 2.

Table 2: Electronic spectral bands, Magnetic susceptibility and Molar conductivity of the prepared ligand and complexes

Complexes	Absorption band		Assignment Transition	Magnetic Susceptibility (μeff.)	Molar conductivity (cm^{2}. Ohm^{-1}. Mol^{-1})
	cm^{-1}	Nm			
Phozbt	41666 34482	240 290	π -*π n-π*	…	1
[Pd(κ^{1}-phozbt) Cl(κ^{2}-dppe)]Cl	45454 38461 33333 23809	220 260 300 420	C.T. C.T. $^{1}A_{1}g\rightarrow{}^{1}Eg$ $^{1}A_{1}g\rightarrow{}^{1}B_{1}g$	0.8 Sq. pl	44
[Pt(κ^{1}-phozbt) Cl(κ^{2}-dppe)]Cl	43478 40000 32258 19607 18181	230 250 310 510 550	C.T. C.T. $^{1}A_{1}g\rightarrow{}^{1}Eg$ $^{1}A_{1}g\rightarrow{}^{1}A_{2}g$ $^{1}A_{1}g\rightarrow{}^{1}B_{1}g$	1.0 Sq.pl	31

The results indicated a square planer geometry for both (1 and 2) complexes with magnetic moment (0.8 and 1.0) B.M. respectively. However, the electronic transition values are also indication for the formation of square planer geometry for both of the two complexes.

3.6. Molar conductivity measurements for the synthesized compounds

The molar conductivities of the synthesized compounds were taken at room temperature at (10^{-3} M) solution in dimethyl sulfoxide. It was deduced that both of the synthesized compounds are electrolyte that formed in (1:1) ratio.

4. Biological Activity of the Ligands and Complexes

The ligands and all the synthesized complexes were appraised for antibacterial activity toward gram positive *S. (Stophylococcus) aureus* and gram negative *P. (Pseudomonas) aeruginosa* bacteria by agar diffusion method.

4.1. Procedure

The sensitivity studies of 20 different chemical compounds against two kinds of bacteria determined according to NCCLS and CLSI standards. 20 ml of Muller Hinton agar melted and cooled at 45 °C was flowed into sterile petri dishes and ordered to solidify completely. A lawn of tests pathogen was prepared by evenly spreading 100 µl inoculums ($1.5*10^8$ CFU/ml) (according to 0.5 McFarland standard solution) with the help of a sterilized swab onto the entire surface of Muller Hinton Agar plate (McFarland, 1907). The plates were permitted to dry before applying chemical compound disks. The disks were firmly applied to the surface of agar plates within 15 minutes of inoculation (Wikler *et al.*, 2007). After putting the chemical compound disks on plates incubated for 24 hrs. at 37 °C. Antibacterial activity was designated by measuring the diameter of inhibition zone. Activity of each compounds were compared with known antibiotics; Vancomycin and Impenem and their data are represented in Table (3).

The results of antimicrobial evaluation suggested that ligands and complexes have very good potential to act as antibacterial agents. All ligands and synthesized complexes were more active against gram negative bacteria as compared to gram positive one. Among the tested compounds, the ligands (phozbt and dppe) showed outstanding antibacterial activity against (*P. aeruginosa*) than (*S. aureus*) bacteria as compared to standard (Impenem and Vancomycin) antibiotics. Complex (2) showed comparatively good activity against (*P. aeruginosa*) as compared to the (*S. aureus*). Complex (1) displayed more active against (*P. aeruginosa*) bacteria, while they showed no activity against (*S. aureus*) and KBr was also inactive against both bacteria.

Table 3: The diameter of inhibition of the tested compounds on *S. aureus* and *P. aeruginosa* incubated for 24 hrs. at 37 °C

Complex No.	**Structures**	**Inhibition diameter zone (mm)**	
		P. aeruginosa	***S. aureus***
…	KBr	0	0
…	Phozbt	24	20
…	Dppe	17	…
1	$[Pd(\kappa^1\text{-phozbt})Cl(\kappa^2\text{-dppe})]Cl$	30	0
2	$[Pt(\kappa^1\text{-phozbt})Cl(\kappa^2\text{-dppe})]Cl$	34	17
…	Impenem	40	…
…	Vancomycin	…	21

5. Conclusion

This work comprises the synthesis of new thioester (phozbt) ligands and their mixed ligand palladium and platinum complexes with dppe ligands. With the aids of infrared, Electronic and magnetic susceptibility data, we deduced that both the Pd(II) and Pt(II) compounds have a square planer structure. With the aids of molar conductivity measurements, it has been proposed that all the compounds are electrolytes that formed in (1:1) ratio.

Acknowledgements

The authors are grateful to the chemistry department of. College of Education for their terminating our present studies**.**

References

AL-JIBORI, S., AHMED, B., AHMED, S., KARADA, A., SCHMIDT, H., WAGNER, C. & HOGARTH, G. 2015. Palladium (II) benzisothiazolinate (bit) complexes with amino-, acetylamino-, heterocyclic and phosphine co-ligands. Crystal structure of $[Pd(bit)_2(\kappa^2\text{-dppe})]$. 2EtOH. *Inorganica Chimica Acta*., 436, 7-15.

AL-JIBORI, S., AL-NASSIRY, A., HOGARTH, G. & SALASSA, L. 2013. Platinum and palladium bis (diphenylphosphino) ferrocene (dppf) complexes with heterocyclic N-acetamide ligands: Synthesis and molecular structures of $[MCl(sac)(\kappa^2\text{-dppf})]$(M = Pt, Pd, sac = saccharinate), $[PtCl(ata)(\kappa^2\text{-dppf})]$ and $[Pt(ata)_2(\kappa^2\text{-dppf})]$(ataH = N-(2-thiazolyl) acetamide). *Inorganica Chimica. Acta*., 398, 46-53.

AL-JIBORI, S., AL-NASSIRI, I., AL-HAYALY, L. & JASSIM A. 2002. Mixed ligand transition metal complexes of tertiary phosphines and 5-phenyl-l, 3, 4-oxadiazole-2-thione. *Transition metal chemistry*, 27, 191-195.

ALMAJAN, G., BARBUCEANU, S., SARAMET, I., DINU, M., DOICIN, C. & DRAGHICI, C. 2008. Synthesis and biological evaluation of various new substituted 1, 3, 4-oxadizole-2-thiols. *Revista Chim.*, 59, 395-399.

ARAS, N. & HASSAN, A. 2018, Synthesis and spectroscopic study of 1,2-thiazine system incorporating various ester groups, *ZANCO Journal of Pure and Applied Sciences*, 30 (1); 44-55.

AYDOĢAN, F., TURGUT, Z., ÖCAL, N. & ERDEM, S. 2002. Synthesis and electronic structure of new aryl-and alkyl-substituted 1, 3, 4-oxadiazole-2-thione derivatives. *Turkish Journal of Chemistry*, 26, 159-169.

BRUICE, P. 2006. *Organic Chemistry (4th edition)*. Pearson Prentice Hall.

DALIA, A. & FAIQ, H. 2018. Synthesis of some new Betti bases via one-pot three-component reaction of βnaphthol, primary diamine and substituted aromatic aldehydes, *ZANCO Journal of Pure and Applied Sciences*, 30 (1); 56-64.

GURRALA, S., RAO, J., KUMAR, T. & SWAMY, D. 2010. Synthesis of some novel bis type 2-mercapto benzimidazole derivatives *International Journal of Pharmacy and Therapeutics*, 1, 92-97.

HUSAIN, A. & AJMAL, M. 2009. Synthesis of novel 1, 3, 4-oxadiazole derivatives and their biological properties. *Acta. Pharmaceutica*, 59, 223-233.

JENSEN, K. & NIELSEN, H. 1963. Infrared spectra of some organic compounds of group (VB) elements. *Acta Chem. Scand*, 17, 1875-1885.

JOSHI, S., MORE, U., KULKARNI, M., NELAGUDDAD, K. & KULKARNI, V. 2015. Combined pharmacophore and molecular docking-based in silico study of some pyrrolyl 1, 3, 4-oxadiazole benzothioate derivatives. *Rgush Journal Pharm. Science*, 5, 69-80.

KAZEMI, M. & SHIRI, L. 2015. Thioesters synthesis: recent adventures in the esterification of thiols. *Journal of Sulfur Chemistry*, 36 (6), 613-623.

KUMAR, L., NAIK, P., NAVEEN, M., CHANDRASEKHAR, T., REDDY, A., PENCHALAIAH, N. & SWAMY, G. 2014. Synthesis and biological evaluation of some new 2, 5-disubstituted 1, 3, 4-oxadiazoles from 3-(arylsulfonyl) propanehdrazides. *Indian Journal of Chem*istry, 53, 208-211.

LASSAHN, P., LOZAN, V., WU, B., WELLER, A. & JANIAK, C. 2003. Dihalogeno (diphosphane) metal (ii) complexes (metal = Co, Ni, Pd) as pre-catalysts for the vinyl/addition polymerization of norbornene–elucidation of the activation process with $B(C_6F_5)_3/AlEt_3$ or Ag[closo-1-$CB_{11}H_{12}$] and evidence for the in situ formation of “naked” Pd^{2+} as a highly active species. *Dalton Transactions*, 23, 4437-4450.

MCFARLAND, J. 1907. Preparation of McFarland standard solution. *Journal of American Medical Association*, 49, 1176.

PANGAL, A. & SHAIKH, J. 2013. Various pharmacological aspects of 2, 5-disubstituted 1, 3, 4-oxadiazole derivatives: a review. *Res. J. Chem. Sci.*, 3 (12), 79-89.

SHUBHANGI, W. & PRAVINA, P. 2013. Pharmacological Activities of Triazole, Oxadiazole and Thiadiazole. *International Journal of Pharma and Bio Sciences***,** 4, 310 – 332.

WIKLER, M., COCKERILL, F., CRAIG, W., DUDELY, M., ELIOPOULOS, G., HECHT, D., HINDLER, J., LOW, D., SHEEHAN, D., TENOVER, F. & TURNIDGE, J. 2007. Performance standards for antimicrobial susceptibility testing; seventeenth informational supplement. *Clinical and Laboratory standards institute (CLSI),* 2, 1-177.

ZANCO Journal of Pure and Applied Sciences
The official scientific journal of Salahaddin University-Erbil
https://zancojournals.su.edu.krd/index.php/JPAS

ISSN (print):2218-0230, **ISSN (online):** 2412-3986, **DOI: http://dx.doi.org/10.21271/zjpas**

RESEARCH PAPER

Determination of Rare Earth Elements by ICP-MS in some Geological Samples in (Sulaimani) Kurdistan Region of Iraq.

Ahmad M.Abdulla[1], Kurdistan A.Hama[2]

1Department of Chemistry, College of Science, University of Sulaimani, Sulaimani, Kurdistan Region, Iraq
2Department of Geology, College of Science, University of Sulaimani, Sulaimani, Kurdistan Region, Iraq

ABSTRACT:

Rare Earth Elements(REEs) were evaluated in three locations in sulaimani, Kurdistan region , five types of rock were selected (alkaline, peralkaline, mafic ,iron ore and intermediate rocks).Decomposition of the rock samples carried out by Lithium MetaBorate fusion ,the final sample solutions were prepared in 4% HNO_3.ICP-MS technique was selected for analysis of Rare Earth Elements in the rock sample ,results show presence of economic level of some Rare Earth Elements in Qaladza location (Bulfat mountain group),the high grade of Rare Earth Elements deposited in Nepheline synite.The best accuracy and precision were obtained by ICP-MS technique, the D.L for most Rare Earth Elements are between (0.01-0.3 ppm),with (0.999)of correlation coefficient , the solutions of the blank, standard solutions are monitored throughout the analysis and the analysis of duplicate also performed to obtain a good accuracy from our analysis.

KEY WORDS: Rare Earth Elements (REEs), ICP-MS, Nepheline synite, Igneous rocks.
DOI: http://dx.doi.org/10.21271/ZJPAS.32.1.7
ZJPAS (2020) , 32(1);52-64 .

1.INTRODUCTION

Rare earth elements (*REEs*) are recognized as 17 elements with approximate physicochemical feature by the (IUPAC). Fifteen of the element from atomic number (Z=57 and Z=71) as follow lanthanum(La), cerium(Ce), praseodymium(Pr), neodymium(Nd),promethium(Pm),samarium(Sm), europium(Eu),gadolinium(Gd),terbium(Tb),dysprosium(Dy),holmium(Ho),erbium(Er),thulium(Tm),ytterbium(Yb) and lutetium(Lu).Scandium(Sc) Z=21) and yttrium((Y) Z=39) are somewhat apart from the lanthanide series(Ramos et al., 2016, Alonso et al., 2012).

Promethium(Pm) is not found *free* in nature and generally banned since all of its isotopes are radioactive with short half-live(Du and Graedel, 2013). *REEs* are regularly divided into light (LREE) and heavy (HREE) categories. The term (LREE) covers the La-Gd portion of lanthanide sequence (Z=57-64). Lanthanum characterized by filling up the 4f shell electrons, and one clockwise-spinning electron is added to each subsequent lanthanide until Gd heaviest of (LREE) is reached, the term (HREE) covers the Tb-Lu portion of the lanthanide sequence (Z=65-71) plus Y(Z=39) (Simandl, 2014). Depending on Environmental Protection Agency/ United States 2012, the abundance of *REEs* in the earth crust demonstrates that the lower atomic numbers of lanthanides are more abundant than one with higher atomic numbers as given in (Table 1). In technological applications, the character of the *REEs* and their geological distribution is quite comparable to each

---

* **Corresponding Author:**
Ahmad Mohamad Abdulla
E-mail: ahmad.abdullah@univsul.edu.iq
Article History:
Received: 19/08/2019
Accepted: 06/10/2019
Published: 25/02 /2020

other (Chakhmouradian and Wall, 2012).The use of *REEs* have been found in a multitude electronic device, industry and medicine due to their unique electronic configurations so they are classified as "strategic critical metals", *REEs* due to their ability of forming, alloyed with other metals, valuable and distinctive optical characteristics, including fluorescence and coherent light of emission, essential for laser device (Massari and Ruberti, 2013, Rojano et al., 2019).

For determination of *REEs* in real samples, several analytical methodologies have been applied such as; (INAA) Instrumental Neutron Activation Analysis(Aliyu et al., 2018), (XRF) X-Ray Fluorescence spectrometry(Schramm, 2016, Silva et al., 2020), (ICP-AES) Inductively Coupled Plasma Atomic Emission Spectrometry(Zybinsky et al., 2019), (ICP-OES) Inductively Coupled Plasma Optical Emission Spectrometry(Li et al., 2019), and (*ICP-MS*) Inductively Coupled Plasma Mass Spectrometry(Druzian et al., 2016, Gorbatenko and Revina, 2015, Zawisza et al., 2011). The most commonly used technique to analyse trace elements in geological samples is an(*ICP-MS*) a technique that incorporate multi-element capability, speed and high sensitivity(Li et al., 2017, Longerich et al., 1990). Even modern analytical technique as (*ICP-MS*) require pre concentration step, especially for elements like (Lu). A critical confirmation of analytical value must be carried out and quality control must be of the order of the day to assure the reliability of the data(El-Taher, 2010). Due to different type of sample, *ICP-MS* suffer from mass spectral interference such as isobaric, polyatomic ion and doubly charged ions, and from the influence matrix effect, as well as the variation in mass depends on the sensitivity of the instrument during analytical run, therefor all these effect can only be achieved by providing the fully quantitative measurement *ICP-MS* that minimized or corrected for, thus measurement will take place by selecting a compromise experimental condition, optimization of ion optic voltage, spiking sample with internal isotope (Lin et al., 2000).

The purpose of the present study is to validate the best target for ultra-trace *REE*-bearing mineral in five different types of rock as follows (alkaline, peralkaline, mafic, iron ore and intermediate rock) from sulaimani province, specially these present in economical level, and this performed by rapid and accurate analytical method like *ICP-MS* for different samples in different locations and zones.

Table(1). Estimated crustal abundance of *REE*s (Ganguli and Cook, 2018, Kumari et al., 2015, Long et al., 2012).

Elements	Atomic number	Estimate range (ppm)
Lanthanum	57	5-39
Cerium	58	20-70
Praseodymium	59	3.5-9.2
Neodymium	60	12-41.5
Promethium	61	10^{-18}
Samarium	62	4.5-8
Europium	63	0.14-2
Gadolinium	64	4-8
Terbium	65	0.65-2.5
Dysprosium	66	3-7.5
Holmium	67	0.7-1.7
Erbium	68	2.1-6.5
Thulium	69	0.2-1
Ytterbium	70	0.33-8
Lutetium	71	0.35-1.7
Yttrium	39	24-70

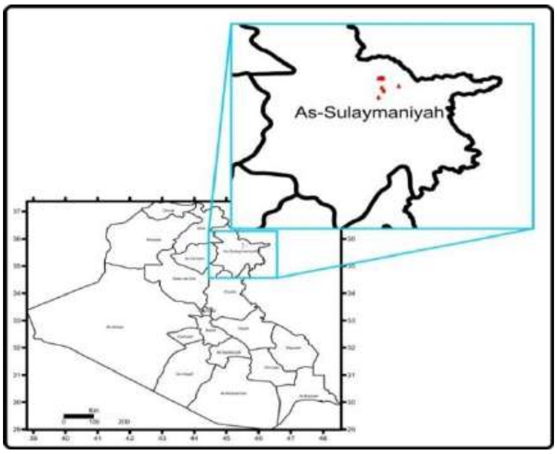

Figure (1): Map showing sampling sites.

2. MATERIALS AND METHODS

2.1 Apparatus

Analysis of *Rare earth elements*. Were done by ALS OMAC Laboratories Limited Ireland, using *ICP-MS* with the LMB Lithium MetaBorate fusion method ME-MS81 and MSA Labs Canada's group, using method IMS-300, IMS-310, by using an *ICP-MS* perkin Elmer Nexion 300D was used for determination of *REEs* in rock samples. The optimum operating conditions for *ICP-MS* are summarized in (Table 2). Different parameters such as (RF power, plasma gas flow, auxiliary gas flow, and optimized the samples were injected through a peristaltic pump.

Table (2): Operating parameters for REE determination using ICP-MS.

RF Power	1500 W
Plasma gas	18 L/Min
Carrier gas	1.08 L/Min
Aux gas	1.2 L/Min
Peripump	4 Rpm
Data acquisition	Dwell time per AMU;50 ms
Reps	10 Sweeps /reading ,1 reading

2.2 Reagents and Reference Materials

The standard solution for the elements were prepared from following stock solutions; IV-*ICP-MS* 71A, Delta-STD-179 , IV-*ICP-MS*71B With solution matrix 4% HNO_3 , 0.7% LMB (Lithium Meta Borate).The concentration of *REEs* in the series of the standard solutions described in (Table 4).

Table (4): Including standard solutions for each element.

	Ce	Dy	Er	Eu	Gd	Ho	La	Lu	Nd	Pr	Sm	Tb	Tm	Y	Tb
10(ppb) Cal solution	1.90%	0.40%	1.00%	0.70%	1.50%	1.00%	1.30%	1.50%	1.50%	2.30%	1.80%	2.10%	1.90%	2.30%	2.20%
100(ppb)Cal solution	2.70%	1.80%	2.00%	4.40%	2.10%	1.50%	3.00%	2.10%	2.90%	3.60%	3.30%	4.30%	1.90%	3.40%	3.30%

2.3 sample collection

The study areas (**Fig.1**) were chosen on the basis of *igneous rock* (granitoid pegmatite, granite, *Nephelen Syanite* , basalt, gabbro, diorite **,** chromitite and magnetite) referring the geological map of sulaimani region. In this study we have selected three areas of different climates with the help of geology department /college of science e.g. (MOC) Mawat ophiolite complex (11samples), (POC) Penjwen Ophiolite complex (4 samples), the (BMG) Bulfat Mountain Group/Qaladze city (6 samples), as summarized in(Table 3).

Table (3): Including some description about these rocks.

Sample NO.	**Rock type**	**Location**	**description**
MO1	basalt	MOC	is a mafic volcanic *igneous rock*, dark or black in color(Lapena and Marinucci, 2018).
MO2	gabbro	MOC	mafic plutonic coarse -grained *igneous rocks* compose equally to basalts, basalt , represent as a magma that has

			crystallized slowly at depth(Gill, 2010).
MO3,MO4	diorite	MOC	Is intermediate, between that of mafic gabbro and felsic granite. dark gray, holocrystalline, with fine grained (1—2 mm) equigranular texture and compact block structure(Li et al., 2005).
MO6,MO7,MO8, MO9,MO10,MO 11	Granitoid pegmatite	MOC	Pegmatites are plutonic felsic *igneous rocks* with very coarse-to gigantic-sized textures. It is a combination of gigantic crystal size and extreme enrichment of rare elements, Which symbolises the world's most famous granitic pegmatites(Simmons, 2007). Although pegmatites were the first bedrock source of REEs exploited in the first half of the 1900s to meet an

			increasing demand for Ce, Y(Chakhmouradian and Zaitsev, 2012) .
MO5	chromite	MOC	chromite occurs exclusively in mafic and ultramafic igneous rocks(Koleli and Demir, 2016). it is chromium mixed with iron oxide, with vary amounts of magnesium and aluminium, the general formula being (Fe,Mg)O.(Cr,AI,Fe)$_2$0$_3$(Gu and Wills, 1988).
PO14,PO15	magnetite	POC	Magnetite or ferrous ferrite (FeO, Fe2O3 or Fe3O4) is an iron oxide(iron ore) which has an inverse spinel structure with Fe(III) ions distributed randomly between octahedral and tetrahedral sites, and Fe(II) ions in octahedral site(Sulistyaningsih et al., 2017).
PO12,PO13	granite	POC	Granite is a common type of felsic intrusive *igneous rock* consisting of quartz, feldspars,

			and micas which is granular and phaneritic in texture. Granites can be predominantly white, pink, or gray in color, depending on their mineralogy(Johannes, 1996).
BG16,BG17,BG18, BG19,BG20,BG21	*Nepheline syenite*	BMG	is a light-colored alkaline *igneous rock* formed mainly of alkali feldspar and *nepheline* in appreciable amounts. It is similar in appearance to coarse-grained granite but characterized by absence of quartz(Abouzeid and Negm, 2014).

2.4. Procedure

2.4.1. Lithium MetaBorate Fusion (LMB)

0.15g of a powder sample and 0.7 % of LMB were placed in a platinum crucible at 1000 C^o for 1 hour in muffle furnace. The residue was leached from the cooled crucible by an additional 4% HNO_3 solution. The solution obtained was transferred to a volumetric flask and then diluted to a final volume of 100 ml with distilled water.

3. RESULTS AND DISCUSSIONS

Three sets of igneous rocks were used for preparation of sample solutions, which expected to contain different amount of *REEs*, the focal point to this study for these rocks which contain economic grade of lanthanide. *REEs* occur naturally in diversity of mineral type. LREE are found in bastansite, monazite, ancylite, lanthanite, stillwellite, allanite, cerianite, britholite and laporite, while HREE and Y(yttrium) are mostly associated with minerals such as xenotime, yttrotantalite, euxenite, samarskite and gadolinite(Khan et al., 2017). Above all, *Rare Earth Elements* resources are distributed among many mineral deposits, but only a portion will be economic to develop and mine. Only quite abundant deposits can be called reserve of rare earth, but that amount cannot be reliable practically and economically. Generally *ICP-MS* technique is the best for determination of trace contents of *REEs* in the rock sample due to its good sensitivity and selectivity(Li et al., 2017, Longerich et al., 1990). As shown from results the D.L for most *REEs* by this technique is between (0.01-0.3ppm), the correlation coefficient R-squire

(0.999-0.9999) after calibrations, aqueous quality control solutions are analysed at regular intervals throughout the run to achieve best sensitivity for results. To obtain good selectivity an internal standard method also used to correct for drift, c(Chakhmouradian and Wall, 2012) correlation factor and alternate masses are used for correct spectral interference, digested blanks, certified reference materials and duplicates are monitored also throughout the analysis.

According to crustal abundance of individual *REEs* that indicate in (Table 1), some type of different samples in (Table 5) are from Mawat Ophiolite (MO),as follows; the mafic rock e.g.(MO1, MO2) and intermediate rock e.g.(MO3 , MO4), these types in which mentioned above carried minimum amount of *REEs* deposit. However granitic pegmatite in e.g. (MO6, MO7 until MO11) which contain relative concentration of (Ce) specially in MO6, so we cannot interdependent of the Mawat pegmatite for determining economic grade of *REEs* . Particular content of the *REEs* in (MO6) are not desirable for description.

In (Table 6) in which four cases collected in Asnawa deposit from Penjwen district each of this type e.g.(PO12 and PO13) is a granite rock, peralkaline granites carry relative grade of *REEs* in addition allanite and monazite. Which are typical LREE hosts in most granitoid, peralkaline varieties contain HREE and Y minerals as xenotime. Iron ore in magnitite rock mineral e.g. (PO14 and PO15) in which Fe-ore relative enrichment of REE-bearing mineral.

The results that are given in (Table 7) are the *Rare Earth Elements* distribution in six selected main rare-earth deposit from Bulfat Mountain in Qaladze city. The concentration of LREE and HREE ploted across the *Nepheline syenite* zones (Figure 2 and 3) the bulfat *Nepheline syenit*e show uniform distribution pattern of LREE and HREE, with LREE being more enriched relative to HREE. The relatively high concentration of LREE in *Nepheline synite* in Bulfta group may be related to occurrence of Monazite at the border zone. The summation of LREE and HREE concentration pattern show gradual decreasing toward the core of the *Nepheline* bodies. Moreover, the relation between LREE and HREE in different zone are variable with the LREE been more enriched as compared to HREE in the border zone with inverse relation toward the core zone (Figure 4).

Table (5): Certified and consensus values of *REEs* in (11) different samples in Mawat Ophiolite Complex.

Sample location	Mawat Ophiolite Complex											
Sample No.	**MO1**	**MO2**	**MO3**	**MO4**	**MO5**	**MO6**	**MO7**	**MO8**	**MO9**	**MO10**	**MO11**	**D.L**
REE(ppm)												
La	0.6	0.4	0.3	0.8	1.8	13.4	2.4	3.5	1.7	1.3	0.5	0.5
Ce	0.6	0.4	0.3	2.2	2.9	30.8	14.4	11.3	7.5	5.6	2	0.5
Pr	0.21	0.07	0.09	0.35	0.56	0.39	2.87	1.51	1.25	0.88	0.34	0.03
Nd	1	0.3	0.5	2.4	1.8	15.6	13.3	5.2	5	3.6	1.6	0.1
Sm	0.42	0.31	0.41	1.31	0.56	3.36	5.92	1.61	1.8	1.61	0.88	0.03
Eu	0.17	<0.03	0.14	0.93	0.44	0.9	0.05	<0.03	<0.03	<0.03	<0.03	0.03

Gd	0.71	0.11	0.58	1.35	1.01	3.39	0.86	1.19	1.11	1.2	0.57	0.05
Tb	0.1	0.03	0.08	0.25	0.19	0.55	0.05	0.21	0.2	0.26	0.11	0.01
Dy	0.94	0.5	0.93	1.59	1.31	3.42	0.55	1.1	1	1.45	0.51	0.05
Ho	0.21	0.05	0.15	0.4	0.35	0.66	0.3	0.17	0.17	0.24	0.1	0.01
Er	1.05	0.23	0.62	1.6	1.01	1.98	0.21	0.52	0.51	0.73	0.3	0.03
Tm	0.17	0.01	0.07	0.14	0.14	0.31	0.05	0.1	0.09	0.14	0.07	0.01
Yb	0.71	0.06	0.69	0.19	1.15	2.13	0.22	0.63	0.62	1.07	0.35	0.03
Lu	0.12	<0.03	0.1	0.18	0.15	0.37	0.01	0.09	0.1	0.17	0.05	0.01
Y	7.1	1.7	5.8	13.8	8.1	16.3	2	5.5	5.5	8.3	3.3	0.5
Σ REE	14.11	4.17	10.76	28.49	21.32	93.56	43.19	32.63	25.55	26.15	10.68	
Total LREE	3.71	1.59	2.32	9.34	8.92	67.84	39.8	24.31	18.36	13.79	5.89	
Total HREE	10.4	2.58	8.44	19.15	12.4	25.72	3.39	8.32	8.19	12.6	4.79	

Table (6): Certified and consensus values of *REEs* in (4) different samples in Penjwen Ophiolite Complex.

Sample location	Penjwen Opheolite Complex				
Sample No.	**PO12**	**PO13**	**PO14**	**PO15**	**D.L**
REE (ppm)					
La	54.5	13.2	17	4.5	0.5
Ce	74.8	18.9	25.3	12.8	0.5
Pr	8.56	2.35	4.11	2.01	0.03
Nd	30.2	10.1	14.3	10.4	0.1
Sm	5.56	3.8	4.08	3.27	0.03
Eu	2.2	1.83	0.82	1.51	0.03

Gd	5.18	3.9	4.01	3.9	0.05
Tb	0.77	0.7	0.63	0.77	0.01
Dy	4.2	3.91	3.29	4.76	0.05
Ho	0.82	0.79	0.71	1.01	0.01
Er	2.41	2.13	1.86	2.87	0.03
Tm	0.36	0.33	0.33	0.41	0.01
Yb	2.1	1.89	1.67	2.49	0.03
Lu	0.33	0.3	0.24	0.38	0.01
Y	21.9	21	20.3	25.1	0.5
Σ REE	213.89	85.13	98.65	76.18	
Total LREE	181	54.08	69.62	38.39	
Total HREE	32.89	31.05	29.03	37.79	

Table (7): Certified and consensus values of *REEs* in (6) different sample in Bulfat Mountain Group.

Sample Location	Bulfat Mountain Group					
Sample No.	**BG16**	**BG17**	**BG18**	**BG19**	**BG20**	**BG21**	**D.L**
REE(ppm)							
La	39	14.2	15.9	8.2	0.3	0.8	0.5
Ce	72.6	31.8	33.8	16	0.5	1.6	0.5
Pr	8.2	4.01	4.1	1.89	0.05	0.21	0.03
Nd	30.3	16	16.2	7.2	0.2	0.8	0.1
Sm	5.38	3.51	3.29	1.5	0.08	0.21	0.03
Eu	1.8	1.06	0.89	0.75	0.03	0.07	0.03
Gd	4.76	3.48	3.33	1.46	0.07	0.2	0.05

Tb	0.71	0.6	0.56	0.26	0.01	0.04	0.01
Dy	3.87	3.60	3.33	1.67	0.08	0.22	0.05
Ho	0.75	0.82	0.7	0.35	0.02	0.07	0.01
Er	2.25	2.41	1.98	1.17	0.05	0.31	0.03
Tm	0.34	0.36	0.28	0.2	0.02	0.11	0.01
Yb	2.22	2.1	1.74	1.21	0.07	1.25	0.03
Lu	0.37	0.33	0.28	0.22	<0.01	0.35	0.01
Y	19	21.9	17.8	9.4	0.5	1.7	0.5
Σ REE	192.74	106.18	104.18	51.48	1.98	7.94	
Total LREE	162.04	74.06	77.51	37	1.23	3.89	
Total HREE	30.7	32.12	26.67	14.48	0.75	4.05	

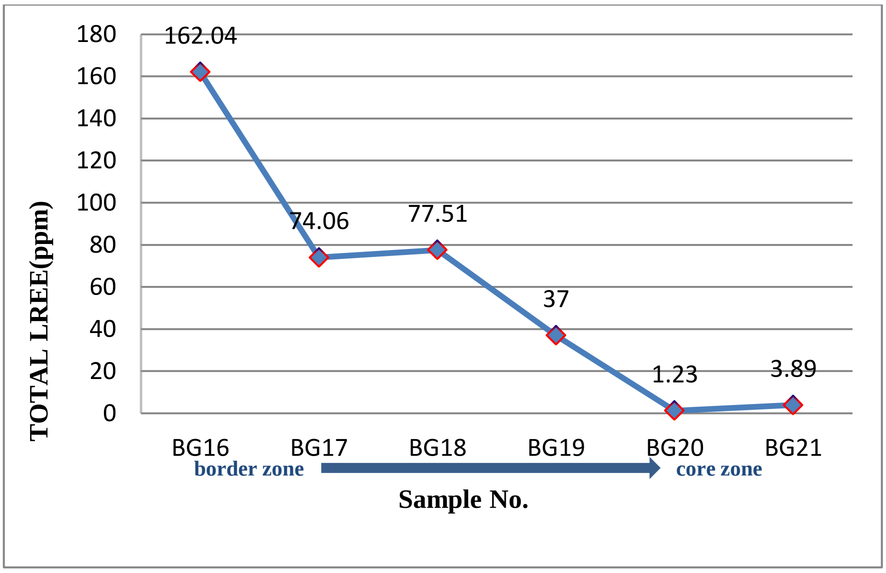

Figure (2): Total (LREE) pattern across the bulfat *Nepheline syenite* zones.

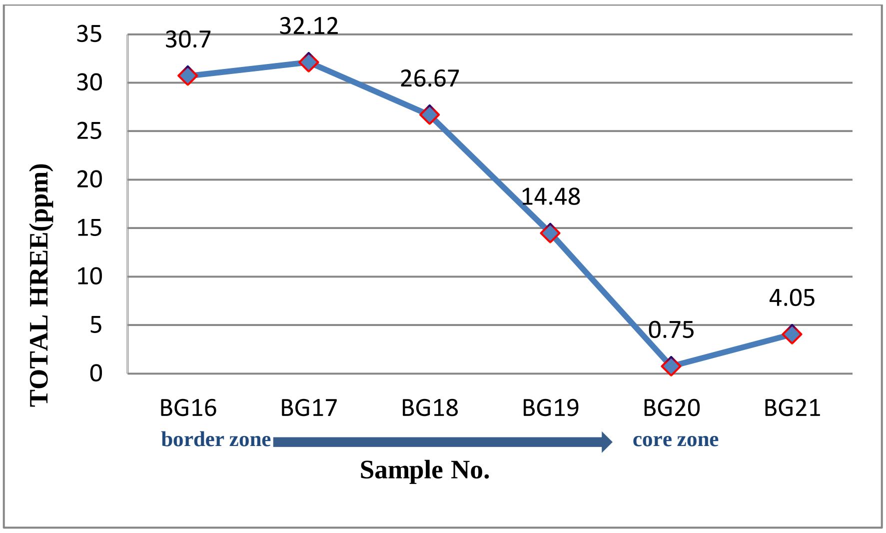

Figure (3): Total (HREE) pattern across the Bulfat *Nepheline syenite* zones.

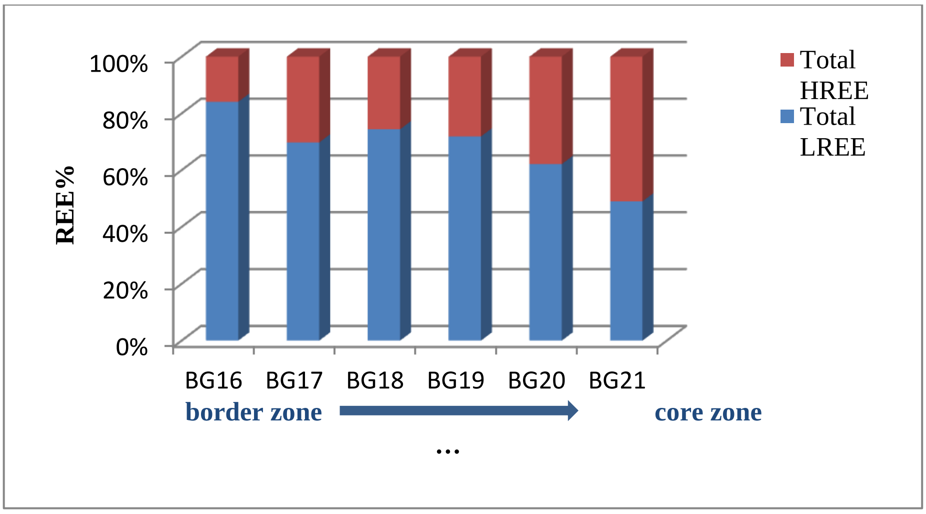

Figure (4): Relationship between (LREE) and (HREE) in deferent zones Bulfat *Nepheline syenite* zones.

4. CONCLUSIONS

Accurate and reproducible method was reported for determination of *REEs* in some geological samples, by dissolution of powder sample with the aid of LMB and measurement with ICP-MS technique. This protocol applied to twenty one *igneous rock*, based on the analytical data of three groups of *igneous rock* sample in Sulimani province (MOC-POC and BMG) of variable rock type including (Basalt, Gabbro, diorite, Chromite, Granoited Pegmatite, Granite, Magnetite, and in *Nepheline synite*), for future the best candidate for *REEs* in which more economic and valuable deposits for exploration and extraction is in *Nepheline synite* from Bulfate group, the high concentration of *REEs* in this type of rock is probably related to occurrence of *REE* bearing mineral monazite.

Acknowledgments

This study was financially supported by the Sulaimni University -Sulaimni /Iraq. The Author acknowledges with many thanks to the College of science geology department Dr.Yousif O.Mohammad and Dr.Kamal H.Karim for the rocks identifications and documentations. We would also like to acknowledge other people's support that we cannot describe in this opportunity.

References

ABOUZEID, A.-Z. M. & NEGM, A.-T. A. 2014. Characterization and beneficiation of an Egyptian nepheline syenite ore. *International Journal of Mineralogy,* 2014.

ALIYU, A. S., MUSA, Y., LIMAN, M., ABBA, H. T., CHAANDA, M. S., NGENE, N. C. & GARBA, N. 2018. Determination of rare earth elements concentration at different depth profile of Precambrian pegmatites using instrumental neutron activation analysis. *Applied Radiation and Isotopes,* 131**,** 36-40.

ALONSO, E., SHERMAN, A. M., WALLINGTON, T. J., EVERSON, M. P., FIELD, F. R., ROTH, R. & KIRCHAIN, R. E. 2012. Evaluating rare earth element availability: A case with revolutionary demand from clean technologies. *Environmental science & technology,* 46**,** 3406-3414.

CHAKHMOURADIAN, A. R. & WALL, F. 2012. Rare earth elements: minerals, mines, magnets (and more). *Elements,* 8**,** 333-340.

CHAKHMOURADIAN, A. R. & ZAITSEV, A. N. 2012. Rare earth mineralization in igneous rocks: sources and processes. *Elements,* 8**,** 347-353.

DRUZIAN, G. T., PEREIRA, L. S., MELLO, P. A., MESKO, M. F., DUARTE, F. A. & FLORES, E. M. 2016. Rare earth element determination in heavy crude oil by USN-ICP-MS after digestion using a microwave-assisted single reaction chamber. *Journal of Analytical Atomic Spectrometry,* 31**,** 1185-1191.

DU, X. & GRAEDEL, T. E. 2013. Uncovering the end uses of the rare earth elements. *Science of the Total Environment,* 461**,** 781-784.

EL-TAHER, A. 2010. Rare earth elements content in geological samples from eastern desert, Egypt, determined by instrumental neutron activation analysis. *Applied Radiation and Isotopes,* 68**,** 1859-1863.

GANGULI, R. & COOK, D. R. 2018. Rare earths: A review of the landscape. *MRS Energy & Sustainability,* 5.

GILL, R. 2010. *Igneous rocks and processes: a practical guide*, John Wiley & Sons.

GORBATENKO, A. & REVINA, E. 2015. A review of instrumental methods for determination of rare earth elements. *Inorganic materials,* 51**,** 1375-1388.

GU, F. & WILLS, B. 1988. Chromite-mineralogy and processing. *Minerals Engineering,* 1**,** 235-240.

JOHANNES, W. 1996. holtz F (1996) Petrogenesis and Experimental Petrology of Granitic Rocks. Springer-Verlag, Berlin.

KHAN, A. M., BAKAR, N. K. A., BAKAR, A. F. A. & ASHRAF, M. A. 2017. Chemical speciation and bioavailability of rare earth elements (REEs) in the ecosystem: a review. *Environmental Science and Pollution Research,* 24**,** 22764-22789.

KOLELI, N. & DEMIR, A. 2016. Chromite. *Environmental Materials and Waste.* Elsevier.

KUMARI, A., PANDA, R., JHA, M. K., KUMAR, J. R. & LEE, J. Y. 2015. Process development to recover rare earth metals from monazite mineral: a review. *Minerals Engineering,* 79**,** 102-115.

LAPENA, M. H. & MARINUCCI, G. 2018. Mechanical Characterization of Basalt and Glass Fiber Epoxy Composite Tube. *Materials Research,* 21.

LI, F., GONG, A., QIU, L., ZHANG, W., LI, J., LIU, Y., LIU, Y. & YUAN, H. 2017. Simultaneous determination of trace rare-earth elements in simulated water samples using ICP-OES with TODGA extraction/back-extraction. *PloS one,* 12**,** e0185302.

LI, F., GONG, A., QIU, L., ZHANG, W., LI, J. & LIU, Z. 2019. Diglycolamide-grafted Fe3O4/polydopamine nanomaterial as a novel magnetic adsorbent for preconcentration of rare earth elements in water samples prior to inductively coupled plasma optical emission spectrometry determination. *Chemical Engineering Journal,* 361**,** 1098-1109.

LI, Y., SONG, W., WU, G., WANG, Y., LI, Y. & ZHENG, D. 2005. Jinning granodiorite and diorite deeply concealed in the central Tarim Basin. *Science in China Series D: Earth Sciences,* 48**,** 2061.

LIN, S., HE, M., HU, S., YUAN, H. & GAO, S. 2000. Precise determination of trace elements in geological samples by ICP-MS using compromise conditions and fine matrix-matching strategy. *Analytical sciences,* 16**,** 1291-1296.

LONG, K. R., VAN GOSEN, B. S., FOLEY, N. K. & CORDIER, D. 2012. The principal rare earth elements deposits of the United States: a summary of domestic deposits and a global perspective. *Non-Renewable Resource Issues.* Springer.

LONGERICH, H., JENNER, G., FRYER, B. & JACKSON, S. 1990. Inductively coupled plasma-mass spectrometric analysis of geological samples: a critical evaluation based on case studies. *Chemical Geology,* 83**,** 105-118.

MASSARI, S. & RUBERTI, M. 2013. Rare earth elements as critical raw materials: Focus on international markets and future strategies. *Resources Policy,* 38**,** 36-43.

RAMOS, S. J., DINALI, G. S., OLIVEIRA, C., MARTINS, G. C., MOREIRA, C. G., SIQUEIRA, J. O. & GUILHERME, L. R. 2016. Rare earth elements in the soil environment. *Current Pollution Reports,* 2**,** 28-50.

ROJANO, W. J. S., DOS ANJOS, T., DUYCK, C. B. & SAINT'PIERRE, T. D. 2019. The determination of rare earth elements in environmental samples with high Ba concentration by quadrupole inductively coupled plasma mass spectrometry employing sulfuric acid for the removal of barium interference. *Microchemical Journal***,** 104026.

SCHRAMM, R. 2016. Use of X-ray Fluorescence Analysis for the Determination of Rare Earth Elements. *Physical Sciences Reviews,* 1.

SILVA, C. D., SANTANA, G. P. & PAZ, S. P. 2020. Determination of La, Ce, Nd, Sm, and Gd in mineral waste from cassiterite beneficiation by wavelength-dispersive X-ray fluorescence spectrometry. *Talanta,* 206**,** 120254.

SIMANDL, G. 2014. Geology and market-dependent significance of rare earth element resources. *Mineralium Deposita,* 49**,** 889-904.

SIMMONS, S. Pegmatite Genesis: Recent advances and areas for future research. Granitic Pegmatites: The State of the Art–International Symposium proceedings, 2007.

SULISTYANINGSIH, T., SANTOSA, S. J., SISWANTA, D. & RUSDIARSO, B. 2017. Synthesis and characterization of magnetites obtained from mechanically and sonochemically assissted co-precipitation and reverse co-precipitation methods. *Int J Mater, Mech Manuf,* 5**,** 16-9.

ZAWISZA, B., PYTLAKOWSKA, K., FEIST, B., POLOWNIAK, M., KITA, A. & SITKO, R. 2011. Determination of rare earth elements by spectroscopic techniques: a review. *Journal of Analytical Atomic Spectrometry,* 26**,** 2373-2390.

ZYBINSKY, A., KOLOTOV, V., KARANDASHEV, V. & KORDYUKOV, S. 2019. Determination of Rare-Earth and Accompanying Elements in Niobium−Rare-Earth Ores by Inductively Coupled Plasma Atomic Emission Spectrometry Using Model Calibration and a Mathematical Approach for Resolving Spectral Interferences. *Journal of Analytical Chemistry,* 74**,** 213-225.

ZANCO Journal of Pure and Applied Sciences
The official scientific journal of Salahaddin University-Erbil
https://zancojournals.su.edu.krd/index.php/JPAS

ISSN (print):2218-0230, **ISSN (online):** 2412-3986, **DOI:** **http://dx.doi.org/10.21271/zjpas**

RESEARCH PAPER

Kinetic Study of Lornoxicam Hydrolysis

Sawsan Hasan Hammodi Ameen , Dana Muhammad Hamad Ameen

Department of Pharmaceutical chemistry , College of pharmacy, Hawler Medical University.

ABSTRACT:

Gastrointestinal tract (GIT) side effects due to the local action of lornoxicam considered the most common problem that associated with using of this analgesic drug. Masking of the enolic alcohol OH group of lornoxicam to overcoming this problem was the aim, however, applying Williamson ether synthesis led to amide hydrolysis. Therefore, the objective of this study was shifted to study the hydrolytic kinetics and the influence of different bases as a function of time and temperature in the reaction media.

The effects of all bases used in the study on the hydrolysis process of lornoxicam have been studied; NaOH was found to be the strongest followed by Na_2CO_3 and K_2CO_3. All three temperatures (25°C, 50°C and 80°C) have approximately similar effect except reflux condition that accelerates the hydrolysis process compare with the others. The hydrolysis process is proportional with time.

Williamson ether synthetic procedure that followed to synthesize lornoxicam prodrugs was failed despite attempting different conditions. Using bases were induced the hydrolysis process of lornoxicam. The hydrolysis rate accelerated under reflux more than other conditions. In addition, reaction time gives more hydrolysis process.

KEY WORDS: lornoxicam; NSAIDs; amide hydrolysis; kinetic study.
DOI: http://dx.doi.org/10.21271/ZJPAS.32.1.8
ZJPAS (2020) , 32(1);65-74 .

1.INTRODUCTION :

One of the most consumed drugs over the years either by prescription or over-the-counter was NSAIDs. (Bacchi *et al.*, 2012) Discovery of NSAIDs since 1899 led to an important advancement in the painkillers field, they belong to a wide class of therapeutic agents ranging from the classic drug aspirin to the recent development of selective COX-2 inhibitors in the 1990s.(Rao and Knaus, 2008)

Oxicams are an important class of NSAIDs drugs which do not contain a carboxyl group. The term “oxicam” used to describe NSAIDs belonging to enolic acid class, which differs structurally from other classes of NSAIDs; they are containing a fused thiazine dioxide ring and an extended different carboxamide substitution. (Xu *et al.*, 2014)

Piroxicam was the first member of this class introduced in 1982 in the United States by the Pfizer. After piroxicam, other oxicams, including meloxicam, isoxicam, tenoxicam, and lornoxicam compound **1**, were introduced and they gained a huge acceptance in the treatment of acute and chronic inflammatory conditions. (Gouda *et al.*, 2017)

Lornoxicam **1** is a relatively new NSAIDs belongs to oxicam class with a potent analgesic, anti-inflammatory and antipyretic properties. The drug

* **Corresponding Author:**
Sawsan Hasan Hammodi Ameen
E-mail: sawsanhasan.87s@gmail.com

Article History:
Received: 25/08/2019
Accepted: 08/10/2019
Published: 25/02 /2020

was first marketed in 1995 and it is in clinical use in many European countries. (Homdrum *et al.*, 2006) The drug differs from other oxicam compounds in its rapid onset, short duration of action (the half-life is about 4 hrs.). Lornoxicam is the most potent balanced cyclooxygenase inhibitor, the ratio of COX 1: COX 2=1:1. (Kar *et al.*, 2016).

Although lornoxicam has lower side effects due to its short duration of action, (Rawal *et al.*, 2010) it still causing a wide range of adverse effects like other members of NSAIDs. GIT side effects due to the local action mechanism considered the most common problem that associated with using of these analgesic drugs (Russell, 2001). Many studies were conducted to overcome this problem by synthesis of prodrugs that are pharmacologically inactive derivatives of active drugs. Prodrugs undergo chemical and/or enzymatic biotransformation after administration resulting in the release of active agents. The parent drug subsequently elicits the desired pharmacological effect. (Halen *et al.*, 2009)

There are many studies indicate that the enolic hydroxy group of oxicams play an important role in their physico-chemical and pharmacological properties. Therefore, derivatization of this enolic group via alkylation or acylation is expected to change all these properties. (Jayaselli *et al.*, 2008) This is exemplified by the development of the ampiroxicam, an ether carbonate derivative of piroxicam, droxicam, piroxicam pivalic ester and cinnoxicam, piroxicam cinnamate. (Nakka *et al.*, 2011) These derivatives are stable under gastric conditions and cause lower GIT irritation due to masking alcoholic OH group. They are sufficiently labile toward hydrolysis to allow release of the parent drug after absorption. (Jornada *et al.*, 2015)

In this work, masking of enolic OH group of lornoxicam by using base and alkyl or acyl halide was the aim however, using base to produce alkoxide ion according to Williamson ether synthesis (Massah *et al.*, 2007, Hallmann *et al.*, 2015) led to amide hydrolysis. Numerous research reports on degradation of lornoxicam under hydrolytic conditions (especially basic conditions) are available in literature (Modhave *et al.*, 2011, Sindhu *et al.*, 2015) however, There were no previous studies explained hydrolysis process of lornoxicam inside the reaction media. Therefore, the objective of our study was shifted to study the hydrolytic kinetics and the influence of different bases and conditions (temperature and time) in the reaction media.

2. MATERIALS AND METHODS:

This experimental study had been done at Hawler Medical University/ College of Pharmacy/ Pharmaceutical and Organic Chemistry Lab, between 2nd of January 2018 to 8th of April 2019.

2.1 Statistical Analysis

The data were entered and analyzed by using Origin pro 2017(64-bit) SR$_2$ b9.4.2.380 and Excel 2010.

General procedure for the synthesis of prodrugs of lornoxicam

To a stirred solution of (2.5 mmol) of the following bases (NaOH, Na_2CO_3 or K_2CO_3) in 20 mL of solvent, (2.5 mmol) of lornoxicam was added. The solution stirred at room temperature for 2 h. an equivalent volume of alkyl or acyl halide (RX) was added to the homogenous solution, and stirred for 1-7 days at room temperature or under heat effect (at 25°C, 50°C and reflux), then the progress of the reactions was followed by TLC, After completion of the reaction, the solution was added to the ice bath with continuous stirring until a precipitate was obtained. The precipitate was filtered, washed more than one time with ice water and left to dry at room temperature, rotary evaporator was used to evaporate the solvent for some compounds. Ethanol was used to recrystallize all synthesized products. Final step was confirmed for all synthesized products by different techniques such as: TLC, measuring of melting point and using FTIR apparatus.

2.2Kinetic study for lornoxicam hydrolysis: Determination of wavelength of maximum absorption

A stock solution (100 µg/ml) was prepared by using 10 mg of drug dissolved in 100 ml 0.05N NaOH. An UV-visible spectroscopic scanning (200–450 nm) was used to determine the λmax for the detection of lornoxicam using 0.05N NaOH as a blank, figure 5 (A). (Bhavsar *et al.*, 2010)

Calibration Curve:

Six solutions at different concentrations (5-30 µg/ml) were prepared from the standard stock solution. Absorbance for all samples were recorded, calibration curve was plotted and evaluated by its correlation coefficient (R^2). Calibration curve shows straight line with a correlation coefficient (R^2) = 0.999 and (p value <0.001).

Study of the effects of different bases and temperatures on the reaction:

To study the effect of the base on the reaction media, the following procedure was used:(2.5 mmol) of one of the following bases (NaOH, Na_2CO_3 or K_2CO_3) was added to 250 ml of Distilled water, 0.1gm of lornoxicam was added to the solution and the solution stirred at 25°C, 50°C, 80°C and on reflux, samples taken every 6 hrs. for 3 days and analyzed by UV-visible spectrophotometer to measure the absorbance. Concentrations were also calculated by using absorbance.

3.RESULTS:

IR spectrums had been recorded for all synthesized compounds. After attempting different conditions to prepare ester of lornoxicam, the reaction was failed to occur and the IR spectrums of most of synthesized compounds have no peak of ester. However, the peak of ester appeared in some IR spectrum figures (2) and (4) but, this peak mixed with the hydrolysis of amide linkage. (The amide hydrolyzed to carboxylate then the carboxylate esterified to an ester, figure (4)).

The maximum absorbance (λ max) of lornoxicam (compound **1**) and the hydrolyzed product (compound **4**) also determined by UV-spectroscopic apparatus. The λ max of lornoxicam was 375.06 nm while 232.24 nm was the λ max for the hydrolyzed compound, figure (5).

The kinetic study for the hydrolysis process studied by using different bases (NaOH, Na_2CO_3 and K_2CO_3) at different temperatures 25°C, 50°C, 80°C and on reflux. Figure (6) explains effect of both bases and temperatures on the hydrolysis process.

4.DISCUSSION:

Ether and ester derivatives of lornoxicam **2** have been prepared by various procedures (Jayaselli et al., 2008, Siddiqui *et al.*, 2010, Redasani *et al.*, 2017, Aras Najmaddin Hamad, 2018) using different bases alkyl and acyl halide (shown in Scheme 1), and all the attempted conditions were listed in Table (1).

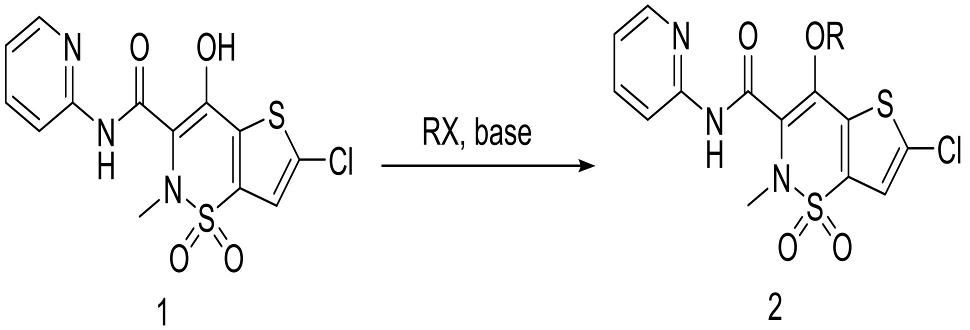

R= $CH_3(CH_2)_2$, $CH_3(CH_2)_3$, $CH_3(CH_2)_4$, $CH_3(CH_2)_5$, 3-(NO_2) $C_6H_4CH_2$, CH_3CH_2CO, C_6H_5CO, 4-(Br) C_6H_4CO, 4-(NO_2) C_6H_4CO, 4-(CH_3) C_6H_4CO. X =Br. or Cl. and base is (NaOH, Na_2CO_3 or K_2CO_3)

Scheme (1). Synthetic strategy for ether and ester lornoxicam derivatives **2**.see Table (1).

Table (1): Attempted conditions for the synthesis of ether and ester lornoxicam prodrugs.

No.	Base	Alkyl or acyl halide	Solvents	Condition	Time	Occurrence of reaction
1	NaOH	Bromo propane	DMSO	r.t.	24h.	-ve
2	NaOH	Bromo butane	DMSO	r.t.	24h.	-ve
3	NaOH	Bromo propane	DMSO	r.t.	24h.	-ve
4	Na_2CO_3	Bromo butane	DMSO	r.t.	24h.	-ve
5	Na_2CO_3	Bromo hexane	DMSO	50 °C	24h.	-ve
6	K_2CO_3	Bromo pentane	Acetonitrile	r.t.	5days	-ve
7	Na_2CO_3	Bromo propane	Ethanol	Reflux	5h.	-ve
8	NaOH	Bromo pentane	Ethanol	Reflux	24h.	-ve
9	K_2CO_3	3-Nitrobenzyl chloride	Methanol	Reflux	10h.	-ve
10	K_2CO_3	3-Nitrobenzyl chloride	Ethanol	Reflux	24h.	-ve
11	K_2CO_3	Propoyl chloride	Ethanol	r.t.	7 days	-ve
12	K_2CO_3	Benzoyl chloride	Ethanol	r.t.	7 days	+ve
13	TEA	Benzoyl chloride	Chlorform	r.t.	4 days	+ve
14	K_2CO_3	4-bromo benzoyl chloride	Ethanol	Reflux	4 days.	-ve
15	TEA	4- bromo benzoyl chloride	Chlorform	25° C	2 days	-ve
16	TEA	4- bromo benzoyl chloride	Chlorform	25° C	7 days	-ve
17	K_2CO_3	4- bromo benzoyl chloride	Ethanol	r.t.	7 days	+ve
18	K_2CO_3	4- bromo benzoyl chloride	Ethanol	25° C	2 days	-ve
19	K_2CO_3	4- bromo benzoyl chloride	Ethanol	25° C	10h.	-ve
20	K_2CO_3	4- bromo benzoyl chloride	DMSO	25° C	24h.	-ve

21	K_2CO_3	4- bromo benzoyl chloride	Ethanol	25° C	4h.	+ve
22	K_2CO_3	4.Nitro benzoyl chloride	Ethanol	25° C	2days	+ve
23	K_2CO_3	4. Methyl benzoyl chloride	Ethanol	25° C	24h.	-ve
24	NaOH	4. Methyl benzoyl chloride	Ethanol	25° C	24h.	-ve

According to Williamson ether, synthesis of prodrugs of lornoxicam were made as shown in scheme (1), by using firstly NaOH to produce alkoxide and then different alkyl halides (bromopropane, bromobutane, bromopentane and bromohexane) were used to attack this alkoxide via SN^2 mechanism and produce ether derivatives. However, the reaction did not progress as expected. Different conditions were tested including the addition of different bases such as Na_2CO_3 and K_2CO_3 instead of NaOH and using different solvents such as DMSO, acetonitrile and ethanol. All these attempts did not get positive results when detected by TLC and FT-IR.

After failed reactions by using aliphatic alkyl halide and different bases, aliphatic alkyl halide has been replaced by the aromatic (3-Nitrobenzyl Chloride), since it is supposed to be more reactive, high concentration of base and different solvents were used., There was even no product by using aromatic alkyl halide.

After that, aliphatic acyl halide (propoyl chloride) has been tried to produce ester prodrug in ethanol in the presence of K_2CO_3 as a base. The solution stirred for one week followed by TLC, no reaction was occurred.

Aromatic acyl halides (benzoyl chloride, 4-bromo-benzoyl chloride, 4-nitrobenzoyl chloride and 4-methylbenzoyl chloride) and K_2CO_3, NaOH or TEA were used to produce alkoxide and the solvents were ethanol, DMSO or chloroform, the reactions were done under different conditions, as listed in the table (1).

There is a clear effect of the concentration of the acyl halide on the reaction observed in the FT-IR spectrum, which shows one single, sharp and clear peak at 1715 cm^{-1} figure (2) when small concentration of the acyl halide (1 equivalent) has been used, while using high concentration (3 equivalent) give two peaks of ester at 1716 and 1785 cm^{-1} figure (4). The esterification reaction occurred, however, accompanied by hydrolysis of the amide linkage. As a result, we found the hydrolysis was interested issue, therefore, hydrolysis process and the influence of some variables on the reaction media was studied.

This hydrolysis confirmed by loss of NH peak of amide of the lornoxicam and instead 2 peaks belong to primary amine (2-aminopyridine compound **5**) were appeared around 3090-3500 cm^{-1}as in figure (2).

Moreover, when high concentration of acyl halide (3 equivalent) has been used, two peak of ester appeared indicated that two reaction process occurred one on the enolic OH and the other on the carboxylic acid side chain and this also confirms the occurrence of amide hydrolysis, figure (4).

There is a clear difference between the UV-visible spectrum of the starting material and the hydrolyzed product as in figure 5 (A) and (B). The λ max of lornoxicam was 375.06 nm while 232.24 nm was the λ max for the hydrolyzed material. The difference in λ max confirms that a new different product was produced during the reaction but it was not possible to identify the product by using UV-visible spectrophotometer so, IR spectroscopy was used to determine the structure of the hydrolyzed product, figure (3).

The IR spectrum of the hydrolyzed product under a basic condition (NaOH) shows that an extremely broad absorption occur at a region between 3700-2400 cm^{-1} indicating the presence of OH group that belongs to the carboxylic acid side chain for compound **4,** figure (3). In addition, carbonyl stretching absorption which usually occurs at 1730-1700 cm^{-1} undergo shifting to a lower frequency due to hydrogen-bonding and appeared at 1637 cm^{-1}as shown in scheme (3). (Pavia *et al.*, 2008)

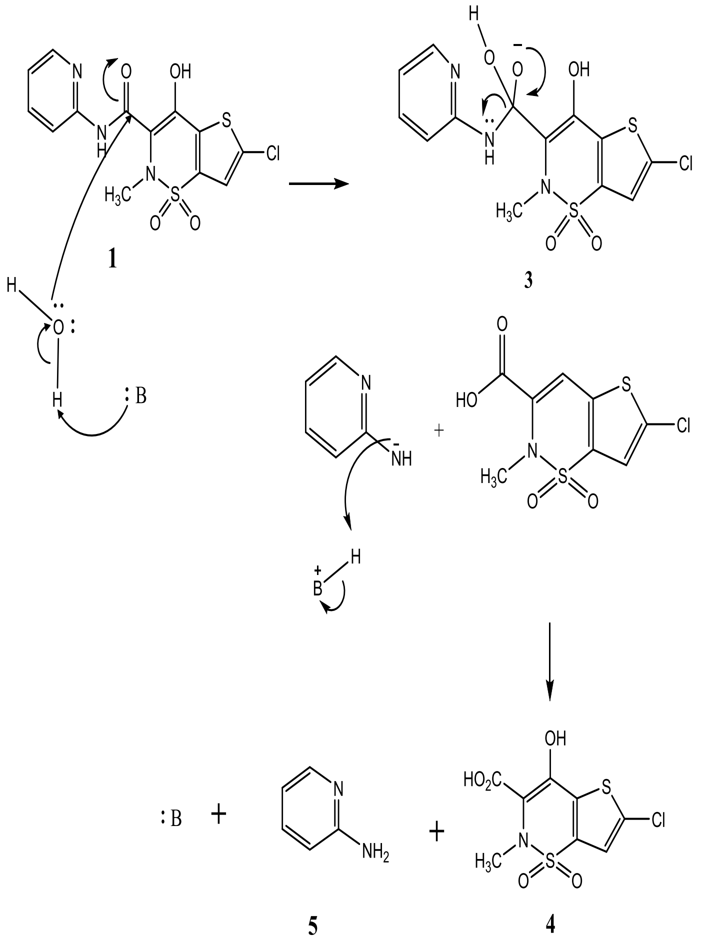

Scheme (2): The hydrolysis mechanism of lornoxicam under basic conditions.

Scheme (2) shows the mechanism of lornoxicam hydrolysis under basic condition. When Na_2CO_3 and K_2CO_3 used the hydrolysis process followed a mechanism as shown in scheme (2), while when NaOH utilized as a base, the OH group of NaOH will attack the carbonyl carbon in the structure of lornoxicam directly to give the first intermediate and compound **4** will be in the form of sodium carboxylate salt.

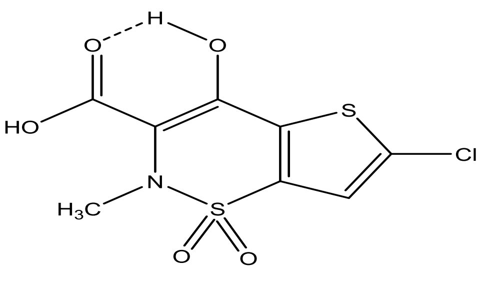

6

Scheme (3): hydrogen bonding that occurs in the hydrolyzed product.

The hydrolysis of lornoxicam occurred before the esterification reaction was completed; it is difficult for this reaction to occur due to different reasons. The presence of enolic OH group is important to complete the reaction but sometime this group disappeared may be due hydrogen bonding that occurred inside the structure of lornoxicam or due to Tautomerism. Tautomerism very common in oxicam group and all members in this class can present in more than one tautomer form depending on the surrounding conditions. (Jayaselli et al., 2008, Franco-Pérez *et al.*, 2011, Ivanova *et al.*, 2015) The amide linkage is also prone to hydrolysis by the presence of base as a catalyst. Numerous research reports on degradation of lornoxicam under hydrolytic conditions (especially basic conditions). (Modhave et al., 2011, Shah *et al.*, 2014)

The effect of different bases on the hydrolysis of lornoxicam was studied, NaOH was used at different temperature. The concentration of lornoxicam decreased with time, at the beginning of the reaction the concentration was approximately 13 µg/ml and after 72 h. declined to about 7.5 µg/ml, this occurred at all temperatures except with reflux, the concentration decreased sharply from 11.1 µg/ml to 3.5 µg/ml . Figure 6 (A) shows that the time affects the process of hydrolysis, by increasing the time the rate of the hydrolysis was increasing. The temperatures (25, 50 and 80°C) affected the hydrolysis process in a similar manner, but the rate of the hydrolysis reaction was increased on the reflux condition which means that reflux has the greatest effect on the rate of the reaction.

The second utilized base was Na_2CO_3, in which at all temperatures the starting material concentration at zero time was ≃ 12 µg/ml decreased to ≃ 8 µg/ml at the end of the reactions, while, on the reflux, the concentration changing from 11.5 to 6 µg/ml. The concentration decreased in all reactions when the time was increased as seen in figure 6 (B).

In addition lornoxicam underwent hydrolysis by using K_2CO_3 as a base, the concentration reduced approximately by 4.5 µg/ml at the first three reactions while the changing was ≃ 6 µg/ml at the forth reaction (reflux condition). From figure 6 (C), it is obvious that at reflux condition the hydrolysis rate was faster than the others and the time had also an obvious effect, by rising the time the hydrolysis of lornoxicam increased.

All bases have been compared during the study for hydrolysis process of lornoxicam, NaOH was found to be the strongest base followed by Na_2CO_3 and K_2CO_3. Temperatures and time have an obvious effect on the hydrolysis process. (Muhamad *et al.*, 2016) According to the effect of temperatures, the three conditions (at 25, 50 and 80°C) have similar effect during all reactions with the exception of reflux condition that accelerate the hydrolysis rate more than the other conditions.

5.CONCLUSION:

The synthesis of lornoxicam prodrugs applying Williamson ether synthetic procedure was failed and the hydrolysis of the drug occurred despite using different bases (Na_2CO_3, K_2CO_3 and NaOH) attempting many solvents (DMSO, acetonitrile, chloroform and ethanol), at various temperatures (starting from room temperature up to refluxing) and trying different alkyl halides and acyl halide.

Among all bases, NaOH was the strongest base to induce hydrolysis process, followed by Na_2CO_3 and K_2CO_3. Three temperatures 25°C, 50°C and 80°C have similar effect during all reactions with the exception of reflux condition that has higher effect on the hydrolysis rate. The time affects the degradation of lornoxicam by the same manner in all reactions, by rising the hours of the reactions the hydrolysis process increasing also.

Acknowledgements:

I would like to express my sincere gratitude and thanks to Dr.Kezhal S. Mahmood, Mr. Sarbast M. Ahmed and Miss Asmaa Ghanm for their help and guidance.

Conflict of interest:

Authors have no conflict of interest.

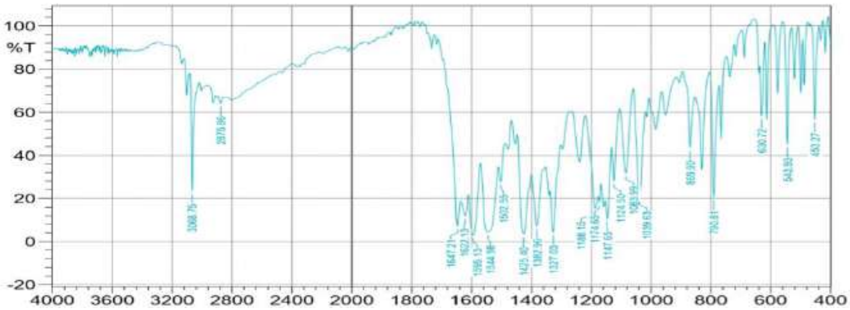

Figure 1: IR spectrum of lornoxicam (compound **1**).

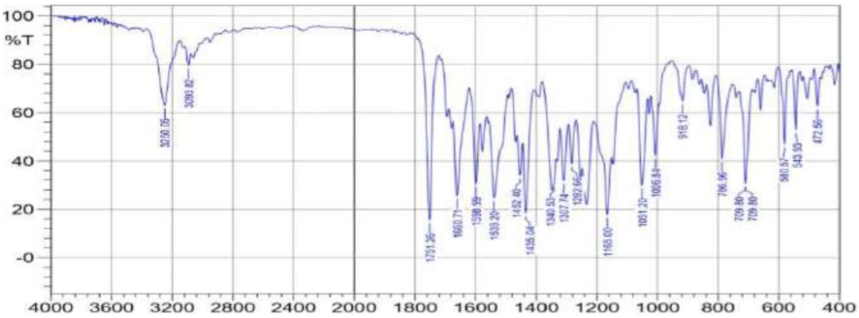

Figure 2: IR spectrum of ester product (compound **2** when R=benzoyl chloride).

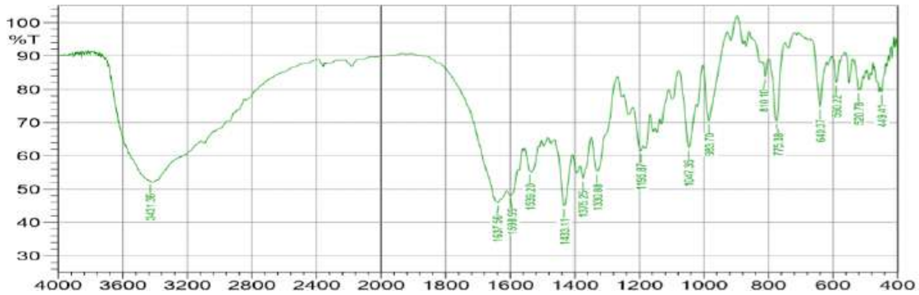

Figure 3: IR spectrum of the hydrolyzed product under basic condition (NaOH), compound **4.**

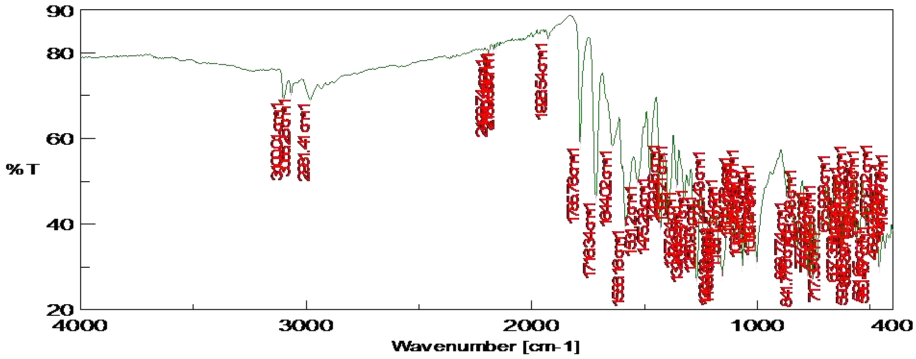

Figure 4: IR spectrum of ester product (compound **4** when acyl halide=4- bromo benzoyl chloride (3eq.))

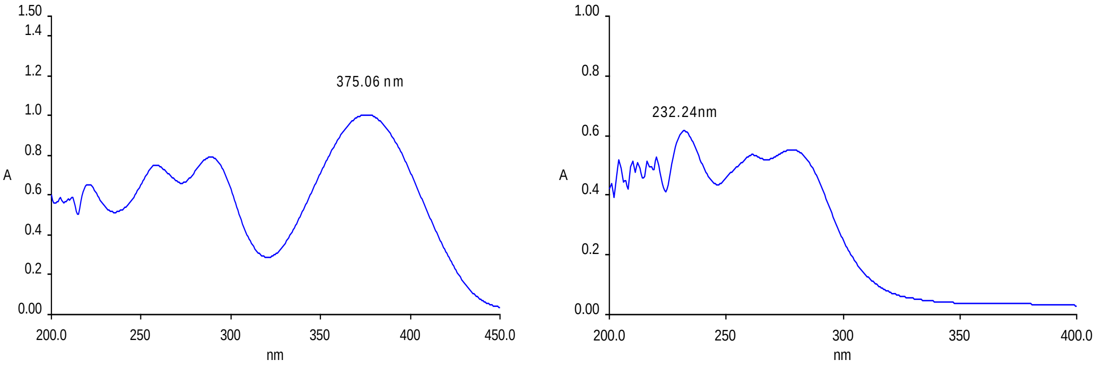

A B

Figure 5: UV- spectrum of A: lornoxicam with maximum absorbance at 375.06 nm.

B: the hydrolyzed product under basic condition (NaOH) with maximum absorbance at 232.24 nm.

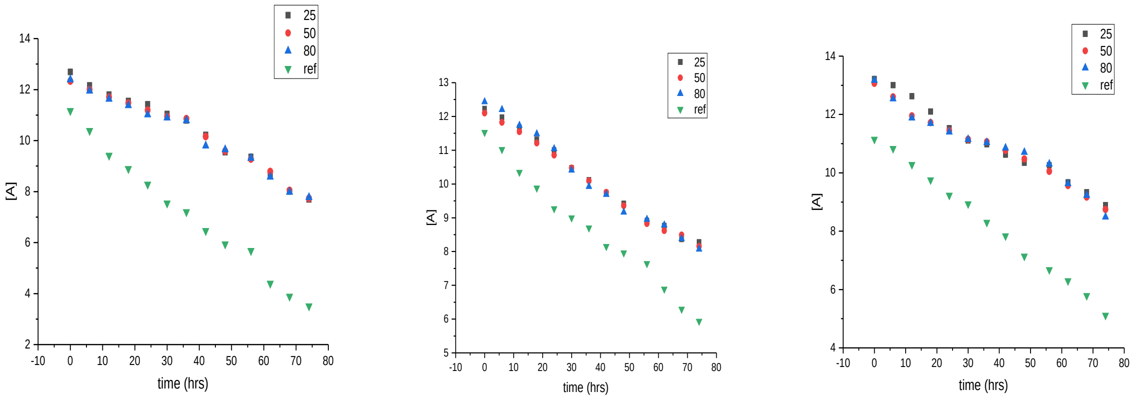

A B C

Figure 6: The hydrolysis process at different temperatures by using different bases, A: NaOH, B: Na_2CO_3, and C: K_2CO_3. [A] is the concentration of lornoxicam.

REFERENCES:

ARAS NAJMADDIN HAMAD, H. A. M. 2018. Synthesis and spectroscopic study of 1,2-thiazine system incorporating various ester groups. *ZANCO Journal of Pure and Applied Sciences,* 30**,** 44-55.

BACCHI, S., PALUMBO, P., SPONTA, A. & COPPOLINO, M. F. 2012. Clinical pharmacology of non-steroidal anti-inflammatory drugs: a review. *Anti-Inflammatory & Anti-Allergy Agents in Medicinal Chemistry (Formerly Current Medicinal Chemistry-Anti-Inflammatory and Anti-Allergy Agents),* 11**,** 52-64.

BHAVSAR, K., GAIKWAD, P., BANKAR, V. & PAWAR, S. 2010. Development and validation of uv-spectrophotometric method for simultaneous estimation of paracetamol and lornoxicam in bulk and tablet dosage form.

FRANCO-PÉREZ, M., MOYA-HERNÁNDEZ, R., ROJAS-HERNÁNDEZ, A., GUTIÉRREZ, A. & GÓMEZ-BALDERAS, R. 2011. Tautomeric Ratio and Prototropic Equilibrium Constants of Tenoxicam, a 1H and 13C NMR Theoretical and Experimental Study. *The Journal of Physical Chemistry B,* 115**,** 13593-13598.

GOUDA, M. A., HUSSEIN, B. H. & EL-SAID SHERIF, Y. 2017. Synthesis and medicinal importance of oxicams and their analogues. *Synthetic Communications,* 47**,** 1709-1736.

HALEN, P. K., MURUMKAR, P. R., GIRIDHAR, R. & YADAV, M. R. 2009. Prodrug designing of NSAIDs. *Mini reviews in medicinal chemistry,* 9**,** 124-139.

HALLMANN, S., FINK, M. J. & MITCHELL, B. S. 2015. Williamson ether synthesis: an efficient one-step route for surface modifications of silicon nanoparticles. *Journal of Experimental Nanoscience,* 10**,** 588-598.

HOMDRUM, E.-M., LIKAR, R. & NELL, G. 2006. Xefo® rapid: a novel effective tool for pain treatment. *European surgery,* 38**,** 342-352.

IVANOVA, D., DENEVA, V., NEDELTCHEVA, D., KAMOUNAH, F. S., GERGOV, G., HANSEN, P. E., KAWAUCHI, S. & ANTONOV, L. 2015. Tautomeric transformations of piroxicam in solution: a combined experimental and theoretical study. *Rsc Advances,* 5**,** 31852-31860.

JAYASELLI, J., CHEEMALA, J., GEETHA RANI, D. & PAL, S. 2008. Derivatization of enolic OH of piroxicam: a comparative study on esters and sulfonates. *Journal of the Brazilian Chemical Society,* 19**,** 509-515.

JORNADA, D., DOS SANTOS FERNANDES, G., CHIBA, D., DE MELO, T., DOS SANTOS, J. & CHUNG, M. 2015. The prodrug approach: A successful tool for improving drug solubility. *Molecules,* 21**,** 42.

KAR, S., DAS, D. & MONDAL, A. 2016. The Analgesic Efficacy of Preoperative Lornoxicam in Prevention of Postoperative Pain after Septoplasty. *J Neurol Neurophysiol,* 7**,** 2.

MASSAH, A. R., MOSHARAFIAN, M., MOMENI, A. R., ALIYAN, H., NAGHASH, H. J. & ADIBNEJAD, M. 2007. Solvent-Free Williamson Synthesis: An Efficient, Simple, and Convenient Method for Chemoselective Etherification of Phenols and Bisphenols. *Synthetic communications,* 37**,** 1807-1815.

MODHAVE, D. T., HANDA, T., SHAH, R. P. & SINGH, S. 2011. Stress degradation studies on lornoxicam using LC, LC–MS/TOF and LC–MSn. *Journal of pharmaceutical and biomedical analysis,* 56**,** 538-545.

MUHAMAD, S. G., ESMAIL, L. S. & HASAN, S. H. 2016. Kinetic studies of bioethanol production from wheat straw. *ZANCO Journal of Pure and Applied Sciences,* 28**,** 97-103.

NAKKA, M., NALLAPATI, S. B., REDDY, L. V., MUKKANTI, K. & PAL, S. 2011. Synthesis, characterization and anti-bacterial screening of Piroxicam based sulfonates. *J. Chem. Pharm. Res,* 3**,** 581-8.

PAVIA, D. L., LAMPMAN, G. M., KRIZ, G. S. & VYVYAN, J. A. 2008. *Introduction to spectroscopy,* Cengage Learning.

RAO, P. & KNAUS, E. E. 2008. Evolution of nonsteroidal anti-inflammatory drugs (NSAIDs): cyclooxygenase (COX) inhibition and beyond. *Journal of Pharmacy & Pharmaceutical Sciences,* 11**,** 81-110s.

RAWAL, N., KRØNER, K., SIMIN-GEERTSEN, M., HEJL, C. & LIKAR, R. 2010. Safety of Lornoxicam in the Treatment of Postoperative Pain. *Clinical drug investigation,* 30**,** 687-697.

REDASANI, V. K., BHALERAO, O. C., KALASKAR, M. G. & SURANA, S. J. 2017. Synthesis and evaluation of novel mutual prodrugs of Piroxicam. *Journal of Pharmaceutical Chemistry,* 4**,** 1-4.

RUSSELL, R. 2001. Non-steroidal anti-inflammatory drugs and gastrointestinal damage—problems and solutions. *Postgraduate medical journal,* 77**,** 82-88.

SHAH, D., RANA, J. P., CHHALOTIYA, U. K., BALDANIA, S. & BHATT, K. 2014. Development and validation of a liquid chromatographic method for estimation of dicyclomine hydrochloride, mefenamic acid and paracetamol in tablets. *Indian journal of pharmaceutical sciences,* 76**,** 529.

SIDDIQUI, H. L., ZIA-UR-REHMAN, M., ELSEGOOD, M. R. & WEAVER, G. W. 2010. Methyl 2-methyl-4-(oxiran-2-ylmethoxy)-2H-1, 2-benzothiazine-3-carboxylate 1, 1-dioxide. *Acta Crystallographica Section E: Structure Reports Online,* 66**,** o333-o333.

SINDHU, A., DEVESWARAN, R., BHARATH, S. & SHARON, F. 2015. Development and Validation of a HPTLC Method for the Estimation of Lornoxicam in Bulk Drug and in Tablet Dosage Form. *Pharmaceutical Methods,* 6**,** 109.

XU, S., ROUZER, C. A. & MARNETT, L. J. 2014. Oxicams, a class of nonsteroidal anti-inflammatory drugs and beyond. *IUBMB life,* 66**,** 803-811.

ZANCO Journal of Pure and Applied Sciences
The official scientific journal of Salahaddin University-Erbil
https://zancojournals.su.edu.krd/index.php/JPAS

ISSN (print):2218-0230**, ISSN (online):** 2412-3986**, DOI: http://dx.doi.org/10.21271/zjpas**

RESEARCH PAPER

Computational study of optical properties, and enantioselective synthesis of di-substituted esters of hydantoic and thiohydantoic acids

Hiwa Omer Ahmad*

*Department of Pharmaceutical Chemistry, College of Pharmacy, Hawler Medical University. Hawler, Kurdistan Region, Iraq.

ABSTRACT:

The title compounds with different optically active substituted ester of hydantoic and thiohydantoic were synthesized by the reaction of corresponding enantio-pure amino acids methyl ester hydrochloride with phenylisocyanate/thiocyanate in the presence of triethylamine. The duration of reaction was limited to avoid racemisation and produce high enantio-enriched compounds. Low values of ELUMO-HOMO gap 0.14, 0.16, 0.15, 0.15, and 0.10 eV were observed for compounds 1, 2, 3, 4, and 5, respectively indicate soft, and high reactivity compounds. Values of ELUMO-HOMO gap also show that the compounds can easily decompose spontaneously to their elements. The order of synthesized compounds based on increasing reactivity depends on LUMO-HOMO energy gap represent as follows; 5>1>3, 4>2. Thermodynamic energies have been calculated for synthesized compounds including Enthalpy and Gibbs free energy.

KEY WORDS: Density functional theory calculations; Energy, Molecular electrostatic potential, hydantoic acids.
DOI: http://dx.doi.org/10.21271/ZJPAS.32.1.9
ZJPAS (2020) , 32(1);75-94 .

1.INTRODUCTION :

The reaction of α-amino acids with isocyanate or isothiocyanate generally takes place in basic aqueous solution to produce ureido acids. (Scheme 1.1). (Ware, 1950)

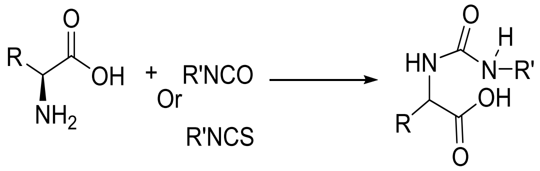

Scheme 1.1: The condensation of amino acids with isocyanate or isothiocyanate.

If a large excess of base is used, racemization and/or formation of hydantoin or thiohydantoin(Ballard *et al.*, 2018) take place without formation of optically active hydantoic and thiohydantoic acid. Previously reported that ester of isocyanate reacts with an amine to produce ester of hydantoic acid.(Lombardino and Gerber, 1964)

Computational methods provide accurate, easy and time saving techniques for drug design.(Abdallah, 2019) Orbital energies calculation has been used to obtain ionization potential (*IP*) and electron affinity (*EA*) values for neutral molecules. The negative values of the highest occupied molecular orbital energy ($-E_{HOMO}$) and the lowest unoccupied molecular orbital energy ($-E_{LUMO}$) gives information to ionization potential and electron affinity,

* **Corresponding Author:**
Mukhlis Hamad Aali
E-mail: Hiwa.omar@hmu.edu.krd
Article History:
Received: 14/09/2019
Accepted: 14/10/2019
Published: 25/02 /2020

respectively (i.e., IP =-E_{HOMO} and EA =-E_{LUMO}). (Shankar *et al.*, 2009)

The energy level of $E_{LUMO-HOMO}$ for all synthesized compounds elucidate physical and chemical information such as ionization potential (IP), electron affinity (EA), electronegativity (χ), electrophilicity index (ω), hardness (η), softness (S) and chemical potential (μ).

2.Experimental section

2.1 Materials and methods

All starting compounds were obtained from Fisher Scientific, Sigma-Aldrich, Alfa Aesar, Fluorochem, Acros Organic, BDH, and Lancaster Synthesis and used without any further purification. ^{1}H-NMR and ^{13}C-NMR spectra were recorded on Brukeravance (400 MHz) spectrometer. Parts per million is a unit of chemical shift and tetra-methylsilane expressed as a standard. NMR spectra were recorded in solutions in the deuterated solvent mentioned in method section.

Optical rotations were measured with a Schmidt-Haensch Polartronic 1 in a 5.00 cm path length cell. The solvent and concentration (expressed in g/100 ml) of the solutions LCMS experiments were performed using a Waters 2790 liquid chromatography system and a Waters ZQ mass spectrometer. Samples were loaded using a Gilson 232XL auto-sampler. Low-resolution mass spectrometric data were determined using a Fisons VG Platform II quadrupole instrument using electrospray ionisation (ES), unless otherwise stated. High-resolution mass spectrometric data were obtained in electrospray (ES) mode unless otherwise reported, on a Waters Q-TOF micro-mass spectrometer.

2.2 Molecular Modeling

Gaussian 09W was used to perform ab initio molecular orbital (MO) calculations.(Frisch *et al.*, 2016) employing the B3LYP functional and the 6–31 G basis set for all atoms.(Becke, 1993) For molecular structures optimization, GaussView 5.0.9 program was used for HOMO and LUMO surfaces area and electron distribution. (Frisch *et al.*, 2000)

2.3 Energy Minimization Procedure

The chemical compounds with the correct stereochemistry were drawn on Chemdraw professional 16.0 and stored in mol format in Gaussian view 5.0.9.

2.4 Chemistry

2.4.1. General procedure

Corresponding amino acids methyl ester hydrochlorides were dissolved in dichloromethane in a round bottom flask in the presence of triethyleamine. Phenyl isocyanate/isothiocyanate was added to the solution. The mixture was allowed to shake at room temperature in ultrasonic bath for 10 mins. Acetic water was used to wash and organic solvent evaporated by rotary evaporator.

Synthesis of methyl (phenylcarbamoyl)-L-phenylalaninate (1)

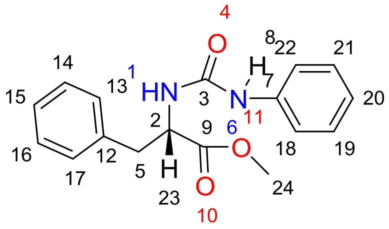

1

A mixture of L-phenyl alanine methyl ester hydrochloride salt (1 g, 4.63 mmol) and Et_3N (0.2 ml, 1.44 mmol) in 5 ml of CH_2Cl_2, phenylisocyanate (0.2 ml, 2.0 mmol) was slowly added.

Yield= 79.0 %, $[\alpha]_D^{20}$ = +51.3° (0.033 g/5 ml in acetone), HRMS calculated for $C_{17}H_{18}N_2O_3$ m/z [ES]$^-$ 321.1225; found 321.1215; ^{1}H-NMR (400 MHz, Chloroform-d): δ 6.39 – 6.28 (m, 7H, Ar), δ 6.23 – 6.19 (m, 2H), Ar), δ 6.15 (td, *J* = 7.1, 1.4 Hz, 1H, Ar), δ 6.01 (s, 1H, N**H**$_8$), δ 4.68 (d, *J* = 7.9 Hz, 1H, N**H**$_1$), δ 3.94 (dt, *J* = 7.9, 6.0 Hz, 1H, C**H**), δ 2.83 (s, 3H, CH3), δ 2.24 (dd, *J* = 13.8, 5.7 Hz, 1H, C**H**A), δ 2.14 (dd, *J* = 13.8, 6.3 Hz, 1H, C**H**B).^{13}C-NMR (101 MHz, d_6-DMSO): δ 172.9 (C9), δ 154.7 (C3), δ 137.9 (C7), δ 135.7 (C12), δ 129.0 (Ar), δ 128.9 (Ar), δ 128.2 (Ar), δ 126.8 (Ar), δ 123.5 (Ar), δ 120.5 (Ar), δ 53.6 (**C**2), δ 52.1 (**C**24), δ 37.9 (**C**5).

Synthesis of methyl (S)-2-phenyl-2-(3-phenylureido)acetate (2)

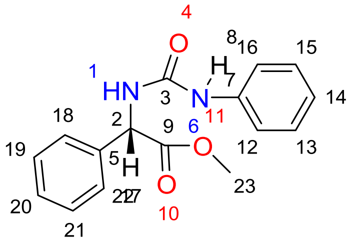

2

A mixture of L-Phenylglycine methylester hydrochloride (1 g, 4.97 mmol) and Et_3N (0.2 ml, 1.44 mmol) in 5 ml of CH_2Cl_2, phenylisocyanate (0.5 ml, 4.2 mmol) was slowly added.

Yield= 28.0 %, $[\alpha]_D^{20}$= +35.6° (0.15 g/5 ml in acetone), HRMS calculated for $C_{16}H_{16}N_2O_3$ m/z $[ES]^-$ 284.1157; found 284.1161; ^{1}H-NMR (400 MHz, Chloroform-*d*): δ 7.47 – 7.34 (s, 9H, Ar), δ 7.23 (s, 1H, N**H**$_8$), δ 7.01 (m, 1H, Ar), δ 6.37 (broad, s, 1H, NH$_1$), δ 5.63 (s, 1H, C**H**), δ 3.75 (s, 3H, OC**H3**). ^{13}C-NMR (101 MHz, $CDCl_3$): δ 172.9 (C9), δ 155.3 (C3), δ 138.7 (C7), δ 137.3 (C5), δ 129.7 (Ar), δ 128.9 (Ar), δ 127.6 (Ar), δ 124.2 (Ar), δ 121.2 (Ar), δ 57.6 (**C**2), δ 53.3 (**C**23).

Synthesis of methyl (phenylcarbamoyl)-L-alaninate (3)

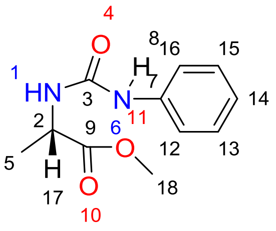

3

L-alanine methyl ester hydrochloride salt (1.0 g, 7.19 mmol) and Et_3N (1.4 ml, 10.75 mmol) in 25 ml of CH_2Cl_2, phenylisocyanate (1.5 ml, 12.56 mmol) was slowly added.

Yield= 47.0 %, $[\alpha]_D^{20}$= +72.5° (0.06 g/5 ml in acetone), HRMS calculated for $C_{11}H_{14}N_2O_3$ m/z $[ES]^-$ 222.1004; found 222.1004; ^{1}H- NMR (400 MHz, Chloroform-*d*): δ 7.36 – 7.22 (m, 5H, Ar + 1H, N**H**$_8$), δ 7.08 (tt, *J* = 6.8, 1.7 Hz, 1H, Ar), δ 5.85 (broad, s, 1H, N**H**$_1$), δ 4.61 (q, *J* = 7.2 Hz, 1H,C**H**), δ 3.78 (s, 3H, OC**H3**), 1.45 (d, 7.2 Hz, 3H, C**H3**). ^{13}C-NMR (101 MHz, $CDCl_3$): δ 172.3 (C9), δ 155.9 (C3), δ 138.9 (C7), δ 129.5 (Ar), δ 123.9 (C14), δ 120.9 (Ar), δ 52.9 (**C**2), δ 49.2 (**C**18), δ 19.1 (**C**5).

Synthesis of methyl (phenylcarbamoyl)-L-valinate (4)

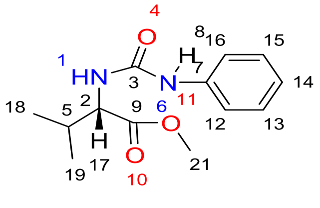

4

A mixture of L-valine methyl ester hydrochloride salt (1.0 g, 5.96 mmol) and Et3N (1.5 ml, 10.76 mmol) in 25 ml of CH_2Cl_2, phenylisocyanate (0.5 ml, 4.2 mmol) was slowly added.

Yield= 40.0 %, M.p. $[\alpha]_D^{20}$ = +76.3° (0.04 g/5 ml in acetone), HRMS calculated for $C_{13}H_{18}N_2O_3$ m/z $[ES]^-$ 250.1317; found 250.1317; ^{1}H-NMR (400 MHz, Chloroform-*d*): δ 7.14 (s, 1H, N**H**$_8$), δ 6.97 – 6.88 (m, 4H, Ar), δ 6.72 – 6.62 (tt, *J* = 6.7, 1.7 Hz, 1H, Ar), δ 5.57 (d, *J* = 8.9 Hz, 1H, N**H**$_1$), 4.17 (dd, *J* = 8.8, 4.9 Hz, 1H, CH17), δ 3.38 (s, 3H, OC**H3**), δ 1.80 (m, 1H, C**H**), 0.62 (d, *J* = 6.8 Hz, 3H, CH3), 0.53 (d, *J* = 6.9 Hz, 3H, CH3). ^{13}C-NMR (101 MHz, $CDCl_3$): δ 174.1 (C9), δ 156.1 (C3), δ 138.4 (C7), δ 129.2 (2xC, Ar), δ 123.8 (C14), δ 120.8 (2xC,Ar), δ 58.1 (**C**2), δ 52.3 (**C**21), δ 31.3 (**C**5), δ19.5 (**C**19), δ17.9 (**C**18) .

Synthesis of methyl (phenylcarbamothioyl)-L-alaninate (5)

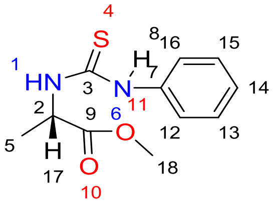

5

L-Alanine methyl ester hydrochloride (3.3 g, 23.5 mmol) and and Et_3N (1.5 ml, 10.76 mmol) in 100 ml of CH_2Cl_2, phenylisocyanate (2 ml, 16.8 mmol) was slowly added.

Yield= 60.0 %, $[\alpha]_D^{20}$= +41.7° (0.15 g/5 ml in acetone), HRMS calculated for $C_{11}H_{14}N_2O_2S$ m/z [ES]- 238.0777; found 238.0776; ^{1}H-NMR (400 MHz, Chloroform-d): δ 8.36 (s, 1H, N**H**$_8$), δ 7.55 – 7.20 (m, 5H, Ar), δ 6.76 (d, J = 7.5 Hz, 1H, N**H**$_1$), δ 5.19 (p, J = 7.2 Hz, 1H, C**H**), δ 3.78 (s, 3H, OC**H**$_3$), 1.45 (dd, 7.2, 1.0 Hz, 3H, C**H**$_3$). ^{13}C NMR (101 MHz, CDCl3): δ 180.1 (C3), δ 174.1 (C9), δ 136.4 (C7), δ 130.6 (2XC, Ar), δ 127.7 (C14), δ 125.2 (2XC, Ar), δ 53.8 (C2),), δ 53.1 (C18), δ 18.9 (C5).

3.Discussion

3.1. Chemistry

In this study, different substituted esters of hydantoic and thiohydantoic acids were synthesized by the reaction of corresponding optically active amino acids methyl ester hydrochloride with substituted isocyante/isothiocyante in the presence of triethylamine. To avoid racemisation (Ballard *et* *al.*, 2019) amount of triethylamine and reaction time has been decreased. (Scheme 2) 5,5-disubstituted hydantoins were synthesized previously (Jawhar *et al.*, 2018)

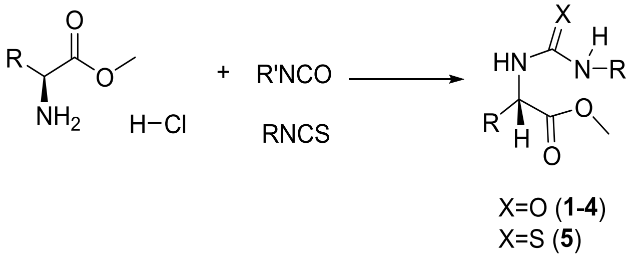

Scheme 2: Synthesis of compound **1**-**5**

All synthesized compounds have been characterized by ^{1}H-NMR and ^{13}C-NMR spectra. The ^{1}H- NMR spectra of compounds **2**, and **3** showed a broad singlet at δ 6.37, 5.85 ppm, respectively due to NH group in the compound . while, The ^{1}H- NMR spectra of compounds **1**, and **4** showed doublet at δ 4.68 ppm (d, *J* = 7.9 Hz, 1H, NH) and δ 5.7 ppm (d, *J* = 8.9 Hz, 1H, NH), respectively due to the hydrogen attached to the streogenic centre. Hydrogen attached to the streogenic centre showed doublet triplet at δ 3.94 ppm with *J* = 7.9, 6.0 Hz, and doublet doublet at δ 4.17 with *J* = 8.8, 4.9 Hz for compounds **1**, and **4**, respectively.

The ^{13}C-NMR spectrum showed peaks which are in agreement with number of chemically equivalent carbons present in all compounds.

3.2 Energy profile

To determine insight into the energy behavior between the compounds, selected physicochemical parameters were also calculated using B3LYP functional basis methods. (Table 1)

Table 1 shows different negative values of energy based on the aromatic and aliphatic substituents on the chiral position. Energy values for compounds **3** and **5** are approximately not far from each other because of their similarity in molecular structure attached to Chiral center with C=O and C=S difference. Energy profile values have been determined by the Hartree-Fock and B3LYP functional basis set for all atoms for **1-5.** (Table 1)

Table 1: Energy profile (in kcal/mol)

Energy/ kcal/mol		
6-31G		
Compounds	Hartree-Fock	B3LYP
1	-612790.21	-623560.62
2	-585692.07	-592487.81
3	-692899.44	-473199.81
4	-517611.70	-520857.24
5	-672830.49	-675972.48

3.3 Frontier Molecular Orbital (FMO) Analysis

Difference of energy between lowest unoccupied molecular orbital (LUMO) and highest occupied molecular orbital (HOMO) in gas phase at the B3LYP level is an important factor to calculate molecular reaction potentials (Fareghi- Alamdari *et al.*, 2015)

The B3LYP method and basis set of 6-31G has been used to obtain E_{HOMO}, E_{LUMO} and LUMO-HOMO energy gap (Eg; Δ) of compounds 1-**5**. Molecular orbital properties such as energy and frontier electron density are essential to give molecular reactivity information. Figure 1 shows values of HOMO energy (E_{HOMO}) and the LUMO energy (E_{LUMO}) of **1** is -0.31 eV and -0.017 eV, respectively. The energy of the HOMO is mainly related on the ionization potential and focused around carbonyl and nitrogen attached to the phenyl ring. While, the electron affinity can be observed by LUMO energy which is focused on benzyle attached to the chiral position. The differences of energy between both molecular orbital $E_{LUMO\text{-}HOMO}$ calculated as a small value 0.14 eV for compound **1** is simply show higher reactivity compare with compounds **2**,**3** and **4**.

LUMO-HOMO energy gap for compound **2** shows 0.16 eV indicates less reactive compare with the other synthesized compounds. LUMO-HOMO energy gap for compounds **3** and **4** show values of 0.15 and 0.15 eV respectively, which observe similar softness and reactive compounds. A value of 0.10 eV is a LUMO-HOMO energy gap for compound **5** show high reactive compound compare with other synthesized compounds. (See supporting information) Hence, we can conclude synthesized compounds in order of increasing reactivity based on LUMO-HOMO energy gap as follows; **5**>**1**>**3**, **4**>**2**. The HOMO for all synthesized compounds is mostly located along the carbonyl and substituent attached to nitrogen. The LUMO is mostly located over the groups attached to the streogenic center.

Recently, Koopman's theory has been used to calculate ionization potential for different compounds by Chong *et al*.(Chong *et al.*, 2002) using orbital energies which is equal to a negative value of HOMO energy (IP =- E_{HOMO}). A negative value of LUMO energy is equal to electron affinity (EA = -E_{LUMO}) (Shankar et al., 2009, Rocha *et al.*, 2015). The chemical hardness η of the molecule based on the molecular orbital can be calculated by the following equation (equation 1) (Galván *et al.*, 2015)

$$\eta = \left(\frac{E_{LUMO} - E_{HOMO}}{2}\right) \qquad \textbf{Equation 1}$$

While, electro negativity χ can be obtained by equation 2

$$\chi = -\frac{E_{LUMO} + E_{HOMO}}{2} \qquad \textbf{Equation 2}$$

Hence, Chemical hardness η is equal to the energy gap between LUMO and HOMO divided by two and the half-way between the LUMO and HOMO corresponds to electro negativity χ of the molecule. Hardness η and softness η values give information of the molecule about reactivity and stability. Therefore, Other chemical properties can be calculated by using LUMO and HOMO energy values for instance; hardness η = IP-EA/2, electrophilicity index $\omega = \mu^2 /2\eta$, electro-negativity χ = IP+EA/2, chemical potential μ=-χ, , softness s = 1/2η and.(Rocha et al., 2015)(Table 2) Table 2 shows small values of $E_{LUMO\text{-}HOMO}$ gap indicating a soft molecule, more reactive, and higher polarizable compound than high values of $_{ELUMO\text{-}HOMO}$. Values also show that the compound can easily decompose spontaneously to its elements.(Rao *et al.*, 2016)

Table 2: Reactivity properties, HOMO and LUMO energies, HOMO–LUMO energy gap of 1.

Molecular parameters	**B3LYP/6-31G**
EHOMO (eV)	-0.31
ELUMO (eV)	-0.17
ΔELUMO-HOMO (eV)	0.14
Ionization potential, IP (eV)	0.31
Electron affinity, EA (eV)	0.17
Electronegativity, χ (eV)	0.24
Chemical potential, μ (eV)	-0.24
Chemical hardness, η (eV)	0.07
Chemical softness, s (eV-1)	7.14
Global electrophilicity index ω	0.41

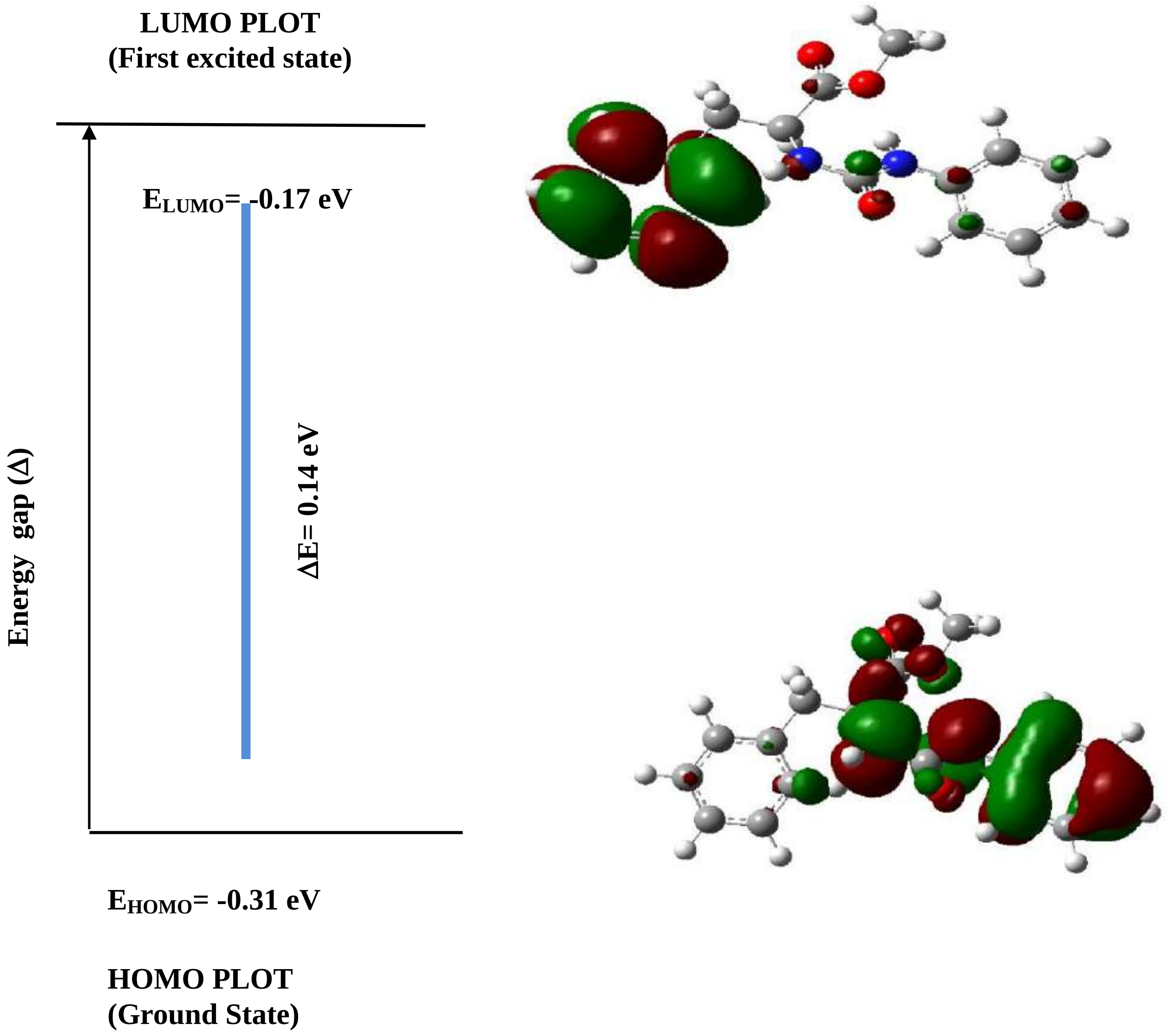

Figure 1: Molecular orbitals and LUMO and HOMO energy gap of **1**

3.4 Molecular electrostatic potential

The molecular electrostatic potential (MEP) is a tool to give a good correlation between physicochemical properties and molecular structure reactivity to express binding site of drug and nucleophile and electrophile position of the molecule. (Scrocco and Tomasi, 1978) (Rao et al., 2016). Red color region in Figure 2 for compound **5** shows a maximum electron density which is cover phenyl attached to the nitrogen, C=O, and sulfur. Electron density lowest region (Blue color) corresponds to the hydrogen atoms bound to the methyl on the chiral centre and oxygen of ester, and carbon attached to the nitrogen.(Kubinyi *et al.*, 2006, Moro *et al.*, 2005) (Figure 2) Molecular electrostatic potential surface for compounds **1-4** represent variety of electron distribution with different color areas. (See supporting information Figure S14-17)

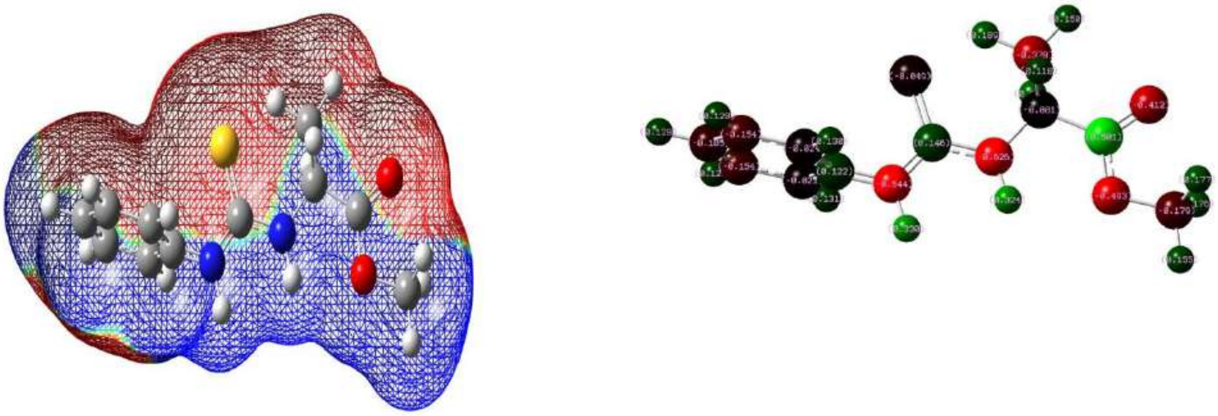

Figure 2: Molecular electrostatic potential surface and charge distribution value for compound **5**.

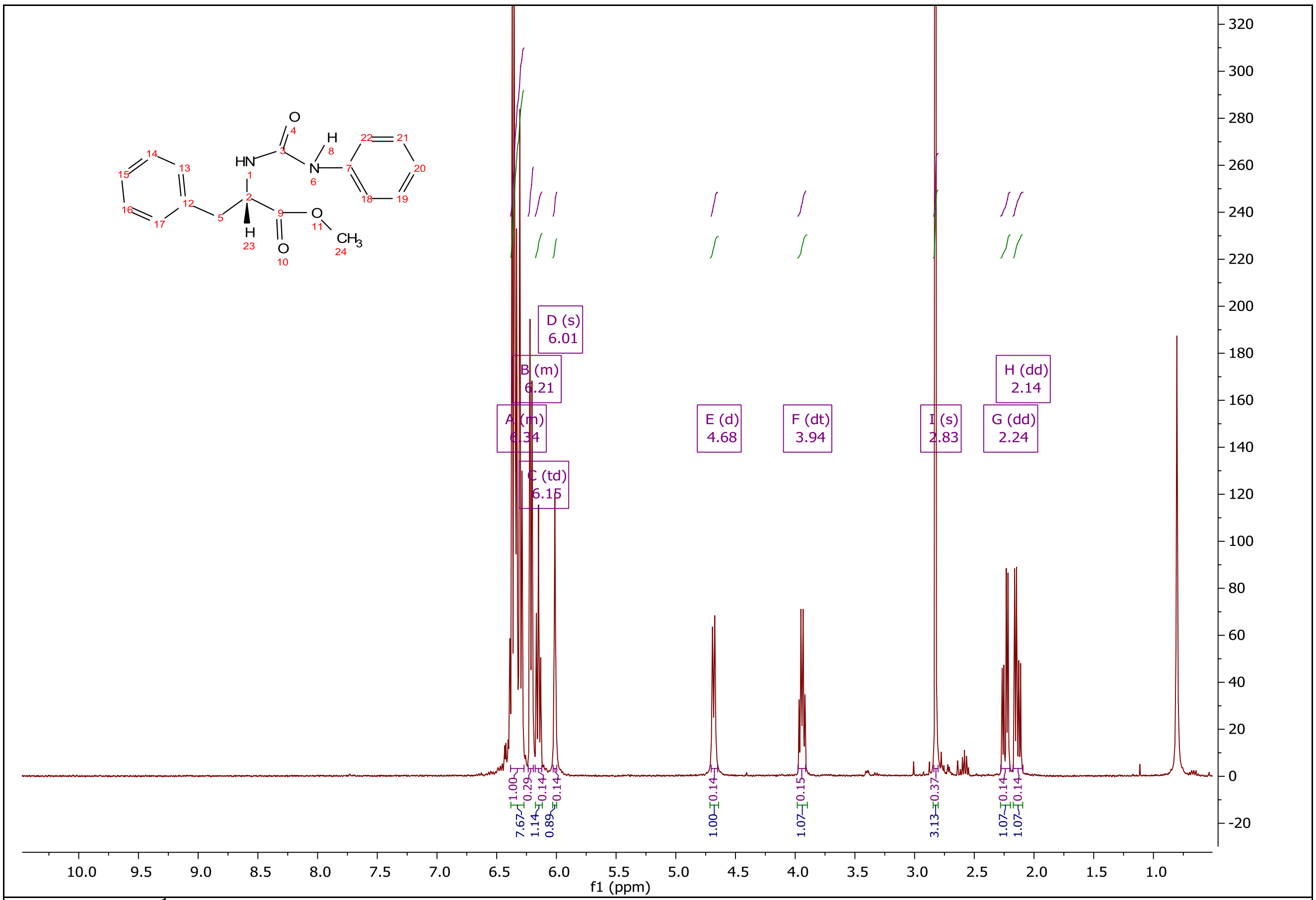

Figure S1: ^{1}H-NMR spectrum of **1**

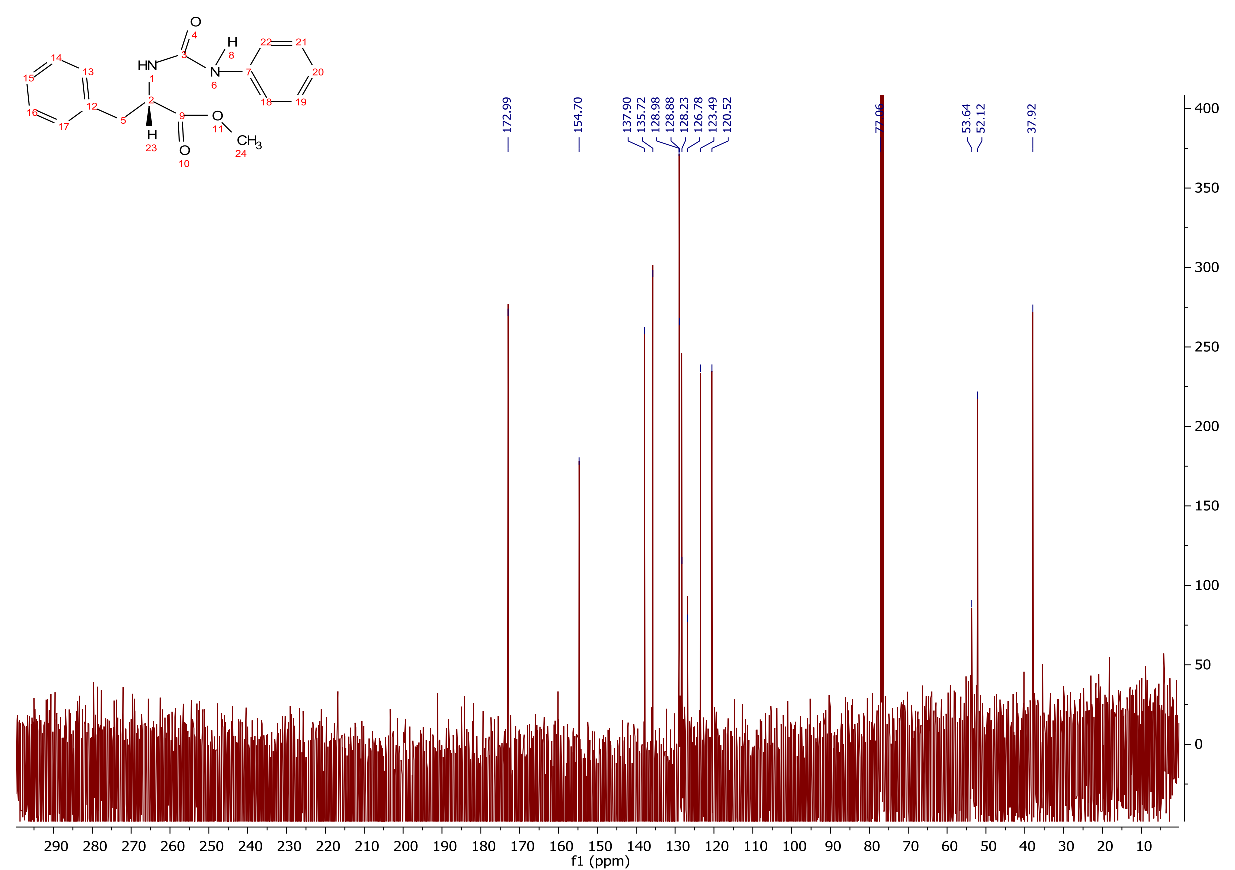

Figure S2: ^{13}C -NMR spectrum of **1**

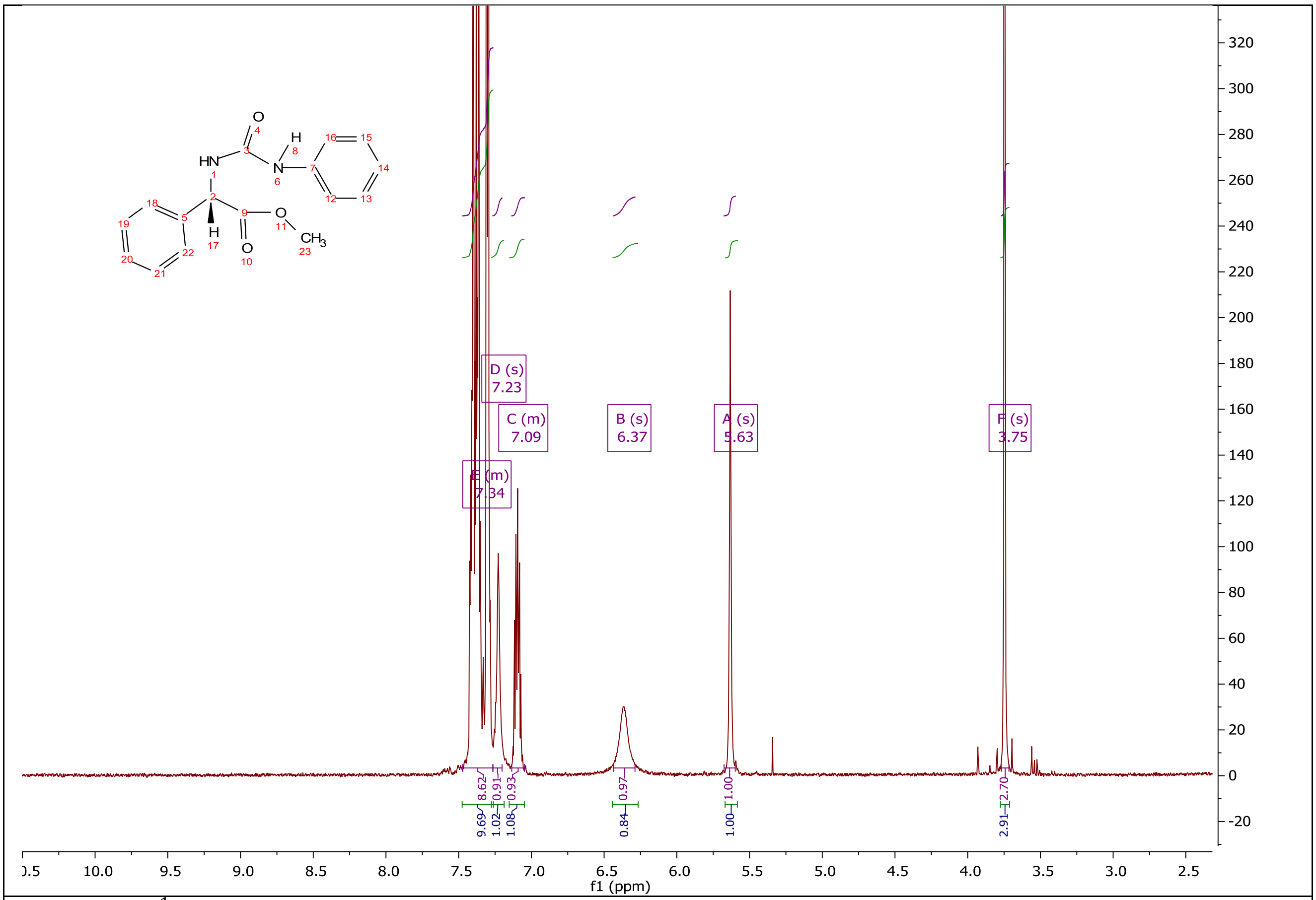

Figure S3: ^{1}H- NMR spectrum of **2**

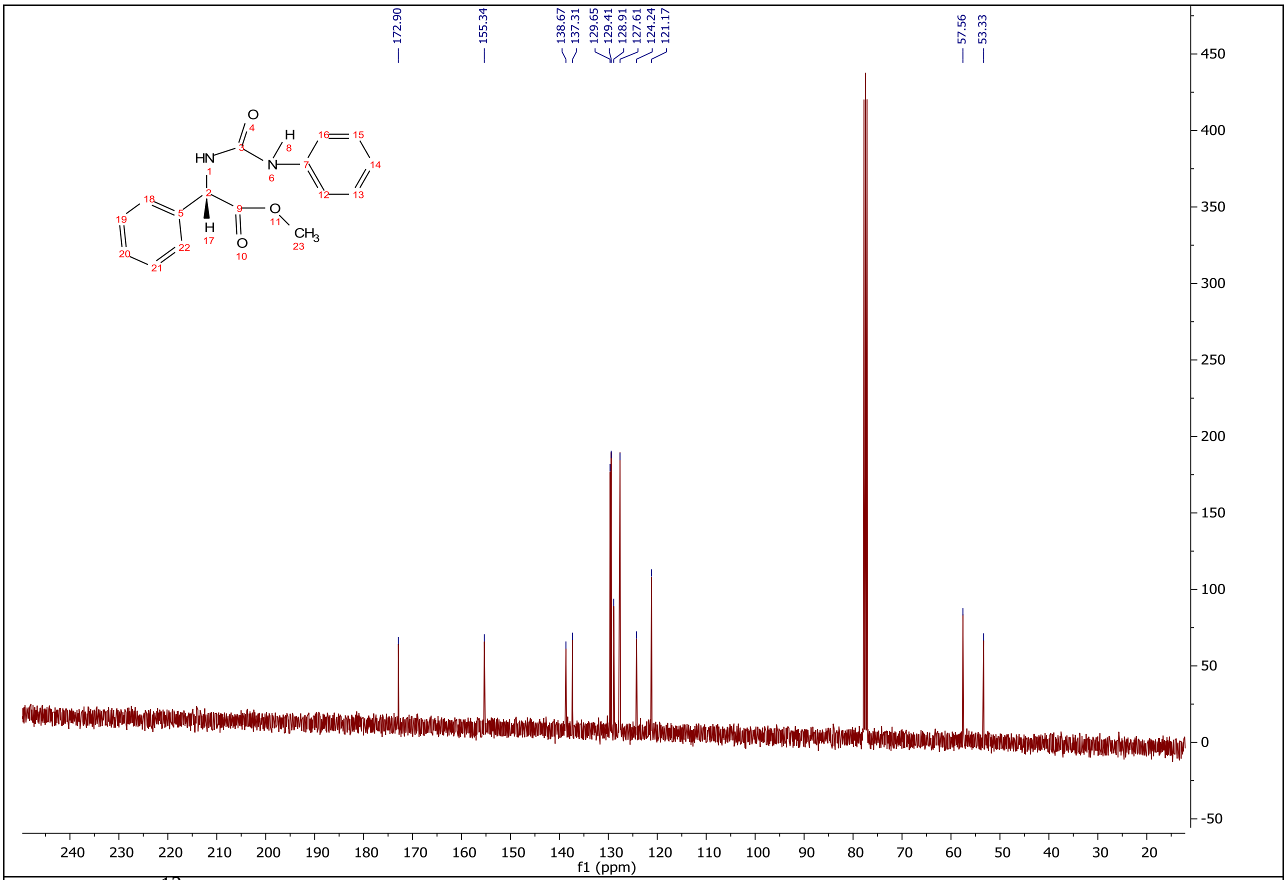

Figure S4: ^{13}C -NMR spectrum of **2**

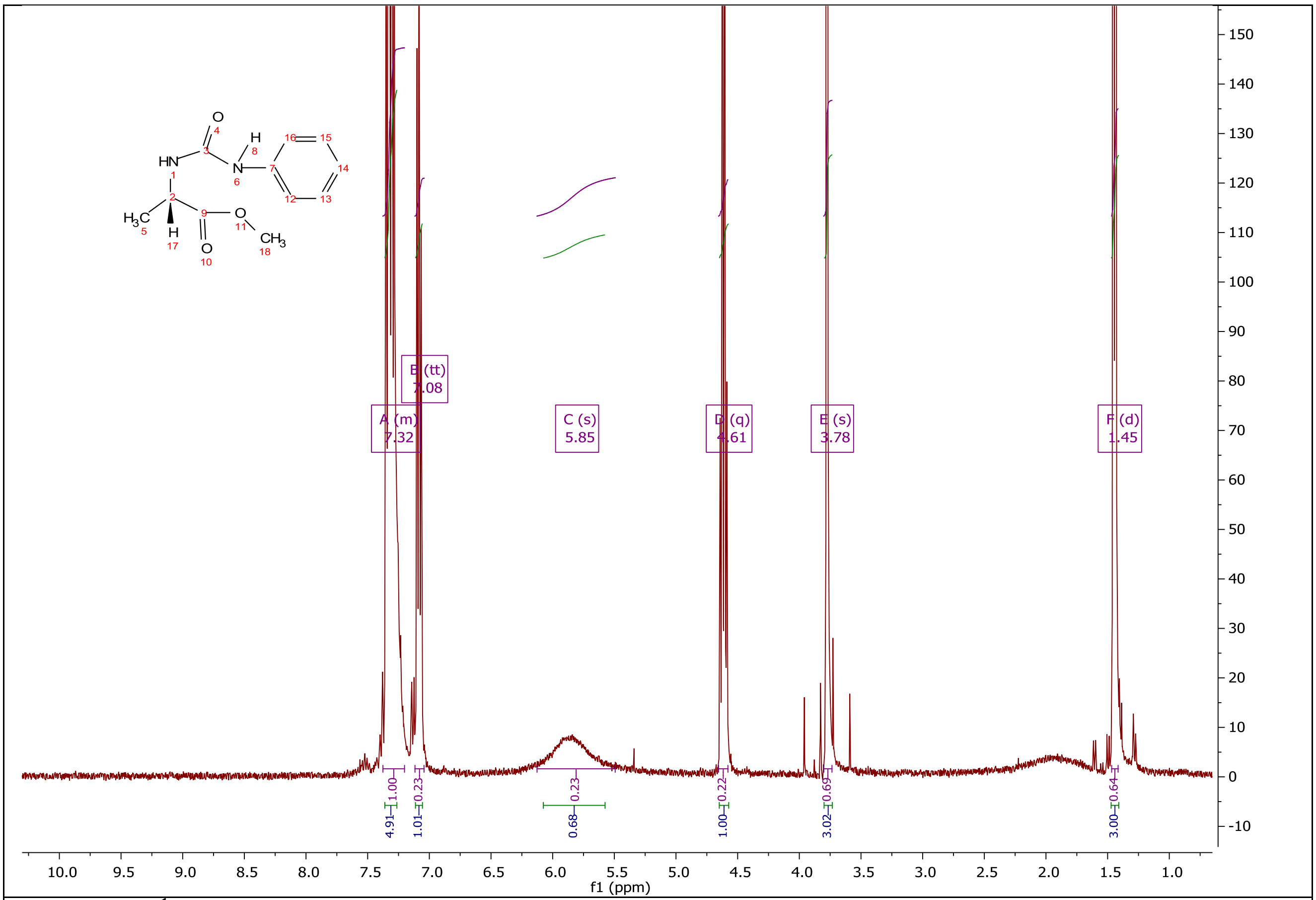

Figure S5: ^{1}H-NMR spectrum of **3**

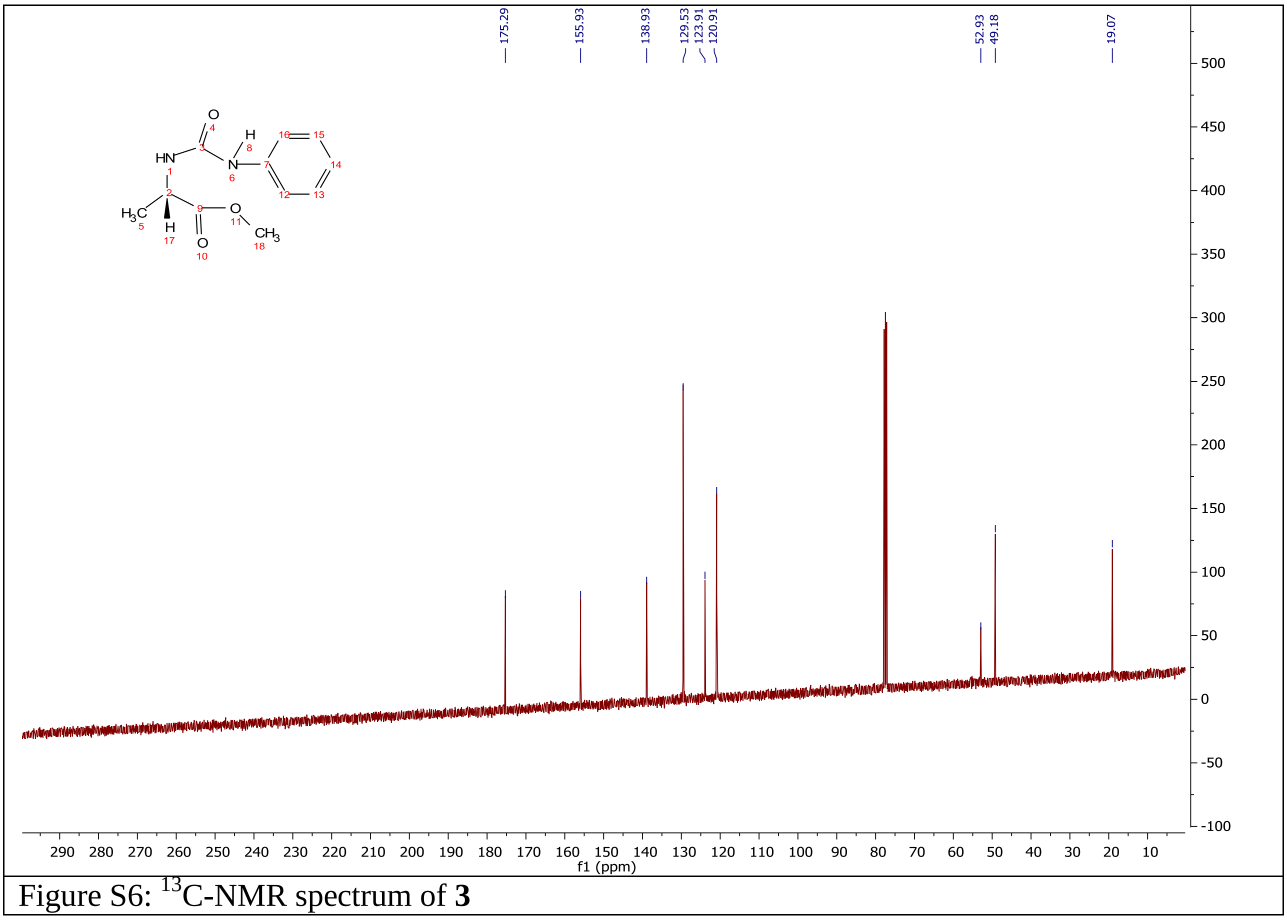

Figure S6: ^{13}C-NMR spectrum of **3**

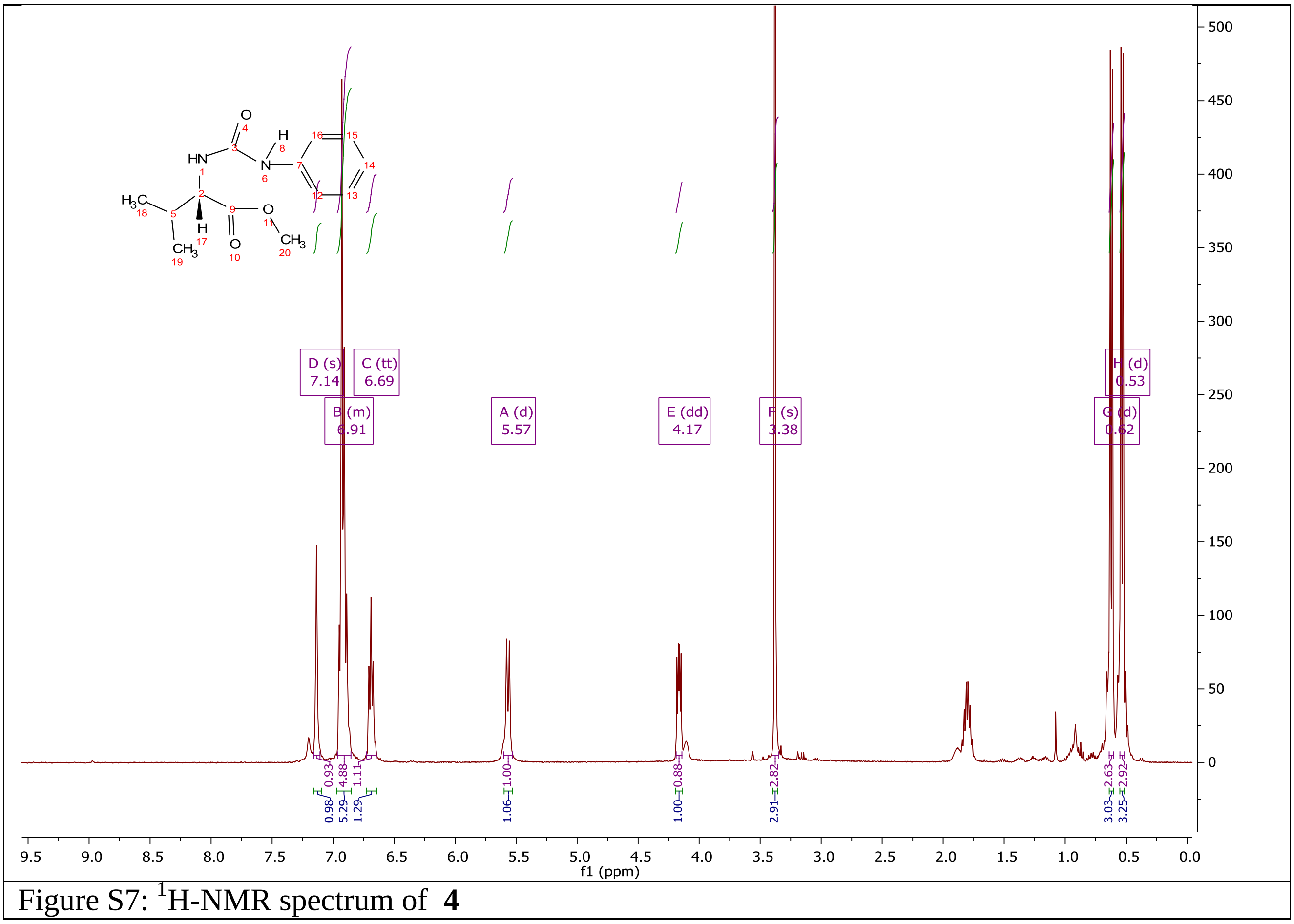

Figure S7: ^{1}H-NMR spectrum of **4**

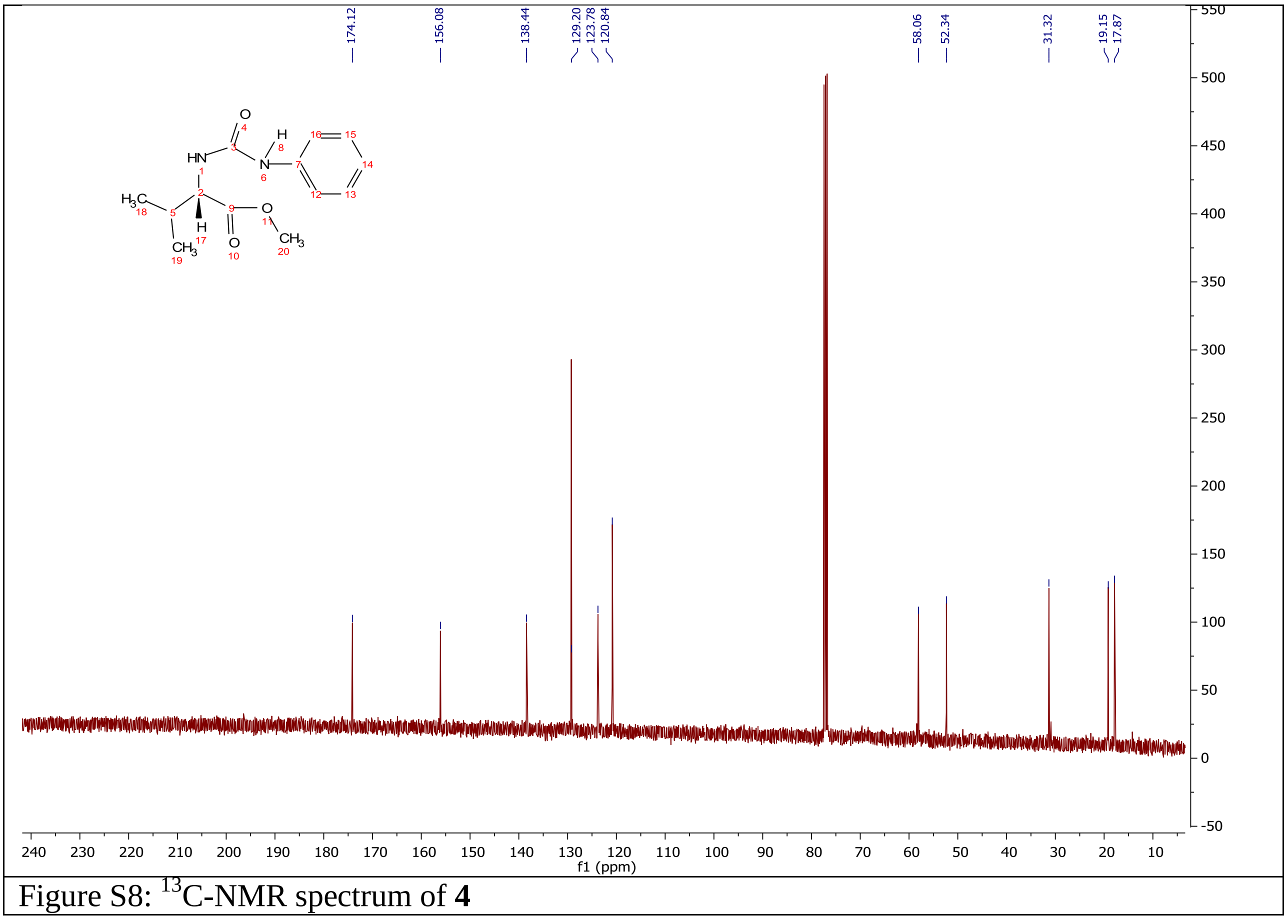

Figure S8: ^{13}C-NMR spectrum of **4**

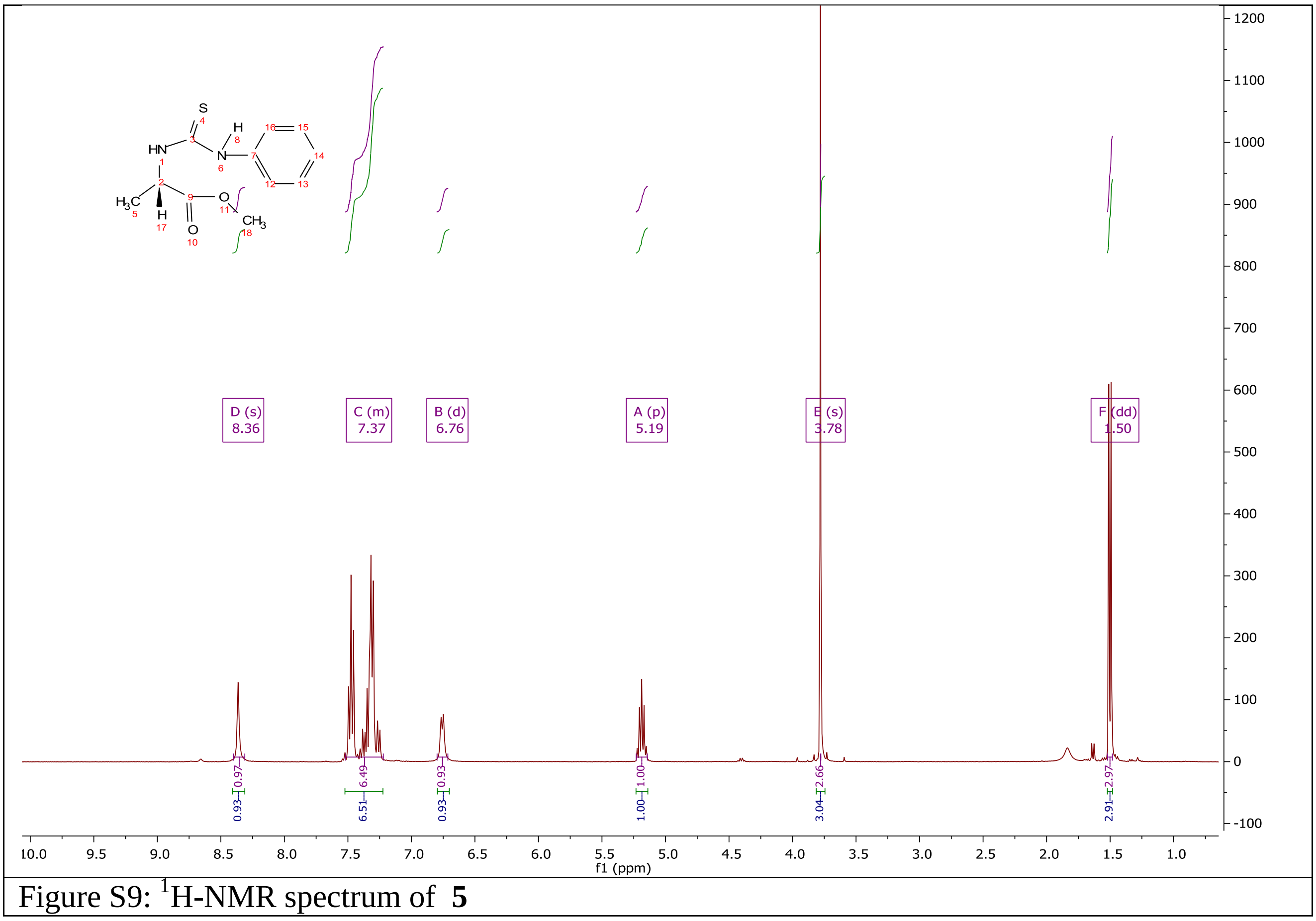

Figure S9: ^{1}H-NMR spectrum of **5**

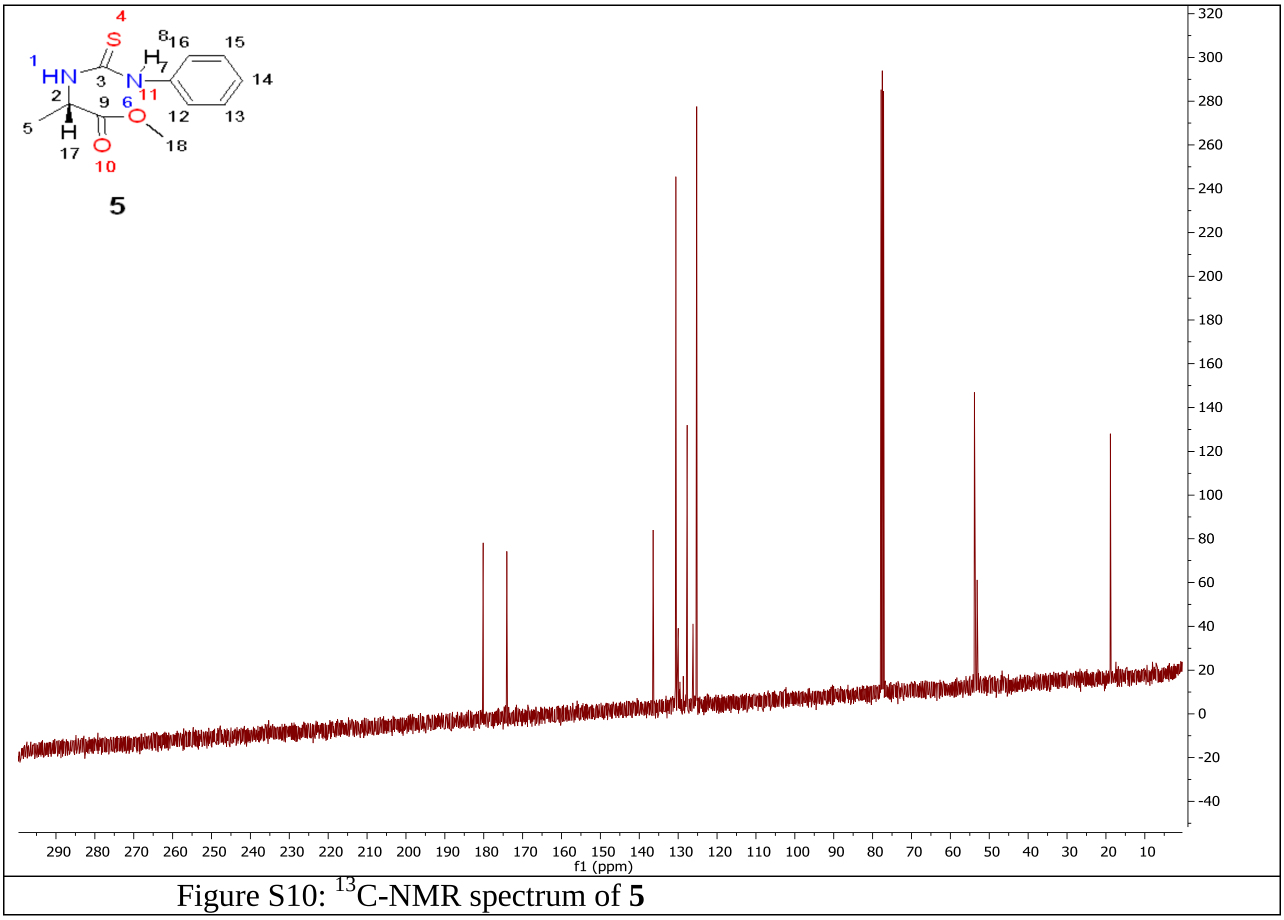

Figure S10: ^{13}C-NMR spectrum of **5**

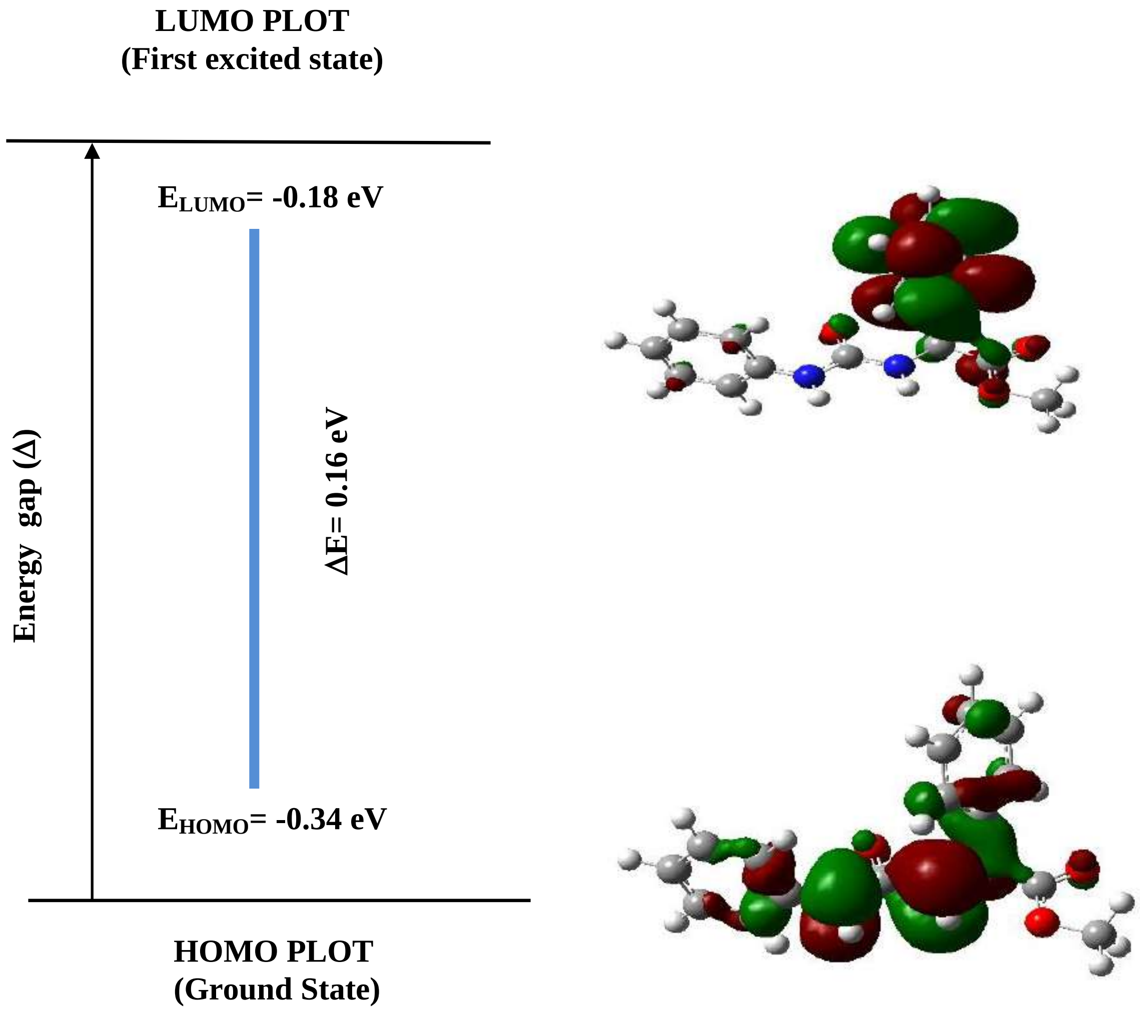

Figure S11: Frontier molecular orbitals of **2** (Δ: Energy gap between LUMO and HOMO)

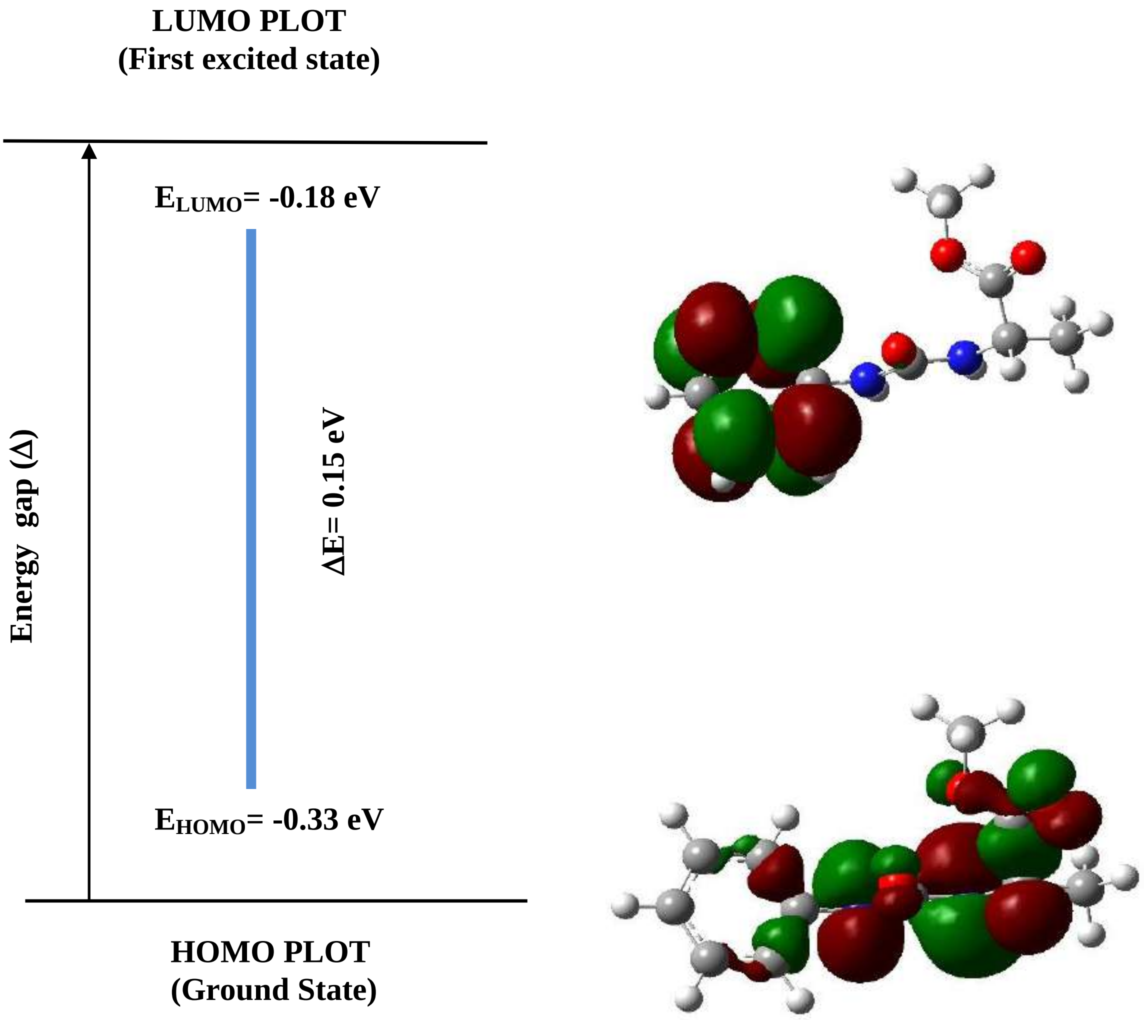

Figure S12: Frontier molecular orbitals of **3** (Δ: Energy gap between LUMO and HOMO)

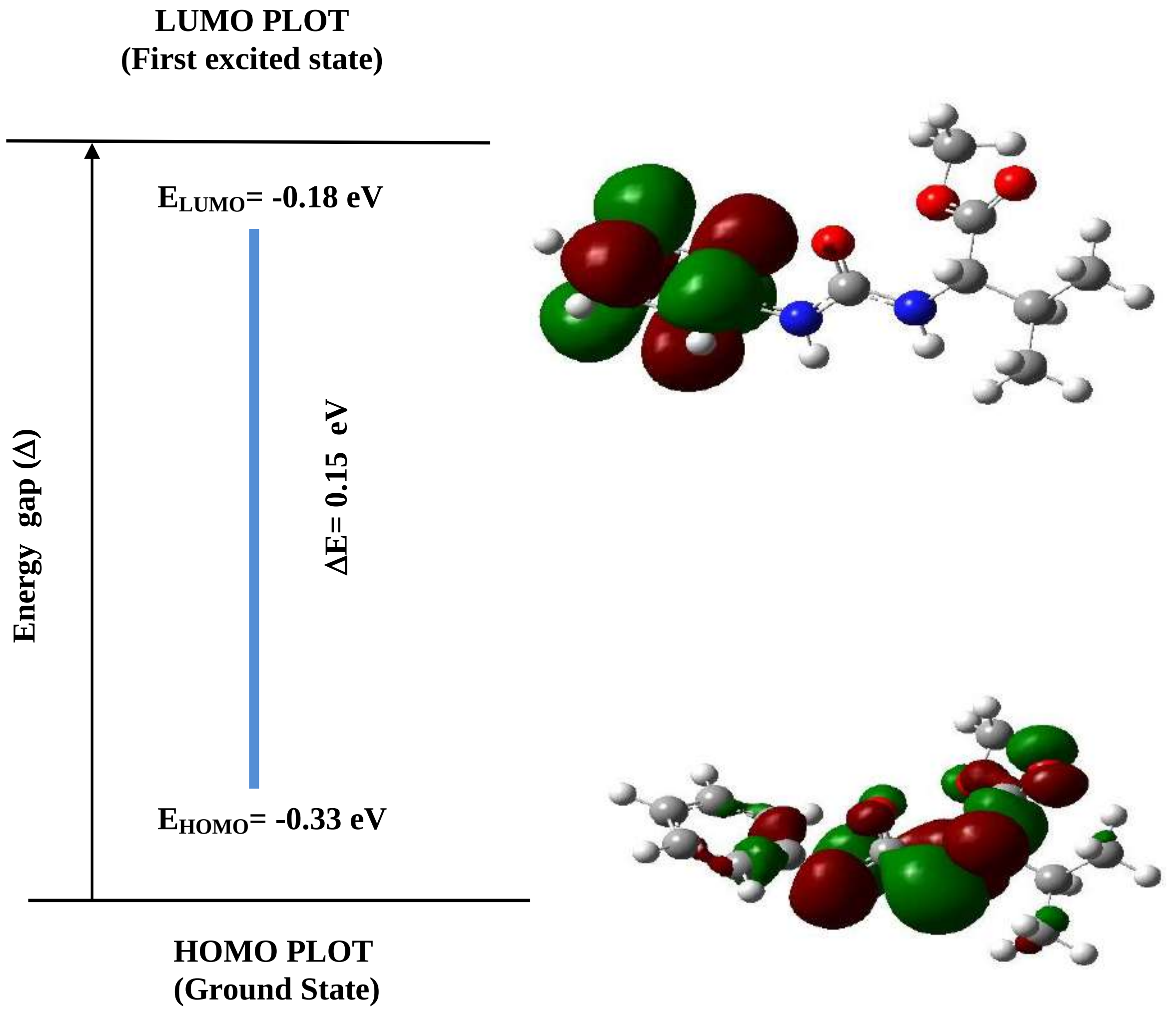

Figure S13: Frontier molecular orbitals of **4** (Δ: Energy gap between LUMO and HOMO)

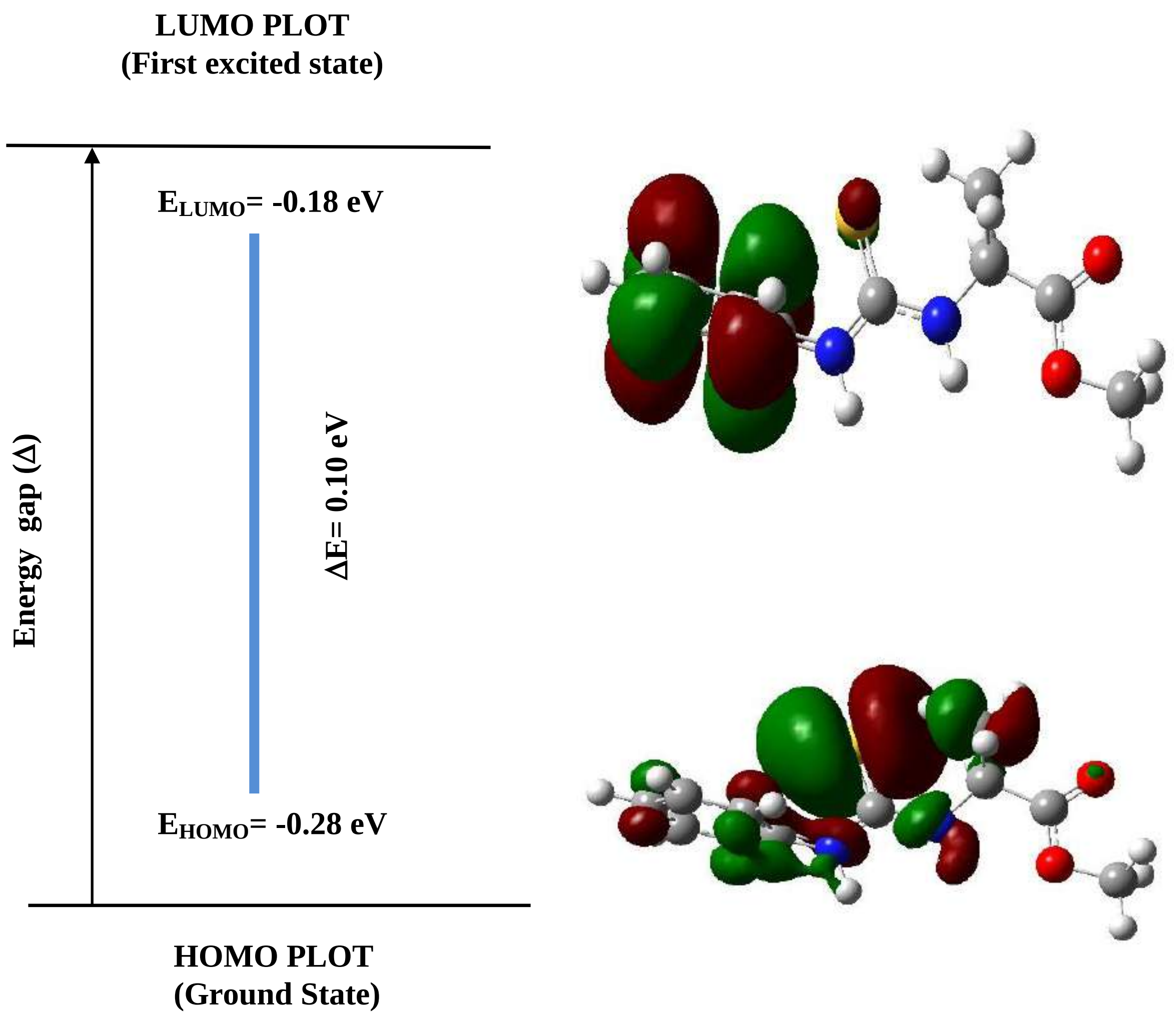

Figure S14: Frontier molecular orbitals of **5** (Δ: Energy gap between LUMO and HOMO)

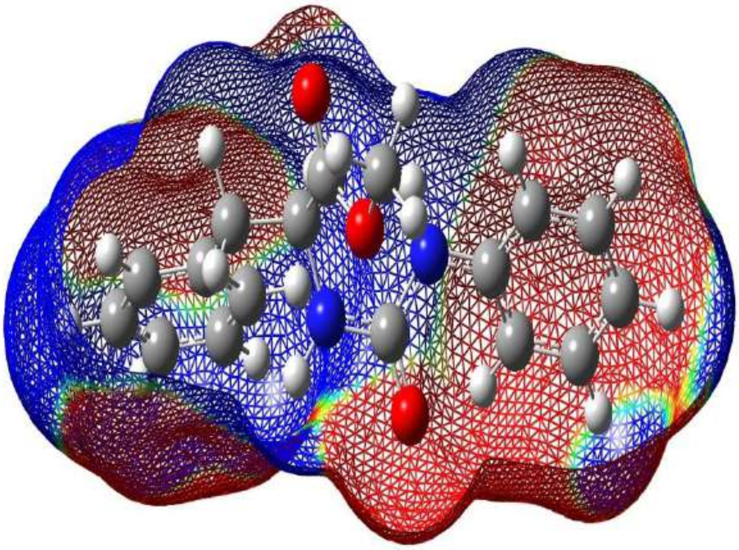

Figure S15: Molecular electrostatic potential for compound **1**.

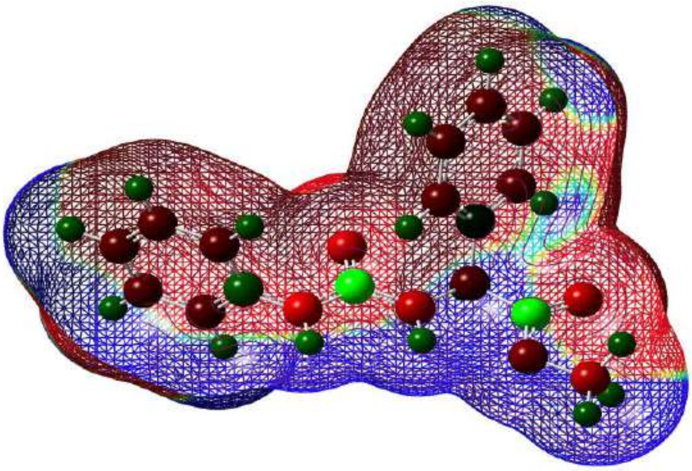

Figure S16: Molecular electrostatic potential for compound **2**.

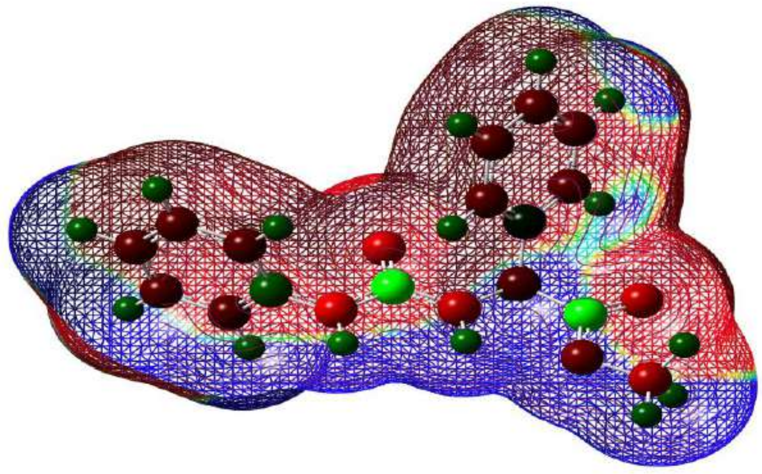

Figure S17: Molecular electrostatic potential for compound **3**.

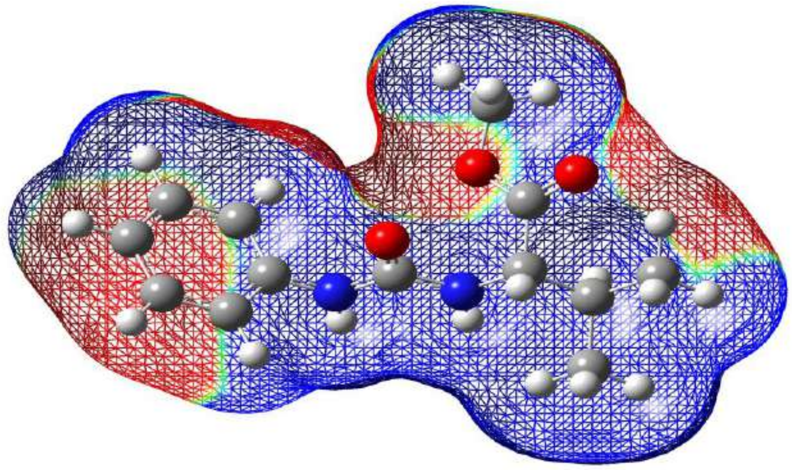

Figure S18: Molecular electrostatic potential for compound **4**.

3.5 Thermodynamic parameters

Thermodynamic parameters for all synthesized compounds have been calculated by using B3LYP/6-31G level in Gaussian 09 W. All values such as Molar heat capacity constant volume (Cv)(Abdullah et al., 2016), relative energy (E), enthalpies (ΔH), entropies (S) and Gibbs free energy (ΔG) are shown in Table 3.

Table 4 shows negative values of relative energy, Gibbs free energy and enthalpies of **1**-**5**.

Table 3: Thermodynamic parameters of **1-5**

Compounds	E(kcal/mol)	ΔG(kcal/mol)	ΔH(kcal/mol)	S(cal/molK)	C_V(cal/molK)
1	217.728	-623483	-623437	155.739	76.097
2	198.920	-598831	-598787	148.857	71.195
3	163.752	-478544	-478505	131.711	58.136
4	201.128	-527850	-527807	144.993	68.439
5	162.432	-681201	-681161	134.346	59.307

Conclusions

Different substitituted esters of hydantoic and thiohydantoic acids have been synthesized with optical active properties. A complete structural, NMR, Mass and thermodynamic parameters have been calculated for compounds **1**-**5**. The relatively low value of $E_{LUMO-HOMO}$ gap indicates low chemical stability and high reactivity of compounds **1**-**5**. The positive values of thermodynamic parameters suggest high reactivity of compounds **1**-**5**. The differences of energy between both molecular orbitals $E_{LUMO-HOMO}$ calculated as a small value 0.10 eV for compound **5** which simply shows higher reactivity than the other compounds mentioned in this study.
LUMO-HOMO energy gap for compound **2** shows 0.16 eV indicates less reactive compound in comparison with other synthesized compounds. LUMO-HOMO energy gap for compounds **3**, and **4** show values of 0.15, and 0.15 eV, respectively which observe approximately similar softness and reactive compounds. A value of 0.14 eV is a LUMO-HOMO energy gap for compound **1** show less reactive than compound 5 and more reactive than other synthesized compounds. Hence, we can conclude synthesized compounds in order of increasing reactivity based on LUMO-HOMO energy gap as follows ; **5**>**1**>**3, 4**>**2**.

4.References

ABDALLAH, H. 2019. Theoretical study for the inhibition ability of some bioactive imidazole derivatives against the Middle-East respiratory syndrome corona virus (MERS-Co). *ZANCO Journal of Pure and Applied Sciences,* 31**,** 71-78.

ABDULLAH, B. J., OMAR, M. S. & JIANG, Q. J. 2016. Grüneisen Parameter and Its Related Thermodynamic Parameters Dependence on Size of Si Nanoparticles. *ZANCO Journal of Pure and Applied Sciences,* 28**,** 126-132.

BALLARD, A., AHMAD, H. O., NARDUOLO, S., ROSA, L., CHAND, N., COSGROVE, D. A., VARKONYI, P., ASAAD, N., TOMASI, S. & BUURMA, N. J. 2018. Quantitative prediction of rate constants for aqueous racemization to avoid pointless stereoselective syntheses. *Angewandte Chemie,* 130**,** 994-997.

BALLARD, A., NARDUOLO, S., AHMAD, H. O., COSGROVE, D. A., LEACH, A. G. & BUURMA, N. J. 2019. The problem of racemization in drug discovery and tools to predict it. *Expert opinion on drug discovery,* 14**,** 527-539.

BECKE, A. D. 1993. Density‐ functional thermochemistry. III. The role of exact exchange. *The Journal of chemical physics,* 98**,** 5648-5652.

CHONG, D., GRITSENKO, O. & BAERENDS, E. 2002. Interpretation of the Kohn–Sham orbital energies as approximate vertical ionization potentials. *The Journal of Chemical Physics,* 116**,** 1760-1772.

FAREGHI‐ ALAMDARI, R., ZANDI, F. & KESHAVARZ, M. H. 2015. A new model for prediction of one electron reduction potential of nitroaryl compounds. *Zeitschrift für anorganische und allgemeine Chemie,* 641**,** 2641-2648.

FRISCH, A., NIELSON, A. & HOLDER, A. 2000. Gaussview user manual. *Gaussian Inc., Pittsburgh, PA,* 556.

FRISCH, M. J., TRUCKS, G. W., SCHLEGEL, H. B., SCUSERIA, G. E., ROBB, M. A., CHEESEMAN, J. R., SCALMANI, G., BARONE, V., PETERSSON, G. A., NAKATSUJI, H., LI, X., CARICATO, M., MARENICH, A. V., BLOINO, J., JANESKO, B. G., GOMPERTS, R., MENNUCCI, B., HRATCHIAN, H. P., ORTIZ, J. V., IZMAYLOV, A. F., SONNENBERG, J. L., WILLIAMS, DING, F., LIPPARINI, F., EGIDI, F., GOINGS, J., PENG, B., PETRONE, A., HENDERSON, T., RANASINGHE, D., ZAKRZEWSKI, V. G., GAO, J., REGA, N., ZHENG, G., LIANG, W., HADA, M., EHARA, M., TOYOTA, K., FUKUDA, R., HASEGAWA, J., ISHIDA, M., NAKAJIMA, T., HONDA, Y., KITAO, O., NAKAI, H., VREVEN, T., THROSSELL, K., MONTGOMERY JR., J. A., PERALTA, J. E., OGLIARO, F., BEARPARK, M. J., HEYD, J. J., BROTHERS, E. N., KUDIN, K. N., STAROVEROV, V. N., KEITH, T. A., KOBAYASHI, R., NORMAND, J., RAGHAVACHARI, K., RENDELL, A. P., BURANT, J. C., IYENGAR, S. S., TOMASI, J., COSSI, M., MILLAM, J. M., KLENE, M., ADAMO, C., CAMMI, R., OCHTERSKI, J. W., MARTIN, R. L., MOROKUMA, K., FARKAS, O., FORESMAN, J. B. & FOX, D. J. 2016. Gaussian 16 Rev. B.01. Wallingford, CT.

GALVÁN, J. E., GIL, D. M., LANÚS, H. E. & ALTABEF, A. B. 2015. Theoretical study on the molecular structure and vibrational properties, NBO and HOMO–LUMO analysis of the POX3 (X= F, Cl, Br, I) series of molecules. *Journal of Molecular Structure,* 1081**,** 536-542.

JAWHAR, Z. S., AHMAD, H. O., HAYDAR, A. A., ABDULLAH, H. A. & MAHAMAD, S. A. 2018. One-Pot Synthesis, Pharmacological Evaluation, Docking Study, and DFT Calculations for Selected Imidazolidine-2, 4-Diones. *Science Journal of University of Zakho,* 6**,** 150-154.

KUBINYI, H., FOLKERS, G. & MARTIN, Y. C. 2006. *3D QSAR in drug design: recent advances,* Springer Science & Business Media.

LOMBARDINO, J. G. & GERBER, C. F. 1964. Preparation and hypoglycemic activity of some 3, 5-disubstituted hydantoins. *Journal of Medicinal chemistry,* 7**,** 97-101.

MORO, S., BACILIERI, M., FERRARI, C. & SPALLUTO, G. 2005. Autocorrelation of molecular electrostatic potential surface properties combined with partial least squares analysis as alternative attractive tool to generate ligand-based 3D-QSARs. *Current drug discovery technologies,* 2**,** 13-21.

RAO, Y. S., PRASAD, M., SRI, N. U. & VEERAIAH, V. 2016. Vibrational (FT-IR, FT-Raman) and UV–Visible spectroscopic studies, HOMO–LUMO, NBO, NLO and MEP analysis of Benzyl (imino (1H-pyrazol-1-yl) methyl) carbamate using DFT calculaions. *Journal of Molecular Structure,* 1108**,** 567-582.

ROCHA, M., DI SANTO, A., ARIAS, J. M., GIL, D. M. & ALTABEF, A. B. 2015. Ab-initio and DFT calculations on molecular structure, NBO, HOMO–LUMO study and a new vibrational analysis of 4-(dimethylamino) benzaldehyde. *Spectrochimica Acta Part A: Molecular and Biomolecular Spectroscopy,* 136**,** 635-643.

SCROCCO, E. & TOMASI, J. 1978. Electronic molecular structure, reactivity and intermolecular forces: an euristic interpretation by means of electrostatic molecular potentials. *Advances in quantum chemistry.* Elsevier.

SHANKAR, R., SENTHILKUMAR, K. & KOLANDAIVEL, P. 2009. Calculation of ionization potential and chemical hardness: a comparative study of different methods. *International Journal of Quantum Chemistry,* 109**,** 764-771.

WARE, E. 1950. The chemistry of the hydantoins. *Chemical Reviews,* 46**,** 403-470.

ZANCO Journal of Pure and Applied Sciences
The official scientific journal of Salahaddin University-Erbil
https://zancojournals.su.edu.krd/index.php/JPAS

ISSN (print):2218-0230**, ISSN (online):** 2412-3986**, DOI: http://dx.doi.org/10.21271/zjpas**

RESEARCH PAPER

Morphological and Molecular Phylogenetic Analyses Reveal a New Record to the Flora of Iraq: *Azolla filiculoides*

Asaad M Mahmood[1], Mohammed I Khalil[1], Khalid F. Darweesh[1]
[1]Department of Biology, College of Education, University of Garmian, Kalar, KRG/Iraq

ABSTRACT:

Azolla filiculoides is an aquatic fern native to Americas. The species has dispersed through Europe and Asia. Recently, it has been identified in northern part of Iran. However, there is no evidence confirms the presence of *Azolla sp.* in Kurdistan region of Iraq. The aim of the present study was to identify the species of *Azolla* found in Tanjaro river/northern part of Iraq. We studied morphological characteristics including trichomes, leaf branches, and three phylogenetic positions such as *rbcl*, *rps4* and *trnG-trnR* of the species. The morphological and phylogeny investigations were compared with other identified species (reference species). Our results showed that the morphological characteristics are more similar to *Azolla filicluloides* than other species. Based on the phylogenetic trees, the position of the observed species was closer to *Azolla filiculoides* than others. These results indicated that the *Azolla* species found in Tanjaro river is more likely *c.*

KEY WORDS: Ferns, *Azolla*, Molecular Markers, Phylogeny, Morphology, Kurdistan, Iraq
DOI: http://dx.doi.org/10.21271/ZJPAS.32.1.10
ZJPAS (2020) , 32(1);95-103 .

1.INTRODUCTION :

Azolla species are small aquatic ferns belong to family Azollaceae, they grow on the surface of fresh water of ponds, lakes or streams, these plants were named for the first time by Lamarck in 1783 (Sood et al., 2008, Papaefthimiou et al., 2008). *Azolla* is associated symbiotically with prokaryotic cyanobacterium conferring high rates of nitrogen fixation, which is used as a biofertilizer with rice crops in several countries specifically in Asia (Bhuvaneshwari and Singh, 2015, Papaefthimiou et al., 2008). Based on its morphological and reproductive patterns, *Azolla* has seven distinct species that are grouped into two sections including Rhizosperma and Euazolla. The first section includes *A. nilotica and A. pinnata* (Plazinski et al., 1988), whereas the latter section consists of five species of *Azolla*, namely *A. filiculoides*, *A. caroliniana*, *A. mexicana*, *A. rubra*, *A. microphylla* (Lumpkin and Plucknett, 1980). Following the introduction of *Azolla*, it is readily transported locally by activities of human, animal and waterfowl that they are subsequently considered facilitators (Brochet et al., 2009).

Previous molecular studies have suggested a taxonomic treatment according to the recognition of the two above-stated sections only (Pereira et al., 2011). The knowledge of fern biology and the processes that govern the evolution of land plants and specifically ferns are limited because of a dearth of genomic information. The genome of *A. . filicluoides* is relatively 0.75 Gb (Obermayer et al., 2002), a characteristic distingush them from other ferns, a group which is notorious for large genomes that are averagely 12 Gb (Sessa and Der, 2016). Many studies use plastid intergenic (*trnG-trnL*), and genes (*rps4* and *rbcL*) sequences to do phylogentic analysis and allow us to better

---

* **Corresponding Author:**
Asaad M Mahmood1
E-mail: asaad@garmian.edu.krd
Article History:
Received: 18/09/2019
Accepted: 24/10/2019
Published: 25/02 /2020

identify a certain species of *A*zolla in relation with other species (Metzgar et al., 2007, Lu et al., 2015, Madeira et al., 2019). The most notorious member of this group of ferns, *A. filiculoides* is the most damaging invasive alien in several parts of the world. This species has been introduced into parts of Africa, South East Asia and northern Iran for use as a natural biofertilizer for rice (Lumpkin and Plucknett, 1980). However, there is no previous evidence confirming the presence of *Azolla* into northern parts of Iraq.

Proper identification of the host and invasive *Azolla sp.* is critical in biological control studies and conservation strategies (Madeira et al., 2016). However, the identification of *Azolla sp.* is notoriously difficult (Evrard and Van Hove, 2004). Morphological similarity and diminutive stature of *Azolla sp.* have caused a long history of mistaken identifications and have occasionally led to taxonomic confusion (Reid et al., 2006). Fortunately, numerous molecular taxonomies for *Azolla sp.* have been investigated in recent years. Such publications have helped scientists to clarify the taxonomy, and have also provided molecular barcodes for the identification of field samples of *Azolla* (Lu et al., 2015, Madeira et al., 2016, Li et al., 2018, Madeira et al., 2019)

The aim of the present study was to confirm a thorough morphological and molecular analysis of *Azolla* in the north part of Iraq in order to understand which species is present. This identification is of importance to reveal a new plant of the flora of Iraq and to world map of ferns, specifically *Azolla sp.*

2. MATERIALS AND METHODS

2.1. Study Area

Samples of the aquatic fern *Azolla* sp. were collected from three different sites of freshwater of an irrigation drainage of Sharazoor area at different times (figure 1, A and B). The collection sites are specifically located in the Northern part of Iraq, Kurdistan Region, Al-Sulaymaniyah Governorate. Its latitude is 35.566864 with a longitude of 45.416107. The Global Positioning System (GPS) data of Al-Sulaymaniyah governorate is 35° 34' 0.7104" N and 45° 24' 57.9852" E. Geographic positions of the collection sites were recorded using GPS (Garmin 72, USA). The respective sample was collected in the field where located specifically on Tanjaro river (Figure 2).

Figure 1. Density of the *Azolla* sp. in the studied area, (A) Dense mat (B) thin mat of *Azolla*

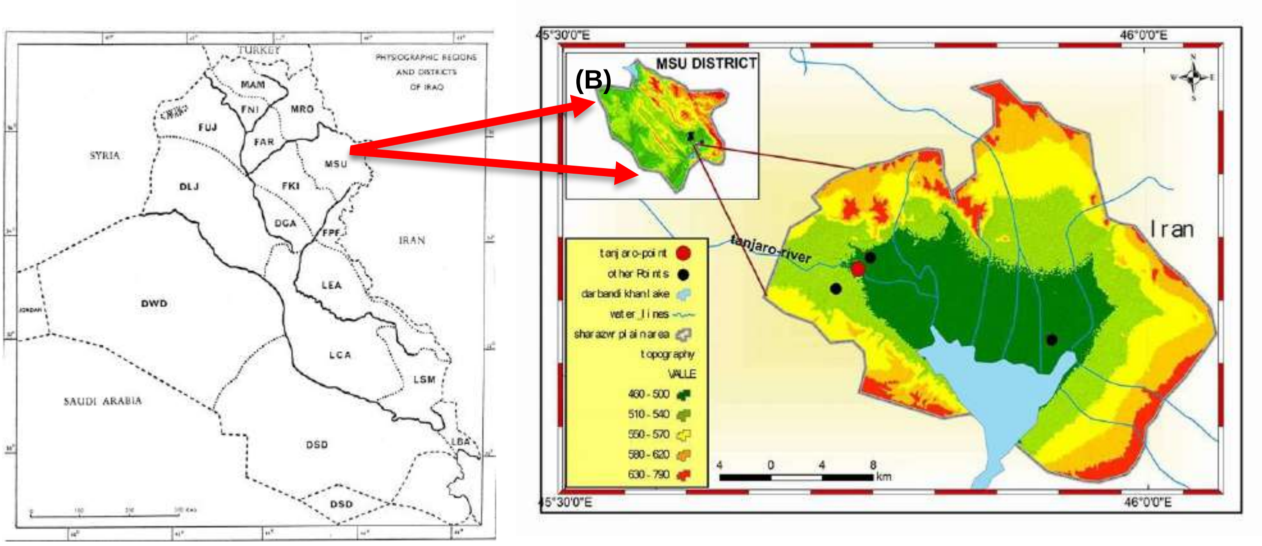

Figure 2: (A) Map of physiographic regions and districts of Iraq (Guest et al., 1966), (B) the geographic distribution map of the studied *Azolla sp.* in MSU (Sulaimania district)

2.2. Morphological Study

Trichomes, leaf branches, leaf surfaces and leaf margin shapes were morphologically examined using the stereo microscope (Meiji Model RZ, USA). In addition, in terms of getting a new herbarium number, a part of the sample was preserved in 70% Ethyl alcohol and subsequently sent to the Iraqi National Herbarium, Ministry of Agriculture-Baghdad.

2.3. Molecular Phylogeny Analysis

DNeasy® Plant Mini kit (Qiagen, UK) was used to extract DNA from the studied sample following the manufacturer's instructions. According to protocols that were previously established (Pryer et al., 2004, Metzgar et al., 2007), three plastidal amplifications (Table 1), *rbcl*, *rps4* and *trnG-trnR* were attempted for the respective sample using the polymerase chain reaction (PCR) (Eppendorf™ Mastercycler™ Nexus Thermal Cycler). The PCR reaction was a mixture of 20 µl containing 10 ng (2 µl) of the template, 10 µl 2X BioMix PCR master mix (Bioline, UK,), 6 µl (10 pmol) of forward and reverse primer (German) and 2 µl of free RNAse water with the following steps: one cycle at 95 °C for 5 min; 35 cycles at 95 °C for 30 s, 56 °C for 30 s, 72 °C for 1 min; and ended with one cycle at 72 °C for 10 min. PCR reactions were run at 90 volts for 45 minutes in a horizontal gel electrophoresis unit (Fisher scientific, USA). The gel was visualized under a UV lamp and followed by capturing a clear picture using a Nikon digital camera.

PCR products were purified and sequenced, the sequencing reactions were investigated for both strands of all three purified PCR products using HiSeq4000 (Illumina, San Diego, USA) of Macrogen Inc., Korea. Information of primers used for amplification and sequencing reactions are shown in table 1.

All sequences were examined and aligned for identities and contaminations using the National Center for Biotechnology Information nucleotide-nucleotide BLAST (blastn) search (Altschul et al., 1997) table 2. To construct phylogenetic trees, DNA sequences were aligned using Clustal W in Bioedit version 7.0.5.3 (Hall, 1999). The alignments include 1595 bp (rbcL), 308 bp (rps4), and 1080 bp (trnG-trnR). The aligned genetic sequences were concatenated into one mega database using Mesquite (Maddison and Maddison, 2018). The phylogenetic trees were built using Mega X software version 10.1 (Kumar et al., 2018). The maximum likelihood tree was produced using Hasegawa-Kishino-Yano with Gamma distribution (HKY+G) model as best fit substitution model (it had low Corrected Akaike information criterion value in compare with other models).

Initial tree(s) for the heuristic search were obtained automatically by applying Neighbor-Join and BioNJ algorithms to a matrix of pairwise distances estimated using the Maximum Composite Likelihood (MCL) approach, and then selecting the topology with superior log likelihood value. A discrete Gamma distribution was used to model evolutionary rate differences among sites (5 categories (+G, parameter = 0.3444)) Maximum parsimony tree was generated using 500 replicates with Subtree-Pruning-Regrafting (SPR) algorithm (Nei and Kumar, 2000). The initial trees were obtained by the random addition of sequences (10 replicates). The analysis involved 7 nucleotide sequences. The Neighbor-Joining (NJ) tree was built using Neighbor-Joining method (Saitou and Nei, 1987). The evolutionary distances were computed using the Maximum Composite Likelihood method (Tamura et al., 2004).

Table 1: Primers used to amplifying and sequencing DNA amplicons in *Azolla sp*. retrieved from (Metzgar et al., 2007).

Locus	Primer	Sequence (5' to 3')	Amplicon size (bp)
rbcL	ESRBCL1F ESRBCL1361R	ATGTCACCACAAACGGAGACTAAAGC TCAGGACTCCACTTACTAGCTTCACG	**1300**
rps4	RPS5F TRNSR	ATGTCCCGTTATCGAGGACCT TACCGAGGGTTCGAATC	**1200**
trnG-trnR	TRNG1F TRNG63R	GCGGGTATAGTTTAGTGGTAA GCGGGAATCGAACCCGCATCA	**1300**
	TRNG353R TRNR22R	TTGCTTMTAYGACTCGGTG CTATCCATTAGACGATGGACG	**1200**

Table 2. GeneBank accession number of the species used in this study. All species had *trnG-trnR, rbcL, and rps4* genetic sequences in genebank. Except *Azolla nilotica* had only *rps4*. The symbol (×) means no genetic information exist in genebank.

No.	Species	*trnG-trnR*	rbcL	rps4
1.	*A.filiculoides*	JX280884.1	KM360662.1	EF520913.1
2.	*A. caroliniana*	EF520894.1	EF520919.1	EF520906.1
3.	*A. pinnata*	EF520902.1	AM177355.1	EF520907.1
4.	*A. nilotica*	×	×	EF520912.1
5.	*A. mexicana*	EF520897.1	EF520922.1	EF520911.1
6.	*A. microphylla*	EF520896.1	EF520921.1	EF520908.1

3. RESULTS

Morphological results of the present study were observed that the trichome types were unicellular, although bicellular trichomes are rarely recognized on the upper leaf lobe of the studied species (figure 3, A). In addition, green, yellowish or dark-red in colour, adventitious roots, branched protostelic stem and two rows tile-like bilobate leaves are morphological characteristics of the studied *Azolla* (figure 1, A and B, and figure 3, B, C and D).

In addition, clear sequences of the respective genes were used to produce phylogenetic trees in order to genetically identify the studied species of *Azolla*. Results showed that the most likely tree

(Figure 4) produced from maximum likelihood (ML) analysis of the combined genetic sequences (*rbcl*, *rps4* and *trnG-trnR*) was well resolved (bootstrap test, 500 replicates). Based on ML tree, *Azolla sp.* is sister to *A. filiculoides* (bootstrap value=64%).

In addition, the most parsimonious tree (388 steps. consistency index= 0.828125, retention index = 0.810345), and composite index = 0.787371) (Figure 5) built from maximum parsimony analysis where all the branches were well resolved (no polytomies, Bootstrap values ≥ 50 %). Results also showed that position of *A.* species is in the same clade where *A. pinnata*, *A. nilotica, and A. filiculoides* are exist and it is much closer to the latter species than others.

In a similar pattern with parsimony tree, the Neighbor-Joining tree (Figure 6) also revealed that the position of *Azolla sp.* is in the same clade of *A. filiculoides*, *A. nilotica, and A. pinnata*. The branch of *Azolla sp.* and *A. filiculoides* is considerably resolved (polytomy, Bootstrap value <50 %).

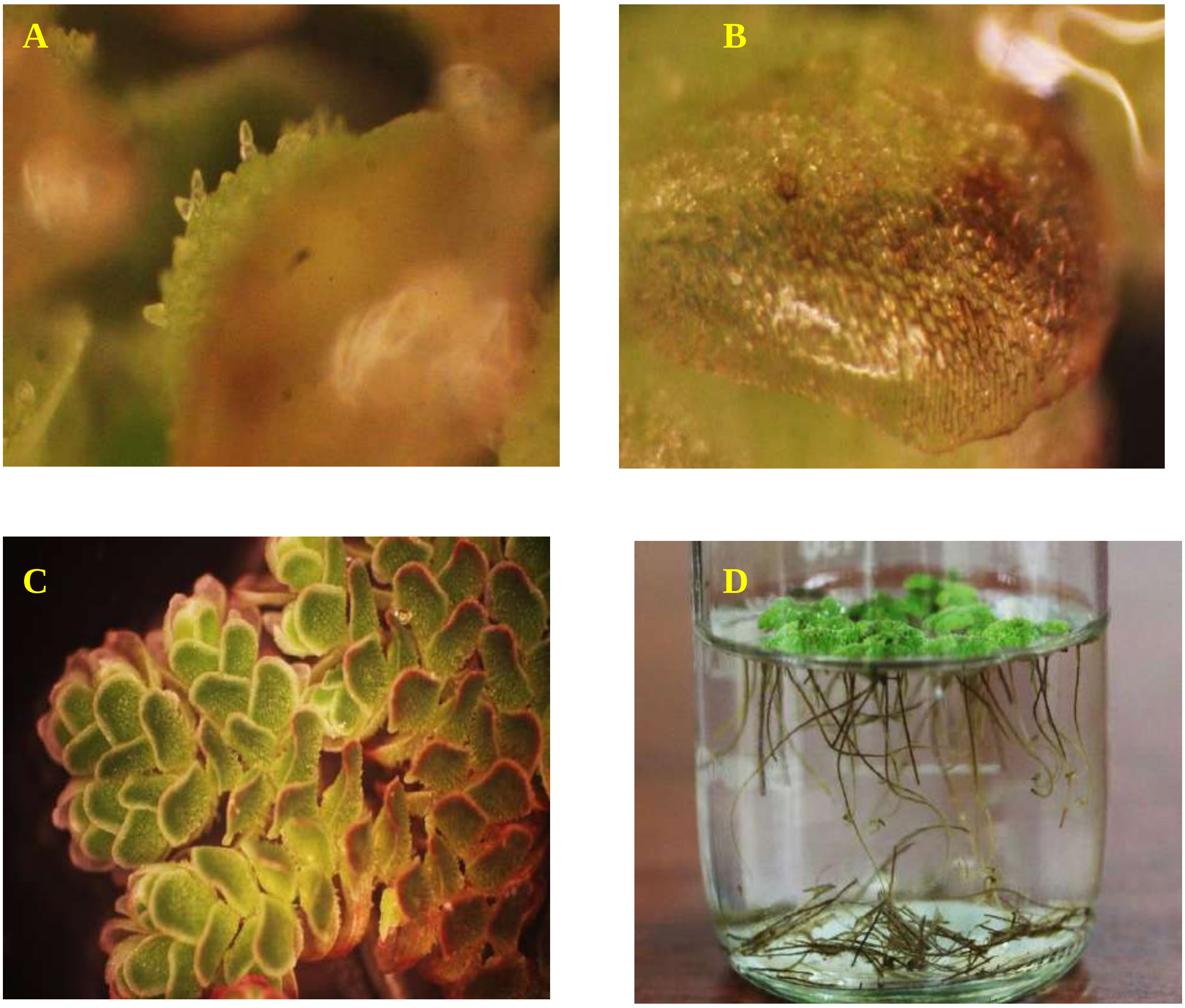

Figure 3: (A) leaf surface, (B) unicellular and bicellular trichomes, (C) branching pattern and leaf margins, (D) root length of *Azolla sp.*

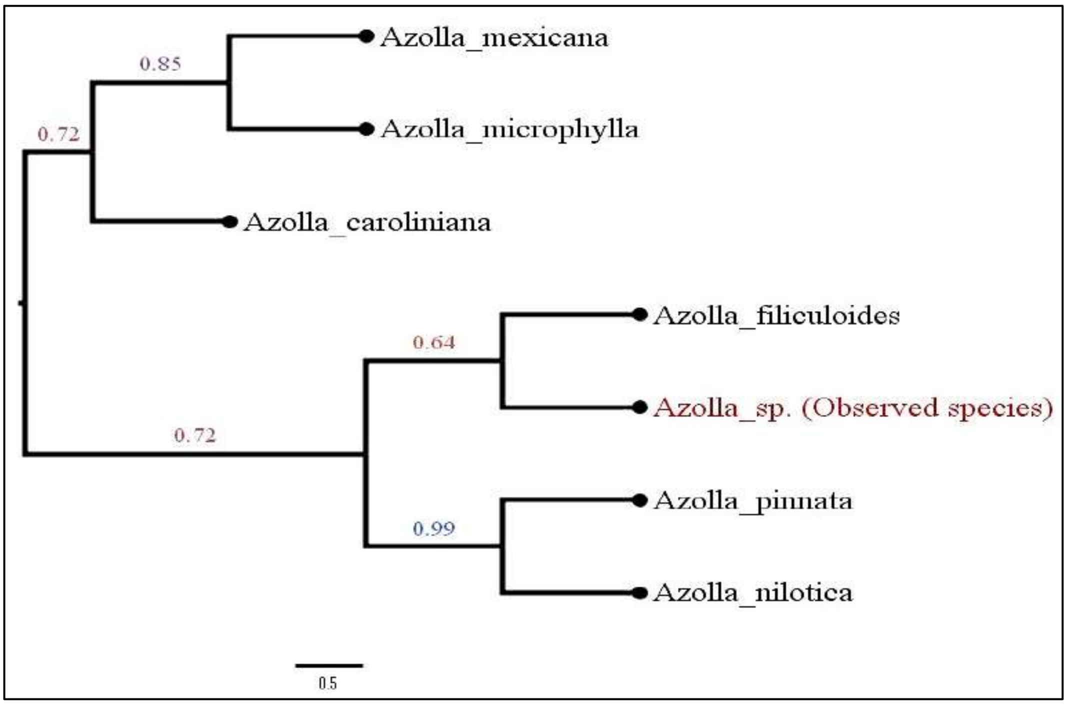

Figure 4. Maximum Likelihood method based on the Tamura-Nei model. The percentage of replicate trees in which the associated taxa clustered together in the bootstrap test (500 replicates) are shown next to the branches. The analysis involved 7 nucleotide sequences. Codon positions included were 1st+2nd+3rd+Noncoding. There were a total of 2985 positions in the final dataset.

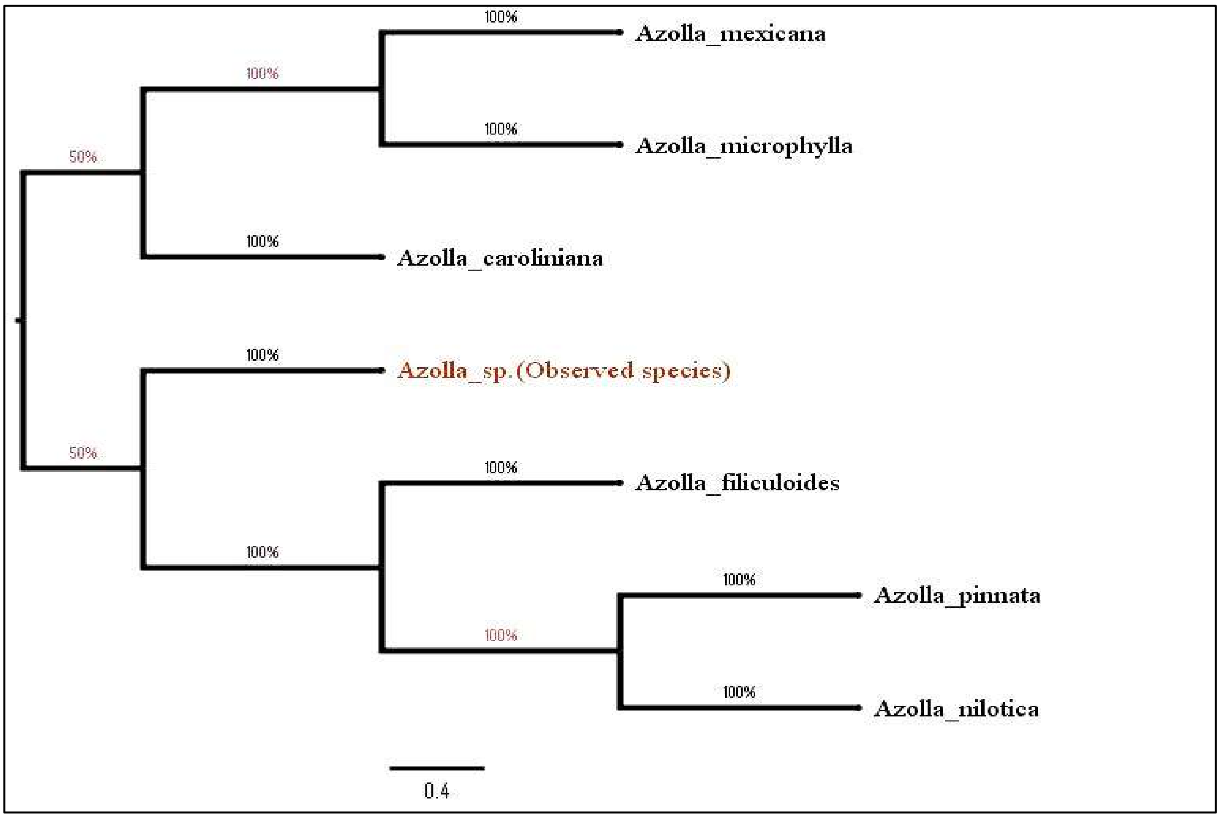

Figure 5. Maximum parsimony tree. The percentage of replicate trees in which the associated taxa clustered together in the bootstrap test (500 replicates) are shown next to the branches. The analysis involved 7 nucleotide sequences. Codon positions included were 1st+2nd+3rd+Noncoding. There were a total of 2985 positions in the final dataset.

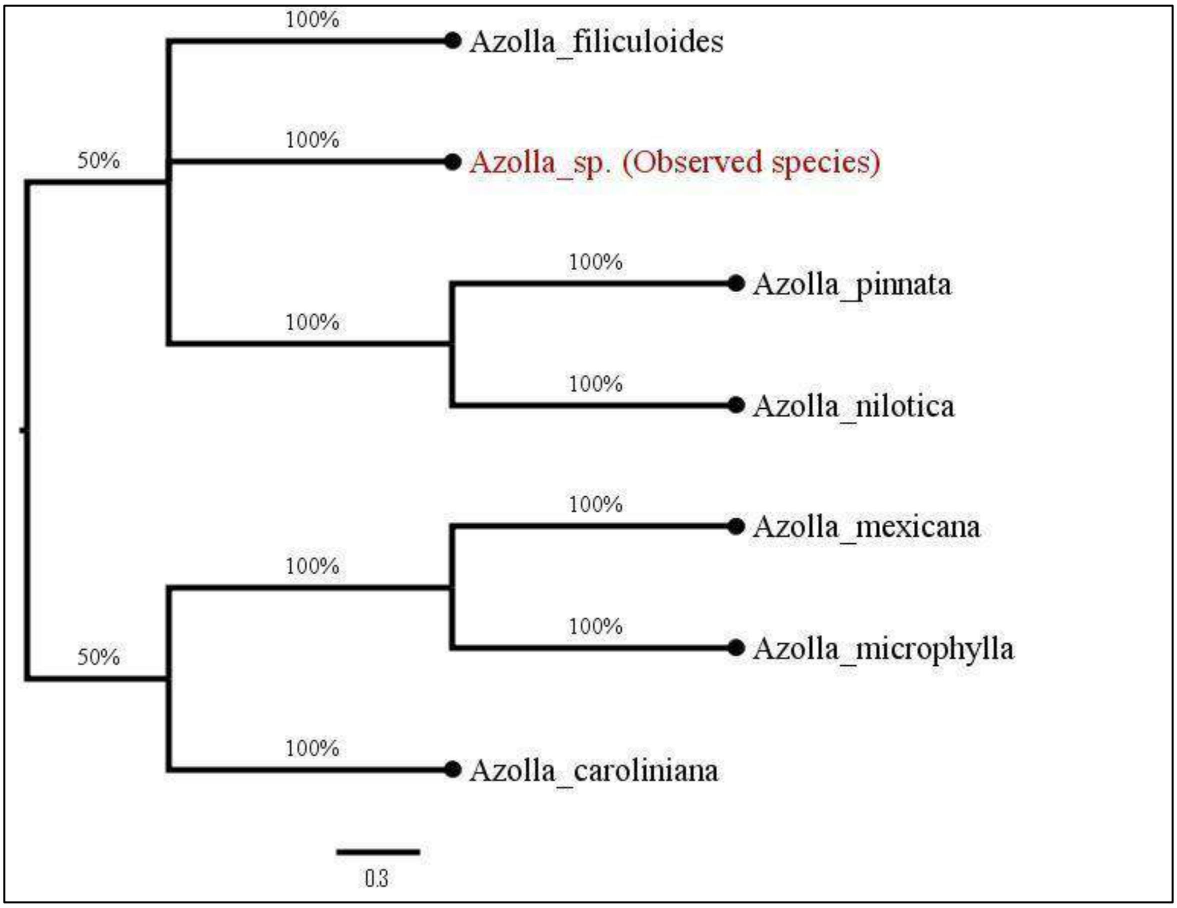

Figure 6. Neighbor-Joining tree. The percentage of replicate trees in which the associated taxa clustered together in the bootstrap test (500 replicates) are shown next to the branches. The analysis involved 7 nucleotide sequences. Codon positions included were 1st+2nd+3rd+Noncoding. There were a total of 2985 positions in the final dataset.

4. DISCUSSION

The existence of this plant has never been recorded in Iraq and it has probably aliened or invaded the region at least 20 years ago. According to our investigations with local farmers, it is confirmed that this plant exists in the study area since 1996. The respective *Azolla sp.* had been successfully registered at the National Herbarium of Iraq and had been given the specimen number 58730. Despite the registration of the studied fern, there were no clear evidence confirms its species type. Previous studies have shown a large consensus in regards to the unique status of *A. filiculoides*, which is the presence of unicellular trichomes on upper leaf lobes (Evrard and Van Hove, 2004). However, trichome structures of each *A. caroliniana, A. mexicana, A. microphylla* have nearly been characterized to be bicellular (Lumpkin and Plucknett, 1982, Jonsell, 2000). Although the cellular number(s) of the respective *Azolla* is dubitable, leaf branches and leaf surfaces, root pattern, leave colours indicate that this species is more likely A. *filiculoides* (Myśliwy and Szlauer-Łukaszewska, 2017).

Morphological results were mostly similar to previous studies of *A. filiculoides*, but making decision in regards to the species type of the respective *Azolla* is relatively hard. To overcome this issue, phylogenetic analysis was investigated considering three position of the chloroplast DNA.

Based on phylogenetic and morphological results, it is indicated that the *Azolla* species found in Tanjaro River is more likely *Azolla filiculoides*. According to maximum likelihood (ML) tree (figure 4), the respective species of *Azolla* is more closely related to *Azolla filiculoides* (collected form GeneBank) than other species. In addition, the result of Maximum Parsimony (MP) and

Neighbor-Joining (NJ) trees (Figure 5 and 6) confirm that what ML tree revealed, in which the *Azolla* in the Tanjero River is *Azolla filiculoides*. The existence of such wetland exotic species (non-native species) for the first time in the study area could be due to many reasons. For example, the climatic conditions of the river could be optimum for their growth and propagations. The existence of same species has been observed in north of Iran (Hashemloian and Azimi, 2009). The study area is adjacent to the northern part of Iran. This means that the species might been dispersed through water from Iran to north of Iraq. The other factor behind the species dispersal is human activities such as trading, tourism and animal. The role of migratory ducks in the long-distance dispersal of native plants and the spread of exotic plants in Europe (Brochet et al., 2009). The introduction of this new species into Kurdistan/Iraq flora has useful and harmful patterns at same time. It could be useful by providing ecological benefits to the river. For example, this species is a good nitrogen fixer and it can purify the water from heavy metals (Brouwer et al., 2018). In addition, it could be a good replacer of protein for fishes (Mosha, 2018). On the other hand, the high dispersal rate of the species within a short period may compete other aquatic species and vanish them from their natural habitat (Myśliwy and Szlauer-Łukaszewska, 2017).

5. CONCLUSION

In conclusion, this study has shown the importance of incorporating phylogenetic analyses beside morphological studies in taxonomic studies. The existence of *Azolla filiculoides* in north Iraq add a new record to flora of Iraq. This new record has two benefits: increasing the plant biodiversity in Iraq and for ecological and agricultural managements. This finding might pave the way for ecologists to do further works on such species. For example, species richness, estimation the invasive status of the species and its effects on availability of water and soil nitrogen. Furthermore, the existence of such species in the rivers will improve the growth of fishes. Fisheries can use this species as a natural protein source instead of commercial one to propagate their wealth.

REFERENCES

ALTSCHUL, S. F., MADDEN, T. L., SCHÄFFER, A. A., ZHANG, J., ZHANG, Z., MILLER, W. & LIPMAN, D. J. 1997. Gapped BLAST and PSI-BLAST: a new generation of protein database search programs. *Nucleic Acids Research,* 25**,** 3389-3402.

BHUVANESHWARI, K. & SINGH, P. K. 2015. Response of nitrogen-fixing water fern Azolla biofertilization to rice crop. *3 Biotech,* 5**,** 523-529.

BROCHET, A. L., GUILLEMAIN, M., FRITZ, H., GAUTHIER- CLERC, M. & GREEN, A. J. 2009. The role of migratory ducks in the long- distance dispersal of native plants and the spread of exotic plants in Europe. *Ecography,* 32**,** 919-928.

BROUWER, P., SCHLUEPMANN, H., NIEROP, K. G., ELDERSON, J., BIJL, P. K., VAN DER MEER, I., DE VISSER, W., REICHART, G. J., SMEEKENS, S. & VAN DER WERF, A. 2018. Growing Azolla to produce sustainable protein feed: the effect of differing species and CO2 concentrations on biomass productivity and chemical composition. *Journal of the Science of Food and Agriculture,* 98**,** 4759-4768.

EVRARD, C. & VAN HOVE, C. 2004. Taxonomy of the American *Azolla species* (Azollaceae): a critical review. *Systematics and Geography of Plants***,** 301-318.

HALL, T. A. BioEdit: a user-friendly biological sequence alignment editor and analysis program for Windows 95/98/NT. Nucleic Acids Symposium Series, 1999. [London]: Information Retrieval Ltd., c1979-c2000., 95-98.

HASHEMLOIAN, B. D. & AZIMI, A. A. 2009. Alien and exotic Azolla in northern Iran. *African Journal of Biotechnology,* 8.

JONSELL, B. 2000. *Azolla Lam*. *Flora Nordica,* 1**,** 89.

KUMAR, S., STECHER, G., LI, M., KNYAZ, C. & TAMURA, K. 2018. MEGA X: molecular evolutionary genetics analysis across computing platforms. *Molecular Biology and Evolution,* 35**,** 1547-1549.

LI, F.-W., BROUWER, P., CARRETERO-PAULET, L., CHENG, S., DE VRIES, J., DELAUX, P.-M., EILY, A., KOPPERS, N., KUO, L.-Y. & LI, Z. 2018. Fern genomes elucidate land plant evolution and cyanobacterial symbioses. *Nature Plants,* 4**,** 460.

LU, J. M., ZHANG, N., DU, X. Y., WEN, J. & LI, D. Z. 2015. Chloroplast phylogenomics resolves key relationships in ferns. *Journal of Systematics and Evolution,* 53**,** 448-457.

LUMPKIN, T. A. & PLUCKNETT, D. L. 1980. Azolla: botany, physiology, and use as a green manure. *Economic Botany,* 34**,** 111-153.

LUMPKIN, T. A. & PLUCKNETT, D. L. 1982. *Azolla as a green manure: use and management in crop production*, Westview Press, Inc.

MADDISON, W. & MADDISON, D. 2018. Mesquite: a modular system for evolutionary analysis Version 3.40 2018.

MADEIRA, P. T., DRAY JR, F. A. & TIPPING, P. W. 2019. Molecular identification of Azolla in the Yangtze River Watershed, China. *Aquatic Botany***,** 103149.

MADEIRA, P. T., HILL, M. P., DRAY JR, F., COETZEE, J., PATERSON, I. & TIPPING, P. 2016. Molecular identification of Azolla invasions in Africa: The Azolla specialist, Stenopelmus rufinasus proves to be an excellent taxonomist. *South African Journal of Botany,* 105**,** 299-305.

METZGAR, J. S., SCHNEIDER, H. & PRYER, K. M. 2007. Phylogeny and divergence time estimates for the fern genus *Azolla* (Salviniaceae). *International Journal of Plant Sciences,* 168**,** 1045-1053.

MOSHA, S. 2018. A Review on Significance of *Azolla* Meal as a Protein Plant Source in Finfish Culture. *J Aquac Res Development,* 9**,** 2.

MYŚLIWY, M. & SZLAUER-ŁUKASZEWSKA, A. 2017. Fern Azolla filiculoides at New Sites in Oder River (Poland)—Invader or Ephemeral? *Polish Journal of Ecology,* 65**,** 405-415.

NEI, M. & KUMAR, S. 2000. *Molecular evolution and phylogenetics,* Oxford university press.

OBERMAYER, R., LEITCH, I. J., HANSON, L. & BENNETT, M. D. 2002. Nuclear DNA C‐ values in 30 species double the familial representation in pteridophytes. *Annals of Botany,* 90**,** 209-217.

PAPAEFTHIMIOU, D., VAN HOVE, C., LEJEUNE, A., RASMUSSEN, U. & WILMOTTE, A. 2008. Diversity and host specificity of azolla cyanobionts 1. *Journal of Phycology,* 44**,** 60-70.

PEREIRA, A. L., MARTINS, M., OLIVEIRA, M. M. & CARRAPIÇO, F. 2011. Morphological and genetic diversity of the family Azollaceae inferred from vegetative characters and RAPD markers. *Plant Systematics and Evolution,* 297**,** 213-226.

PLAZINSKI, J., FRANCHE, C., LIU, C.-C., LIN, T., SHAW, W., GUNNING, B. & ROLFE, B. 1988. Taxonomic status ofAnabaena azollae: An overview. *Plant and Soil,* 108**,** 185-190.

PRYER, K. M., SCHUETTPELZ, E., WOLF, P. G., SCHNEIDER, H., SMITH, A. R. & CRANFILL, R. 2004. Phylogeny and evolution of ferns (monilophytes) with a focus on the early leptosporangiate divergences. *American Journal of Botany,* 91**,** 1582-1598.

REID, J. D., PLUNKETT, G. M. & PETERS, G. A. 2006. Phylogenetic relationships in the heterosporous fern genus *Azolla* (Azollaceae) based on DNA sequence data from three noncoding regions. *International Journal of Plant Sciences,* 167**,** 529-538.

SAITOU, N. & NEI, M. 1987. The neighbor-joining method: a new method for reconstructing phylogenetic trees. *Molecular Biology and Evolution,* 4**,** 406-425.

SESSA, E. & DER, J. 2016. Evolutionary genomics of ferns and lycophytes. *Advances in Botanical Research.* Elsevier.

SOOD, A., PRASANNA, R., PRASANNA, B. & SINGH, P. 2008. Genetic diversity among and within cultured cyanobionts of diverse species of Azolla. *Folia Microbiologica,* 53**,** 35.

TAMURA, K., NEI, M. & KUMAR, S. 2004. Prospects for inferring very large phylogenies by using the neighbor-joining method. *Proceedings of the National Academy of Sciences,* 101**,** 11030-11035.

ZANCO Journal of Pure and Applied Sciences
The official scientific journal of Salahaddin University-Erbil
https://zancojournals.su.edu.krd/index.php/JPAS

ISSN (print):2218-0230, **ISSN (online):** 2412-3986, **DOI:** **http://dx.doi.org/10.21271/zjpas**

RESEARCH PAPER

Synthesis and characterization complexes of bis (2-mercaptobenzimidazole) mercury (II) with transition metal (Ni (II), Pd (II), and Pt (II))

Nhiyat H. Hassan[1], Hikmat A. Mohammad[2]

[1,2]Department of Chemistry, College of Education, University of Salahaddin-Erbil, Kurdistan Region, Iraq

ABSTRACT:

Treatment of 2-Mercaptobenzimidazol (HL) with the mercuric acetate ($Hg(OAc)_2$) give the complex[$Hg(L)_2$] **(1).** Then the multinuclear complexes of the type [$M_2Hg_2(L)_4Cl_4$] were prepared through the reaction of complex **(1)** with each of $NiCl_2.6H_2O$, $PdCl_2$ and $PtCl_2$ in (2:2) molar ratio. All complexes were described using infrared spectra, Proton Nuclear Magnetic Resonance , Carbon 13- Nuclear Magnetic Resonance , ultraviolet-visible, atomic absorption spectroscopy, CHNS analysis, molar conductivity, determination of Chloride Percentage and magnetic susceptibility measurements.The heterocyclic ligand is expected to be coordinated to two or single metal atom through the nitrogen atom and sulphur atom or by only sulphur atom.

KEY WORDS: 2-Mercapto benzimidazole: Ni (II), Pd (II), Pt (II), Hg(II).
DOI: http://dx.doi.org/10.21271/ZJPAS.32.1.11
ZJPAS (2020) , 32(1);104-109 .

INTRODUCTION :

The coordination chemistry of heterocyclic thiones has attracted a large attention for their potentially ambidentate or multi-group donor capacity. Either the exocyclic S or heterocyclic N(or S)atoms are ready for connected to form complexes with transition metals and the possibility exists that coordination with harmful metal ions in an organism could occur (Rafael et al., 2002).

Heterocyclic compounds that containing thiones form complexes with many metal ions and this have been known for many years ago (Aranzazu et al., 2006).

They are characterized by thione-thiol tautomerism (Rapper et al., 1984). Transformation thiol to thione is significant from the point of heterocyclic compound (Obot et al., 2014). Those ligands which containing sulphur, especially thiolates, are widely applied as briding ligands in the design of transition-metal (Shan et al., 2010), Structure (1)

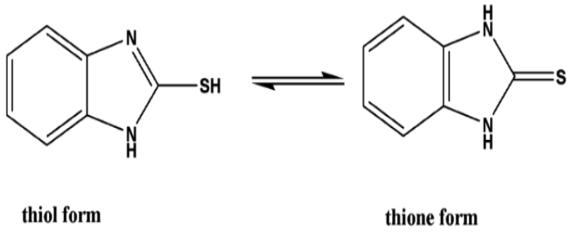

Structure (1) Tautomerism of benzimidazole-2-thione to thiol

1. MATERIALS AND METHODS

---

* **Corresponding Author:**
Nhiyat. H. Hassan
E-mail: nhiyat.hassan@su.edu.krd
Article History:
Received: 25/04/2019
Accepted: 03/10/2019
Published:25/02/2020

All materials ($NiCl_2.6H_2O$, Palladium (II) chloride, Platinum (II) chloride, 2-Mercaptobenzimidazol (HL)) were obtained from Yahoo Chem. China. The Shimadzu infrared spectrophotometer in the range 400-4000 cm^{-1} was used to record the infrared (IR) spectra through using KBr discs. Furthermore, for detecting the Far IR spectra, the pye Unicam 300s was used in the range 200-4000 cm^{-1} by means of CsI discs. Additionally, to detect the (^1H, and ^{13}C)-NMR spectra, we used a Bruker 300 MHZ Ultra-shied. While an Ultraviolet-Visible spectrometer, AE-UV1609 (UK) CO was utilized to record Electronic spectra. To measure the conductivity of all complexes, we used a conductivity meter 4200 (0.93 cell constant) (UK). Elemental Analyzer, Atomic absorption spectra were recorded on a pye unicam sp(flam-AAS). The Magnetic susceptibility data were measured on a Bruker BM6 instrument at 25 ^oC following the faraday method.

1.1 Synthesis of $[Hg(L)_2]$ Complex (1)

A solution (Zora et al., 2002) of 2-mercaptobenzimidazloe (HL) (0.4g, 2.73 mmol) in 30 ml of MeOH was added slowly to a solution of mercuric acetate ($Hg(OAc)_2$) (0.4 g, 1.26 mmol) in 30 ml of MeOH solution. Then filtered off the colorless crystalline that formed, after that cleaned with cold MeOH and dried in air. (Formula: $C_{14}N_4H_{10}S_2Hg$, Yield: 0.5g, 80%, d.p.:252-255 ^oC, Color: White)

1.2 Preparation of $[M_2Hg_2(L)_4Cl_4]$ Complexes (2,3,4)

This type of the complexes (Butrus et al., 2012) were prepared by reaction (2mmol) of metal chloride salts with (0.4g) $NiCl_2.6H_2O$ dissolved in 10ml of ethanol, and (0.3g) $PdCl_2$, (0.5g) $PtCl_2$ was suspended in 10ml methanol to a solution include (0.99g,2mmol) $[Hg(L)_2]$ in 10ml of DMSO , the blend was stirred at 25^oC for four days. The coloured precipitation was formed, filtered-off, washed with di ethyl ether and dried in an oven at 50 ^oC. (formula: $C_{28}H_{20}N_8S_4Hg_2Ni_2Cl_4$, Yield: 1g, 40% , d.p..: 261-265 ^oC, Color: Orange, $C_{28}H_{20}N_8S_4Hg_2Pd_2Cl_4$, Yield: 1.1g, 38.4% , d.p..: 272-275 ^oC, Color: Brown, $C_{28}H_{20}N_8S_4Hg_2Pt_2Cl_4$, Yield: 1.1g, 39.2% , d.p..: 255-260 ^oC, Color: Green).

Table(1) Physical parameters(such as colors, molecular weight, melting points, yield) for the prepared complexes **.**

No .	Complexes symbol	Color	M.Wt g/mol	d.p.(°C)	Yield %
1	$[Hg(L)_2]$	White	498	252-255	80
2	$[Ni_2Hg_2(L)_4Cl_4]$	Orange	1252	261-265	40
3	$[Pd_2Hg_2(L)_4Cl_4]$	Brown	1350.6	275-272	38.4
4	$[Pt_2Hg_2(L)_4Cl_4]$	Green	1526	260-255	39.2

Table (2) Elemental analysis for the prepared complexes **.**

No.	Complexes symbol	C	H	N	S	Hg	Ni	Pd	Pt	cl
1	$[Hg(L)_2]$	--	--	--	--	--	--	--	--	--
2	$[Ni_2Hg_2(L)_4Cl_4]$	26.7 (25.98)	1.5 (1.77)	8.9 (8.87)	10.1 (10.30)	31.9 (31.38)	9.3			11.3 (11.5)
3	$[Pd_2Hg_2(L)_4Cl_4]$	24.8 (23.91)	1.4 (1.52)	8.2 (8.27)	9.4 (9.55)	29.7 (29.81)		15.7		10.5 (10.61)
4	$[Pt_2Hg_2(L)_4Cl_4]$	22 (21.88)	1.3 (1.29)	7.3 (7.39)	8.3 (8.48)	26.2 (---)			25.5	9.3 (9.6)

2. RESULTS AND DISCUSSION

2.1 Analysis of elements for prepared complexes

The elemental analysis data of the C, H, N, S, Ni, Pd, Pt, Hg and Cl of the prepared complexes are presented in Table 1. These data are in consistent with the propose stoichiometry's. Table 1 shows physical parameters such as colors, molecular weight and melting points of the prepared complexes.

2.2 Ultraviolet-visible and Magnetic Susceptibility of the Prepared Complexes

For all complexes, the uv.vis spectra were done in DMSO (10^{-3} M) solution at 25 °C.

The electronic spectrum of complex (1) **[Hg(L)$_2$]** two bands observed at (37037 and 32258) cm^{-1}, these transitions bands were attributed to Metal-ligand charge transfer transitions of Hg(II) in linear geometry (Kennedy et al., 1972).

The electronic spectrum of complex (2) **[Ni$_2$Hg$_2$(L)$_4$Cl$_4$]** Ni^{+2} gave two high intensity bands at 18518cm^{-1} and 22300 were attributed to transitions $^1A_1g \longrightarrow {}^1A_2g$ and $^1A_1g \longrightarrow {}^1B_1g$ respectively, both transitions are in a square planar geometry. Other high energy band keep an eye on at 37037 cm^{-1} which assigned to Ni^{+2} $\longrightarrow$ C=N charge transfer transition (Sutton , 1968, Leka et al., 2005, AI-Adeli, 2009, Mohammed et al., 2011, Nanhai et al., 2001, Tariq, 2013).

The ultra-visible spectrum of complex(3) **[Pd$_2$Hg$_2$(L)$_4$Cl$_4$]**, Pd^{+2} gave three spin allowed transitions at 18181cm^{-1}, 22321 cm^{-1} and 25000 cm^{-1} were attributed to $^1A_1g \longrightarrow {}^1A_2g$, $^1A_1g \longrightarrow {}^1B_1g$ and $^1A_1g \longrightarrow {}^1Eg$ transitions respectively. Other high energy band observed at 31250 cm^{-1} is assigned to Pd^{+2} $\longrightarrow$ C=N charge transfer transition, these transitions are reasonable to square planar geometry of the complexes (Sutton ,1968, Leka et al., 2005, Ali, 2007, Ibrahem et al., 2008).

The electronic spectrum of complex(4) **[Pt$_2$Hg$_2$(L)$_4$Cl$_4$]**; Pt^{+2} gave three high intensity bands at 18115 cm^{-1}, 20000 cm^{-1} and 23809 cm^{-1} were assigned to transitions $^1A_1g \longrightarrow {}^3B_1g$, $^1A_1g \longrightarrow {}^1A_2g$ and $^1A_1g \longrightarrow {}^1B_1g$ respectively,. Other high energy band appear at 34482 cm^{-1} are assigned to Pt^{+2} $\longrightarrow$ C=N charge transfer transition all transitions are attributed to square planar geometry of complexes (Kennedy et al., 1972, Sutton , 1968, Irshad et al., 2010).

The effective magnetic moment value of the prepared complexes (2,3,4) [M$_2$Hg$_2$(L)$_4$Cl$_4$] are ($\mu_{eff.}$ =zero) B.M., which indicates that they are diamagnetic and have square planar geometry around M(II) where (M=Ni, Pd, Pt) (Butrus et al., 2012, Sutton , 1968, Irshad et al., 2010, Nikiforova et al., 2006, Khullar et al., 1975, James et al., 1993).

2.3 The Proton Nuclear Magnetic Resonance, Carbon 13 Nuclear Magnetic Resonance spectra of complexes (2, 3, 4)

The Proton Nuclear Magnetic Resonance spectra of prepared complexes were measured in d$_6$-DMSO solvent. The ^{1}H-NMR for aromatic ring protons were appeared at (δ =6.8-7.1) ppm, (δ =5.9-9.2) ppm and (δ =6.8-8.8) ppm for complexes Ni^{+2}, Pd^{+2} and Pt^{+2} respectively. The ^{1}H-NMR for (NH) amine protons were appeared at (δ =2.2) ppm, (δ =3.9-4.0) ppm and (δ =3.8-4.3) ppm for complexes Ni^{+2}, Pd^{+2} and Pt^{+2} respectively (Tariq, 2013, Mohammed et al., 2015), Table 3.

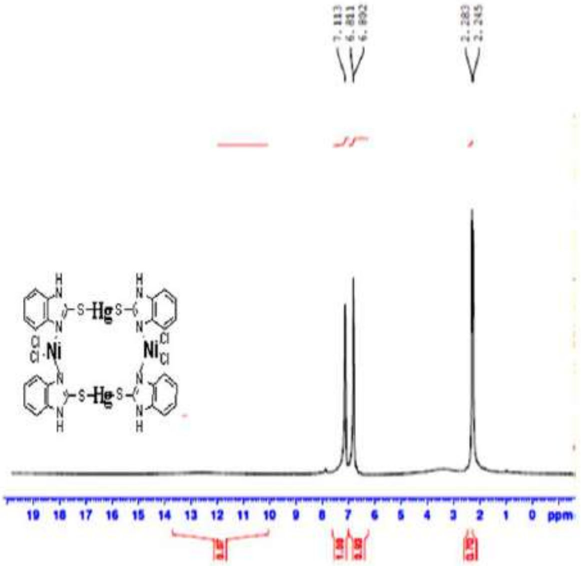

Figure 1: The ^{1}H-NMR of [Ni$_2$Hg$_2$(L)$_4$Cl$_4$]

Table (3) ^{1}H-NMR data for prepared complexes .

no.	Str. Formula	δ / ppm	no. Proton	Group
2	$C_{28}H_{20}N_8S_4Hg_2Ni_2Cl_4$	7.1-6.8	20H	4Ph
		2.2	4H	4NH
3	$C_{28}H_{20}N_8S_4Hg_2Pd_2Cl_4$	9.2-5.9	20H	4Ph
		4.0-3.9	4H	4NH
4	$C_{28}H_{20}N_8S_4Hg_2Pt_2Cl_4$	8.8-6.8	20H	4Ph
		4.3-3.8	4H	4NH

The nuclear magnetic resonance (^{13}C-NMR) of the prepared complexes in the solvent (d$_6$-DMSO) gave four singlet peaks (C1, C2, C3, C4) and each peak is equivalent to two atoms of carbon and to the presence of symmetry in the complexes as scale in Table 4.

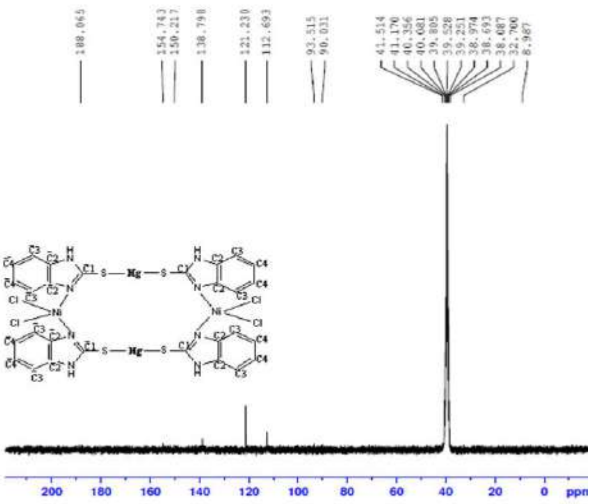

Figure 2: The ^{13}C-NMR of $[Ni_2Hg_2(L)_4Cl_4]$

Table (4) ^{13}C-NMR data for prepared complexes.

no.	Structure formula	δ/ppm	Group
2	$C_{28}H_{20}N_8S_4Hg_2Ni_2Cl_4$	150.217	$\mathbf{C_1,C_1^-}$
		138.798	$\mathbf{C_2,C_2^-}$
		112.693	$\mathbf{C_3,C_3^-}$
		121.230	$\mathbf{C_4,C_4^-}$
3	$C_{28}H_{20}N_8S_4Hg_2Pd_2Cl_4$	140.826	$\mathbf{C_1,C_1^-}$
		133.509	$\mathbf{C_2,C_2^-}$
		109.429	$\mathbf{C_3,C_3^-}$
		121.653	$\mathbf{C_4,C_4^-}$
4	$C_{28}H_{20}N_8S_4Hg_2Pt_2Cl_4$	153.597	$\mathbf{C_1,C_1^-}$
		---	$\mathbf{C_2,C_2^-}$
		112.520	$\mathbf{C_3,C_3^-}$
		122.891	$\mathbf{C_4,C_4^-}$

2.4 Infrared spectra for the ligand and prepared complexes

The spectra of the ligand exhibited band at 1514 cm^{-1} due to the **V**(C=N) group of the ligand and when the complexes were formed this spectra were shifted to higher or lower frequency in the range (1622-1490)cm^{-1} which indicate that the ligand was bonded to the metal ion through N atom of **V**(C=N)group (Kennedy et al., 1972, Mohammed et al., 2013, Anandarajagopal et al., 2010, Ganesh et al., 2011, Akira et al., 1970, Rehman et al., 2013), also the ligand showed band at (736)cm^{-1} due to the **V**(C-S) group of the ligand and this band was shifted to higher or lower frequency in the range (742-725)cm^{-1} during the complexes which indicate that the ligand was bonded to the metal ion through sulphur atom (Zora et al., 2002, Butrus et al., 2012, Irshad et al.,2010, Khullar et al.,1975) .The infrared spectra of the prepared complexes show band in the range (451-412) cm^{-1}, which are attributed to **V** (M-N) . On the other hand, it has been observed that in the spectra of all compounds, the bands at (310-290) cm^{-1} were assigned to V (Hg-S) (Carlo et al., 1977, Musa, 1998, Awaz, 2015). Also bands in the range (330-280) cm^{-1}, which are attributed to **V** (M-Cl) (Butrus et al., 2012, Oztekin et al., 2005, Nakamoto, 1997, Joseph et al., 2001).

2.5 Molar conductivity for the prepared complexes

At 25^{o}C the molar conductivities were measured for (10^{-3} M) solution in DMSO. From the obtained results it was concluded that the prepared complexes are non electrolytical complexes.

3. CONCLUSIONS

The current study includes synthesis of complexes of bis (2-mercaptobenzimidazole) mercury (II) with Ni (II), Pd (II), and Pt (II). From the magnetic susceptibility values, the geometry of the complexes were determined. The structure of Hg(II) complex was linear, whereas the a square planer is the geometry for the complexes of Ni(II), Pd(II) and Pt(II) metal ions. As stated by the molar conductivity data, it is recommended that the complexes are non-electrolyte.

Acknowledgements

The authors are grateful to the chemistry Department. College of Education for their helping and support.

Conflict of Interest

There is no conflict of interest.

Reference

AI-Adeli, M. H. M. 2009. Synthesis, Semi-Empirical/PM3 studies of the Benzaldehyde [5-(2-hydroxyphenyl)-,3,4-oxzdiazol-2-yi] hydrazine and some Their transition Metal Complexes. *National J. Chem*., 33, 89-103.

Akira, O., Toshio, T. & Iwao, T.1970. The Syntheses and Properties of Benzothiazole or Benzimidazole Derivative Adducts of Tin(II, IV) and Antimony(II) Halides. *Bull. Chem. Soc. Jpn*., 43, 2840-2844.

Ali**.**, A. M. 2007. Synthesis and characterization of the Ligand 2-[(6-Nitro-2-benzothiazolyl)azo]-4,6-dimethylphenol (6-NBTADMP) and It's Complexes with Fe(II), Ni(II),Cu(II), Zn(II), Cd(II), Pd(II) and Ag(I) Ions. *National J. Chem*., 28, 676-686**.**

ANANDARAJAGOPAL, K., RAVI, T. N., BOTHARA, K. G., ANBU, S. J., DINESHKUMAR, C. & PROMWICHIT, P. 2010. 2-Mercaptobenzimidazole Derivatives: Synthesis and Anticonvulsant Activity. *Advances Appl. Sci. Res*., 1(2), 132-138.

ARANZAZU, M., ELENA, C., FRANCISCO, A. J. & MARIANO, L. 2006. Pyridine-2-thionate as a versatile ligand in Pd(II) and Pt(II) chemistry: the presence of three different co-ordination modes in $[Pd_2(\mu_2\text{-}S,N\text{-}C_5H_4SN)(\mu_2\text{-}K^2\ S\text{-}C_5H_4SN)(\mu_2\text{-}dppm)(S\text{-}C_5H_4SN)_2]$. *Dalton Trans*., 609-616.

BUTTRUS, N. H. & SAEED, F. T. 2012. Synthesis and Steuctural Studies on Some Trasition metal complexes of Bis-(benzimidazole-2-thio) ethane, propane and butane ligands. *Res. J. Chem. Soc.*, 2(6), 43-49.

CARLO, P. & GIUSEPPE, T. 1977. Transition metal complexes of deprotonated 2-mercaptobenzoxazole. Study of the thio-thioketo form equilibrium. *Can. J. Chem*., 55, 1409-1414**.**

GANESH, A., BETHI, S., MATTA, V. & SAIKRISHNA, K. 2011.Synthesis of 3-(1H-Bnzimidazol-2-yl Amino) 2-Phenyl-1, 3-Thiazolidin-4-One as Potential CNS Depressant. *Int. J. Pharm. Techn. Res*., 3(1), 360-364.

HUSSEIN, A. J .2015. Synthesis and characterization of some new pyrazoline compounds derived from azo-benzaldehyde. *Zanco J. Pure & Appl. Sci*., 27(1), 51-58.

IBRAHEM, S. K., ABDUL-HAMEED, F. M. & ALIAS, M. F. 2008. Preparation and characterization and biological activities of some metal complexes of new n[4-bi(5-thion-1,3,4-oxadiazole-2yl)methane)metyl] dibutyl amine and theoretical study. *J. AI-Nahrain Univ. Sci.*, 11(2), 24-36.

IRSHAD, A. & JYOTSANA, 2010. Synthesis and Structural studies of Pd(II) and Pt(II) complexes with 2-thiobenzimidazolyl acetic acid. *Oriental J. Chem*., 26(4), 1529-1532**.**

JAMES, H. E., ELLEN, K. A. & RICHARD, K. L. 1993. *"Inorganic Chemistry,Principles of Structure and Reactivity 4th"* , Harper Collins College Publishers, P. 463.

JOSEPH, J., WENDY, C. I., ROBIN, P. G., CHARLES, M. A. & KENIN, N. B. 2001. Synthesis and characterization of mercaptoimidazole, mercaptopyrimidine and mercaptopyridine complexes of platinum(II) and platinum(III). The crystal and molecular strucres of tetra(2-mercaptobenzimidazole)- and tetra(2-mercaptoimidazole)platinum(II) chloride. Inorg. Chim. Acta, 315, 36-43. 47191.

KENNEDY, B. P. & LEVER, A. B. P. 1972. Studies of the Metal-Sulfur Bond. Complexes of thePyeidine Thiols. *Can. J. Chem*., 50, 3488-3507.

KHULLAR, I. P. & AGARWALA, U. 1975. Complexes of 2-mercaptobenzothiazole with Cu(II), Ni(II), Co(II), Cd(II), Zn(II), Pb(II), Ag(I) and Ti(I). *Can. J. Chem*. 53, 1165-1171.

LEKA, Z. B., LEOVAC, V. M., LUKIC, S., SABO, T. J., TRIFUNOVIC, S. R. & KATALIN, S. M. 2005. Synthesis and physic-chemical characterization of new dithiocarbamato ligand and its complexes with Copper(II), Nickel(II) and Palladium(II). *J. Therm. Anal. Cal*., 29, 1-5.

MOHAMMED, A. R., SHETHA, N. F. & AMAL, S. S. 2013. Synthesis of 2-mercaptobenzimidazole and Some of its Derivatives. *J. AI-Nahrain Univ*., 16(2), 77-83.

MOHAMMED, R. M. H. & RASHEED, E. M. 2011. Synthesis, characterization and Biological Study of Cr(III), Mn(II), Co(II), Ni(II), Cu(II) and Zn(II) Complexes with a New Tetradentatae Schiff Base Ligand. *Iraqi National J. Chem.* 43, 392-402.

MOHAMMED, K. S., CHAWISHLI, L. H. & HUSSEIN, A. J. 2015. Synthesis and spectroscopic characterization of some diazodibenzyloxy pyrazolines from some diazodibenzyloxy chalcones. *Zanco J. Pure & Appl. Sci*., 27(2), 53-60.

MUSA**,** F. H. 1998. Preparation and characterization of Dioxadiazol and Ditriazol Complexes with Dilvalent; Co, Ni, Cu, Zn and Hg. *Iraqi J. Chem*., 24(2), 238-245.

NAKAMOTO**,** K. 1997 *"Infrared and Raman Spectra of Inorganic Coordination Compounds" 5th Ed., Part B,* John Wiley and Sons, New York**,** PP. 23, 53, 60, 116173, 187, 322, 214, 166.

NANHAI S., & SINHA, R. K**.**2001. Preparation, characterization and electrical conductivity of heterometallic complexes derived from 2-sulfanylbenzothiazolate. *Inorg. Chem. Commun.*, 4, 454-458**.**

NIKIFOROVA, M. E., TALISMANOVA, M. O., ALEKSANDROV, G. G., KOTOVSKAYA, S. K., SIDOROV, A. A., NOVOTORTSEV, V. M., IKORSKII, V. N., CHARUSHIN, V. N., EREMENKO, I. L. & MOISEEV, I. I.2006. Unusual magnetic nehavior of the new supramolecular ensemble $[Ni_2L_4]_2$. $[NiCl_2(LH)_2(MeCN)_2]$ .4MeCN (LH is 2-mercaptobenzimidazole). *Russ. Chem. Bulletin Int. Edition*, 55(12), 2181-2186.

OBOT, I. B., GASEM, Z. M. & UMOREN, S. A. 2014. Understanding the Mechanism of 2-mercaptobenzimidazole Adsorption on Fe(110), Cu(111) Suefaces: DFT and Molecular Dynamics Simultions Approaches. *Int. J. Elec. Sci*., 9, 2367-2378.

OZTEKIN, A., BERRIN, O., UFUK, A. & FATMA, G. 2005. Synthesis, characterization and Genotoxicity of Platinum(II) Complexes With Subtituted Benzimidazole Ligands. *Turk. J. Chem*., 29, 607-615.

RAFAEL, C., JULIO, C. J., EVA, G., MARIA, H. R., SANCHEZ, A., JUAN, M. L., ENRIQUE, M., FERNANDES, E. & FRANCISCA, S. 2002. Thiourea derivatives and their nickel (II) and platinum (II) complexes: antifungal activity. J. Inorg. Bio chem., 89, 74-82.

RAPER, E. S., JACKSON, A. R. W. & GARDINER, D. J. 1984. Imidazoline-2-Thione Semihydrate: Crystal Structure, Spectroscopy and Thermal Analysis. *Inorg. Chim. Acta.*, 84, L_1-L_4.

REHMAN, M., IMRAN, M., ARIF, M. & M. FAROOQ, 2013. Metal-based Antimicrobial agents: Synthesis, characterization and biologicl studies of Mannich base derivatives of Benzimidazole and their Metal complexes. *Sci. J. Chem*., 1(5), 56-66.

SHAN, C., RONG, Y., ZHEN, Z., SHU, C., QI, Z., XIAO, W., FEI, W. & CAN, L. 2010. A Series of Polynuclear Comlpexes of d^{10} Metals With Interesting Luminescent Properties. *Cryst. Growth and Design*, 10(3), 1155-1160.

SUTTON, D. 1968. *"Electronic Spectra of Transition Metal Complexes",* McGraw-Hill. London, P.1.

Tariq, F. A. 2013. *Synthesis and characterization of some transition metal and zinc complexes with (benzimidazole2-thio) alkane, their halid salts and their uses in sulfur compounds removal from diesel fuel*. Ph. D. Thesis.college of science. Mosul Univ. Iraq.

ZORA, P., ZELJKA, S., DUBRAVKA, C. M., GORDANA, P., MASA, R. & GERALD, G. 2002. Mercury(II) Complexes with Heterocyclic Thiones-Preparation and Characterization of the 1:1 and 1:2 Mercury(II) Complexes with Benzo-1,3-imidazole-2-thione. *Eur. J. Inorg. Chem*., 171-180.

ZANCO Journal of Pure and Applied Sciences
The official scientific journal of Salahaddin University-Erbil
https://zancojournals.su.edu.krd/index.php/JPAS

ISSN (print):2218-0230, **ISSN (online):** 2412-3986, **DOI: http://dx.doi.org/10.21271/zjpas**

RESEARCH PAPER

Detection of Aerolysin Gene in *Aeromonas hydrophila* from Suspected Farming Fishes (*Cyprinus carpio*), Erbil Province / Iraq

ibrahim ramadhan ibrahim[1], Shamall Mohamad Amin Abdullah[1], Abdulkarim Yasin Karim[2]

[1]Department of Fish Recourses and Aquatic Animals, College of Agriculture Salahaddin University-Erbil, Kurdistan Region, Iraq
[2]Department of Biology, College of science Salahaddin University-Erbil, Kurdistan Region, Iraq

ABSTRACT:

Aeromonas hydrophila consider as the most common pathogenic bacteria which infect many farming fishes and due to many economical losses annually this bacteria found in fresh, brackish waters and ponds. The present study conducted to determine the most reliable method for the diagnosis of *A. hydrophila* from common carp (*Cyprinus carpio*), in Agriculture college fish farmduring a farming (May 2017 to October 2018).Results of the present study showed that 60 bacterial samples out of 115 bacterial samples were gram-negative, however 40 samples were motile and only 29 samples showed positive hemolysis on blood agar. Result of molecular diagnosis showed that only 18 bacterial samples have Aerolysin gene (1482 bp).

KEY WORDS: Aerolysin, *Aeromonas hydrophila*, *Cyprinus carpio,* Polymerase chain reaction.
DOI: http://dx.doi.org/10.21271/ZJPAS.32.1.12
ZJPAS (2020) , 32(1);110-114 .

1.INTRODUCTION :

Many fishes in ponds are considerable affected by the disease from “motile Aeromonas septicaemia” (MAS) which infect warm water fish including common carp, *A. hydrophila* is one of the most common species which associated indeed relationship with human diseases as well (Allen *et al.*, 2010) and (Barzani and Mustafa, 2015).

Aeromonasis the Gram-negative rods, facultative anaerobic, motile and non spore forming bacteria, usually present acutely in aquatic ecosystems (Barzani and Mustafa, 2015),either surface or underground water such as fresh, estuarine, marine, groundwater, drinking water and ponds (Nakano *et al.*, 1990), (Ashbolt *et al.*, 1995) and (Janda and Abbott, 2010).

There are many virulence factors in *A. hydrophila*, including protease, aerolysin, and enterotoxin toxin, which cause disease in humans and fish (Zhu *et al.*, 2007). The whole sequence of the aerolysin nucleotide gene is located on a 1.8-kb ApaI-EcoRI fragment and consists of 1,479 bp that contain an ATG initiation codon and a TAA termination codon (Igbinosa *et al.*, 2017), (Singh *et al.*, 2010) and (Singh *et al.*, 2009).

The present study aimed to determine the most reliable method for the diagnosis of *A. hydrophila* from common carp (*Cyprinus carpio*), and comparing between molecular diagnosis by PCR (Polymerase Chain Reaction), standard microbiological diagnosis (Gram-stain, Culturing and other techniques) and Vitek II system

2.Materials and methods

Bacterial sample isolated from115 common carp farming fishes (30-39 cm in length and 1200-2000 gm in weight as shown in figure (1) which were collected from Agriculture College fish farm (Grda-Rasha 8 km away from capital

---

*** Corresponding Author:**
Ibrahim Ramadhan Ibrahim1
E-mail: ibrahim.ibrahim@su.edu.krd
Article History:
Received: 17/07/2019
Accepted: 26/09/2019
Published: 25/02 /2020

Erbil city) during a farming season (May 2017-October 2018). The fishes labeled and transported alive in a cool box containing the fish's water pond to the laboratory of Microbiology, Biology Department, College of Science, University of Salahaddin- Erbil for microbiology examination.

Figure 1. Common carp (*Cyprinus carpio*) farming fishes.

3.Collection, isolation and identification

Microbiological tests have been done by taking sterile swab from 115suspected farming fishes, exactly swabs have been taken from ulcers which were visible by naked eye examination throughout the body of collected fishes, suspected fishes for pathogenic *A. hydrophila* from the present study were shown in figure (2).All samples immediately transferred to laboratory and subjected directly to microbiological examinations. All swabs were inoculated on blood agar and incubated aerobically at 37°C for 24h then sub cultured on nutrient agar, suspected bacterial colonies were purified based on the size, shape, color and patterns of hemolysis and non-hemolysis on 5% and were subjected to Gram's staining(Parker and Shaw, 2011). In addition, oxidase and catalase test done according to the method by (Sørum, 2006).

Figure 2.suspected common carp with ulcers on their bodies for pathogenic *Aeromonas hydrophila.*

3.1Gram Stain

Gram stain was used for microscopic examination of bacterial shape, according to this stain bacterium can be divided into two groups: Gram negative and Gram positive (Janda et al., 1984) and(Ashith et al., 2019).

3.2Vitek II system

Biochemical profiles with the Vitek II system (bioMérieux, Lyon) was utilized for identification of *A. hydrophila* after selection of the appropriate card according to the gram stain and growth condition of bacterial samples(Izzati, 2019)

.

3.3Detection of Aerolysin gene by Polymerase Chain Reaction

The bacterial DNA extracted after incubation at 37°C in Luria Bertani (LB) broth by using Jena Bioscience kit (Germany) and according to the manufacturer's instructions with some modification has been done and primers were designed for Aerolysin gene (1482 bp). Following, the constructed primers were then matched concurrently with other sequences in the GenBank database in order to check their identity and resemblance with the gene Aerolysin from *A. hydrophila* and other bacterial species. Aero-F: 5'CGCGGATCCGGCTTGTCATTGATCATAT CC 3'

Aero-R:
5’CCGCTCGAGTTATTGATTGGCAGCTGGC 3’

Aerolysin gene of *A. hydrophila* was amplified by PCR. The reaction mixture is a total of 50µl consisted 25 µl master mix, 1 µl of each primer, 20 µl of ddH2O and 3 µl (30 ng)of bacterial genomic. Amplification condition was obtained with an initial denaturation step at 95 °C for 5 min, followed by 30 cycles at 95°C for 30 sec, and annealing at 65°C for 30 sec, 72 °C for 1 min and final extension 72°C for 4 min (Chacon et al., 2003).

To confirm the size, location and quality of the PCR-specific product for specific primers, amplicons were separated by gel electrophoresis. A standard technique was used to prepare the electrophoresis tank (De Gregoris et al., 2011).

Gel was ready to produce 1 percent gel for electrophoresis by combining 70 ml of Ix TAE (TrisAcitate EDTA) with 0.70 g agarose and high electrical power run off for about 4 minutes. Each sample was then added 2.5 µl of the Orange G dye (1/10 sample quantity). 25 µl of 1 kb ladder was prepared as follows to calibrate the gel; 21.5 µl of molecular water, 2.5 µl of Orange G dye and I µl of ladder (100bp, Promega).

4.Results:

All bacterial samples (115 samples) were addresses into microbiological tests such as (Gram stain, Motility test, Blood agar diagnosis, Catalase and Oxidase test) then they were diagnosed by vitek II and finally PCR run for Aerolysin done for the positive samples of vitek II test.

Results showed that 60 samples out of 115 samples were Gram-negative, however 40 samples were motile and only 29 samples showed positive hemolysis on blood agar (Table 1) and showed positive result for both test of catalase and oxidase.

Table 1. Number of positive for *Aeromonas hydrophila* samples by microbiological tests (Gram-stain, Mobility test, and blood culturing).

Microbiological tests	Number of positive samples/ 115	Positive samples %
Gram-stain	60	52.1
Motility test	40	34.7
Blood agar	29	25.2

Vitek II system analysis done after the selection of the appropriate card according to the gram stain and growth condition of bacterial sample (*A. hydrophila*), the result of this analysis confirmed that only 20 samples were *A. hydrophila* out of 29 suspected sample from final microbiological results.

Genotypic detection of aerolysin gene was done by PCR, special primers for aerolysin gene designed as mentioned in methodology section, out of 20 infected fishes with *A. hydrophila* (Vitek) only 18 samples showed the presence of whole coding region of Aerolysin gene and the size(1482 bp), Agarose gel electrophoresis done for PCR product and amplicons with (1479 bp) were considered as positive samples which confirm the presence of *A. hydrophila* as showed in figure (3).

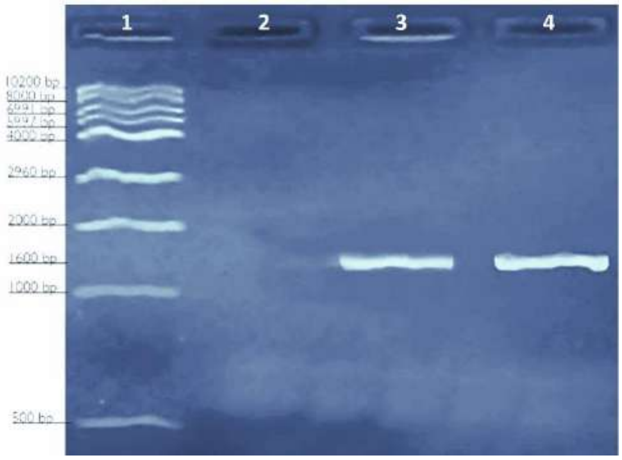

Figure 3. Polymerase chain reaction products on gel electrophoresis (1.5%) for Aerolysin gene

(1482) bp gene for *Aeromonas hydrophila.* Lane 1: 1 kb Ladder, Lane 2: negative PCR control, Lane 3: positive PCR control and Lane 4: positive bacterial sample.

5.Discussions

Fish considered as the most world-wide source of nutrient which contains many types of essential amino acids (Skibniewska*et al.,*2013), *C. carpio* present in Asia, Europa and other part of world like Iraq-Kurdistan region (Aziz and Muhammad, 2017). The most considerable bacterial group which cause disease to many fish including common carp are motile Aeromonas (Allen *et al.,* 2010). Many researchers reported various disease caused by Aeromonas spp. such as gastroenteritis (Chopra et al., 1993), endocarditis (Brouqui and Raoult, 2001) and meningitis (Ouderkirk *et al.,* 2004). Aerolysin toxin considered as the most common virulence factor of *A. hydrophila* (Igbinosa *et al.,* 2017).

PCR diagnosis is more accurate than culturing gram stain examination and Vitek II system because PCR technique depend on the presence of the target gene while culturing technique depend on the morphology, shapes and enzymes of the bacteria (Pongsachareonnont *et al.,* 2017), (Panangala *et al.,* 2007) and (Balaky *et al.,* 2019). Furthermore, identification based on variations in one or two phenotypic features does not show true environmental diversity and enables inaccurate identification when comparing outcomes acquired in distinct laboratories (Cherkaoui *et al.,* 2010). Also identification by Vitek II system is not enough accurate which depend on the purity of sample, thus various qualitative levels of identification were assigned based on the numerical probability calculation *(Izzati, 2019).*

Detecting the Aerolysin toxin is more recommended which is a virulence factor used by bacteria in order to penetrate the cell and produce pore secondarily ulcer than diagnosis by culture or gram stain (Geny and Popoff, 2006).

The present study conducted to detection Aerolysin gene by PCR for the diagnosis of *A. hydrophila* from common carps, PCR assay confirmed that 18 of infected fishes with *A. hydrophila* showed positive Aerolysin gene similar result concluded by (Wang *et al.,* 2003). Previous study concluded only 79% of infected fishes with same bacteria showed cytotoxic gene positive (Ørmen and Østensvik, 2001). The present study is totally agreed with recent study (Leitner *et al.,* 2013), which preferred molecular techniques over the microbiological methods for the diagnosis of *A. hydrophila*in common carp. More-ever previous study consider microbiological methods consider as the basic for the diagnosis of pathogenic bacteria (Agger *et al.,* 1985).

In conclusion, Polymerase chain reaction is a method that takes less time and more accuracy to diagnose pathogenic *A. hydrophila* in common carp as it depends on genotype rather than phenotype characters.

6.References

AGGER, W. A., MCCORMICK, J. & GURWITH, M. J. 1985. Clinical and microbiological features of Aeromonas hydrophila-associated diarrhea. *Journal of Clinical Microbiology,* 21**,** 909-913.

ALLEN, H. K., DONATO, J., WANG, H. H., CLOUD-HANSEN, K. A., DAVIES, J. & HANDELSMAN, J. 2010. Call of the wild: antibiotic resistance genes in natural environments. *Nat Rev Microbiol,* 8**,** 251-9.

ASHBOLT, N., BALL, A., DORSCH, M., TURNER, C., COX, P., CHAPMAN, A. & KIROV, S. 1995. The identification and human health significance of environmental aeromonads. *Water Science and Technology,* 31**,** 263.

ASHITH, V., DEEPTHI, C., JOSEPH, R. M., RAMASWAMY, A. & VIVEKANANDHAN, G. 2019. Detection of Hemolytic Activity of Aeromonas sp Isolated from Water Samples of Coastal Area, Kochi. *Biotechnological Research,* 5**,** 9-15.

AZIZ, D. M. & MUHAMMAD, S. I. 2017. Molecular identification and Phylogenetic tree of some fish (Cyprinidae) in Dukan Lake, Kurdistan of Iraq. *ZANCO Journal of Pure and Applied Sciences.,* 29**,** 140-145.

BALAKY, S. T. J., ABDULKHALIK, H., HUSSEN, B. M., HASSAN, H. & MAWLOOD1, A. H. 2019. Molecular Identification of Acinetobacter baumanii and Acinetobacter genomic species 13TUUsing PCR. *ZANCO Journal of Pure and Applied Sciences*, Vol. 31, no. 1, Feb. 2019, pp. 17-22.

BARZANI, K. & MUSTAFA, A. K. 2015. Bacteriological and Molecular Study of Aeromonas sobria Isolated From Different Sources in Erbil Province. *ZANCO Journal of Pure and Applied Sciences.,* 27**,** 11-18.

BROUQUI, P. & RAOULT, D. 2001. Endocarditis due to rare and fastidious bacteria. *Clinical microbiology reviews,* 14**,** 177-207.

CHACON, M. R., FIGUERAS, M. J., CASTRO-ESCARPULLI, G., SOLER, L. & GUARRO, J. 2003. Distribution of virulence genes in clinical and environmental isolates of Aeromonas spp. *Antonie Van Leeuwenhoek,* 84**,** 269-78.

CHERKAOUI, A., HIBBS, J., EMONET, S., TANGOMO, M., GIRARD, M., FRANCOIS, P. & SCHRENZEL, J. 2010. Comparison of two matrix-assisted laser desorption ionization-time of flight mass spectrometry methods with conventional phenotypic identification for routine identification of bacteria to the species level. *Journal of clinical microbiology,* 48**,** 1169-1175.

CHOPRA, A. K., HOUSTON, C. W., PETERSON, J. W. & JIN, G.-F. 1993. Cloning, expression, and sequence analysis of a cytolytic enterotoxin gene from Aeromonas hydrophila. *Canadian Journal of Microbiology,* 39**,** 513-523.

DE GREGORIS, T., ALDRED, N., CLARE, A. S. & BURGESS, J. G. 2011. Improvement of phylum- and class-specific primers for real-time PCR quantification of bacterial taxa. *J Microbiol Methods,* 86**,** 351-6.

GENY, B. & POPOFF, M. R. 2006. Bacterial protein toxins and lipids: pore formation or toxin entry into cells. *Biol Cell,* 98**,** 667-78.

IGBINOSA, I. H., BESHIRU, A., ODJADJARE, E. E., ATEBA, C. N. & IGBINOSA, E. O. 2017. Pathogenic potentials of Aeromonas species isolated from aquaculture and abattoir environments. *Microbial pathogenesis,* 107**,** 185-192.

IZZATI, M. 2019. *PERBANDINGAN HASIL IDENTIFIKASI BAKTERI GRAM NEGATIF MENGGUNAKAN TEKNIK BIOKIMIA OTOMATIS (VITEK® 2) DAN MALDI-TOF MS (VITEK® MS).* Universitas Sebelas Maret.

JANDA, J. M. & ABBOTT, S. L. 2010. The genus Aeromonas: taxonomy, pathogenicity, and infection. *Clinical microbiology reviews,* 23**,** 35-73.

JANDA, J. M., DIXON, A., RAUCHER, B., CLARK, R. B. & BOTTONE, E. J. 1984. Value of blood agar for primary plating and clinical implication of simultaneous isolation of Aeromonas hydrophila and Aeromonas caviae from a patient with gastroenteritis. *J Clin Microbiol,* 20**,** 1221-2.

LEITNER, E., KESSLER, H. H., SPINDELBOECK, W., HOENIGL, M., PUTZ-BANKUTI, C., STADLBAUER-KÖLLNER, V., KRAUSE, R., GRISOLD, A. J., FEIERL, G. & STAUBER, R. E. 2013. Comparison of two molecular assays with conventional blood culture for diagnosis of sepsis. *Journal of microbiological methods,* 92**,** 253-255.

NAKANO, H., KAMEYAMA, T., VENKATESWARAN, K., KAWAKAMI, H. & HASHIMOTO, H. 1990. Distribution and characterization of hemolytic, and enteropathogenic motile Aeromonas in aquatic environment. *Microbiology and immunology,* 34**,** 447-458.

ØRMEN, Ø. & ØSTENSVIK, Ø. 2001. The occurrence of aerolysin-positive Aeromonas spp. and their cytotoxicity in Norwegian water sources. *Journal of applied microbiology,* 90**,** 797-802.

OUDERKIRK, J. P., BEKHOR, D., TURETT, G. S. & MURALI, R. 2004. Aeromonas meningitis complicating medicinal leech therapy. *Clinical Infectious Diseases,* 38**,** e36-e37.

PANANGALA, V. S., SHOEMAKER, C. A., VAN SANTEN, V. L., DYBVIG, K. & KLESIUS, P. H. 2007. Multiplex-PCR for simultaneous detection of 3 bacterial fish pathogens, Flavobacterium columnare, Edwardsiella ictaluri, and Aeromonas hydrophila. *Diseases of aquatic organisms,* 74**,** 199-208.

PARKER, J. L. & SHAW, J. G. 2011. Aeromonas spp. clinical microbiology and disease. *Journal of Infection,* 62**,** 109-118.

PONGSACHAREONNONT, P., HONGLERTNAPAKUL, W. & CHATSUWAN, T. 2017. Comparison of methods for identifying causative bacterial microorganisms in presumed acute endophthalmitis: conventional culture, blood culture, and PCR. *BMC Infect Dis,* 17**,** 165.

SINGH, V., SOMVANSHI, P., RATHORE, G., KAPOOR, D. & MISHRA, B. 2009. Gene cloning, expression and homology modeling of hemolysin gene from Aeromonas hydrophila. *Protein Expression and Purification,* 65**,** 1-7.

SINGH, V., SOMVANSHI, P., RATHORE, G., KAPOOR, D. & MISHRA, B. 2010. Gene cloning, expression, and characterization of recombinant aerolysin from Aeromonas hydrophila. *Applied biochemistry and biotechnology,* 160**,** 1985-1991.

SØRUM, H. 2006. Antimicrobial drug resistance in fish pathogens. *Antimicrobial resistance in bacteria of animal origin.* American Society of Microbiology.

WANG, G., CLARK, C. G., LIU, C., PUCKNELL, C., MUNRO, C. K., KRUK, T. M., CALDEIRA, R., WOODWARD, D. L. & RODGERS, F. G. 2003. Detection and characterization of the hemolysin genes in Aeromonas hydrophila and Aeromonas sobria by multiplex PCR. *Journal of clinical microbiology,* 41**,** 1048-1054.

ZHU, D., LI, A., WANG, J., LI, M. & CAI, T. 2007. Cloning, expression and characterization of aerolysin from Aeromonas hydrophila in Escherichia coli.

ZANCO Journal of Pure and Applied Sciences
The official scientific journal of Salahaddin University-Erbil
https://zancojournals.su.edu.krd/index.php/JPAS

ISSN (print):2218-0230**, ISSN (online):** 2412-3986**, DOI: http://dx.doi.org/10.21271/zjpas**

RESEARCH PAPER

Growth, Yield and Yield Components of Wheat (*Triticum aestivum* L.), Chickpea and Wild mustard as Influenced by Intercropping in Different Row Proportions

Aryan S. A. Dizayee[1]*, Sami Mohammad Amin Maaroof [2]

[1&2]Department of Field Crops, College of Agricultural Engineering Sciences, Salahaddin University-Erbil, Kurdistan Region, Iraq

A B S T R A C T:

A field experiment was conducted at Grdarasha Experimental Farm / College of Agricultural Engineering Sciences / Salahaddin University – Erbil, located at (36.2° N, 44.1° E and elevation 470 m) during the winter season of (2016-2017) to study the performance of wheat (*Triticum aestivum* L.), chickpea (*Cicer arietinum* L.) and wild mustard (*Sinapis arvensis* L.) in intercropping. Seven treatments were initialized from combination of either single, double or triple (row: species) were arranged in a standard replacement series. Aiming to study growth, yield and yield component of wheat (A), chickpea (B) in the presence of the invading wild mustard weed (C), which is the common invader weed in the area. Wheat species possessed the highest significant mean values of plant height (123.0 cm), spike length (13.9 cm), grain yield (182.0 g plant^{-1}), straw yield (752.5 g plant^{-1}), while wild mustard showed superiority in all studied traits except in silique length and grain number. silique^{-1}.

KEY WORDS: Intercropping, Growth, Yield Components, Relative yield, Row: Species Ratio.
DOI: http://dx.doi.org/10.21271/ZJPAS.32.1.13
ZJPAS (2020) , 32(1);115-126 .

1. INTRODUCTION

In the developing countries at tropic and sub tropic regions, lands are often utilized by a special method called intercropping where as two or more crops are grown simultaneously on the tract (Shaker and Nasrollahzadeh, 2014). Bybee-Finley and Ryan (2018) confirmed the legacy of traditional practice of the intercropping pattern throughout the history to increase yield then to insure optimal instinctive use of land in sustainable agriculture. Wheat (*Triticum aestivum* L.) is one of the most important crops in terms of cultivated area and productivity, due to the excellent control over weed invasion (Siyahpoosh *et al*., 2012).

The mineral nutrition significantly contributed in increasing crop yields during the 20th century. (Khursheed and Mahammad, 2015). Chickpea (*Cicer arietinum* L.) is important pulses food, which is traditionally grown under rain-fed environmental conditions in most parts in the world and it is belong to the family Leguminaceae (Erdemci, 2018). Cicer arietinum L. is the main crops that have a role in fixed nitrogen in the nodules of the root, through its role in soil fertility (Qader, 2019). Wild mustard (*Sinapsis arvensis* L.) is an annual winter plant which belongs to *Brassicacea or Crusiferea* plant family it has indeterminate upright growth and may reach a height of more than two and a half meter. This weed proliferates extreme spreading through producing thousands of seeds, which are assisted by the valuable tropical and subtropical weather (Siyahpoosh *et al*., 2012). Weed-crop competition studies possessed many scenarios or experimental designs. Any one of them has a critical importance

---

* **Corresponding Author:**
Aryan Suad Ahmad Dizayee
E-mail: aryan.ahmed@su.edu.krd
Article History:
Received: 01/07/2019
Accepted: 02/10/2019
Published: 25/02 /2020

(Rejmanek *et al*., 1989). Harper (1977), noted that the replacement design is an effective way particularity in the study of the interference between two species of plant crops. However, additive design is widely used to study the competition between the weeds and crops (Aziz, 1991; Wilcox, 1995; Ali, 2000; Bhan and Froud, 2005). In replacement series total plant density is kept fixed within a special care to plant geometry. Total density of all the crops involved in the design was constant. In other word, when the density of one crop components increases or decreases, the density of the other crops changes to maintain a constant total for all partial crop densities seeking for optimizing yield levels (Kaushik *et al*., 2016). Sharma *et al*., (1986) in the other hand detected significant effects of plant density on intercropped plants of wheat and mustard. Intercropping of wheat and mustard according to (Singh and Pal, 1994) reduces their seed yield comparing to their pure stands. Yield and yield components of wheat were significantly affected by intercropping of chickpea, lentil and rapeseed (Malik *et al*., 1998). Intercropping can increase the productivity of both yield and grain quality by integrating the use of water, fertilizer, space, and other resources (Thorsted *et al*., 2006; Lithourgidis *et al*., 2011). Selection of suitable cultivars and sowing time plays an important role in obtaining higher yields due to good utilizing of residual soil moisture and nutrients from the soil (Mandal *et al*., 1996; Sekhar *et al*., 2015; Kaushik *et al*., 2016). Cultivation of chickpea with cereal crops (barley, wheat, etc.) or oilseed (mustard, linseed, etc.) is well known to farmers of non-insured rain fed areas (Poddar *et al*., 2017). The importance of intercropping is the possibility of increasing the quantity and improving the quality not only by increasing production costs; but also by modifying farm management (Willey, 1979). Intercropping facilitates different resources of returns to the farmer from the same land, and reduces crop failure risk of a mono-cropping when susceptible to ecological and economical fluctuations. This approach was backed by (Khan *et al*., 2005). The objective of this study was to evaluate the effect of intercropping and row ratios on some growth parameters and yield components of wheat, chickpea and wild mustard.

2. MATERIALS AND METHODS

The experiment was carried out at Grdarasha Research Farm, College of Agricultural Engineering Sciences / Salahaddin University / in Erbil-Iraq (36.2º N, 44.1º E and elevation 470 m above the mean sea level). In single, double, and triple (row: species) arrangements were used in a standard replacement series to maintain a total number of 6 rows, which forms seven (row: ratio) consortia. Each group represents one intercropping mixture treatment. Combinations were repeated 3 times to form sixty three units of 2 m rows length and 0.2 m inter-row spacing forming an area of 4.8 m^2. Each treatment was duplicated to avoid any probable risk. The experiment was planned based on the Randomized Complete Block Design (RCBD). Wheat (A), chickpea (B) and wild mustard (C) were sown solely or in 1, 2, 3 rows out of 6 rows per each treatment. They form triple (row: crop) ratios named 1A:2B:3C, 1A:3B:2C, 2A:1B:3C, 2A:2B:2C, 2A:3B:1C, 3A:1B:2C and 3A:2B:1C, respectively plus three sole crops as control treatments. Data are represented by error bars with standard error labeled by (Duncan, 1975) letters for 5% significance. Samples were taken from air dried soil in the field at a depth (0 - 30 cm), and then analyzed for some physical and chemical properties as shown in (Table 1). The recorded rainfall during the growing period from (Nov. 2016 to May. 2017) was 218 mm. The seeds were sown in rows on November 26th 2016. Manual weed control repeated twice. Planting densities were chose based on the recommendations of the competent local agricultural authorities. However, wild mustard density was adopted according to its natural abundance in the region as 175, 63 and 38 plants/m^2 for wheat, chickpea and wild mustard respectively. Seeds of the competitor plant species were obtained from the Directorate of Agricultural Research Station, Erbil.

Table (1): Some selected properties of the soil at the experimental sites.

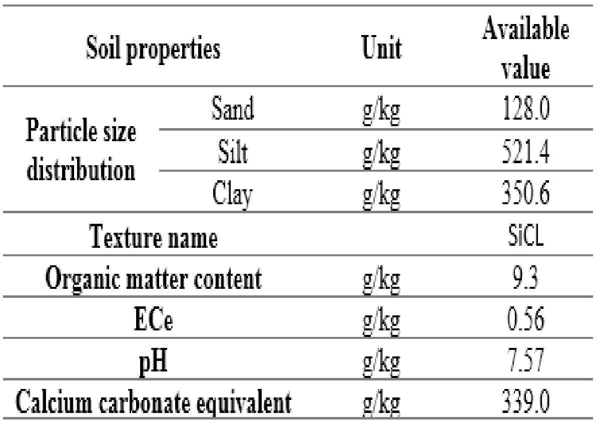

Soil properties		Unit	Available value
Particle size distribution	Sand	g/kg	128.0
	Silt	g/kg	521.4
	Clay	g/kg	350.6
Texture name			SiCL
Organic matter content		g/kg	9.3
ECe		g/kg	0.56
pH		g/kg	7.57
Calcium carbonate equivalent		g/kg	339.0

3. RESULTS AND DISCUSSION

3.1. Days to Flowering

The results of analysis of variance in figure (1) showed that chickpea plant had significant response to number of days to flowering. The highest number was recorded in the mix-consortium 2:3:1 (134.7 days), while 1:2:3 row consortia recorded lowest number of days (129.3). In addition wheat and mustard didn't obtain any significant differences among all treatments.

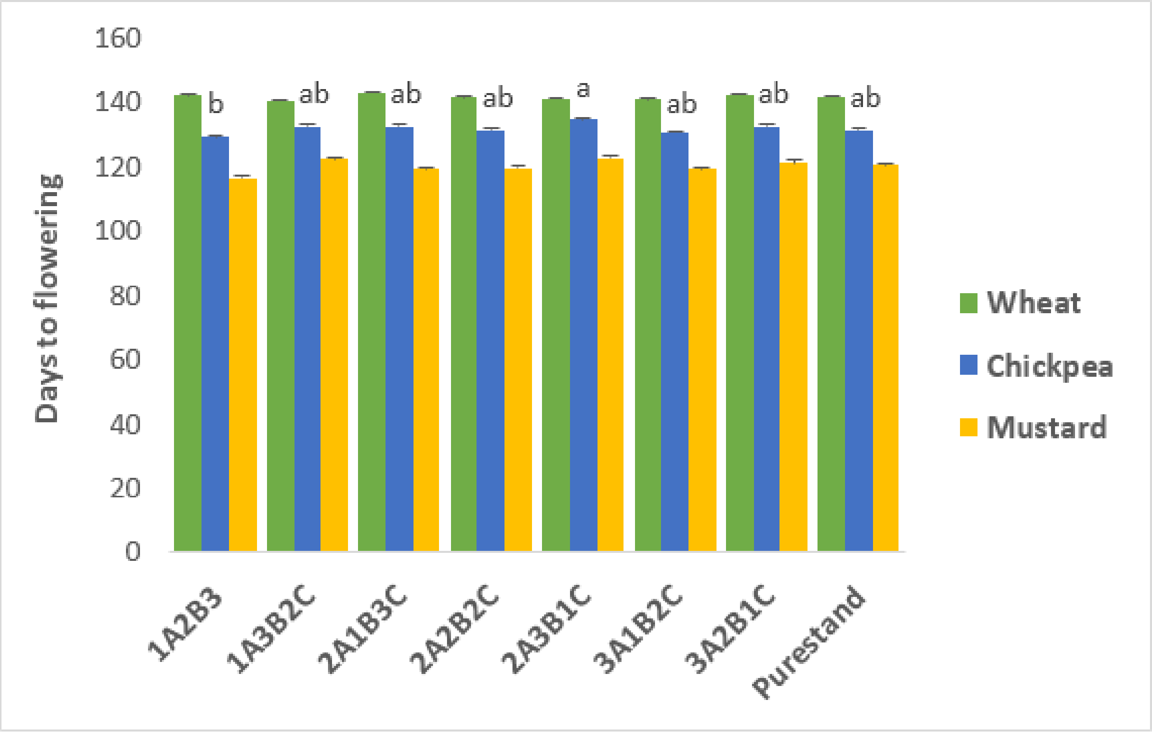

Figure 1: Effect of intercropped species on number of days to flowering.

3.2. Plant Height (cm)

Plant height is an important growth parameter that is affected by genetic and environmental variation. The result in figure (2) indicates the existence of significant differences among all studied factors. The greater plant height (123.0 cm) was showed in the treatments where chickpea and wild mustard was intercropped in 1:2:3 ratios. The wheat recorded minimum plant height of (110.2 cm) at pure stands. Chickpea possessed (77.7 cm) taller plant at 3:1:2 ratio, in addition wild mustard (130.2 cm) the highest mean when planted at 2:3:1 row species consortia. This result is in agreement with the findings of Mandal (1991), who noticed intercropping legume crops significantly increased wheat plant height.

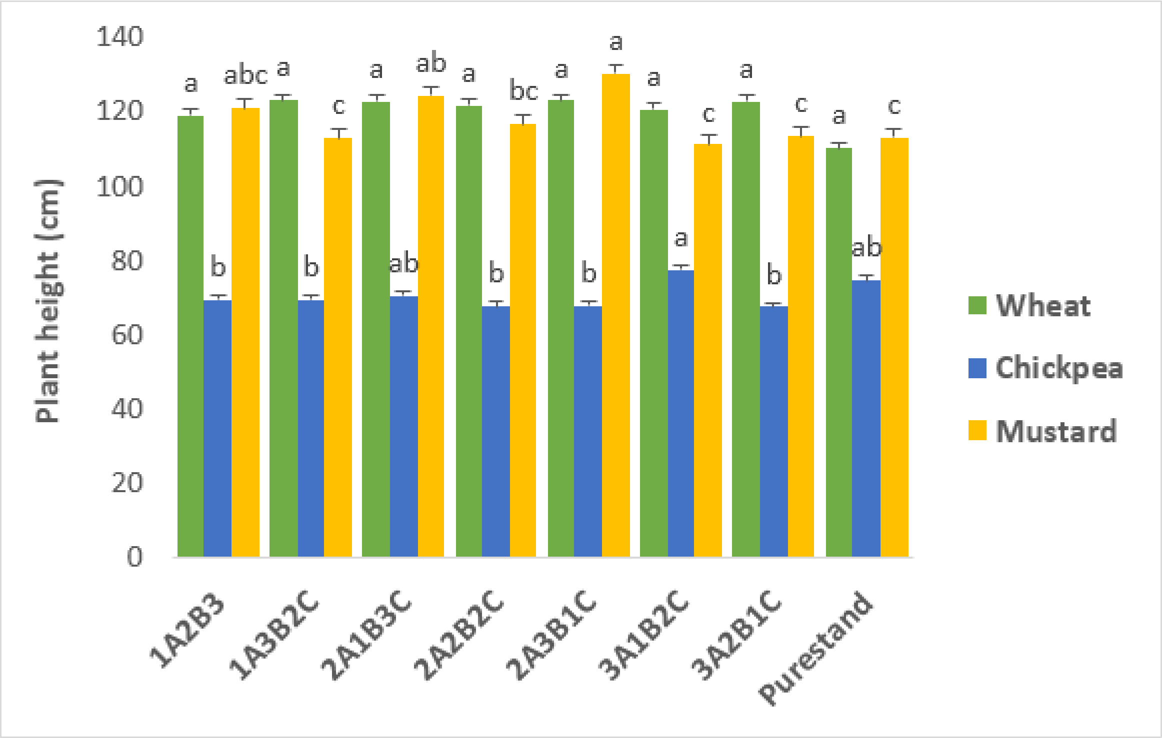

Figure 2: Effect of intercropped species on plant height (cm).

3.3. Number of tillers or branches plant $^{-1}$

Number of wheat tillers and mustard branches responded significantly to mix-culture as they produced (3.3 tillers. plant^{-1}) tiller for wheat and (17.7 branches. plant^{-1}) for mustard at consortia 1:2:3, 1:3:2 and 2:3:1 respectively superior to their pure stands, in addition chickpea obtained the highest mean value (6.0 branches. plant^{-1}) in pure stand, while the lowest value (3.7 branch. plant^{-1}) in mix-consortia 132 ratio (Figure 3). Lemerle *et al*., (2001), note that the number of tillers is the most important yield component in wheat, which reduced with increase competition of weeds. Armin *et al.* (2011) has reported that in condition of competition for nutrients, water and light availability, it will restrict the plant growth and reducing number of tiller per plant. Similar results also found by (Marof, 2008; Marof, 2013).

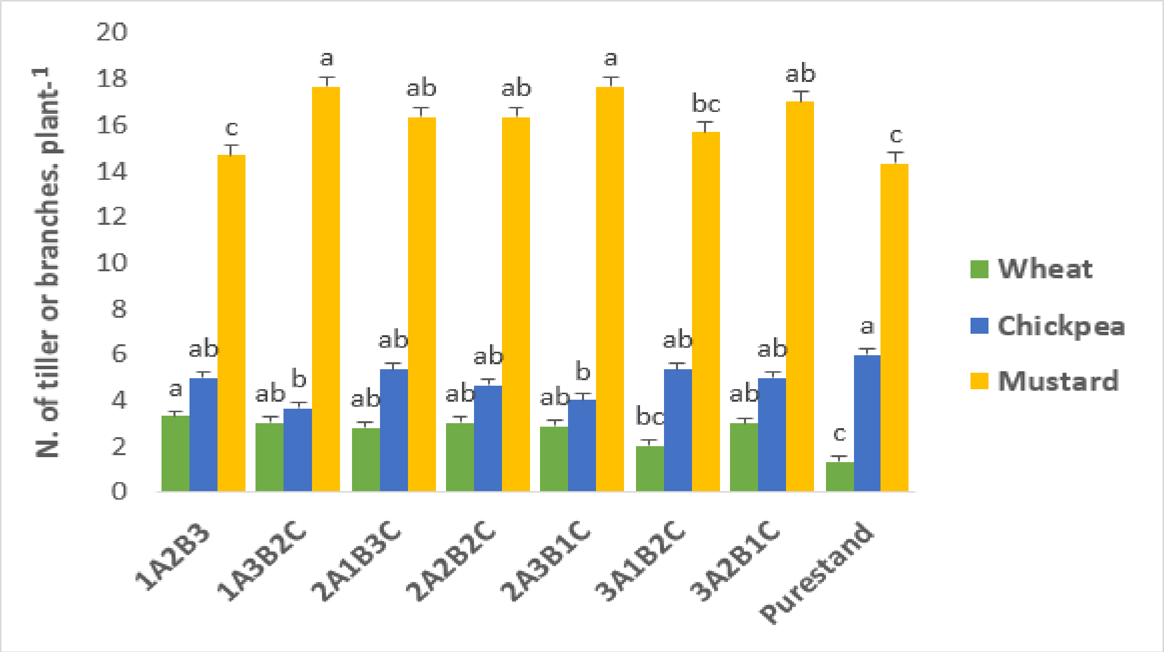

Figure 3: Effect of intercropped species on number of tiller or branch.plant^{-1}.

3.4. Spike or Pod Length (cm)

Statistical analysis of the data figure (4) revealed that chickpea shows non-significant affects in length of reproductive organs pods. However wheat plant recorded longest mean values of (13.9 cm) was possessed in the treatment where wheat was intercropped with chickpea and wild mustard in 1:3:2 ratio, while the smallest was (12.3 cm) planted at 1:2:3 mix consortia. Mustard recorded the longest silique length in the treatment 3:1:2 (2.7 cm), whereas the smallest mean was (2.3 cm) in the treatment 2:1:3 row ratio. Karim and Mamun (1988) reported that competition leads to reduced length of leaves which eventually caused the process of photosynthesis that provided less absorption than required to produce natural spike. These results are in agreement with the findings reported by (Nazir *et al*., 1988; Malik *et al*., 2002; Sinha *et al*., 2009).

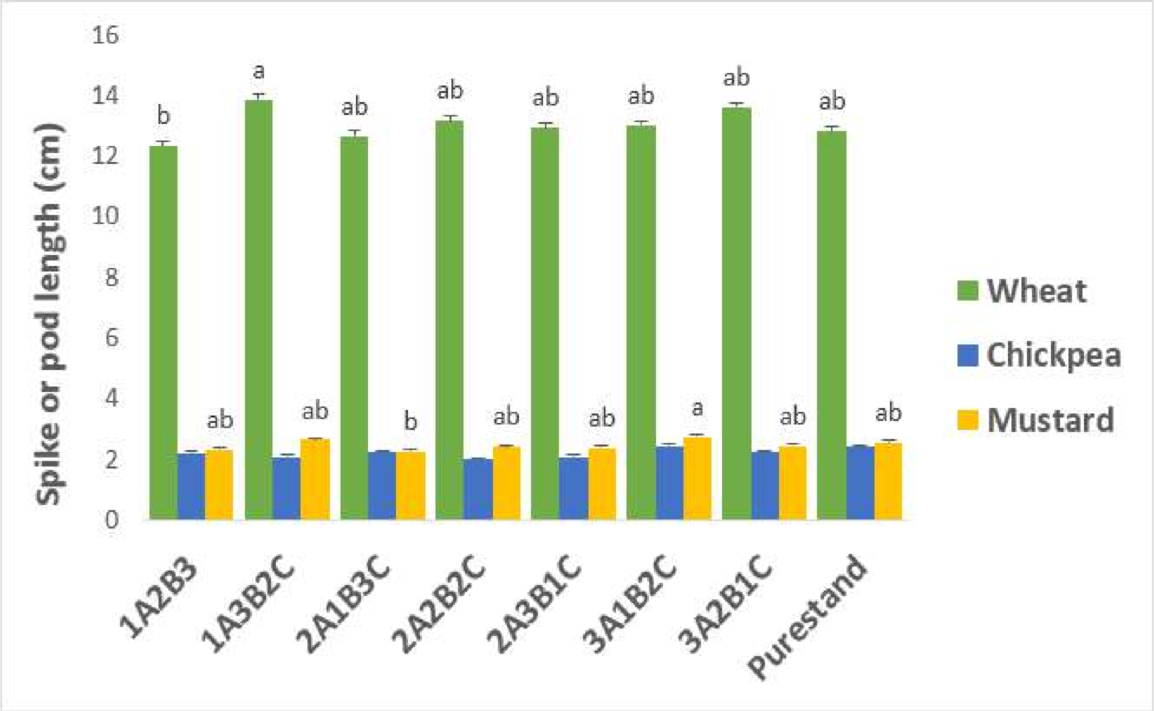

Figure 4: Effect of intercropped species on spike or pod length (cm).

3.5. Grain Number per Spike or Pod

All three competitor plant species in all mix and pure stands showed significant variation number of grain per spike or per pod and silique. The most number of grain was obtained of wheat plant (63.7) at 1:3:2, while the lower mean value was (52.3) in mix-consortia 3:1:2. Chickpea and wild mustard possessed the higher mean value (48.0 and 16.0) in the treatment 1:2:3 and 3:2:1 row ratio, followed by the lower mean was (37.0 and 12.3) in the mix-consortia 3:1:2 and 2:3:1 ratio (Figure 5).

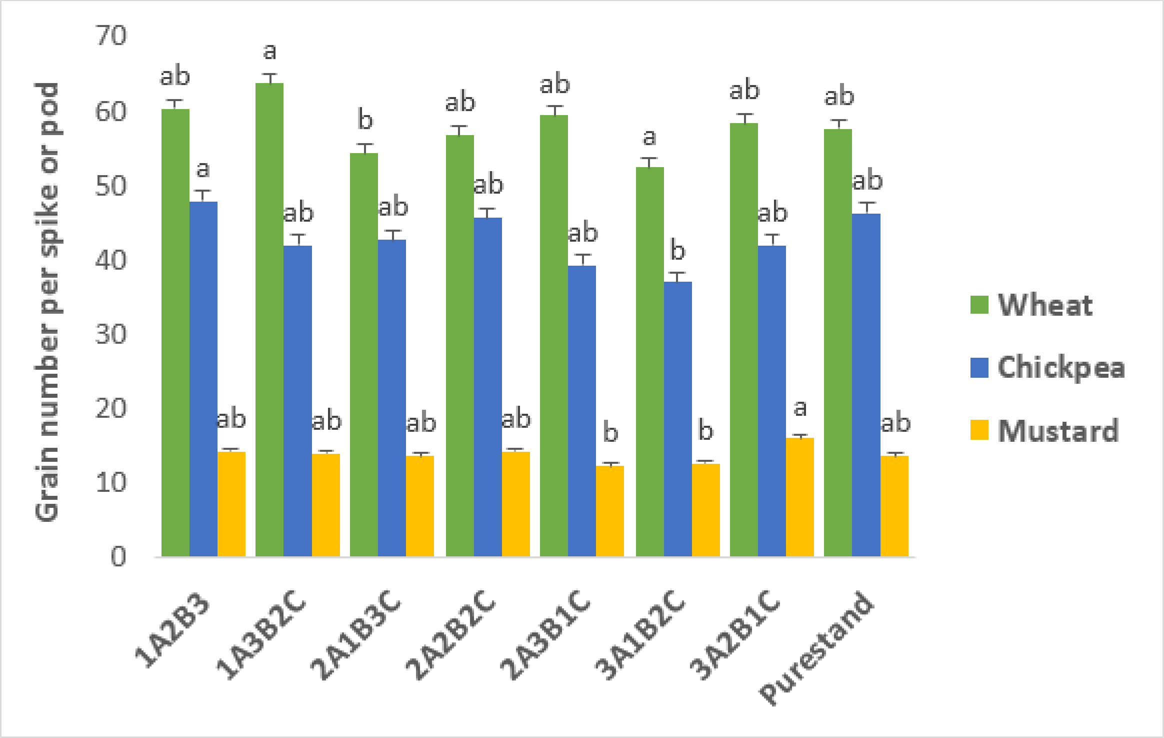

Figure 5: Effect of intercropped species on grain number per spike or pod.

3.6. Days to Maturity

The data Postulated in figure (6) confirm non-significant differences P ≥ 0.05 in the time period required to maturity in general. The highest number was (172.7) showed of wheat at 2:1:3 ratio, followed by mustard weed by (142.7) in 2:2:2 mix- consortium compared with pure stands. The decrease in the length of the plant cycle under rain conditions is one of the main effects of water deficits. (Thompson and Chase 1992), these results are also supported by (Naeem Khan *et al*., 2002; Hassani *et al*., 2006).

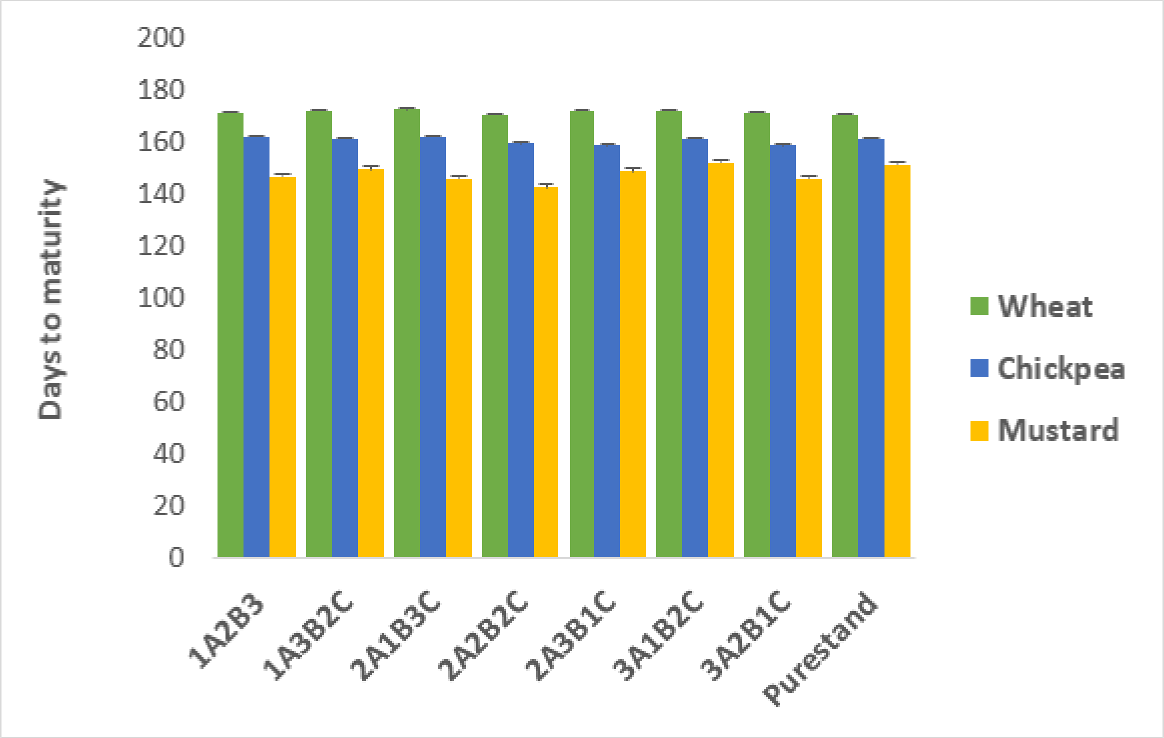

Figure 6: Effect of intercropped species on number of days to maturity.

3.7. Grain Yield (g). m^{-2}

Grain yield displayed in figure (7) shows a wide variation, the highest mean values was (182.0 g. m^{-2}) in the mix consortia 1:2:3, whereas the lowest were at (78.2 g. m^{-2}) in the pure stands of wheat plants. The highest chickpea were (82.4 g. m^{-2}) when intercropped with wheat and mustard at 2:2:2 ratio, but the lowest value was (54.6 g. m^{-2}) in the 3:1:2 row consortia. Wild mustard at pure stand recorded (54.9 g. m^{-2}) which was the highest mean value, while 3:1:2 row consortium recorded lowest value (28.9 g. m^{-2}). There has been a decline in grain yield due to the physiological and morphological characteristics of wheat and weeds that have led to a similar convergence towards the use of natural resources towards final photosynthesis (Sinha *et al*., 2009).

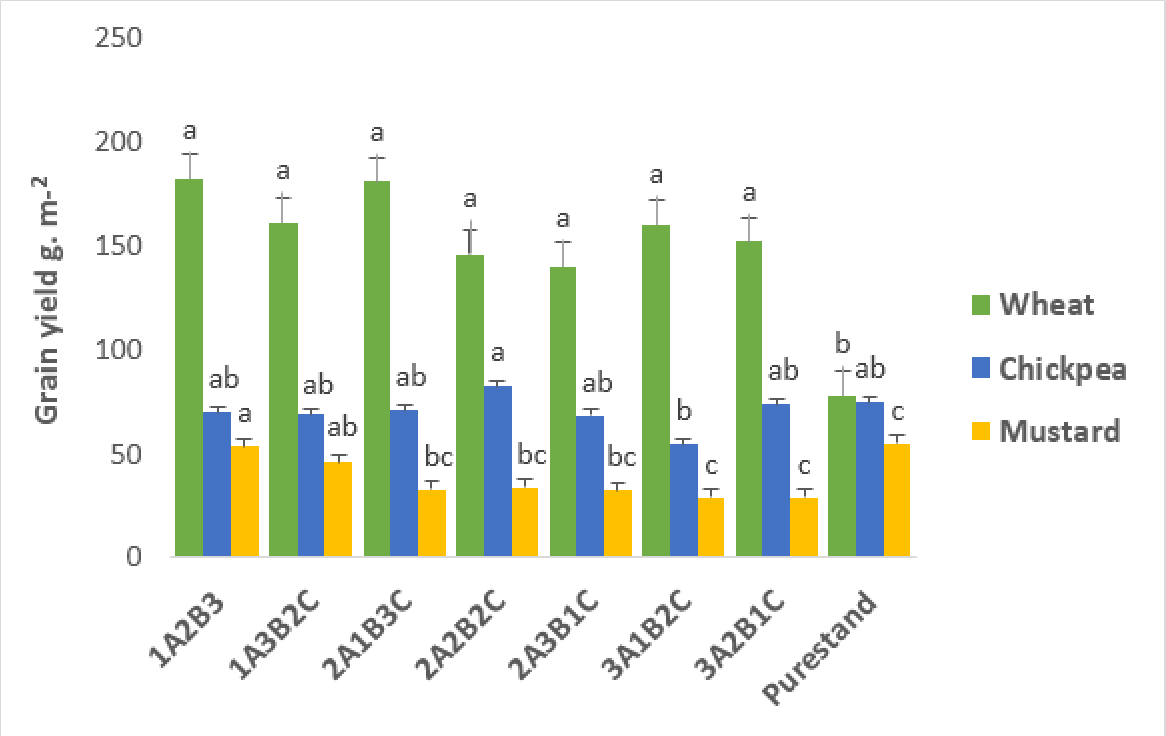

Figure 7: Effect of intercropped species on grain yield (g). m^{-2}.

3.8. Straw Yield (g). m^{-2}

Figure (8) revealed that straw yield recorded highest significant mean value of wheat in the mix stand 1:2:3 was (752.5 g. m^{-2}), whereas the lowest value was (385.7 g. m^{-2}) in the pure stand. Wild mustard cultivated produced higher straw yield (211.9 g. m^{-2}) in the pure stand over all mix-consortia. However chickpea plants showed non-significant effected on mean straw yield over all studied treatments. Hossain *et al.* (2010), suggested that straw yield decreases with increased competition for weeds, because the plant cannot take more light for photosynthesis and tillage production, while disagree results were noted by (Marof, 2008).

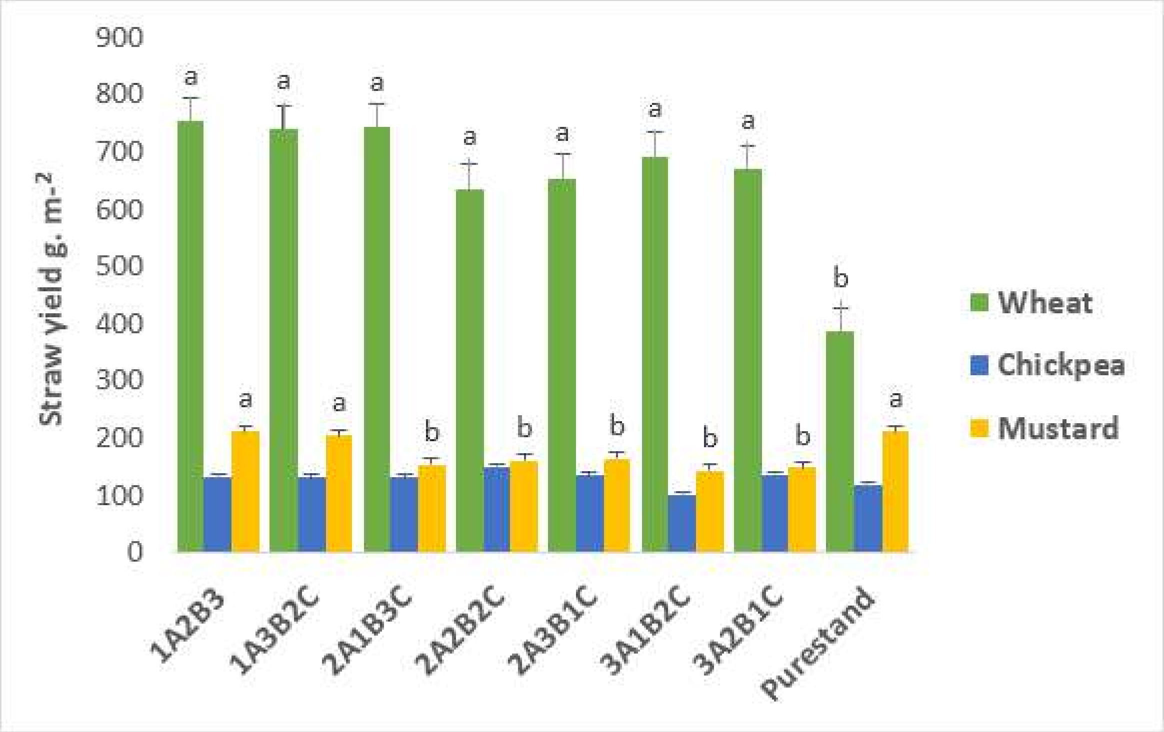

Figure 8: Effect of intercropped species on straw yield (g). m^{-2}.

3.9. Biological Yield (g). m^{-2}

Biological yield is correlated with plant height and number of tillers. The data presented in figure (9) shows that chickpea and wild mustard possessed the highest mean value (233.1 and 266.7 g. m^{-2}) in 2:2:2 mix and pure stand respectively. In addition 3:1:2 row mix-consortia recorded the lowest value which was (155.5 and 171.8 g. m^{-2}) respectively. Additionally wheat plant didn't possess any significant differences over all mix and pure stands in this trait.

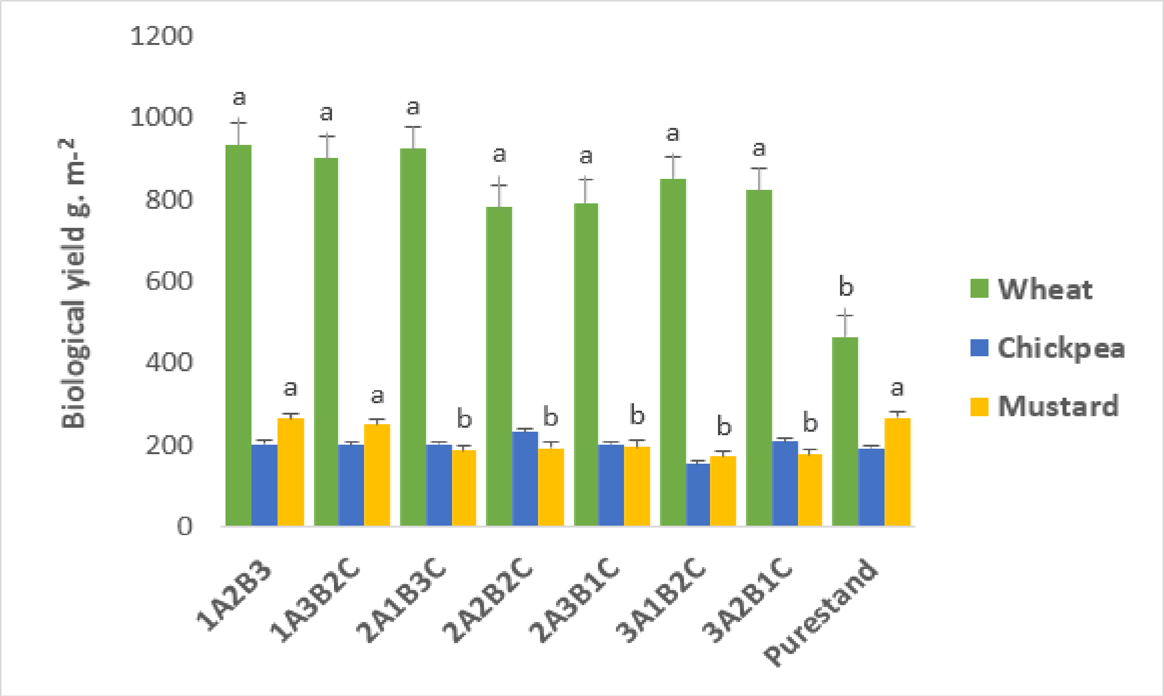

Figure 9: Effect of intercropped species on biological yield (g). m^{-2}.

3.10. Harvest Index

The results of harvest index displayed in figure (10) the higher mean value of cultivated chickpea was (0.38) in pure-stand, whereas the lowest was recorded at 2:3:1 which was (0.33). The maximum was for mustard provided (0.20) in mix consortia 1:2:3 and pure stand respectively. However, wheat plant showed no significant differences among all studied treatments.

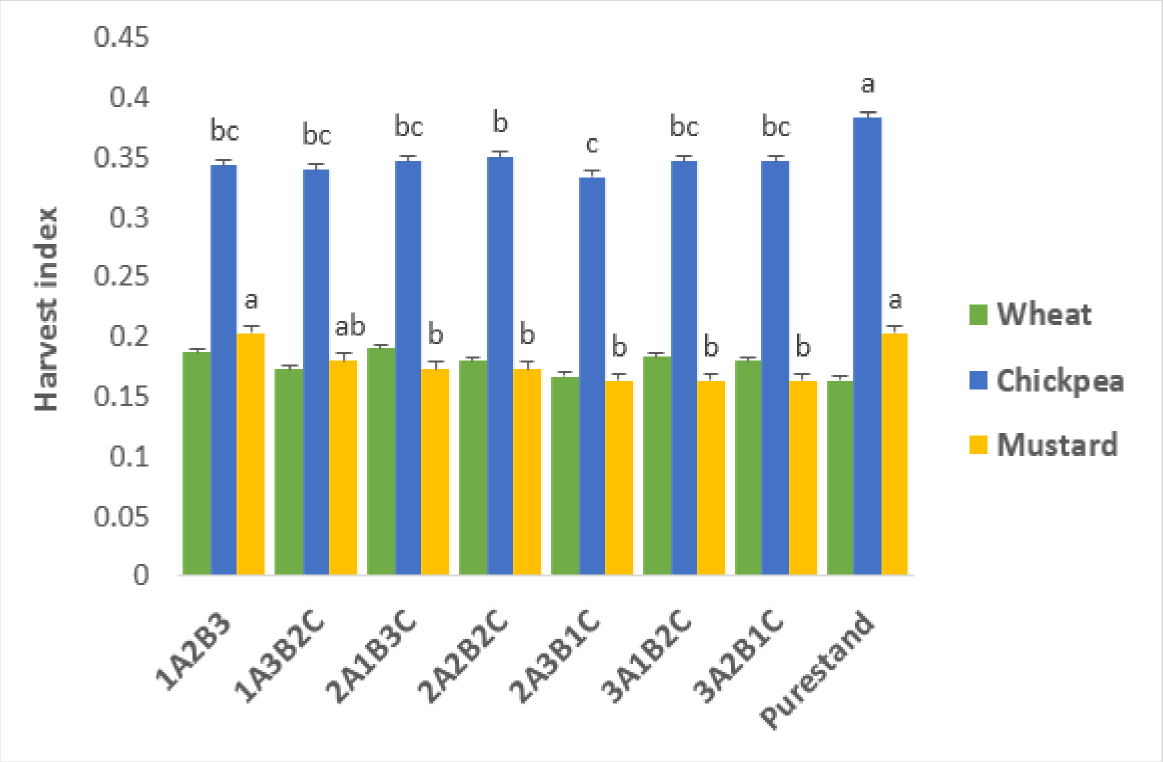

Figure 10: Effect of intercropped species on harvest index.

3.11. Relative Yield and Relative Yield Total

The data presented in figure (11) turns out that partial relative yield of chickpea and mustard plant scored highest significant mean value 1.102 in mix consortium 2:2:2 and 0.979 in 1:2:3 mix consortia over pure stands, while wheat plant didn’t scored any significant effects. Total relative yield scored higher mean value 1.414 in mix consortia 1:2:3 and lower mean value 1.098 in 2:3:1 mix consortium.

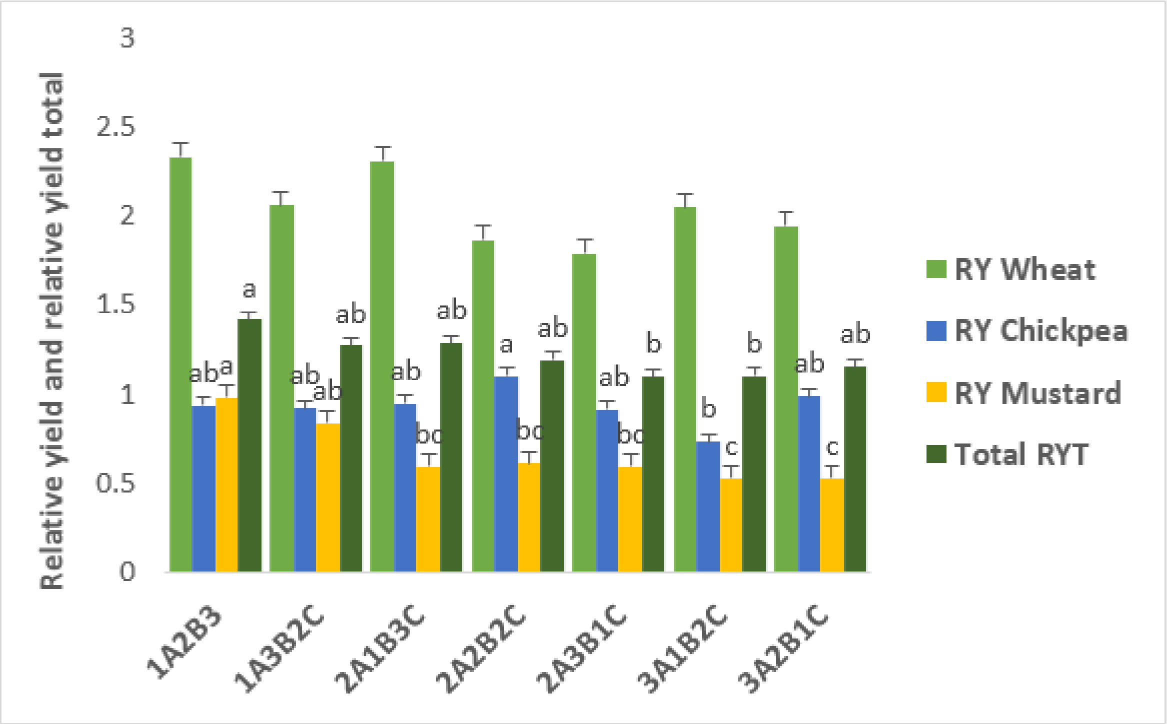

Figure 11: Effect of intercropped species on relative yield and relative yield total.

Table (2): The analysis of variance (ANOVA) for the effect of intercropped species on growth, yield and yield components.

Crop	Source DF	Sum of Squares	df	Mean Square	F	Sig.
	Parameters					
Wheat	Days to flowering	14	7	2	0.857	0.559
	Plant height (cm)	394.8	7	56.4	3.091	0.029
	N. of tiller. plant^{-1}	9.052	7	1.293	3.119	0.028
	Spike length (cm)	5.166	7	0.738	1.665	0.188
	Grain number. spike^{-1}	260	7	37.143	2.19	0.092
	Days to maturity	10.5	7	1.5	0.643	0.715
	Grain yield g. m^{-2}	22390.3	7	3198.61	2.314	0.078
	Straw yield g. m^{-2}	295105	7	42157.8	5.454	0.002
	Biological yield g. m^{-2}	476683	7	68097.6	4.544	0.006
	Harvest index	0.002	7	0	0.581	0.762
Chickpea	Days to flowering	54.5	7	7.786	1.797	0.157
	Plant height (cm)	287.265	7	41.038	1.992	0.12
	N. of branch. plant^{-1}	11.958	7	1.708	1.864	0.143
	Pod length (cm)	0.516	7	0.074	1.351	0.291
	Grain number. pod^{-1}	283.958	7	40.565	1.732	0.172
	Days to maturity	43.833	7	6.262	0.737	0.645
	Grain yield g. m^{-2}	1290.05	7	184.293	1.007	0.462
	Straw yield g. m^{-2}	4445.96	7	635.137	0.971	0.484

	Biological yield g. m^{-2}	9765.76	7	1395.11	0.917	0.519
	Harvest index	0.005	7	0.001	13.321	0
Wild Mustard	Days to flowering	79.167	7	11.31	1.299	0.312
	Plant height (cm)	952.213	7	136.03	4.448	0.006
	N. of branch. $plant^{-1}$	33.292	7	4.756	5.188	0.003
	Silique length (cm)	0.576	7	0.082	1.317	0.304
	Grain number. $silique^{-1}$	26.625	7	3.804	1.049	0.437
	Days to maturity	202	7	28.857	0.63	0.725
	Grain yield g. m^{-2}	2492.85	7	356.121	5.316	0.003
	Straw yield g. m^{-2}	18298	7	2614	5.313	0.003
	Biological yield g. m^{-2}	34028.4	7	4861.19	5.665	0.002
	Harvest index	0.006	7	0.001	2.904	0.037

Significant occurs when $P \leq 0.05$

4. CONCLUSIONS

Intercropping could reduce the yield of mustard to about 30% compared to the yield in its sole cropping. Wheat and chickpea did not show any reciprocal significant harm effects on each other.

Acknowledgements

I heartily thank Field Crops Department, Agricultural Engineering Sciences College, and Salahaddin University - Erbil for their help towards successful completion of the work.

REFERENCES

Ali, Z., Malik, M.A. and Cheema, M.A. 2000. Studies on determining a suitable canola-wheat intercropping pattern. *International Journal of Agriculture and Biology*, *2*(1-2), pp.42-44.

Armin, M., H. gholami and H. Miri. 2011. Effect of Plant Density and Nitrogen Rate on Yield and Yield Components of Wheat in Wild oat-Infested Condition. Advances in Environmental Biology, 5(10): 3084-3090.

Aziz, F.H. 1991. Studies on the effect of timing of fertilizer additions on the competition within and between wheat and syrian cephalaria different plant densities. (Zanko) Sci. J. Salahaddin Univ., 4(3): 35-56.

Bhan, A. and R.J. Froud-Williams. 2005. *Phalaris* spp. competition with wheat using an additive design series. 15th Austr. Weeds Conf., 417-419.

Bybee-Finley, K. and Ryan, M. 2018. Advancing Intercropping Research and Practices in Industrialized Agricultural Landscapes. Agriculture, 8(6), p.80.

Duncan, D.B., 1975. T tests and intervals for comparisons suggested by the data. Biometrics, pp.339-359.

Erdemci, I., 2018. Investigation of genotype× environment interaction in Chickpea genotypes using AMMI and GGE biplot analysis. Turkish Journal Of Field Crops, 23(1), pp.20-26.

Harper, J.L., 1977. Population biology of plants. Academic Press London. PP: 892.

Hassani, H.S.; S.M. Reader and T.E. Miller. 2006. Agronomical and Adaptation Characters of Tritipyrum lines in comparison with Triticale and Iranian Wheat. Asian J. PL.Sci.5 (3): 553-58.

Hossain, A., M.A.S. Chowdhury, T. Jahan, M.A.I. Sarker and M.M.Akhter. 2010. Competitive ability of wheat cultivars against weeds. Bangl. J. Weed Sci., 1(1): 63-70.

Karim, S.M.R. and A.A. Mamun. 1988. Crop-weed competition: Analysis of some perspectives. Bangladesh J. Agril. Sci. 15(1): 65-73.

Kaushik, S.S., Singh, D.V., Rai, A.K., Sharma, A.K. and Negi, R.S. 2016. Response of intercropping and different row ratios on growth and yield of wheat (*Triticum aestivum*) under rainfed condition of kaymore plateau. *5:* PP.15-19.

Khan, M., Khan, R.U., Wahab, A. and Rashid, A. 2005. Yield and yield components of wheat as influenced by intercropping of chickpea, lentil and rapeseed in different proportions. *Pak. J. Agric. Sci*, *42*, pp.1-3.

Khursheed, M.Q. and Mahammad, M.Q. 2015. Effect of different nitrogen fertilizers on growth and yield of wheat. *ZANCO Journal of Pure and Applied Sciences*, *27*(5), pp.19-28.

Lemerle, D., G.S. Gill, C.E. Murphy, S.R. Walker, R.D. Cousens, S. Mokhtari, S.J. Peltzer, R. Coleman and D.J. Luckett. 2001. Genetic improvement and agronomy for enhanced wheat competitiveness with weeds. Aust. J. of Agric. Res., 52(5): 527-548.

Lithourgidis AS, Dordas CA, Damalas CA, Vlachostergios DN. 2011. Annual intercrops: an alternative pathway for sustainable agriculture. Aust J Crop Sci 5:396–410.

Malik, M.A., F. Hassan and I. Aziz. 2002. Feasibility of intercropping lentil and lathyrus in wheat under rainfed condition. Pak. J. Arid Agric. 5(1): 13-16.

Malik, M.A., Hayat, M.A., Ahmad, S. and Haq, I. 1998. Intercropping of lential, gram and rape in wheat under rainfed conditions. Sarhad Journal of Agriculture (Pakistan). 14: 417-421.

Mandal, B.K., Das, D., Saha, A. and Mohasin, M. 1996. Yield advantage of wheat (*Triticum aestivum*) and chickpea (*Cicer arietinum*) under different spatial arrangements in intercropping. *Indian Journal of Agronomy*, *41*(1), pp.17-21.

Mandal, B.K., Dasgupta, S. and Ray, P.K.1985. Effect of intercropping on yield components of wheat, chick pea and mustard under different moisture regimes. *Zeitschrift fur Acker-und Pflanzenbau, Journal of agronomy and crop science*. 155: 261-267.

Mandal, B.K., S. Dasgupta and P.K. Roy. 1991. Effect of intercropping on yield components of wheat, chickpea and mustard under different moisture regimes. Field Crop Absts., 39(10): 7025.

Marof, S.M.A. 2008. Competitive interference between triticale x Triticosecale Rimpaui Wittmac and wheat Triticum spp. L. under two environmental conditions. Ph.D. Desertation. Coll. of Agric. Salahddin University. PP: 181.

Marof, S.M.A. 2013. Utilizing of new models to predict wheat yield losses due to weed competition. Kerkuk University, Agric. Coll. 2nd Sci. Confe. for Agric. Res., PP: 57-62.

Naeem Khan,A.Jan, A.K. Ijaz, M.A. Khan and Ihsanulla. 2002. Response of wheat cultivers to varying seeding rates under rainfed conditions Asian J.PI. Sci. 1(4):343-345.

Nazir, M.S., H.R. Khan, G. Ali and R. Ahmad. 1988. Inter/relay cropping in wheat planted in multi-row strips at uniform plant population. Pak. J. Agric. Res. 9(3): 305-309.

Poddar, R., Kundu, R. and Kumar, S. 2017. Assessment of Chickpea-Spices Intercropping Productivity Using Competitive Indices Under Irrigated Conditions of Haryana. *Agricultural Research*, *6*(3), pp.241-247.

Qader, H.R. 2019. Influence combination of Fruits Peel and Fertilizer Methods on growth and yield of Chickpea (*Cicer areitinum*) L. Plants. *ZANCO Journal of Pure and Applied Sciences*, 31(3), pp. 45-51.

Rejmánek, M., Robinson, G.R. and Rejmankova, E. 1989. Weed-crop competition: experimental designs and models for data analysis. Weed Science, 37(2), pp.276-284.

Sekhar, D., Kumar, P.P. and Rao, K.T. 2015. Performance of chickpea varieties under different dates of sowing in high altitude zone of Andhra Pradesh, India. *Int. J. Curr. Microbiol. App. Sci*, *4*(8), pp.329-332.

Shaker-Koohi, S. and Nasrollahzadeh, S. 2014. Evaluation of yield and advantage indices of sorghum (Sorghum bicolor L.) and mungbean (Vigna radiate L.) intercropping systems. *International Journal of Advanced Biological and Biomedical Research*, *2*(1), pp.151-160.

Sharma, K.C., Sing, Y., Gupta, P.C., Tripathy, S.K., Bhardwaj, A.K. and Singh, S.P. 1986. Plant population and spatial arrangement in wheat-mustard intercropping. *Indian J. Agron*, *31*, pp.154-157.

Singh, O. and Pal, M. 1994. Performance of wheat+ mustard intercropping system in limited irrigation conditions. *Ann. Agric. Res*, *15*, pp.255-259.

Sinha, N.K., D. Singh and D.K. Roy. 2009. Economic threshold levels of little seed canary grass in wheat in north Bihar. Indian J. of Weed Sci., 41(3&4): 154-156.

Siyahpoosh, A., Fathi, G.A., Zand, E., ata Siadat, S., Bakhshande, A. and Gharineh, M.H. 2012. Competitiveness of Different Densities of Two Wheat Cultivars with Wild Mustard Weed Species (Sinapis arvensis) in Different Densities. *World Applied Sciences Journal*, *20*(5), pp.748-752.

Thompson, J.A. and D.L.Chase. 1992. Effect of limited irrigation on growth and yield of a semi-dwarf wheat in southern New South Wales. Australian J. of experimental Agriculture. East Melboume, V : 30, p 727-730.

Thorsted MD, Weiner J, Olesen JE. 2006. Above- and belowground competition between intercropped winter wheat Triticum aestivum and white clover Trifolium repens. J Appl Ecol 43:237–245.

Wilcox, D.H. 1995. Models of interference in monocultures and mixtures of wheat and quack grass. Ph.D. Dissertation. Univ. of Manitoba. PP: 34-45.

Willey RW. 1979. Intercropping, its importance and research needs. Part-I. Competition and yield advantages. Field Crop Abstr 32(1): 1-10.

ZANCO Journal of Pure and Applied Sciences
The official scientific journal of Salahaddin University-Erbil
https://zancojournals.su.edu.krd/index.php/JPAS

ISSN (print):2218-0230**, ISSN (online):** 2412-3986**, DOI: http://dx.doi.org/10.21271/zjpas**

RESEARCH PAPER

Using Double Function Solubility Diagram to Study the Effect of Phosphorus Fertilizer on the Availability of Phosphorus in Different Soil Orders.

Muslim Rasul Arab Khoshnaw[1] and Akram Othman Esmail[1]

[1]Department of Soil and Water, College of Agricultural Engineering Sciences, Salahaddin University-Erbil, Kurdistan Region, Iraq

ABSTRACT

A pot experiment was carried out during autumn growing season of 2016-2017 at the Gerdarasha field of College of Agriculture Engineering Sciences, to study the effect of three dominant soil orders (Mollisols (M), Vertisols (V) and Aridisols (A)), five levels of applied phosphorus fertilizer (0, 80, 160, 240 and 320 kg TSP ha^{-1}) and combination between them on the availability of phosphorus (P) using solubility diagram at booting stage and wheat yield. The factorial experiment was depended using a completely randomized design (CRD) with three replicates. The results indicated that the soil orders were affected the phosphorus status. It appears that the soil order studied was plotted between di calcium phosphate DCP and octa calcium phosphate OCP. The phosphorus availability of the studied soil orders can followed the following series Mollisols (M) > Vertisols (V) > Aridisols (A). The application of phosphorus caused an increase in phosphorus availability or caused shifting the treatments towards the more soluble forms of phosphorus Di calcium phosphate di hydrate (DCPD). The combination of soil orders and levels of applied phosphorus also influenced on phosphorus status. The application of 320 kg.ha^{-1} of triple superphosphate to the Mollisols soil increased the phosphorus status toward the plotted between DCP and DCPD which were the most soluble forms of phosphorus in the phosphorus solubility diagram, which recorded the highest wheat yield (3.66) *Mg* ha^{-1} in combination treatment (Mollisols-TSP$_{320}$). While the lowest grain yield (2.06) *Mg* ha^{-1} was obtain from (Aridisol-TSP$_0$) since this combination treatment was plotted between TCP and OCP or non-soluble and low soluble P-compounds.

KEY WORDS: Solubility Diagram; Phosphorus availability, Soil orders.
DOI: http://dx.doi.org/10.21271/ZJPAS.32.1.14
ZJPAS (2020) , 32(1);127-136 .

INTRODUCTION :

hosphorus is an essential macronutrient for plant growth, and it is limiting crop production in many regions of the world in many agricultural systems in which the application of phosphorus to the soil is necessary to ensure plant productivity.

The recovery of applied P by plant crops in calcareous soils during the growing season is very small, since more than 80% of the P becomes immobile and unavailable for plant uptake due to adsorption, or precipitation (Esmail, et al 2018; Rekani et al. (2017))

Iraqi soils are containing a large amount of calcium carbonate with slightly alkaline pH which causes chemical and physical fixation of 70-90% of applied phosphorus fertilizers as reported by Esmail (2012)

The previous studies conducted by Roy et al. (2006), (Shand, 2007) phosphorus was absorbed as the orthophosphate ion (either as $H_2PO_4^-$ or HPO_4^{2-})

*** Corresponding Author**

Muslim Rasul Arab Khoshnaw

E-mail: muslim.khoshnaw@su.edu.krd

Article History:
Received: 27/08/2019
Accepted: 14/10/2019
Published: 25/02 /2020

depending on soil pH. As the soil pH increased, the relative proportion of $H_2PO_4^-$ and HPO_4^{2-} were increased. P is essential for growth, cell division, root lengthening, seed and fruit development, and early ripening. It is a part of several compounds including oils and amino acids. The P compounds adenosine di phosphate (ADP) and adenosine triphosphate (ATP) act as energy carriers within the plants.

Phosphorus is one of the most important essential macro nutrients for plants, which contributes to numerous vital functions in plants like photosynthesis, energy transfer, respiration and cell division mentioned by Mam Rasul (2016), (Rasheed, 2019).

Iraqi soils illustration different degrees of development according to the dominant local conditions mainly climatic and geological conditions. The results of the morphological, physical and chemical soil properties indicated to the presence of five soil orders included, Aridisols, Entisols, Inceptisols, Mollisols, and Vertisols (Muhaimeed et al., 2014).

For studying the solubility equilibrium of phosphate the double function parameters consisting of phosphate potential $\log H_2PO^-_4$-pH and lime potential ($\log Ca^{2+} + 2pH$) were used to construct a solubility diagram for calcium phosphate minerals. It was assumed that the free ion activity of $H_2PO^-_4$ was controlled by lime potential and pH based on published solubility product (KSP). It was also assumed that the solubility of phosphate in calcareous soils is controlled by a solid phase of calcium phosphate minerals (Lindsay, 1979, Shang and Tiessen, 1998).

Solubility equilibrium experiments generally categorize soils into those with low pH in which iron (Fe) or aluminium (Al) phosphates control P solubility, or those with high pH in which P solubility is controlled by calcium (Ca) phosphates as reported by McDowell et al. (2003).

Phosphorus (P) retention and mobilization take place due to precipitation and adsorption in calcareous soils; however, it is not always easy to distinguish between the two mechanisms. Water-soluble P fertilizers applied to soil react with the soil constituents to form less soluble phosphates. When added to soil containing large amounts of calcium, soluble P is usually precipitated as di calcium phosphate or octa-calcium phosphate as mentioned by (Galaly, 2010, Rasul, 2016, Muhawish and Al-Kafaje, 2017b).

The high response for soil to orthophosphate O.P was recorded with respect to dicalcium phosphate dihydrate (DCPD) at high rate of application and within short and long period of O.P supply within 15and 60 days mentioned by Rahman (2013).

Rasheed, (2019) analysed 120 soils from the wheat grown fields the results indicated that soils that have more available P, the P- compounds were in the form of DCP and TCP but soils that have less available P the P compounds were in the form of TCP and HA (un soluble form).

The objectives of the present work were to investigate the interaction effect of phosphorus levels fertilizer application and soil orders, on grain yield of wheat and phosphorus availability using double function solubility diagram. in calcareous soil.

1.MATERIALS AND METHODS

The studied soils included three dominant soil orders Mollisols (M), Vertisols (V) and Aridisols (A) according to United State Department of Agriculture (USDA) soil Taxonomy (Nachtergaele, 2001), and Global Positioning System (GPS) reading of the selected locations were recorded from **Table (1).**

Soils were included three dominant soil orders which were collected from Hawler, Sulaimani and Duhok governorates from the depth of 0-30 cm, then transported to Gerdarasha field then air-dried and sieved by 4mm sieves for pot experiment. On 24/11/2016 seeds of wheat (*Triticum aestivum* L) was planted.

Table 1. Classification of the studied soils along with their geographic coordinates.

Governorate	Location	Order	Elevation above mean sea level (Altitude (m))	GPS Reading	
				N	E
Hawler	Harrier	Vertisols	619	36°32.793'	44°18.308'
	Hujran	Mollisols	787	36 ° 16.387'	44°17.796'
	Makhmur	Aridisol	271	35.7773774 °	43.562006 °
Duhok	Semeel	Vertisols	569	36.867697 °	42.969343 °
	Zawita	Mollisols	967	36.900077 °	43.146660 °
	Fayda	Aridisol	372	36.712639 °	42.971565 °
Sulaimani	Bakrajo	Vertisols	731	35.529235 °	45.335274 °
	Halabja	Mollisols	501	35.300880 °	45.954688°
	Kfry	Aridisol	177	34.690550 °	44.864398 °

Wheat (*Triticum aestivum* L) is one of the most important cereal grain crops for human nutrition due to high protein content (9% - 15%) and has been cultivated in calcareous soil in the arid and semi-arid region. directly planted in each pot, using factorial (CRD) with three replicates. Each soil order was taken from three locations and regarded as replications. The weight of soil per pots was 10 kg of air-dried soil.

Five levels of triple super phosphate fertilizer (0, 80, 160, 240 and 320 kg TSP ha^{-1}) which equivalent to (0, 0.2, 0.4, 0.6 and 0.8 g TSP for 10 kg $^{-1}$ soil (pot) in three dominant soils orders (M, V, and A), while fixed amount of urea (0.6 g. urea 10 kg^{-1} soils) which equivalent to (240 kg urea ha^{-1}) was added to all pots. After the seeds were planted the pots were watered to field capacity, while subsequently irrigation depended on weighing method whenever needed. The irrigation was done after depletion 75 % of available water depending on weighing method. The soil samples were taken at booting stage for preparing solubility diagram

2.1.Chemical and physical properties

The soils were air-dried, and sieved by 2 mm sieve and stored for laboratory analysis, **Table (2)** shows some chemical and physical properties for the main soil order at different locations.

The soil analysis included Electrical Conductivity, soil calcium carbonate content ($CaCO_3$) hygroscopic moisture content, moisture at field capacity (FC) and wilting point (W.P), Particle size distribution, Soil pH, and organic matter content which were determined according to the standard methods mentioned by (Bashour and Sayegh, 2007). Used the regression equations to estimate the field capacity and wilting point depending upon the clay fraction % .(Klute, 1986, Karim, 1999).

Table 2. The mean for some chemical and physical properties for dominant soil orders Mollisols, Vertisols, Aridisol in Hawler, Sulaimani and Duhok.

Treatment	Particle Size Destitution			hygroscopic moisture%	FC	WP	SP	$CaCO_3$	pH	EC
					%			g kg^{-1}		dS m^{-1}
Mollisols Hawler	Sand	23.00	Silty loam	5.05	21.25	11.59	39.52	300	7.39	0.36
	Silt	56.93								
	Clay	20.06								
Mollisols Sulaimani	Sand	11.41	Siltyloam	6.00	30.35	19.62	56.45	230	7.31	0.54
	Silt	45.59								
	Clay	43.00								
Mollisols Duhok	Sand	17.62	Siltyclay	4.86	30.25	19.53	56.27	210	7.54	0.485
	Silt	39.63								
	Clay	42.75								
Vertisols Hawler	Sand	45.24	Siltyclay	4.24	32.17	21.22	59.83	300	7.47	0.41
	Silt	7.19								
	Clay	47.57								
Vertisols Sulaimani	Sand	4.32	Siltyclay	4.71	35.37	24.04	65.78	268	7.464	0.31
	Silt	40.05								
	Clay	55.63								
Vertisols Duhok	Sand	3.50	Siltyclay	9.20	33.50	22.39	62.30	240	7.47	0.37
	Silt	45.58								
	Clay	50.92								
Aridisol Hawler	Sand	22.02	Clay loam	2.34	24.01	14.03	44.65	488	7.78	0.51
	Silt	50.96								
	Clay	27.02								
Aridisol Sulaimani	Sand	14.37	Siltyclay loam	3.78	25.76	15.58	47.92	460	7.72	0.45
	Silt	54.18								
	Clay	31.45								
Aridisol Duhok	Sand	22.11	Clay loam	2.89	27.78	17.35	51.67	590	7.92	0.46
	Silt	41.36								
	Clay	36.53								

2-2-Determination of soluble Phosphorus for solubility diagram:

Phosphorus in soil has been extracted by using distilled water with 0.01 *M* KCl and determined spectrometric ally according to Murphy and Riley (1962) as described in Black, (1980) using spectrophotometer model (Shimadzo at wave length 880nm). The chemical analysis and calculations for drawing solubility diagram were recorded in **table (3).**

2-3-Phosphate solubility Diagram :

Double function parameters consisting of phosphate potential $\log H_2PO^{-}_{4}$-pH and lime potential ($\log Ca^{2+} + 2pH$) were used to construct a solubility diagram for calcium phosphate minerals. It was assumed that the free ion activity of $H_2PO^{-}_{4}$ was controlled by lime potential and pH based constant of solubility product (Ksp). It was also assumed that the solubility of phosphate in calcareous soils is controlled by a solid phase of calcium phosphate minerals (Lindsay, 1979).

Table 3. pH, (calcium and phosphorus activity), P-potential and lime potential for studied combination treatments.

Code	pH	Soluble P	Ca	P	Ca	Log $H_2PO^-_4$	Log Ca^{+2}	Log Ca^{+2}+2pH	Log $H_2PO^-_4$ -pH
		mg L^{-1}	mg L^{-1}	mole L^{-1}	mole L^{-1}				
Mollisols TSP0	7.53	0.11	64.00	3.66E-06	0.0016	-5.43615	-2.79588	12.26412	-12.9662
Mollisols TSP80	7.55	0.13	64.00	4.11E-06	0.0016	-5.38566	-2.79588	12.30412	-12.9357
Mollisols TSP160	7.88	0.17	108.00	5.34E-06	0.0027	-5.2728	-2.56864	13.18136	-13.1478
Mollisols TSP240	7.84	0.28	50.00	9.14E-06	0.00125	-5.03906	-2.90309	12.77691	-12.8791
Mollisols TSP320	7.87	0.36	111.00	1.15E-05	0.002775	-4.93761	-2.55674	13.18326	-12.8076
Vertisols TSP0	7.58	0.07	68.00	2.3E-06	0.0017	-5.63881	-2.76955	12.39045	-13.2188
Vertisols TSP80	7.61	0.10	108.00	3.17E-06	0.0027	-5.49946	-2.56864	12.65136	-13.1095
Vertisols TSP160	7.66	0.13	72.00	4.21E-06	0.0018	-5.37557	-2.74473	12.56927	-13.0326
Vertisols P240	7.65	0.17	84.00	5.56E-06	0.0021	-5.25527	-2.67778	12.62222	-12.9053
Vertisols TSP320	7.80	0.29	92.00	9.34E-06	0.0023	-5.0298	-2.63827	12.96173	-12.8298
Aridisols TSP0	7.64	0.06	122.00	1.97E-06	0.00305	-5.7056	-2.5157	12.7643	-13.3456
Aridisols TSP80	7.86	0.07	164.00	2.29E-06	0.0041	-5.63946	-2.38722	13.33278	-13.4995
Aridisols TSP160	7.88	0.08	160.00	2.62E-06	0.004	-5.58115	-2.39794	13.36206	-13.4612
Aridisols TSP240	7.88	0.15	132.00	4.7E-06	0.0033	-5.32767	-2.48149	13.27851	-13.2077
Aridisols TSP320	7.89	0.16	140.00	5.06E-06	0.0035	-5.29546	-2.45593	13.32807	-13.1875

3-RESULTS AND DISCUSSION

The results in **Figure. (1)** showed that the soils that have more available phosphate shifted towards DCP the nearest point to DCP was Mollisols, it means an increase in the availability of phosphorus at booting stage for a wheat plant, but for Vertisols located behind Mollisols it means the solubility phosphorus in Vertisols less than Mollisols. On the other hand, Aridisols located near OCP line. It has appeared that the studied soil order plotted between DCP and OCP the first one (DCP) is the more soluble form of P in comparing with OCP. The phosphorus availability of them can follow the following series Mollisols > Vertisols > Aridisols.

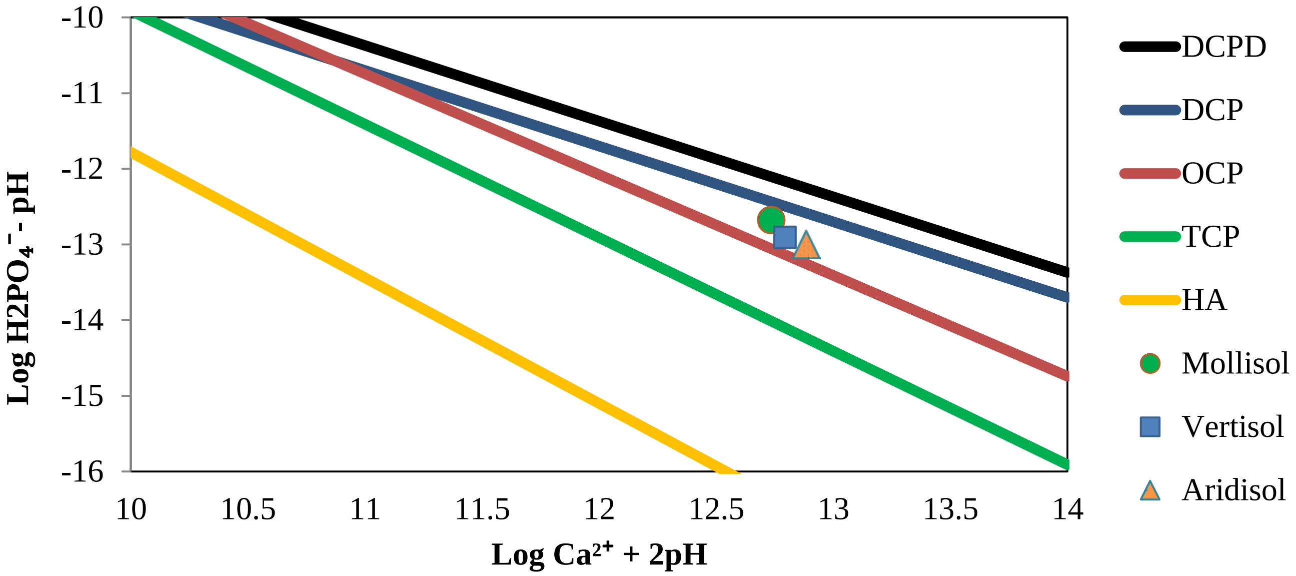

Figure 1. Effect of soil orders on phosphorus status at booting stage for wheat plant

This may be due to higher organic matter content of Mollisols in comparing with other soil orders as recorded in **table (4),** The organic matter is considered as a very important parameter of soil fertility and productivity, however it provides nutrients to the soil, improves water holding capacity and helps the soil to maintain better aeration and soil quality for seed germination and plant root development reported by (Esmail et al., 2018) which could cause hydrolysing P minerals due to releasing organic acids from organic matter reported by Rahman (2013). Or the increase in phosphorus availability at booting stage may be due to the amount of rainfall which may cause dissolving of P due to it is acidic pH (5).

On the other hand, the series of the organic matter content of the soil orders were as follow: M > V >A (31.53, 22,.38, 9,64) mg kg^{-1} **table (4)**. This explains the above series for phosphorus availability depending on solubility diagram. Organic matter may also increase phosphorus solubility through calcium chelating which causes either a permanent or a temporary delay in the formation of basic calcium phosphate.

Table 4.Organic matter content in the soil orders

Orders	Organic matter
	g kg^{-1}
Mollisols	31.53
Vertisols	22.38
Aridisols	9.64

The data analysis in the **table (5)** revealed that the high mean yield value were (3.087, 2.84, 2.71) *Mg* ha^{-1} recorded in soil orders (Mollisols, Vertisols, and Aridisols) respectively explains the above results for phosphorus availability depending on solubility diagram. In Aridisols the amount $CaCO_3$ caused decrease the solubility of phosphorus as mentioned by (Muhawish and Al-Kafaje, 2017a, Rahman, 2013), phosphorus (P) retention and mobilization take place due to precipitation and adsorption in calcareous soils; however, it is not always easy to distinguish between the two mechanisms.

Table 5. Effect of soil orders of wheat yield

Orders	grain yield
	Mg ha^{-1}
Mollisols	3.087
Vertisols	2.84
Aridisols	2.71

Water-soluble P fertilizers applied to soil react with the soil constituents to form less soluble phosphates. When added to soil containing large amounts of calcium, soluble P is usually precipitated as di calcium phosphate or octacalcium phosphate **Figure (2)** shows the effect of levels applied phosphorus on soluble of phosphorus at the booting stage of wheat. Phosphorus application caused shifting the points towards di-calcium phosphate (DCP) and di-calcium phosphate di-hydrate (DCPD) which are more soluble phosphorus compounds. It has appeared from phosphorus solubility diagram, that TSP_0 located on the low soluble form of phosphorus compounds (TCP). While the soils fertilized with TSP_{80}, TSP_{160} and TSP_{240} were plotted between low soluble (OCP) and soluble phosphorus compound (DCP) or application of mentioned TSP levels caused an increase in the availability of phosphorus. On the other hand application of 320 kg TSP ha^{-1} caused shifting the P-status towards the more soluble phosphorus compound (DCPD) or plotted between (DCP and DCPD).

The wheat grain yields were (2.54, 2.85, 3.29) *Mg* ha^{-1} for treatments (TSP_{80}, TSP_{160} ,and TSP_{240}) respectively. The results in figure (2) also explained that the application of different levels of phosphorus caused shifting the points towards di-calcium phosphate (DCP) and di-calcium phosphate di-hydrate (DCPD) which were more soluble phosphorus compounds, it is appeared from phosphorus solubility diagram that the best level was application of 320 kg TSP ha^{-1}, which located between two more soluble phosphorus compounds (DCPD and DCP) caused increase the grain yield to (3.44) *Mg* ha^{-1}, and the lowest yield from TSP_0, which located on OCP line, or (1.51) times increase in grain yield compeering with control reported by (Galaly, 2010, Rasheed, 2019, Rekani et al., 2017). **Figure (3)** illustrated effect of levels applied TSP fertilizers on P-availability at booting stage of the

wheat plant.

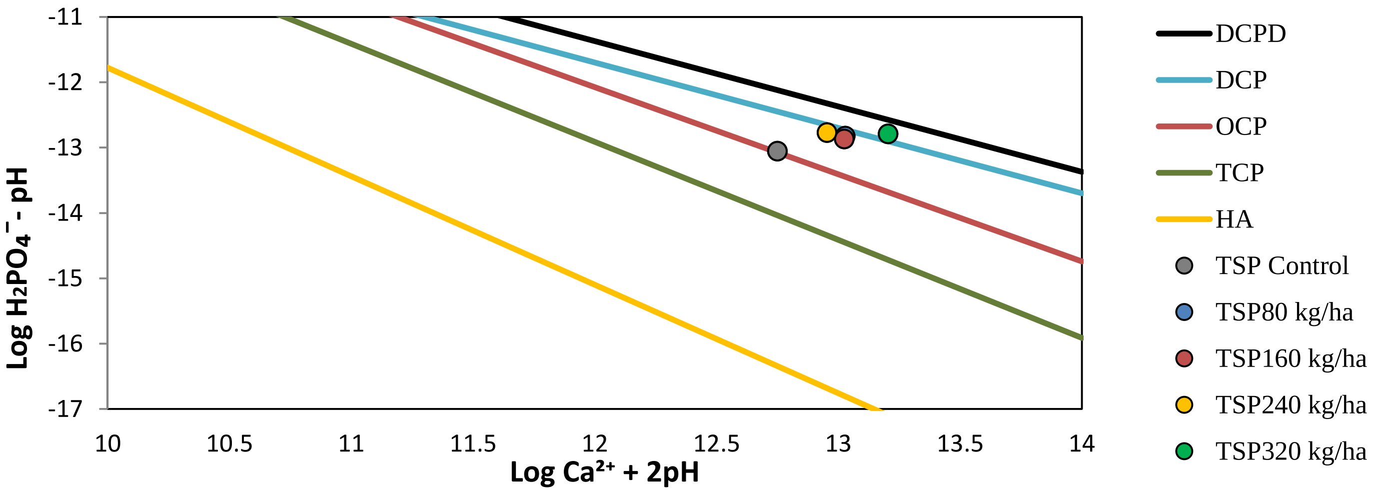

Figure 3. Shows the effect of levels of applaied phosphorus on availability of phosphorus at booting stage of wheat.

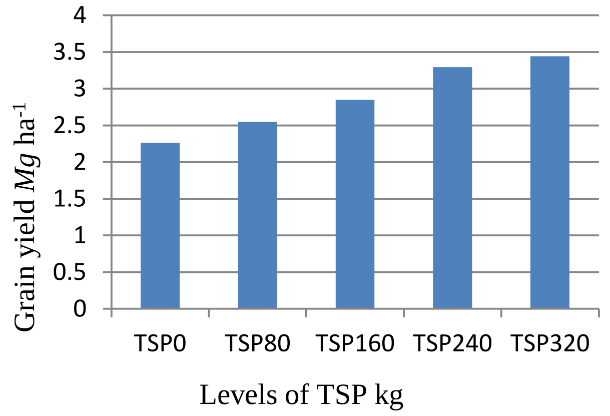

Figure 3. Efect of levels phosphorus on grain wheat

The results in **figure (4)** indicated the effect of combination treatments of phosphorus solubility status. The phosphorus status was divided into four groups as follows:

First group included 6 combination treatments(Mollisols-TSP$_0$, Vertisols-TSP$_0$, Aridisols-TSP$_0$, Mollisols- TSP$_{80}$, Vertisols-TSP$_{80}$ and Vertisols-TSP$_{160}$), which were plotted between OCP and TCP or less soluble group since the phosphorus compounds were OCP or very low soluble TCP.

Second group included only one combination treatment which located on OCP line was (Vertisols -TSP$_{240}$)

The third group was represented 7 combination treatment (Aridisols-TSP$_{80}$, Mollisols-TSP$_{160}$, Aridisols-TSP$_{160}$, Mollisols-TSP$_{240}$, Aridisols-TSP$_{240}$, Vertisols-TSP$_{320}$ and Aridisols-TSP$_{320}$ which were located between OCP and DCP this group shifted towards DCP.

Fourth group included only one combination treatment (Mollisols-TSP$_{320}$) which plotted between soluble phosphorus compounds (DCP and DCPD) this regards as the most soluble phosphorus status.

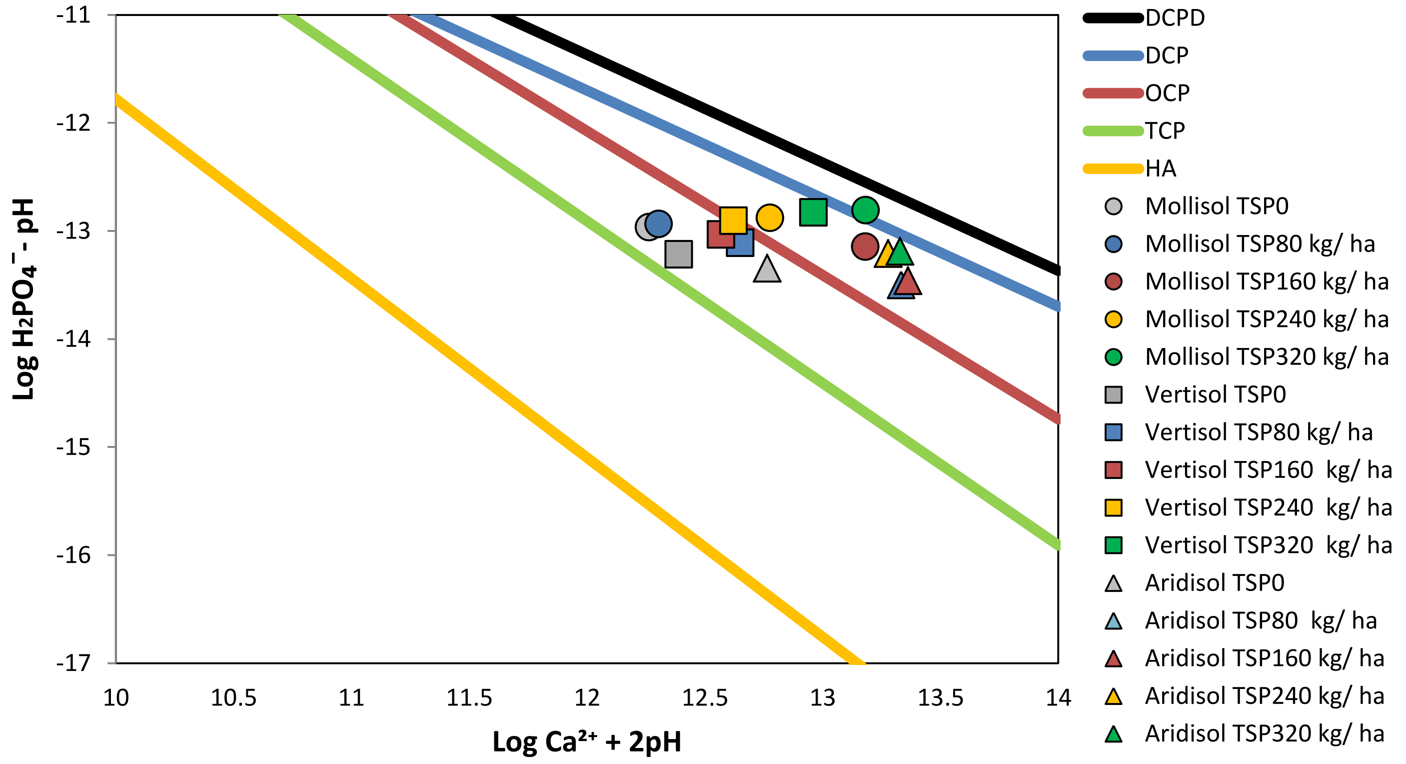

Figure 4. Combination effect soil orders and levels of applied phosphorus on the P- solubility equiliberia at booting stage of wheat plant

The wheat grain yield for the first group were (2.38, 2.38, 2.06, 2.78, 2.55 and 2.88) Mg ha-1 respectively, which the yield for the combination treatment belongs to the second group was (3.06) Mg ha-1, while, the yield for the third group were (2.28, 3.09, 2.58, 3.52, 3.29, 3.34,and 3.31) Mg ha-1 respectively.

On the other hand the highest yield value (3.66) Mg ha-1 was recorded from combination treatment which plotted between DCP and DCPD this may be due to high available phosphorus in the fourth group or the combination treatment of (Mollisols-TSP320) (Figures 4 and 5)

In general moving or shifting the combination treatment toward more soluble phosphorus compound caused an increase in wheat yield due to the role of phosphorus in seed formation and growth mentioned by (Galaly, 2010, Rahman, 2013, Rasheed, 2019, Ahmed and Khoshnaw, 2019). While, the results provide information about the relation between P availability and the dominant soil orders.

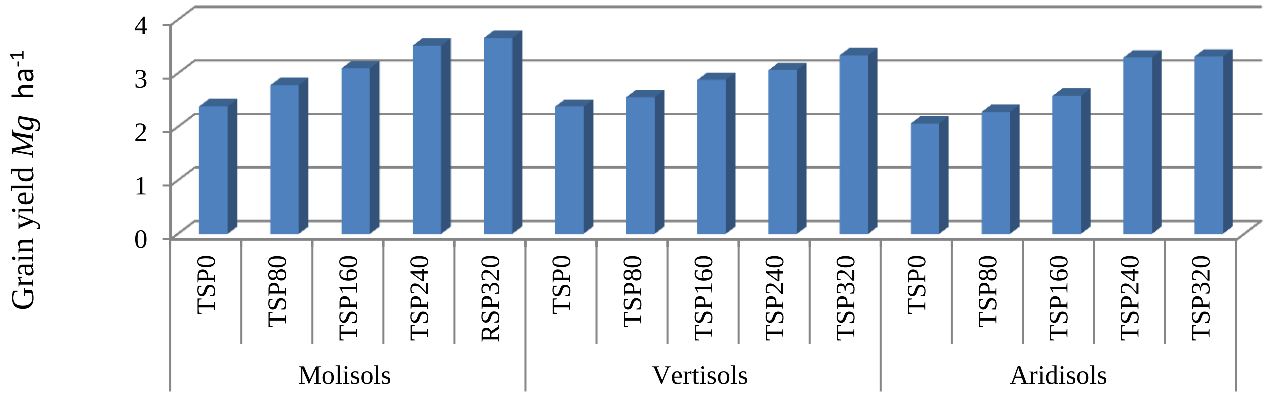

Figure 5. Combination effect of soil orders and levels of applied phosphorus on grain wheat

CONCLUSION

The studied soil orders, levels of applied phosphorus and their combination had a great effect on phosphorus status and wheat yield, due to their effect on forming different phosphorus compounds range between non-soluble to the soluble form of phosphorus compound or from Hydroxyapatite to Di- calcium phosphate di hydrate as explained by solubility diagrams for phosphorus. Application of different levels of phosphorus caused the shifting towards di-calcium phosphate (DCP) and di-calcium phosphate di-hydrate (DCPD). The treatment combination Mollisols TSP_{320} was recorded the highest grain yield.

REFERENCES

AHMED, I. T. & KHOSHNAW, M. R. 2019. Effect of Different Levels of Phosphorus Fertilizer on Heavy Metals Concentration in Corn (Zea mays) Cultivated in Oil Polluted Soil. *Zanco Journal of Pure and Applied Sciences***,** 2218-0230.

BASHOUR, I. I. & SAYEGH, A. H. 2007. *Methods of analysis for soils of arid and semi-arid regions,* FAO.

ESMAIL, A. O. 2012. Effect of Soil Phosphorus Chemical Equilibrium on P-availability for Wheat using Solubility Diagram and (DRIS-Chart) Methods. *Journal Of Kirkuk University For Agricultural Sciences*, 3**,** 43-51.

ESMAIL, A. O., KHOSHNAW, M. R. A., MAHMOOD, B. J. & ABDULRAHMAN, M. K. 2018. Effect of different levels of organic fertilizer and phosphorus on yield, quality and nutrient balance of corn. *journal Kirkuk University For Agricultural Sciences.*, sppecial No**,** 30-37

GALALY, T. 2010. Interaction effect of phosphorus and sulfur on phosphorus availability and some growth parameters of corn plant grown in calcareous soil. *M. Sc. University of Salahaddin College of Agriculture, Department of Soil and Water*.

KARIM, T. 1999. Models to predict water retention of Iraqi soils. *Journal of the Indian Society of Soil Science (India).*

KLUTE, A. 1986. Water retention: laboratory methods. *Methods of soil analysis: part 1—physical and mineralogical methods***,** 635-662.

LINDSAY, W. 1979. Chemical Equilibria in Soils. John Willey & Sons. *New York*.

MCDOWELL, R., DREWRY, J., MUIRHEAD, R. & PATON, R. 2003. Cattle treading and phosphorus and sediment loss in overland flow from grazed cropland. *Soil Research,* 41**,** 1521-1532.

MUHAIMEED, A. S., SALOOM, A., SALIEM, K., ALANI, K. & MUKLEF, W. 2014. Classification and distribution of Iraqi soils. *International Journal of Agriculture Innovations and Research,* 2**,** 997-1002.

MUHAWISH, N. & AL-KAFAJE, R. 2017a. DETERMINING THE OPTIMUM LEVEL OF ORGANIC MATERIAL APPLIED WITH PHOSPHATE ROCK AND THEIR EFFECT ON SOME PHOSPHORUS FORMS IN A GYPSIFEROUS SOIL. *IRAQ JOURNAL OF AGRICULTURE,* 22.

MUHAWISH, N. & AL-KAFAJE, R. 2017b. SOIL ORGANIC CARBON AND PHOSPHORUS STATUS AFTER COMBINED APPLICATION OF PHOSPHATE ROCK AND ORGANIC MATERIALS IN A GYPSIFEROUS SOIL. *The Iraqi Journal of Agricultural Science,* 48**,** 60.

MURPHY, J. & RILEY, J. P. 1962. A modified single solution method for the determination of phosphate in natural waters. *Analytica chimica acta,* 27**,** 31-36.

NACHTERGAELE, F. 2001. Soil taxonomy---a basic system of soil classification for making and interpreting soil surveys. *Geofisica Internacional,* 99**,** 336-337.

RAHMAN, D. K. 2013. The Effect of Peat moss Application on Phosphates Adsorption and Solubility Equilibria in Some Calci-Gypsiferous Soils. *Uuniv. Of Salahaddin –Erbil Iraq M Sc. Thesis.*

.RASHEED, M. S. 2019. Bioavailability of Phosphorus and Zinc in
Calcareous Soils of the Kurdistan region of Iraq. *submitted to the University of Nottingham for the degree of doctor of philosophy*

RASUL, G. A. M. 2016. Effect of phosphorus fertilizer application on some yield components of wheat and phosphorus use efficiency in calcareous soil. *Journal of Dynamics in Agricultural Research,* 3**,** 46-52.

REKANI, O., DOHUK, M., HUSSAIN, M. & DUHOK, U. 2017. Effect of phosphate fertilizer on growth and yield of five cultivars bread wheat. *Iraqi J. Agric. Sci,* 48**,** 1796-1804.

ROY, R. N., FINCK, A., BLAIR, G. & TANDON, H. 2006. Plant nutrition for food security. *A guide for integrated nutrient management. FAO Fertilizer and Plant Nutrition Bulletin,* 16**,** 368.

SHAND, C. 2007. Plant Nutrition for Food Security. A Guide for Integrated Nutrient Management. By RN Roy, A. Finck, GJ Blair and HLS Tandon. Rome: Food and Agriculture Organization of the United Nations (2006), pp. 348, US $70.00. ISBN 92-5-105490-8. *Experimental Agriculture,* 43**,** 132-132.

SHANG, C. & TIESSEN, H. 1998. Organic matter stabilization in two semiarid tropical soils: size, density, and magnetic separations. *Soil Science Society of America Journal,* 62**,** 1247-1257.